FLEXIBLE, ELECTROSPUN POLYACRYLONITRILE BASED CARBON NANOFIBER COMPOSITES FOR ELECTROMAGNETIC INTERFERENCE SHIELDING

A Thesis submitted

In partial fulfilment for the Degree of

Doctor of Philosophy

by

GOVIND KUMAR SHARMA

Department of chemistry

INDIAN INSTITUTE OF SPACE SCIENCE AND TECHNOLOGY

Thiruvananthapuram-695547, Kerala, India

June, 2024

Volume 222 • 25 March 2024 ISSN 0008-6223

ELSEVIER

Carbon

AN INTERNATIONAL JOURNAL

Reporting research on Carbonaceous Materials, their Production, Properties and Applications

EDITOR-IN-CHIEF: **M. Terrones**

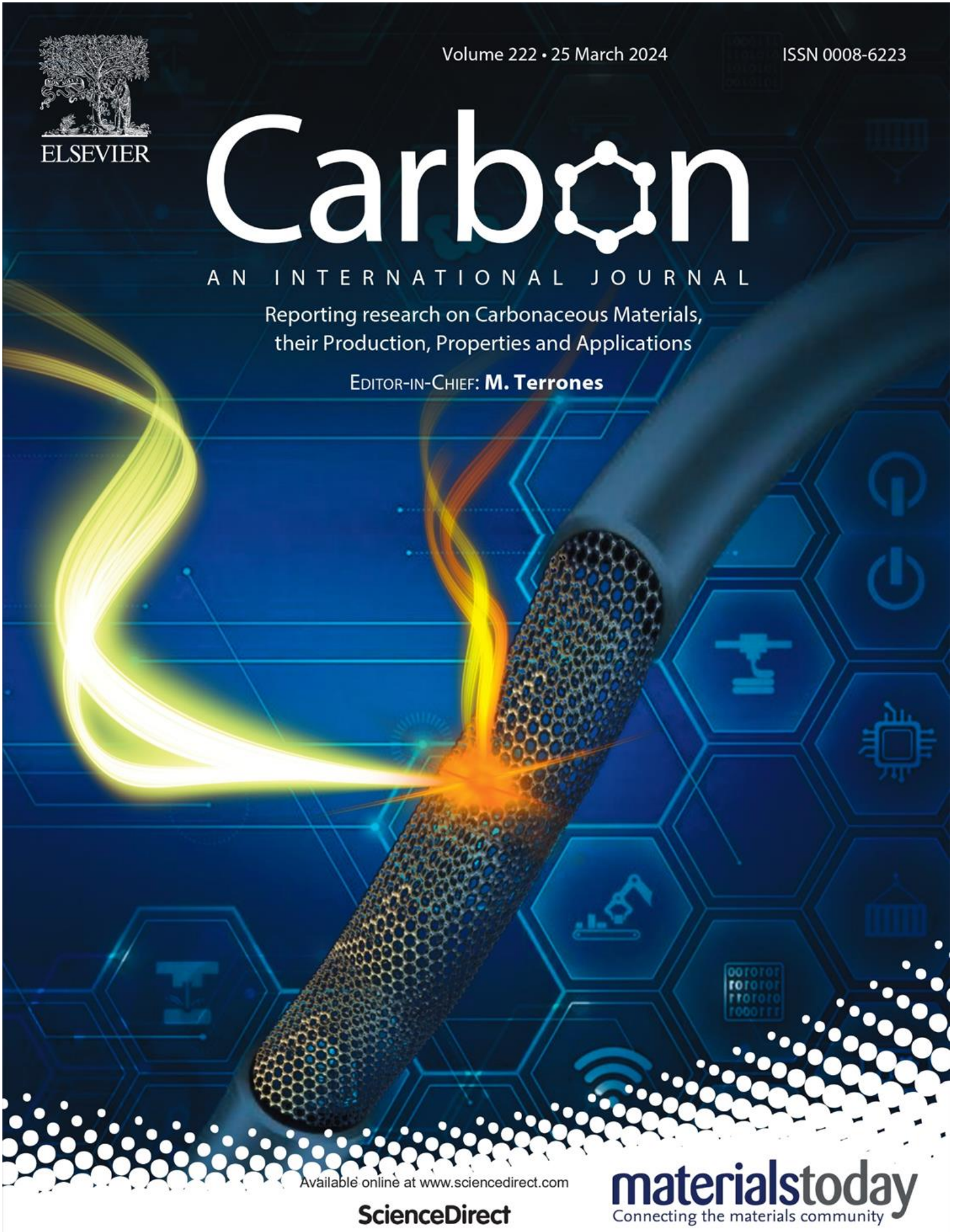

Available online at www.sciencedirect.com

ScienceDirect

materialstoday
Connecting the materials community

Dedicated to my teachers, family, and friends.

Specially dedicated to my younger brother

late. Chander Shekhar Sharma

सत्यमेव जयते

भारतीय अंतरिक्ष विज्ञान एवं प्रौद्योगिकी संस्थान
(वि.अ.आयोग अधिनियम 1956 की धारा-3 के अधीन मानित विश्वविद्यालय घोषित)
भारत सरकार, अंतरिक्ष विभाग, वलियमला पोस्ट, तिरुवनंतपुरम 695 547 भारत

INDIAN INSTITUTE OF SPACE SCIENCE AND TECHNOLOGY
(A Deemed to be University u/s 3 of the UGC Act, 1956)
Government of India, Department of Space
Valiamala P. O, Thiruvananthapuram 695 547 India

www.iist.ac.in

CERTIFICATE

This is to certify that the thesis entitled **FLEXIBLE, ELECTROSPUN POLYACRYLONITRILE BASED CARBON NANOFIBER COMPOSITES FOR ELECTROMAGNETIC INTERFERENCE SHIELDING** submitted by **GOVIND KUMAR SHARMA**, to the Indian Institute of Space Science and Technology, Thiruvananthapuram, in partial fulfilment for the award of the degree of **Doctor of Philosophy**, is a bona fide record of research work carried out by him under my supervision. The contents of this thesis, in full or in parts, have not been submitted to any other Institution or University for the award of any degree or diploma.

Nirmala Rachel James

Supervisor

Professor

Department of Chemistry

Thiruvananthapuram

June 2024

Counter signature of HOD with seal

डॉ. संध्या के. वाई. /Dr. Sandhya K. Y.
आचार्य एवं अध्यक्ष/Professor & Head
रसायन विभाग/Department of Chemistry
भारतीय अंतरिक्ष विज्ञान एवं प्रौद्योगिकी संस्थान
Indian Institute of Space Science and Technology
अंतरिक्ष विभाग, भारत सरकार
Department of Space, Government of India
तिरुवनंतपुरम/Thiruvananthapuram - 695 547

DECLARATION

I declare that this thesis entitled "**FLEXIBLE, ELECTROSPUN POLYACRYLONITRILE BASED CARBON NANOFIBER COMPOSITES FOR ELECTROMAGNETIC INTERFERENCE SHIELDING**" submitted in partial fulfilment of the degree of **Doctor of Philosophy** is a record of original work carried out by me under the supervision of **Dr. Nirmala Rachel James**, and has not formed the basis for the award of any other degree or diploma, in this or any other institution or university. In keeping with the ethical practice in reporting scientific information, due acknowledgements have been made wherever the findings of others have been cited.

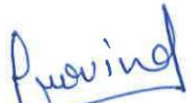

IIST Thiruvananthapuram — **Govind Kumar Sharma**

June 2024 — **SC19D032**

ACKNOWLEDGEMENTS

I would like to express my gratitude to everyone who encouraged and supported me throughout my Ph.D. journey.

First and foremost, I am deeply grateful to my research supervisor Prof. Nirmala Rachel James for her invaluable guidance, continuous support, and patience during my doctoral research work. Her immense knowledge and plentiful experience have encouraged me in all the time of my academic research and daily life. I'm blessed to have her as my Ph.D. supervisor. Her dedication for research and her fast response always motivated me. In addition to my supervisor, I'd like to thank Prof. K Prabhakaran (Former HOD), who offered me the opportunity to work on carbon foam composites for EMI shielding. Discussions with him about carbon-based materials, EMI shielding, and other topics always expanded my knowledge and had great significance to my Ph.D. thesis work. I also like to express my gratitude to Prof. Chinmoy Saha for his insightful suggestions and for providing EMI shielding facilities in Advanced Microwave lab (Department of Avionics).

I express my sincere gratitude to Prof. Kuruvilla Joseph, Dean Academics, IIST, for imparting fundamental knowledge about polymers and polymer composites during my Ph.D. course work. His positive attitude and motivation encouraged me during my research work. I would also like to express my gratitude to my Doctoral committee members: Dr. Roy Joseph (SCTIMST), Dr. R. S Rajeev (VSSC), Dr. V. S Sooraj (IIST), and Dr. Kuruvilla Joseph (IIST). I thank them for their time and effort, also for providing valuable feedback and thought-provoking questions. Their insightful comments have greatly enriched the quality of my work.

I am grateful to the chancellor of IIST, Dr. B. N. Suresh, for his motivational speech on multiple occasions and also for always encouraging space application during research methodology coursework. I express my sincere thanks to the present director, Dr. S Unnikrishnan Nair, former director, Dr. D Sam Dayala Dev, Shri. S. Somanath, and Dr. V. K Dadhwal, of IIST, for providing me with all the research facilities. I would also like to thank the administrative, hostel, and technical staff of IIST for extending their help whenever required. I would like to convey my earnest gratitude to present HOD, Dr. K. Y Sandhya, and former HOD, Dr. K. Prabhakaran of Chemistry Department, IIST for giving me all the assistance I required and the departmental facilities. I thank the office staff, Bindhu J. M, Jayasree R, and Naseema of Chemistry Department for their help related to official work. I

would like to thank technical staff Jayasree L, Bindhu P C, Loveson Albert, and Athul for their assistance. I thank Mr. Satish for Raman spectroscopy (Aerospace Engineering Department, IIST), PSG Coimbatore for TEM analysis, CSIR-NIIST for XPS, and ASD (VSSC) for XRD and SEM analysis.

I want to express my gratitude to other institutes for helping with sample characterization. Prof. Suryasarthi Bose (IISc Bangalore) and his student Dr. Kumari Sushmita for fruitful discussion and EMI shielding tests at the start of my Ph.D. career. Thanks to Prof. Kana M Sureshan (IISER Thiruvananthapuram) and his students, Dr. Rishika Rai and Javed R Pathan for sample characterization. Thanks to Dr. Subodh G. (University of Kerala) and his student Athira Rajan for measuring the dielectric properties.

I would like to thank Dr. Jobin Cyraic, Dr. Gomathi N, Dr. Mary Gladis, Dr. K G Sreejalekshmi, and Dr. Shaiju Nazeer, for their constant feedback throughout my department seminars. Special thanks to Dr. Shaiju for discussing about my Ph.D. thesis and post-doc position during tea time.

Each and every experience throughout the Ph.D. journey is valuable and worth acknowledging because it teaches us to accept change and be adaptive to change. I am grateful to my colleagues, whose support and insightful discussions made my Ph.D. journey easier. I'd like to thank my senior, Sanu Xavier, Dr. Praveen Wilson, Dr. Suijth Vijayan, and Dr. BDS Deeraj, for their assistance and support in choosing EMI shielding materials as my Ph.D. topic. I would like to thank Dr. Vinod Kumar P and Gopika R from the department of Avionics who taught me the fundamentals of VNA and EMI shielding tests. I thank Gaurav Kumar, Kirit More, Nikhil Raj, Rutuj Gharate, Kundan Surse, Anindya Saha, and Shobhit Sharma, for being so helpful with learning MATLAB coding and EM parameters.

I am immensely grateful to my senior lab mates- Yogesh chaudary, Neema, Saisree, Arya, Varsha, Sreekala, Ann Mary, and Chithra Nair, whose encouragement has been an endless source of motivation. The wonderful friends like Kirit More, Ramya P R, Dhiliban S, Surujana, Bhasha, Sreekala, Ann Mary, Varsha, and Chithra Nair during extremely challenging time (COVID-19) makes me feel incredibly grateful and thankful. Juniors lab mates provide us with the most memorable and funniest memories of during experimental time. I thank all my junior lab mates- Ramya, Raji, Sneha, Athira, Prashant Harel Govind, Reshna, Elizabeth, Ardra, Shanshank, Yogesh, Farha, Chithra K R, Dhrisya, Jithu joseph, Sashila, Archana, Krishendu, Rhiya, Gaurav, Atul, Merin, Elsa, Arya, and Julsana.

I express my deepest appreciation to the IIT Gandhinagar community for constantly pushing me to pursue research and for developing my leadership and research skill. Firstly, I thank Dr. Sudhanshu Sharma, who supervised my master's thesis and helped me build my research skills. Proceed to Dr. Arnab Dutta; his pleasant, enthusiastic, positive, supportive and dynamic attitude helped me to enhanced my multitasking ability, along with my scientific research ability. I am indebted to Dr. Chandrakumar appayee, Dr. Iti Gupta, and Dr. Bhaskar Datta to give me opportunity to work on mini project during my M.Sc. course work. I am grateful to Anuj Bisht, Divya Vyas, Praseetha E K, Neha Manav, Varsha, and Pooja Joshi for imparting knowledge on fundamental experimental procedures and enhancing my expertise with instruments. I am very grateful to Sachin Giri and Surya Pratap Singh for downloading the subscription based research articles on my request.

I am grateful to all of my Chemistry faculty for teaching me the fundamentals of Chemistry. Special thanks to Ved Prakash sir and Sahendra sir for teaching me the beauty of Chemistry in an entertaining and simple manner. I am deeply indebted to my Bachelor's professor and Chemistry school teacher (Dr. Amita Puri), whose confidence in me inspired me to pursue higher studies in Chemistry.

I would like to thank all my IIST campus friends for staying with me and extending help whenever needed, both personally and professionally. I specially thank Anindya, Nikhil, shobhit, Pushkar, Rutuj, Paras, Akash Ganguly, Jatin, Akash Mohabe, Abhishek Charri, Gaurav, Dhiliban, Srujana, Kirit more, Yogesh parihar, Vijith, Daanish Handa, Pramod, Avinash, Jyotimoy, Elango, Vibin, Akshay, Srikar, Prankur, Chetan, subareddy, sammuel, Manu, Renjith, James kurain, Jyotish, Deep Raj, Ravi, Sumit, Ranjan, Shanmuk, Karthik, Aibaan, Deepak, Ritik, and Kapil for making IIST stay a wonderful one. I'm also grateful to my sports teacher and coach for teaching in me the concept that practice makes perfect and that only the best team will win the tournament. During my Ph.D., I attempted to put together a strong NRJ team for better research result. I also thank my friend Omesh, Ravindra, Sarvesh, Yogesh, Manas, Surya, Naveen, and Rajveer for boosting my confidence always.

My family's support has been priceless throughout my life and cannot be adequately expressed. But still, I would like to convey my heartfelt gratitude to my grandmother and grandfather for their love, support, and insightful thoughts about life. Special thanks to my mother and father for their dedication and best care for me and, most importantly, providing me with the most excellent education they could at that time. I would like to thank my elder

brother Arvind and Amit for guiding me in science, technology, and their suggestions for future. I thank my sister Priyanka for illustrating some figures in my research articles and also for designing a cover art.

I also thank University Grant Commission New Delhi, India for a research fellowship throughout my Ph.D. Degree.

Indeed, I would like to thank all my well-wishers, teachers, and friends who assisted and supported me throughout my life. My Ph.D. journey is amazing and interesting because of my supervisor, collaborators, lab mates, and colleagues.

ABSTRACT

The rapid advancement of wireless communication technology, 5-G technology, and the miniaturisation of electronic equipment, and complexity of inbuilt circuitry cause electromagnetic interference (EMI) or EM pollution. EMI can affect human health, disturb the regular functioning of electronic equipment and it can also completely damage the electronic equipment. The demand for EMI shielding materials is rapidly increasing as the EM pollution and EMI become more complex. As a result, high-performance EMI shielding materials are required to protect human health and protect the electronic equipment employed in domestic, civil, or military applications. Metals and metal alloys were previously used to protect against EMI. However, metals are restricted in applications in EMI shielding due to their heavy weight, low corrosion resistance, and the emerging demands for flexible and miniaturised equipment. Thus, flexible, lightweight, water proof, and high-performance EMI shielding materials are on great demand.

Polymer composites have emerged as a superior option for EMI shielding materials due to their lightweight nature, corrosion resistance, and ease of manufacture. Polymer composites are promising EMI shielding materials because they can be tailored to meet commercial requirements while eliminating the majority of the disadvantages associated with conventional materials. But mostly, polymers are insulators and hence difficult to acquire EMI shielding properties. Hence, polymer composites which are made conductive by the addition of fillers are being explored for EMI shielding applications. However, composites require high loading of fillers which may cause poor dispersibility of fillers into the polymer matrix, poor interfacial polarization, and poor 3-D interconnected conductive network and may result in inferior EMI shielding properties than expected.

This thesis reports preparation of flexible and hydrophobic EMI shielding materials with synergistic effects of conductive CNF, fillers, and PDMS as polymer matrix. Polyacrylonitrile nanofiber is used as the precursor for carbon nanofibers (CNFs). Electrospinning which is a simple and versatile method for preparation of nanofibers is used in this study to produce 1-D nanostructure fibers with a large surface area, high porosity, and good interconnectivity, which could serve as an effective platform for the absorption and multiple internal reflection of EM waves inside shielding materials. Heat treatment of the electrospun polyacrylonitrile (PAN) nanofiber yielded carbon nanofibers (CNFs). The

carbonization of electrospun PAN fiber formed strong 3-D interconnected electrical conductive with good EMI shielding properties. Two approaches were adopted to enhance the EMI shielding property of CNF. In the first strategy, CNF was subjected to simple post treatment like coating with a conducting polymer while in the second strategy, CNF incorporated with various fillers were explored.

In the first approach, (chapter 4) CNF was coated with poly(3,4-ethylenedioxythiophene): polystyrene sulfonate (PEDOT:PSS) with the assistance of polyvinylpyrrolidone (PVP). The material exhibited high EMI SE of 44 dB in the frequency range of 8-26.5 GHz with a thickness of 0.06 mm due to the synergetic effect of CNF matrix, PEDOT: PSS, and PVP. It also exhibited a SSE_t of 5678 dB cm^2 g^{-1} with low loading of PEDOT:PSS-PVP.

The second approach is to incorporate fillers into the CNF and distribute the fillers thoroughly and uniformly on individual fibres to improve EMI shielding. The incorporation of fillers into CNF first extends the 3-D interconnected electrical conductive network, then improves the electrical conductivity of CNF, it also forms hetero-interfaces that enhance interfacial polarization, and finally forms strong dipole polarization in the presence of EM waves. All of these parameters improved the EMI shielding properties of the fillers-incorporated CNF.

Chapter 5 concerns Tellurium nanoparticles (Te NPs) incorporated CNF (**Te-CNF**) for EMI shielding. Tellurium is a metalloid with a narrow band gap which belongs to chalcogen family and incorporation of Te-NPs in CNF may alter the electronic properties to improve 3-D conductive network. Te NPs also can introduce polarization sites and hetero interfaces in CNF. The Te-CNF exhibited an average EMI SE and SSE_t of 37.1 dB and 9280 dB cm^2 g^{-1} respectively, at a thickness of 0.08 mm and a density of 0.499 g cm^{-1} and possessed a high electrical conductivity of 0.68 S cm^{-1}.

Chapter 6 presents work on Nb_2O_5 NPs incorporated CNF (**Nb_2O_5-CNF**) for EMI shielding applications in wide frequency range (8.2 GHz – 26.5 GHz). Nb_2O_5 is a semiconductor, and their electrical conductivity can be enhanced by addition of carbonaceous materials. Uniform distribution of Nb_2O_5 NPs in 1-D N-doped CNF may increase dielectric loss and sites for polarization loss, interfacial polarization, and multiple internal reflections. The EMI SE of the resulting Nb_2O_5-CNF was improved from 57 dB to 67 dB as the loading of Nb_2O_5 NPs increased from 33 wt.% to 50 wt.%. The thickness of the material was 0.08 mm

and more than 80 percent of SE_T was contributed by SE_A. Nb_2O_5-CNF exhibited high SSE_t value of 3295 dB cm^2 g^{-1} with 33 wt% loading of Nb_2O_5 NPs in CNFs. The excellent EMI shielding performance of Nb_2O_5-CNF can be attributed to their high electrical conductivity due to the formation of conductive paths with CNF and Nb_2O_5, as well as interfacial and dipole polarization due to the presence of Nb_2O_5.

Chapter 7 concerns with preparation of perovskite metal oxide ($La_{0.85}Sr_{0.15}CoO_3$) (LSCO) NPs by sol-gel method followed by calcination at 900 ºC and incorporation of the prepared LSCO NPs into CNFs through electrospinning, followed by heat treatment. As the loading of LSCO NPs in CNFs increases from 10 wt% to 25 wt%, the EMI SE increases from 34 dB to 45 dB with a thickness of 0.08 mm. LSCO-CNFs exhibited high SSE_t value of 7672 dB cm^2 g^{-1} with 25 wt% loading of LSCO NPs in CNFs. The LSCO-CNFs exhibited high EMI shielding properties because of their high electrical conductivity leading to the formation of conductive paths with CNFs, interfacial polarization as well as dipole polarization due to the multicomponent heterogeneous interfaces and the dielectric loss due to the defects produced by Sr doping in $LaCoO_3$.

The effect of alignment of CNF and alignment of $BaTiO_3$ NPs CNF on EMI shielding properties are presented in chapter 8. The alignment of $BaTiO_3$ NPs enhanced their piezoelectric, ferroelectric, and dielectric properties. The aligned $BaTiO_3$-CNF exhibited a higher EMI SE of 81 dB compared to the non-aligned $BaTiO_3$-CNF (61 dB). The high EMI SE value is due to high dielectric properties of $BaTiO_3$ NPs and formation of 3-D electrically conductive network of CNF. The alignment of CNF enhanced the electrical conductivity along the fiber axis. The synergistic effect of $BaTiO_3$ NPs and CNF was improved the EMI shielding performance.

Chapter 9 concerns with carbonic filler namely carbon black super P (CBSP) incorporated into CNF (**CBSP@CNF**). Herein, CBSP covered the surface of the individual fibers and also was incorporated inside the fibers. Due to this, CBSP@CNF possessed high electrical conductivity of 2.5 S cm^{-1} and exhibited excellent EMI shielding property. With a thickness of 0.06 mm and a density of 0.63 g cm^{-3}, CBSP@CNFs showed high EMI SE over a wide frequency range (8.2-26.5 GHz). The highest and average values of EMI SE in the range were 55 dB and 50 dB respectively. The CBSP@CNFs with 9 wt% and 16.6 wt% loading of CBSP exhibited 24,837 and 14741 dB cm^2 g^{-1} of SSE_t, respectively, which is remarkably higher than the most reported EMI shielding materials.

CNF is fragile and brittle in nature. So, in this study, polydimethylsiloxane (PDMS), which is a common flexible substrate has been used to improve the flexibility of CNF. Ease of handling of CNF as well as fillers incorporated CNF could be improved by making flexible PDMS composites of CNF. The PDMS composites of the CNFs discussed above exhibited similar EMI shielding behavior in the frequency range 8.2 – 26.5 GHz.

Carbon nanofibers (CNFs) coated with conducting polymers and incorporated with suitable fillers and their PDMS composites can open up new possibilities towards large scale production of lightweight, flexible, water proof, and easy-to-integrate materials to shield workspaces, surroundings, and complex electronic circuits against unwanted EM radiations.

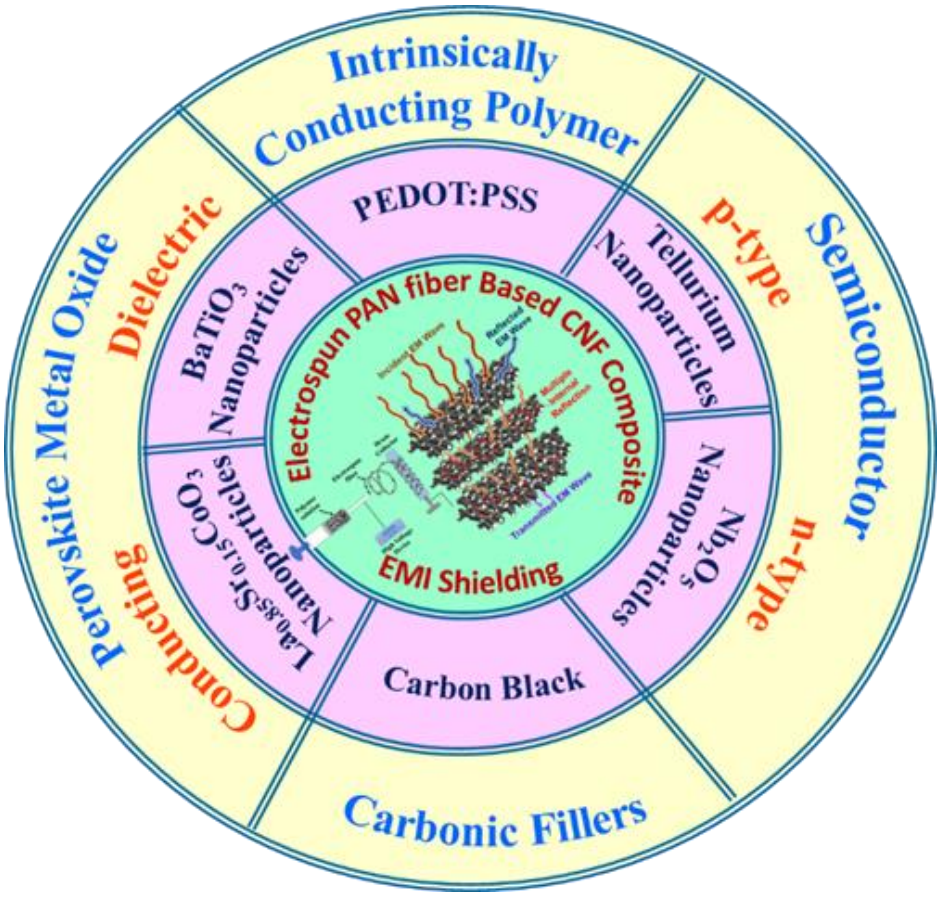

ACS APPLIED NANO MATERIALS

March 22, 2024
Volume 7
Number 6
pubs.acs.org/acsanm

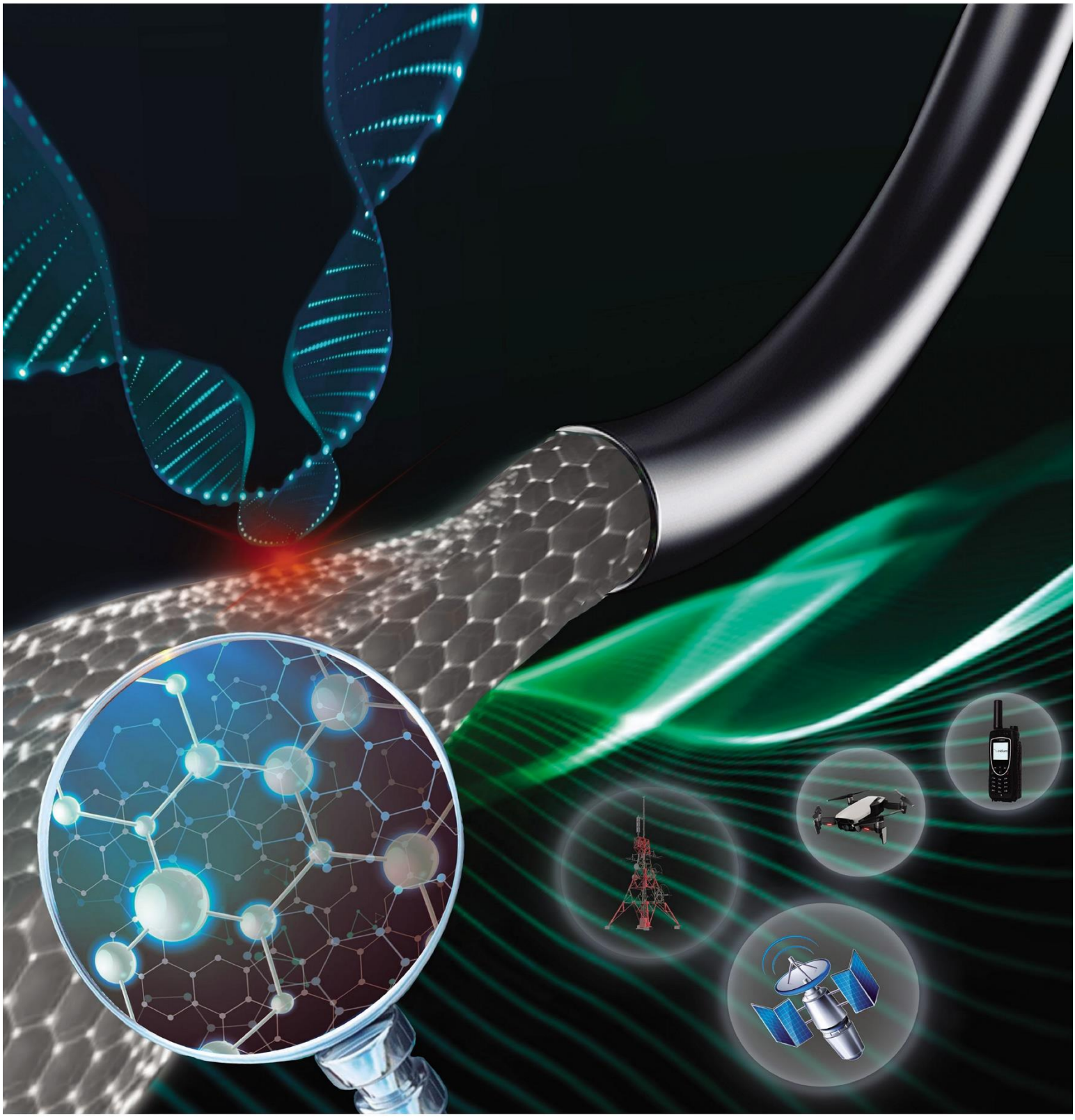

ACS Publications
Most Trusted. Most Cited. Most Read.

www.acs.org

TABLE OF CONTENTS

LIST OF TABLES

LIST OF FIGURES

CHAPTER: 2

CHAPTER: 3

CHAPTER: 5

CHAPTER: 7

CHAPTER: 8

CHAPTER: 9

CHAPTER: 10

ABBREVIATIONS

PAN	Polyacrylonitrile
PDMS	Polydimethylsiloxane
PEDOT	Poly(3,4-ethylene dioxythiophene)
PSS	Polystyrene Sulfonate
PVP	Polyvinylpyrrolidone
PANI	Polyaniline
PEO	Polyethylene oxide
PEG	Polyethylene glycol
PS	Polystyrene
PA6	Polyamide 6
PVDF	Polyvinyl difluoride
PPy	Polypyrrole
EM	Electromagnetic
EMI	Electromagnetic Interference
EMI SE	Electromagnetic Interference shielding effectiveness
CF	Carbon Fiber
CNF	Carbon Nanofiber
EF	Electrospun fiber
NF	Nanofiber
NP	Nanoparticle

VNA	Vector Network analyser
SE	Shielding effectiveness
SE_T	Total shielding effectiveness
SE_R	Shielding effectiveness due to reflection
SE_A	Shielding effectiveness due to absorption
SE_{MR}	Shielding effectiveness due to multiple reflection
SSE	Specific shielding effectiveness
SSE_t	Absolute shielding effectiveness
ICPs	Intrinsic conducting polymer
r-GO	Reduced Graphene oxide
DFT	Density functional theory

NOTATIONS

R	Reflection coefficient
A	Absorption Coefficient
T	Transmission coefficient
S	Scattering parameter
S_{11}	Forward reflection coefficient
S_{21}	Forward transmission coefficient
S_{12}	Reverse transmission coefficient
S_{22}	Reverse reflection coefficient
P_{in}	Incoming Power
P_{out}	Outgoing Power
E_i	Strength of the incident electric field
E_t	Strength of the transmitted electric field
H_i	Strength of the incident magnetic field
H_t	Strength of the transmitted magnetic field
dB	Decibels
δ	Skin depth
f	EM wave frequency
σ	Electrical conductivity
μ_r	Relative magnetic permeability
ε_r	Relative complex dielectric permittivity

ε_r’	Real permittivity
ε_r”	Imaginary permittivity
1-D	One dimensional
2-D	Two dimensional
3-D	Three dimensional
mL	milliliters
h	Hour
µm	micrometer
nm	nanometer

Vol. 9 • No. 1 • January 8 • 2024
www.advmattechnol.com

ADVANCED MATERIALS TECHNOLOGIES

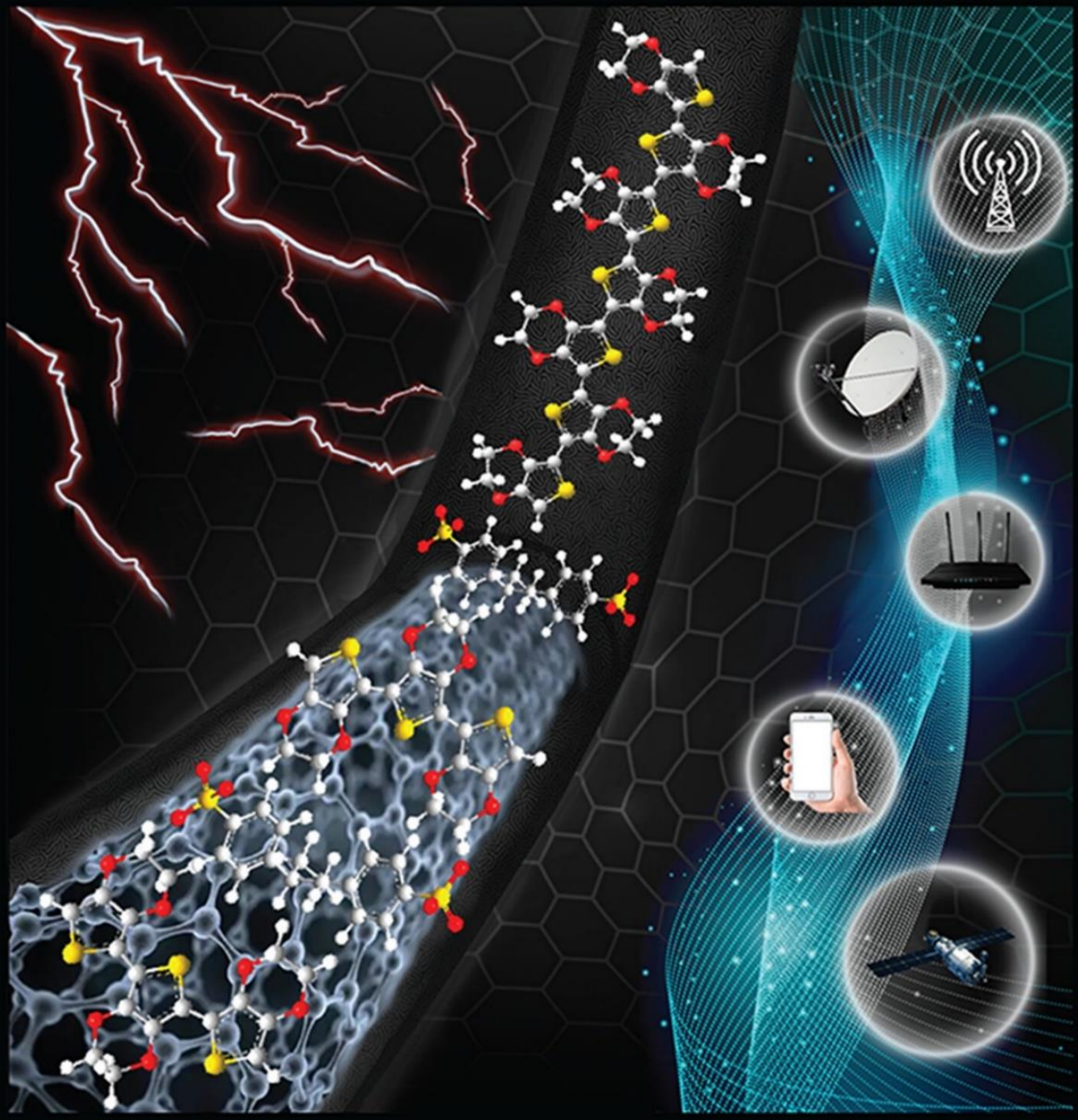

WILEY VCH

CHAPTER: 1

An Introduction to Electrospun Fiber Composites for EMI shielding

Overview

The aim of this chapter is to provide insight into applications of electrospun fiber (EF) composites for electromagnetic interference (EMI) shielding. This chapter summarises the key literature on fabrication methods of electrospun fiber composites for EMI shielding applications, different types of fillers, and their effects on EMI shielding characteristics. This introduction chapter attempts to highlight the enormous potential of electrospinning technology in the development of specialist materials for EMI shielding.

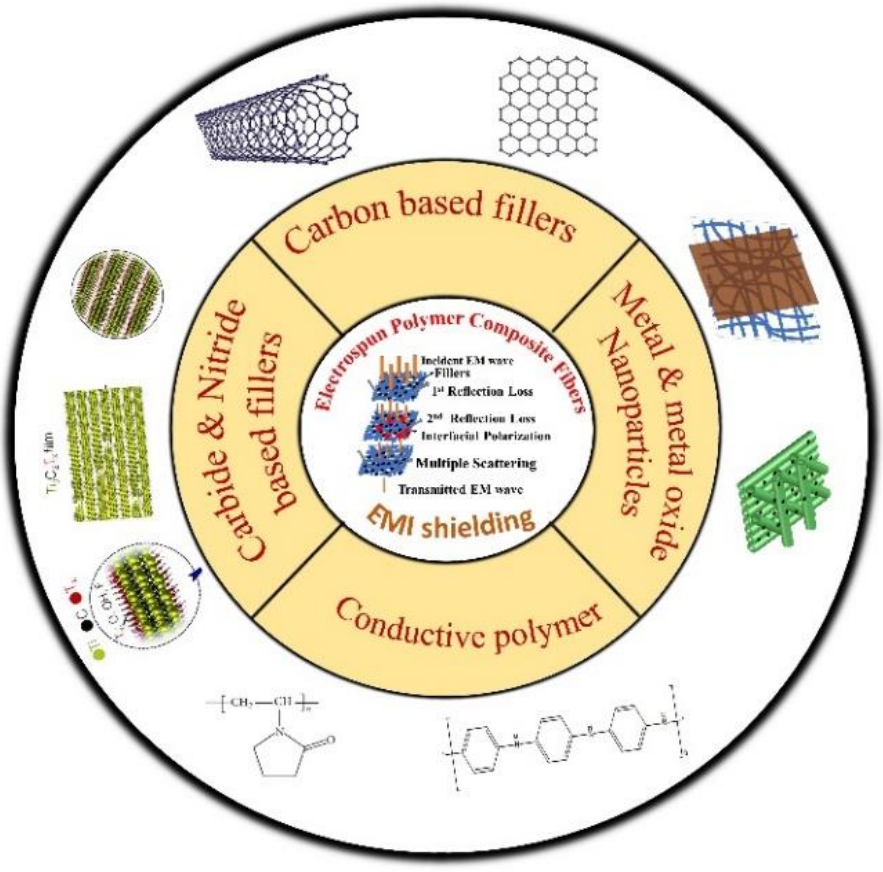

1. Introduction

1.1 EMI Shielding

The widespread usage of wireless technologies, microelectronics, digital technologies, and wearable electronics devices generate undesirable electromagnetic interference (EMI), also known as electromagnetic (EM) pollution. EMI is known to disrupt the normal operation of sensitive electronics in medical, communication, household, and military applications. In addition to EMI, prolonged exposure to EM radiation can have detrimental effects on both human health and lives of other living organisms. The harmful impacts of EMI are further aggravated by the emergence of fifth-generation (5G) and sixth-generation (6G) wireless platforms, the growing use of miniaturized and compact electronic equipment, the mass production of high-frequency medical devices, and the large-scale development of military equipment. As a result, mitigating the harmful effects of EMI is crucial for maintaining human health, life of other organisms, and durability of electronic equipment (Ganguly et al., 2018; Geetha et al., 2009; Hashemi et al., 2022; Shahzad et al., 2016).

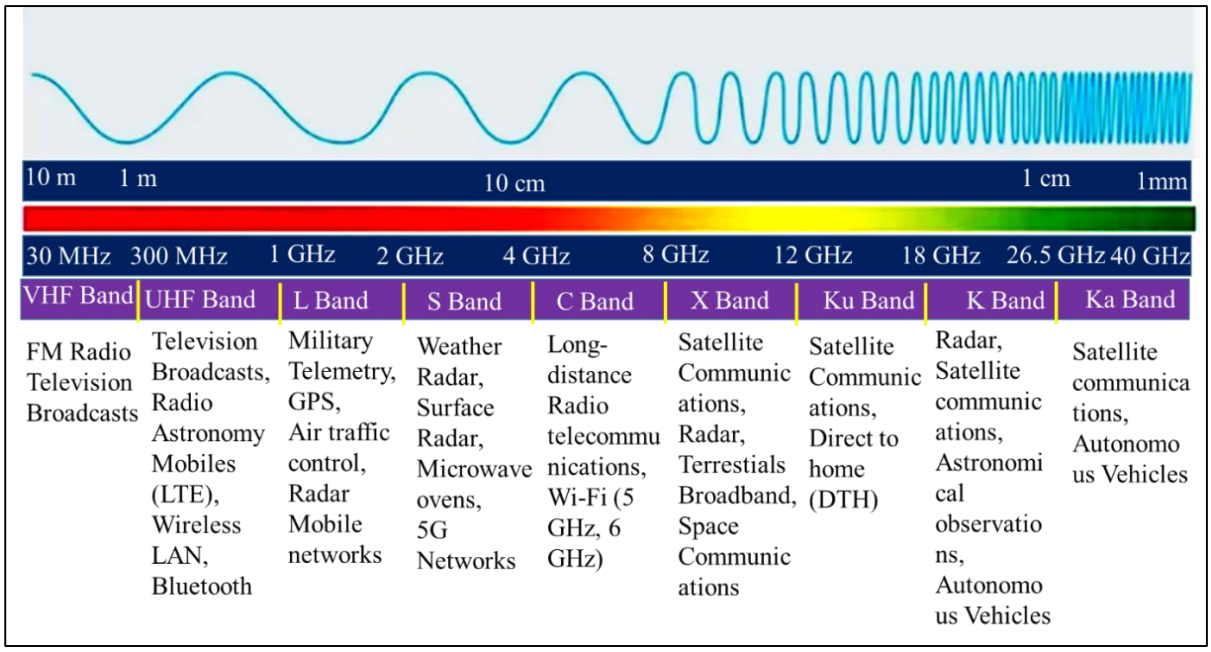

Figure 1.1: Microwave frequency bands and their applications. Reproduced from https://www.rfpage.com/microwave-frequency-bands/

To address these challenges, high-performance EMI-shielding materials are required to reduce the impact of EMI for electronic devices. Most electronic devices used in satellite communication, military equipment, and biological systems operate in the microwave

frequency region as mentioned in **Figure 1.1**. Thus, shielding materials which can perform shielding in this region assume importance.

1.1.1 EMI Shielding Mechanism

EMI shielding materials are designed to protect a specific device or zone from interference by strategically placing the shielding materials to limit unwanted emissions, while also protecting electronic equipment from stray signals. The primary mechanism of EMI shielding is reflection of radiations by mobile charge carriers, which interact with EM fields. For this reason, EMI shielding materials must be electrically conductive. The secondary mechanism of EMI shielding is absorption of EM radiations caused by interaction of the material's electric and magnetic dipoles with the EM radiation. The third process is multiple internal reflections, in which the EM waves are reflected numerous times inside the material due to the interfaces or defect sites present in the material (J. Cheng et al., 2022; Hashemi et al., 2022; D. Jiang et al., 2019; Rajesh Kumar et al., 2021; L. Wang et al., 2021). The remaining EM waves penetrate through the material and is transmitted to the other side, as shown in **Figure 1.2**.

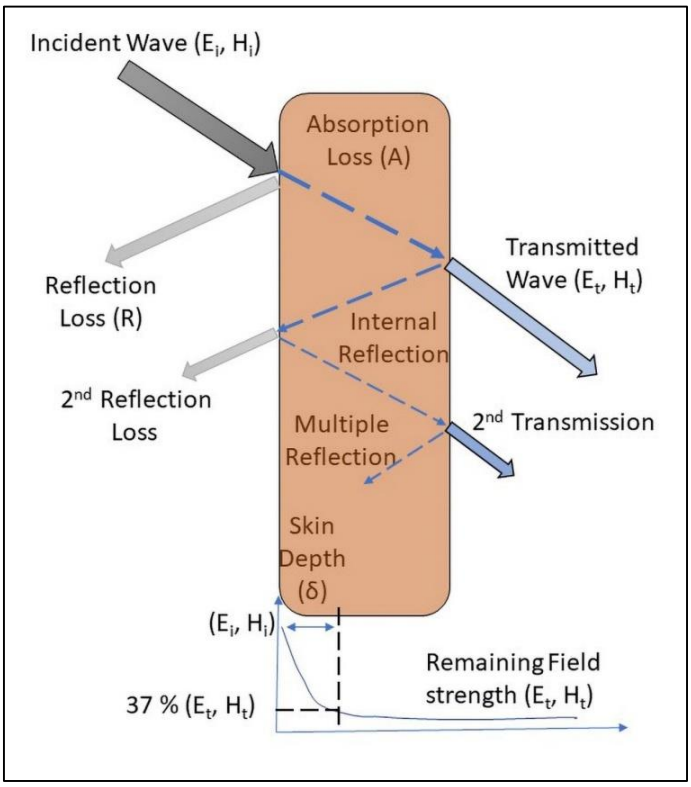

Figure 1.2: Schematic illustration of EMI Shielding mechanism.

1.1.2 EMI Shielding Effectiveness (EMI SE)

The EMI SE measures the ability of a shielding material to attenuate undesirable EM radiations. It is the ratio of incoming power and outgoing power.

$$SE_P = 10 \log \frac{P_{in}}{P_{out}} \quad (1)$$

$$SE_E = 20 \log \frac{E_i}{E_t} \quad (2)$$

$$SE_H = 20 \log \frac{H_i}{H_t} \quad (3)$$

Where SE_p, SE_E, *and* SE_H are the shielding effectiveness represented in terms of power, electric field and magnetic field, respectively. P_{in} and P_{out} are the incoming and outgoing power, E_i and E_t are the strength of the incident electric field and transmitted electric field, and H_i and H_t are the strength of the incident magnetic field and transmitted magnetic field, respectively. The EMI SE is expressed in decibels (dB).

The power of the reflected and transmitted EM wave is controlled by the impedance of materials and the medium. When the EM waves travel inside materials, power of the transmitted EM wave will decrease exponentially. The distance at which the power becomes equivalent to $\frac{1}{e}$ or 37% (where e is Euler's number and $\frac{1}{e}$ = 0.37) of the incident power is known as skin depth (δ) as shown **in Figure 1.2**, and it is calculated using **Equation (4).**

$$\delta = \frac{1}{\sqrt{\pi f \mu \sigma}} \quad (4)$$

where f is EM wave frequency, σ is conductivity, and μ is relative permeability of the shielding material (Ganguly et al., 2018; D. Jiang et al., 2019; Kerkeni et al., 2016)**.**

The total EMI SE (SE_T) is the summation of the contributions of shielding effectiveness by reflection loss (SE_R), absorption loss (SE_A), and multiple internal reflections (SE_M), as mentioned in **Equation (5)**.

$$SE_T = SE_R + SE_A + SE_M \quad (5)$$

The reflection coefficient (R), absorption coefficient (A), and transmission coefficient (T) can be measured from Vector network analyzer (VNA) through scattering parameters (S-parameters) (S_{11}, S_{21}, S_{12}, and S_{22}) according to the following equations, where, S_{11} is forward

reflection coefficient, S_{22} is reverse reflection coefficient, S_{12} is reverse transmission coefficient and S_{21} is forward transmission coefficient.

$$R = |S_{11}|^2 = |S_{22}|^2 \quad (6)$$

$$T = |S_{12}|^2 = |S_{21}|^2 \quad (7)$$

$$A = 1 - R - T \quad (8)$$

The absorption efficiency or effective absorbance (A_{eff}) for EM wave that transmits in the shield material can be described as:

$$A_{eff} = \frac{1-R-T}{1-R} \times 100 \quad (9)$$

SE_R, SE_A, and SE_T are calculated using the following equations:

$$SE_R = 10 \log \left(\frac{1}{1-R}\right) = 10 \log \left(\frac{1}{1-|S_{11}|^2}\right) \quad (10)$$

$$SE_A = 10 \log \left(\frac{1-R}{T}\right) = 10 \log \left(\frac{1-|S_{11}|^2}{|S_{21}|^2}\right) \quad (11)$$

$$SE_T = SE_R + SE_A = 10 \log \left(\frac{1}{|S_{21}|^2}\right) \quad (12)$$

Theoretical calculation of EMI SE is possible by transmission line theory using **equations 13 and 14.** (Ganguly et al., 2018). These equations are generally applicable to calculate EMI SE of metal coating such as electroplating or vacuum deposition based shielding materials.

$$SE_A = 8.7t\sqrt{\pi f \mu \sigma} \quad (13)$$

$$SE_R = -10Log\left(\frac{\sigma}{16 f \epsilon \mu}\right) \quad (14)$$

The specific EMI shielding effectiveness (SSE), absolute EMI shielding effectiveness (SSE_t), and EMI shielding efficiency (%) are calculated by the following equations:

$$SSE = \frac{EMI\ SE}{density} = \frac{dB}{cm^3 g^{-1}} = dB\ cm^3\ g^{-1} \quad (15)$$

$$SSE_t = \frac{SSE}{thickness} = \frac{dB\ cm^3 g^{-1}}{cm} = dB\ cm^2\ g^{-1} \quad (16)$$

$$\text{Shielding efficiency (\%)} = 100 - (10^{SE/10})^{-1} \times 100 \quad (17)$$

For commercial requirements, the EMI SE value and shielding efficiency should be greater than 20 dB and 99 %, respectively. **Table 1.1** illustrates the relation between EMI SE and shielding efficiency (J. Cheng et al., 2022; Ganguly et al., 2018; Geetha et al., 2009; Shukla, 2019; Yali Zhang & Gu, 2022).

Table 1.1: Relation between EMI SE and shielding efficiency (Y.-L. Cheng et al., 2016)

EMI SE (dB)	0 10	20	30	40	50	60	70
Shielding efficiency (%)	0 90	99	99.9	99.99	99.999	99.9999	99.99999

1.2 Polymer Composites for EMI Shielding

Metals and metal alloys are the most common EMI shielding materials. However, typical EMI shielding materials based on metals and alloys are limited in their uses due to their heavy weight, low mechanical flexibility, and poor corrosion resistance. Furthermore, miniaturisation and the desire for flexible electronics demand creation of more effective EMI shielding materials. Reflection is the main mechanism for metal and metal alloy-based shielding materials and hence result in secondary EMI. Thus, flexible, lightweight, and high-performance EMI shielding materials with absorption dominant EMI shielding mechanism are quite important (Kruželák et al., 2021; Sankaran et al., 2018; Shijie Zhang et al., 2023).

Polymer composites have emerged as a better alternative to metal-based EMI shielding materials due to their lightweight, corrosion resistance, and ease of production. Apart from the problems of metal corrosion and secondary EMI, flexibility, miniaturization, and complexity of electronic circuits are the primary reasons for seeking alternative shielding materials. To address these concerns and meet the criteria, polymer composites with easy processability, flexibility, and low density have attracted attention as EMI shielding materials. Polymers are either insulators or intrinsic conductors (ICPs). The primary requirement for EMI shielding material is that they should be electrically conductive. So, polymers which are insulators are used as polymer matrix and ICPs are used as either matrix or fillers for preparing EMI shielding materials. Various types of conductive fillers can be employed to improve the electrical conductivity of polymer composites, which also improves their mechanical properties (Ariati

et al., 2021; Kaliyaraj Selva Kumar et al., 2020; Maruthi, Faisal, & Raghavendra, 2021; Soares et al., 2021; Teixeira et al., 2021; Zahid et al., 2021a, 2021b).

In recent years, many processing techniques have been used to create materials with EMI shielding properties. Electrospinning is a promising technology for developing distinctive materials with distinct morphologies for a variety of applications, including EMI shielding. The last three decades have seen amazing breakthroughs in materials processing techniques, and electrospinning is no exception. The large number of articles in the subject demonstrates the growing interest in using this technology to create novel materials. Investigations on electrospun materials for EMI shielding purposes gained momentum in the last two decades. The electrospinning technology is recognised as a potential processing technique for producing low-thickness, flexible, wearable, and lightweight composite materials with a number of desirable qualities for usage in a wide range of applications, including EMI shielding. The features of electrospun polymer nanofibers, such as large specific surface area, porosity, and significant interconnectedness, can aid in the effective absorption and multiple internal reflections of EM waves within these materials, making them useful in EMI shielding. The EMI shielding properties of electrospun fibres can be improved by using appropriate conductive fillers and post treatments such as coating, electro less deposition, hot pressing, and heat treatment. Thus, electrospun polymer fiber based composite - membranes offer considerable advantages as effective EMI shielding materials in lightweight, flexible, smart, and miniaturised electronic devices in both civil and military applications (Blachowicz et al., 2022b, 2022c, 2022a; Hashemi et al., 2022; Rani et al., 2023; Zheng, Cao, et al., 2023).

1.3 Electrospun fibers (EF) for EMI Shielding

1.3.1 Electrospinning: The technique and principle

Electrospinning (electrostatic fibre spinning) has been developed as an advanced, cutting-edge, and dynamic process since the late 1990s due to its ease in producing nanofibers with a range of materials. It produces micro threads with sizes as small as nanometers (nm) by applying an electric field. Numerous industries, including tissue engineering, filtration, energy, biotechnology, and sensors, use electrospun fibre membranes extensively (Yan Li et al., 2018; X. Shi et al., 2015; J. Xue et al., 2019a; Zhenfang Zhang et al., 2021).

Electrospinning is a voltage-driven technology that employs an electro-hydrodynamic process. A high voltage is applied to the polymer solution, and a liquid droplet is electrified to generate a jet, which is then stretched and elongated to produce fibers. The diameter of these fibres

varies from nm to a few micrometres (J. Xue et al., 2019a). One of the key advantages of electrospinning is its processing versatility, which enables the production of fibres with a wide range of configurations and morphological characteristics. To understand the fundamental principle of electrospinning, consider a spherically charged droplet of a low molecular weight conducting liquid in vacuum. The liquid droplet is subjected to two forces: (1) disintegrative repulsive force and (2) surface tension, both of which attempt to maintain the liquid droplet's spherical shape. **Figure 1.3** illustrates the configuration of a basic electrospinning setup. The basic electrospinning setup consists mostly of three parts: (1) a high voltage power supply, (2) a spinneret (metallic needle), and (3) a grounded collector (metal drum or plate). (B.-S. Lee, n.d.; Yifu Li et al., 2019b; Liang et al., 2020; Mamun et al., 2021).

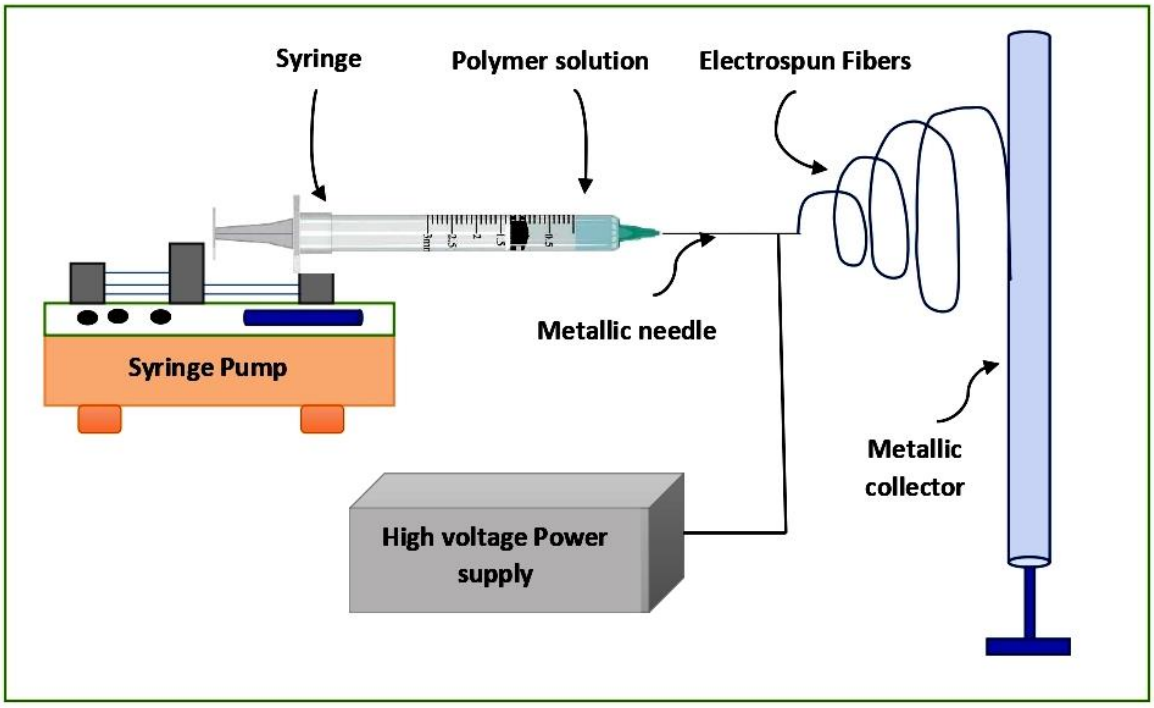

Figure 1.3: Basic set-up of electrospinning.

During the electrospinning process, a high electric voltage is applied to a liquid droplet of polymer solution at the spinneret tip. When the high voltage is gradually increased, the liquid droplet begins to stretch into a conical shape known as a "Taylor cone". The elongation process begins when electrostatic repulsion overcomes surface tension. After the Taylor cone is formed, the charged liquid jet is directed towards the metallic collector. Solid fibres will form as the solvent evaporates from the whipping action that occurs during the flight from the Taylor cone

to the collector, depending on the solution viscosity. As a result, the collector is covered with a non-woven fiber mat (Monfared et al., 2019; Zargham et al., 2012; Zhao et al., 2019).

1.3.2 Parameters that affect the electrospinning process

The electrospinning process depends on operating parameters, material parameters, and ambient parameters that affect the morphology of fiber. The operating parameters consist of the applied voltage or electric field, the flow rate of polymer solution, the distance between the tip of the metallic needle and collector, and the diameter of the needle. A small change in the operating parameters can lead to a significant change in the morphology of fiber (Fadil et al., 2021; X.-X. He et al., 2017; Luo et al., 2012; Rathore & D. Schiffman, 2020; Sundarrajan et al., 2014; C. Yang et al., 2009).

1.3.2.1 Operating Parameters

1.3.2.1 (a) Applied voltage

The applied voltage determines the amount of charges carried by the jet, the degree of electrostatic repulsion among the charges, and the strength of interactions between the jet and the external electric field. Higher voltage facilitates the formation of thinner fibers, but it can also result in more fluid being ejected, resulting in thicker diameter fibers (Tang, Ben Zhong, Alaa S. Abd-El-Aziz, 2014; C. Yang et al., 2009).

1.3.2.1 (b) Flow rate of polymer solution

It is necessary to adjust the flow rate of the polymer solution for a particular voltage in order to maintain a stable Taylor cone during the electrospinning process. A uniform Taylor cone can produce uniform fibers with narrow dispersion during electrospinning. As the flow rate increases, the amount of material passing through the tip increases, resulting in the formation of fiber with a high diameter. At a very high flow rate, the polymeric jet becomes unstable due to the effect of gravitational force and tends to electrospray (Tang, Ben Zhong, Alaa S. Abd-El-Aziz, 2014).

1.3.2.1 (c) The distance between the tip of the metallic needle and the collector

The distance between the tip and the collector can also influence the diameters and shape of nanofibers, however, the effect is not as strong as the other factors. In the electrospinning process, a minimum distance is necessary to allow enough time for solvent evaporation before

the fiber reaches the collector. Thinner fibers result from longer distances. When the distance is too great or too small, beads would form (Yifu Li et al., 2019a, 2019b; J. Xue et al., 2019b).

1.3.2.1 (d) Diameter of the needle

Electrospun nanofibers with small needle diameters are thinner, smoother, and bead-free, and have greater fiber porosity than nanofibers electrospun with large needle diameters. As aforementioned, higher applied voltage, smaller spinneret diameter, and lower polymer solution flow rate result in thinner electrospun nanofibers (J. Xue et al., 2019b; C. Yang et al., 2009; Zargham et al., 2012).

1.3.2.2 Material parameters

The material properties that affect the electrospinning process and fiber morphology include polymer concentration, viscosity of the solution, surface tension of the polymer solution, and other properties related to the solvent as well as the polymer itself (Yifu Li et al., 2019a, 2019b; J. Xue et al., 2019b).

1.3.2.2 (a) Polymer concentration

Amongst the material properties, the polymer concentration plays the most significant role in stabilizing the fibrous structure because it influences other properties such as viscosity of the solution, surface tension, and conductivity of the material (Yifu Li et al., 2019a, 2019b; J. Xue et al., 2019b).

1.3.2.2 (b) Viscosity

The viscosity of the polymer solution has a significant impact on the diameter and shape of the electrospun fiber. It is controlled by polymer properties including molecular weight and polymer solution concentration. When the concentration of polymer in a solution is raised, the viscosity of the solution rises. If the viscosity is too high, then it will be difficult to pump the solution via the syringe pump, or the solution may dry at the needle tip before electrospinning can begin. Higher viscosity results in the increased diameter fibers and lower deposition region (Yifu Li et al., 2019a, 2019b; J. Xue et al., 2019b).

1.3.2.2 (c) Surface Tension

Surface tension is the attraction between molecules in a liquid that is influenced by intermolecular interactions. During electrospinning, the charges on the polymer solution must

be high enough to overcome the solution's surface tension. When a high voltage is applied, the polymer jet begins to form from the needle's tips and elongates and stretches toward the collector, breaking up into minute droplets due to the solution's lower surface tension, which is known as electrospraying. Surface tension causes bead formation when the polymer concentration is low. If the surface tension is low, the formation of the jet begins at a lower voltage. The surface tension of polymer solution can be changed with varying solvents and by adding surfactants (Fadil et al., 2021; Moradipour et al., 2021).

1.3.2.2 (d) Solution conductivity

During electrospinning, the charged liquid (solution) stretches to form fibers due to charge repulsion. The jet carries more charges as the electrical conductivity of the solution rises, reducing the diameter of the electrospun fiber. A small amount of polyelectrolyte (salts) can be introduced to eliminate fiber bead formation since it raises more charges and helps to elongate the jet to produce fibers. The electrospinning of polymer solution is difficult at very high voltages, and fiber formation is impossible if the solution has no conductivity (Yifu Li et al., 2019a, 2019b; J. Xue et al., 2019b).

1.3.2.2 (e) Solvent properties

For electrospinning, solvent choice is critical since it influences solvent's evaporation rate, which is determined by the solvent's vapour pressure. The volatility or vapour pressure of the solvent determines the evaporation rate and, as a result, the solidification rate of the jet. High volatility is not suitable for spinning fibers because the jet may solidify immediately after leaving the spinneret. If the volatility is too low, the fibers will still be wet when deposited onto the collector. The solvent volatility modifies the surface fiber morphology and nano-membrane structure (Yifu Li et al., 2019a, 2019b; J. Xue et al., 2019b).

1.3.2.3 Ambient parameters

The interaction between the electrospinning jet and the surrounding environment such as the temperature and humidity of the surroundings may alter the electrospinning process and fiber morphology. The temperature is inversely proportional to the viscosity of the solution. So, the temperature may affect the properties of the electrospinning solution. Humidity may affect the porosity of fiber because humidity influences solvent evaporation (Yifu Li et al., 2019a, 2019b; J. Xue et al., 2019b).

1.3.3 Applications of electrospun fibers

Electrospinning is widely used in industrial applications due to the attractive features of electrospun fibres. The unique features of electrospun fibres can be summarised as follows. First, electrospun fibres vary in diameter from μm to nm. Second, the fibres are highly porous and aligned. Third, electrospun fibres have a high aspect ratio and surface-to-volume ratio. Fourth, electrospinning allows for the production of fibres with an endless variety of chemical compositions, and fifth, new forms of morphology can be produced by changing the spinneret.

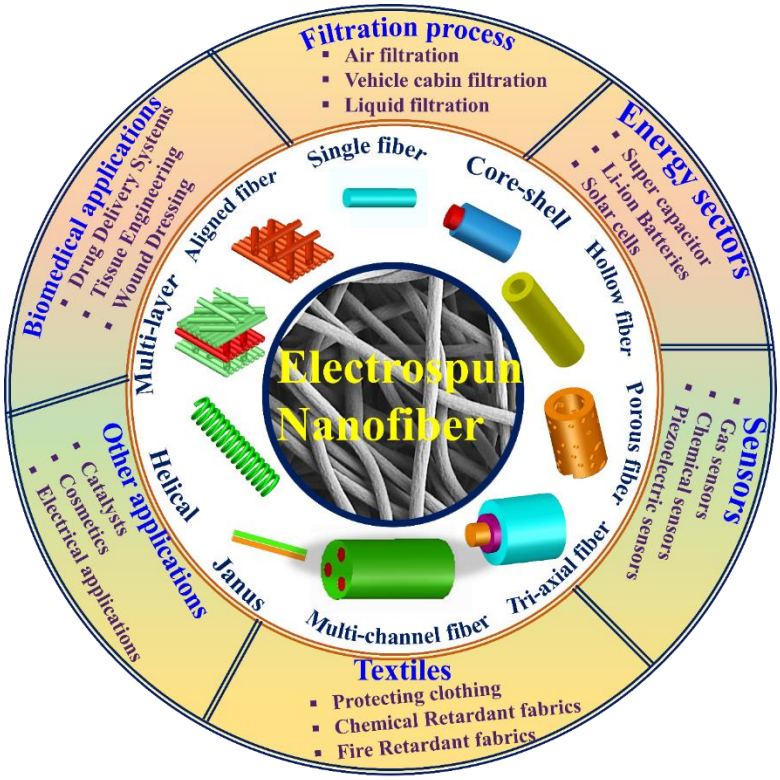

Figure 1.4: Different types of electrospun nanofibers and their applications.

With the combination of these characteristics, electrospun fibres can be employed for biological applications, (Davoodi et al., 2021; Elahi & Lu, 2013a, 2013b; Hoque et al., 2019; Jalaja et al., 2014, 2016; Joseph et al., 2015; Partheniadis et al., 2020; Sagitha et al., 2020; Sarika et al., 2014) filtration, (Jeongan Choi et al., 2015; Graham et al., 2002; S. Jiang et al., 2016; Sundarrajan et al., 2014; M. Zhu et al., 2017) energy sectors, (Bonso et al., 2014; Bredar et al., 2020; R. Chen et al., 2015; Sankar et al., 2021; K. Shi & P. Giapis, 2018; X. Shi et al., 2015) sensors, (Brosha et al., 2000; Fadil et al., 2021; W. Li et al., n.d., 2012; Yan Li et al., 2018; Shingange et al., 2020) textile, catalysis, (Fadil et al., 2021; Zhong, 2016) and electrical applications (H. J. Choi et al., 2019; Hou et al., 2021). **Figure 1.4** illustrates numerous types of nanofibers and their various applications.

1.3.4 Electrospun fibers for EMI Shielding

Electrospun fibers are porous one-dimensional (1-D) structures with low thickness and density. Electrospun fibers have high specific surface area, porosity, and forms interconnected 3-D conductive network which can aid in the multiple internal reflections of EM waves within the materials.

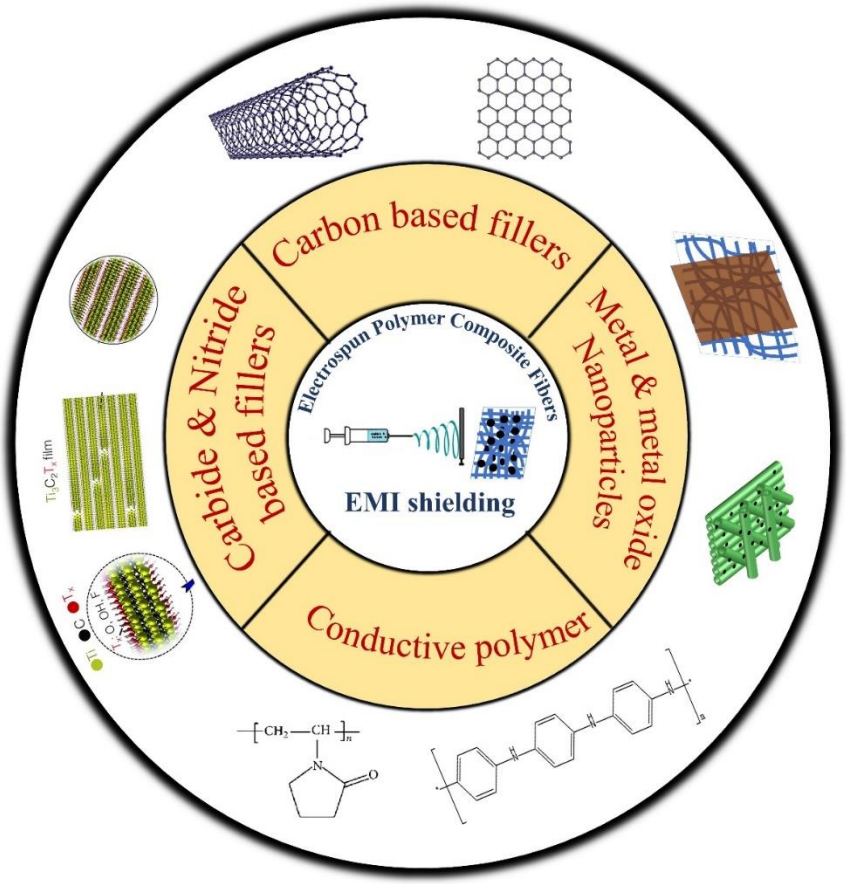

Figure 1.5: Conductive Fillers used in electrospun polymer composite fibers for EMI Shielding.

It is possible to uniformly incorporate different kinds of fillers on individual fibres and produce highly conductive 3-D networked channels for electron transport while providing excellent shielding effectiveness at a lower thickness. The existence of a high number of reflecting surfaces between the fibers transforms electrospun fiber-based mats into multilevel shielding materials. The interfacial polarisation between the conductive fillers and the polymer matrix increases polarisation loss, which contributes to incident EM wave attenuation. Low thickness and density considerably improve the SSE and SSE_t values of electrospun polymer composite fibres. As a result, SSE and SSE_t are critical metrics for distinguishing between electrospun

fiber-based shielding materials and others. (Blachowicz et al., 2022b, 2022c, 2022a; H. Guo, Chen, et al., 2021; Hashemi et al., 2022; Rani et al., 2023; Zheng, Cao, et al., 2023) **Figure 1.5** illustrates the various types of fillers used in electrospun polymer composite fibers for EMI shielding applications.

1.3.4.1 Carbonization of electrospun PAN fiber

Although electrical conductivity is a key requirement for EMI shielding, the majority of electrospun fibres, such as PAN, polyvinyl alcohol (PVA), cellulose, and others, are insulators. Carbonization is a simple method used to make electrospun fibres electrically conductive.

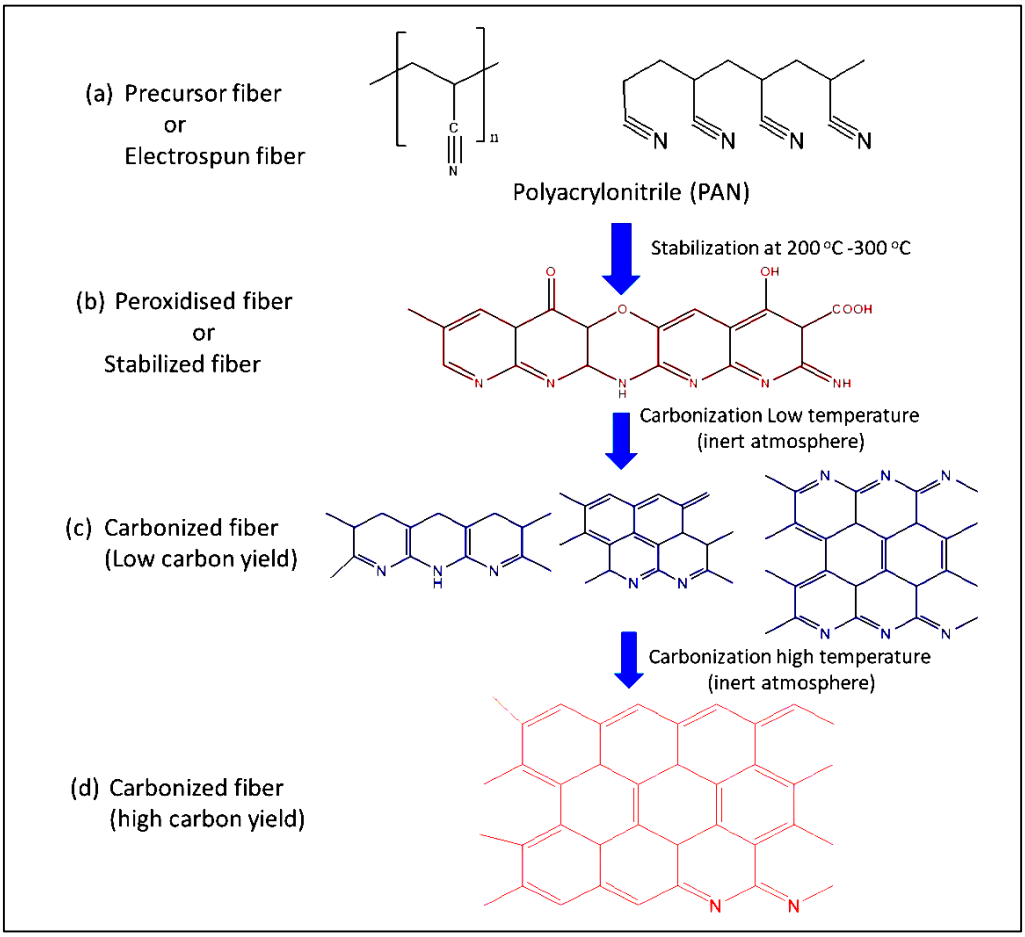

Figure 1.6: Formation of carbonized PAN fiber and their molecular structure of (a) PAN, (b) Stabilized PAN fiber, (c) PAN fiber carbonized at low temperature, and (d) PAN fiber carbonized at high temperature. (Yongjian Xu, Yan Liu, Shenglin Chen, 2020)

Carbonization is the process of heating an organic precursor in an inert atmosphere (argon or nitrogen) to convert it into a substance primarily composed of carbon. The temperature and ramping rate at which carbonization occurs are determined by the composition of the precursor. Initially, the organic material converts to carbon residue, which is followed by the diffusion of

volatile chemicals out of the system. An essential component of the carbonization process is the carbon yield, which is the weight of carbon material obtained after carbonization divided by the weight before to carbonization. Pressure, carbonization atmosphere, heating temperature, and ramping rate have impacts on the carbonized sample. Carbonization of electrospun PAN fiber mats gives high carbon yield and retains the fiber morphology. Electrospun fibers are carbonized at temperatures ranging from 600 ^{o}C to 1600 ^{o}C, depending on the precursor. Prior to carbonization, electrospun fiber is stabilised at temperatures ranging from 200 °C to 300 °C in an air environment (Saha & Schatz, 2012; Schierholz et al., 2019; Shokrani Havigh & Mahmoudi Chenari, 2022a; Storck et al., 2021; T. Wang et al., 2023). The steps involved in carbonization of electrospun PAN fiber are illustrated in **Figure 1.6**.

Carbon fibers (CFs) produced by electrospun fibers are highly promising materials for EMI shielding and come in a variety of morphologies, diameters, and lengths depending on the spinning process. Their excellent mechanical and electrical properties can be changed or modified utilising a variety of ways, including heat treatment, incorporation of conductive fillers and post treatment of carbonized electrospun fibers. The electrical conductivity of the pure carbonized PAN nanofiber changes with carbonization temperature, ranging from 0.2 to 0.5 S cm^{-1}. High-temperature treatment reduces SP^3 hybridized carbon into SP^2 hybridized carbon, which increases electrical conductivity. As the carbonization temperature increases from 700 °C to 900 °C, the electrical conductivity of carbonised PAN increases dramatically from 0.050 S cm^{-1} to 2.60 S cm^{-1}, while the EMI SE value increases from 0.2 dB to 30 dB (Orasugh & Ray, 2022).

1.3.4.2 Electrospun fiber with carbon-based fillers for EMI shielding.

Electrically conductive carbonic fillers-based polymer composites provide new possibilities for high-performance EMI shielding applications. Carbonic filler-based polymer composites have several advantages, including lightweight, oxidation resistance, easy and desirable processability, mobility, and the ability to construct 3-D electrically interconnected conductive network. Nanostructured carbon materials have greatly contributed to the overall growth of materials science and technology, including applications. Carbon nanostructures exhibit features such as lightweight, stability, excellent thermal and electrical conductivity. As a result, carbon nanostructures offer intriguing applications for EMI shielding as well as other capabilities (D. Jiang et al., 2019; Ravindren et al., 2019; Saini & Aror, 2012; Sankaran et al., 2018; Wanasinghe et al., 2020). Carbonic fillers for EMI shielding applications include carbon

black (CB), (H.-J. Choi et al., n.d.; Gupta & Tai, 2019; Kausar, 2016) graphite, graphene, (J. Liu et al., 2021; Sajid et al., 2022; Shayesteh Zeraati et al., 2021) and carbon nanotubes (CNTs) (Li Cao et al., 2014; A. Chaudhary et al., 2017; Yonglai Yang et al., 2005). These electrically conductive carbonic fillers are being widely researched for use in the production of electrospun fiber-based EMI shielding materials.

1.3.4.2 (a) Carbon Black (CB)

Carbon black (CB) is a chemically stable, lightweight material that is commonly used to produce conductive polymer composites for electrostatic discharge dissipation. It is an inexpensive alternative compared to other conductive carbon materials such as CNTs and graphene. However, a high content of CB (>40 wt%) is required to make an electrically conducting composite which restricts its application in a commercial scale. Conventionally, CB is being used as reinforcing filler in tyres and other rubber products. Im et al. utilized the electrospinning and carbonization method to fabricate CB embedded CFs for EMI shielding applications. The electrospinning solution was prepared by dispersion of CB in 10 wt% PAN solution in N, N, dimethylformamide (DMF) and fluorination was carried out to enhance the dispersion of CB in the hydrophobic electrospun solution. Fluorination of CB was also found to improve the electrical conductivity and EMI SE of the carbonised composites. It exhibited an EMI SE value of 50 dB and the electrical conductivity of 38 S cm^{-1} due to the formation of a well-oriented carbon structure upon carbonization ((Im et al., 2009).

1.3.4.2 (b) Graphene

Graphene is a two-dimensional SP^2 hybridized hexagonal packed structure having free electrons, due to which it shows very high electrical conductivity. It enhances the reflection loss, conduction loss, and polarization loss which may contribute to the attenuation of EM waves, making it one of the fascinating fillers for enhancing EMI shielding property. The electrical conductivity of graphene decreases with an increase in the number of graphene layers which in turn leads to excellent thermal conductivity (P. Kumar, 2019; Song et al., 2014). It can be easily homogeneously dispersed with PAN in DMF for electrospinning.

Song et al. fabricated a novel, flexible and lightweight all carbon electrically conductive network with graphene nanosheet (GN) and PAN via electrospinning process followed by carbonization for EMI shielding application in the frequency range of 8-12 GHz (X-band). Carbonization of electrospun composite fiber led to the formation of heterojunctions of CNF-

GN-CNF structure, which acted as an interfacial modifier. At a 31.9 wt% loading of GN, the heterojunctions exhibited 25-28 dB EMI SE with a thickness of 0.27 mm and a high electrical conductivity of 800 S m^{-1}. (Y. Guo et al., 2019) investigated the EMI shielding and thermal properties of polystyrene (PS)/ graphite nanoplatelets (GNPs) composite fiber. The PS/GNPs composite fiber was fabricated by a series of procedures including electrospinning, cold pressing followed by hot- pressing. The orientated GNPs and PS composite exhibited higher EMI SE (33 dB) than random GNPs/PS composite (16 dB) with 35 wt% loadings of GNPs and 3 mm thickness. The orientated GNPs/PS exhibited a higher EMI SE value due to the formation of thermally/electrically conductive networks (Song et al., 2014).

1.3.4.2 (c) Multiwalled Carbon Nanotubes (MWCNTs)

Among the various carbonic filler materials, MWCNT is one of the most promising fillers for EMI shielding applications due to their superior electrical conductivity (10^4 S cm^{-1}) and extraordinary thermal conductivity (over 200 W m^{-1} K^{-1}). (Hone et al., 2000) The electrospun MWCNTs/polymer nanofibers composites have remarkable properties such as lightweight, high porosity, large surface area, excellent thermal and electrical conducting properties, which make them suitable candidates to fabricate conducting polymer composites for high-performance EMI shielding applications with high EM wave absorbency at very low loadings of MWCNTs (Zhichun Zhang et al., 2014)(Nasouri & Valipour, 2015).

Im et al. investigated EMI shielding of polyaniline (PANI) based fibers in the frequency range of 800-4000 MHz. The fibers were fabricated with fluorinated MWCNTs and polyethylene oxide (PEO) via electrospinning method. The presence of PEO enhanced the uniformity of the PANI electrospun fibers, while fluorination treatment improved the dispersion and adhesion of MWCNTs in PANI/PEO fibers and increased the electron donor-acceptor reaction between fluorinated MWCNT and PANI. Because of the excellent electrical conductivity (4.8×10^3 S m^{-1}), 82 wt.% loadings of fluorinated MWCNT in PANI/PEO electrospun fiber showed 42 dB of EMI SE. The permittivity and magnetic permeability properties also significantly increased with the loading of MWCNT and fluorination treatment (Im et al., 2010a).

Salimbeygi et al. investigated the EMI shielding capability of PVA/sodium dodecyl sulphate (SDS)/MWCNTs composite nanofibers in the frequency range of 8- 12 GHz (X-band). The composite nanofibers were fabricated by electrospinning process, as shown in **Figure 1.7**. The composite nanofibers of average diameter 224 ± 30 nm with 10 wt % loading of MWCNT exhibited maximum reflection loss of 15 dB at the frequency of 8 GHz when the thickness of

the nanofiber mat was 1 mm. The electrical conductivity increased as the content of MWCNT increased from 1 wt% to 10 wt%, which resulted in an increase in conductive current and dielectric properties, leading to an improvement in EM absorption characteristics. The tangent loss (tan δ) is an essential parameter in describing the electromagnetic absorbing properties. An increase in the value of tangent loss (tan δ) indicates the enhancement in EM absorption properties (Salimbeygi et al., 2013).

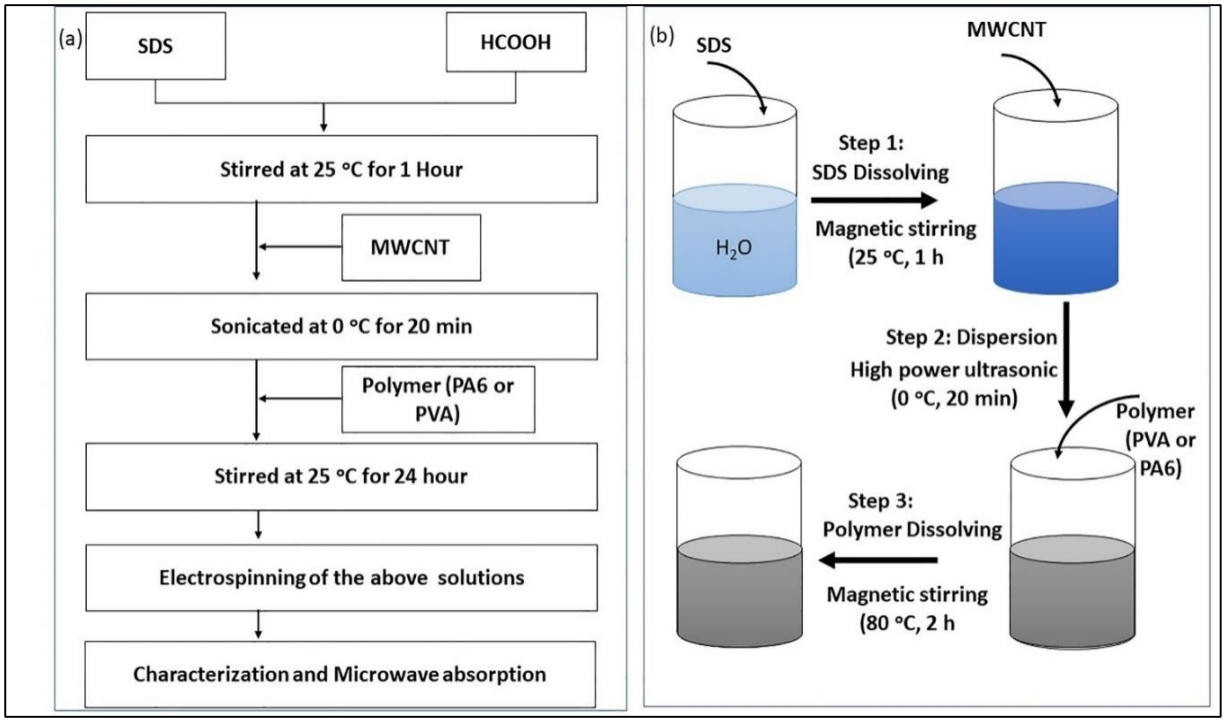

Figure 1.7: Schematic illustration of the (a-b) preparation of Polymer (PVA or PA6)/ SDS/MWCNTs composite nanofibers (Nasouri & Shoushtari, 2017a).

Nasouri et al. investigated the EMI shielding of MWCNTs/PVA composite nanofibers in X-band. A 3 mm thick mat of MWCNTs/PVA composite nanofiber with 7.7 wt% loading of MWCNTs exhibited maximum absorption of 31.5 dB with low reflection (8.8 dB) by response surface methodology (RSM) model, when the incident EM wave frequency was 12 GHz. Here, EMI shielding was calculated using RSM techniques, which are based on response calculation rather than the S-parameter. As the content of MWCNTs increased, the electrical conductivity of MWCNTs/PVA composite nanofibers increased from 2.34×10^{-9} S cm^{-1} to 3.37×10^{-3} S cm^{-1} at 0.75 wt % content of MWCNTs suggesting the formation of conducting network throughout the insulating PVA matrix. The electrical conductivity of MWCNTs/PVA composite nanofibers increased further, reaching 8.12×10^{-2} and 8.70×10^{-1} S cm^{-1} for 2.5 and 10 wt% of MWCNTs, respectively. (Nasouri & Valipour, 2015) investigated the EMI shielding

of polyamide 6 (PA6)/SDS/MWCNTs composite nanofibers in X- band. The PA6/SDS/MWCNTs composite nanofibers are similar to the work reported by Salimbeygi et al. The composite nanofibers (PA6/SDS/MWCNT) were prepared by electrospinning process, as shown in **Figure 1.7**. As the concentration of MWCNT varied from 0 to 10 wt% in PA6/SDS/MWCNTs composite nanofibers, the average diameter decreased from 292 ± 16 nm to 161 ± 12 nm and the reflection loss improved from -4 dB to -18 dB at the frequency of 11.5 GHz. The EM absorption properties increased with an increase in MWCNTs content due to improvement in properties of dielectric and tangent loss (tan δ) (Nasouri & Shoushtari, 2017a).

Nasouri et al. studied the effect of electrospinning parameters on average diameter, surface area, electrical conductivity, and EMI SE of MWCNTs/PVP electrospun nanocomposite fibers in X-band. The electrical conductivity and EMI shielding of MWCNTs/PVP electrospun nanocomposite fibers were found to be functions of the wt% of PVP, the fiber diameter, and specific surface area. This study also investigated the influence of fiber diameter on EMI shielding efficiency. **Figure 1.8** illustrates and compares the EMI shielding mechanism in fibers with thinner and thicker diameters. The nanocomposite fibers with a thinner diameter or higher surface area can achieve higher efficiency of EMI shielding compared to that with a thicker diameter. The electrical conductivity and EMI shielding of MWCNTs/PVP electrospun nanocomposite fibers were improved by increasing the specific surface area and decrease in average diameter of the fibers.

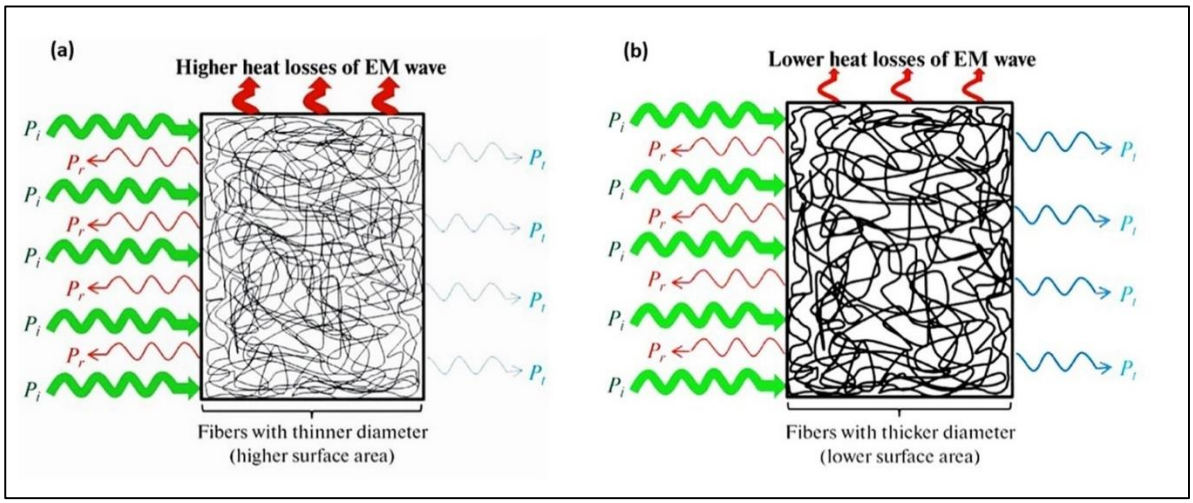

Figure 1.8: The effect of fiber diameter on EMI shielding properties (a) fibers with thinner diameter (b) fibers with thicker diameter. Reproduced from (Nasouri & Shoushtari, 2017b) *copyright 2017, Springer nature.*

From the EMI SE measurement, the shielding due to absorption was found to vary from 18-29 dB with a decrease in the average diameter of MWCNTs/PVP fibers, while shielding due to

reflection was enhanced from 9-13 dB for the same sample. Thus, as the average diameter of MWCNTs/PVP nanocomposites fiber decreases, the EMI shielding due to absorption increases greatly, but that due to reflection only raises a little (Nasouri & Shoushtari, 2017b).

Zhang et al. prepared electrospun electrically conductive nanocomposite fibers with PANI, PAN, and MWCNTs and investigated the microwave absorption in the frequency range of 3.4 – 18 GHz. The electrical conductivity of PANI/PAN/MWCNTs nanocomposite fibers increased from 1.79 S m^{-1} to 7.97 S m^{-1} with increasing the content of MWCNTs from 3.0 wt% to 7 wt%. The reflection loss value of PANI/PAN/MWCNTs nanocomposite fibers was increased from -4.6 to -5.9 dB with increasing the thickness of composites films. (Qavamnia & Nasouri, 2016) prepared composite nanofibers from PS and MWCNTs by electrospinning technique for EMI shielding in X-band. The electrical percolation of MWCNTs/PS composite nanofibers was observed at 0.75 wt% loadings of MWCNTs, and electrical conductivity increased with the loading of MWCNTs up to 7.5 wt%. Further, when the loading was increased to 10 wt%, the electrical conductivity was found to decrease. The highest EMI SE of 32 dB was obtained at 7.5 wt% loading of MWCNTs due to the formation of a conductive network by MWCNTs in the PS nanofibers (Zhichun Zhang et al., 2014).

The significant progress of EMI shielding performance is always compromised with mechanical damage such as cracks, scratch, or large strain in real world applications. These mechanical damage impact on the long-term use of EMI shielding materials and can result in unexpected EM hazards. Hence, it is highly desirable to make use of self-healing materials for EMI shielding. Chen et al. fabricated self-healing EMI shielding materials from aligned carbon nanotube-poly (2-hydroxyethyl methacrylate) (CNT-PHEMA) prepared by magnetic-field-assisted electrospinning and cross-stacking of aligned fabric layers. The composite exhibited 20.42 dB EMI SE in the X-band with 16 stacking layers under a thickness of 2 mm at very low CNT loading (0.17 wt%). Because of the alignment of the CNTs and the porosity of the fabric, EM waves were expected to be effectively absorbed even at low CNT loading. The interaction between Per-6-(1-pyrenebutylamino)-6-deoxy—cyclodextrin CNT (Py—CD-CNT) and adamantine-modified 2-hydroxyethyl methacrylate (HEMA-Ad) matrix in 100% humidity conditions is the basis of material's self-healing mechanism. It is reported that EMI SE_{total} was reduced to 46 % due to crack and after self-healing process 91 % was recovered (Li Chen et al., 2020).

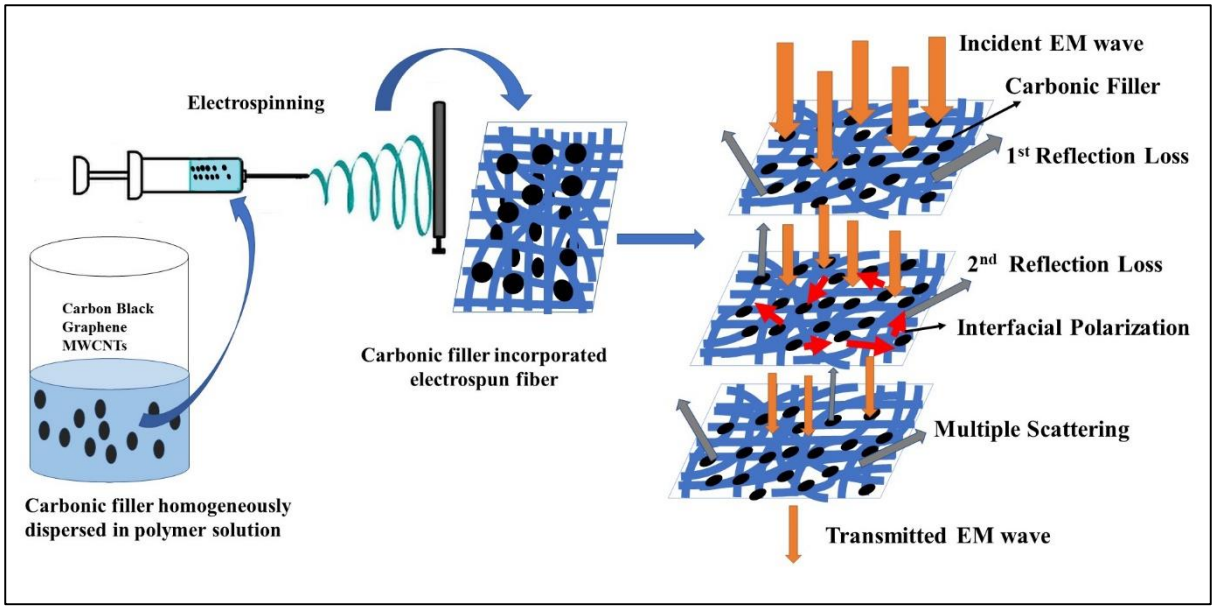

Figure 1.9: Carbonic filler incorporated electrospun fibers for EMI shielding.

Because of the electrical conductivity and the ability to bond and form network with electrospun fibers, carbon-based fillers such as CB, GN, GNP, and MWCNTs are promising candidates as fillers in electrospun composite fibers for EMI shielding applications. However, due to hydrophobic nature and lightweight of these fillers, low loading only could be achieved. Heat treatment or the addition of conducting polymers such PANI or PVP is found to enhances the EMI SE value of the composites. As shown in **Figure 1.9**, the carbon-based fillers can establish connections with the electrospun fiber, aiding in EMI shielding through interfacial polarization and multiple scattering.

1.3.4.3 Electrospun fiber incorporated with metal, metal NPs, and metal oxide for EMI shielding.

The primary mechanism for EMI shielding is reflection, and the secondary mechanism is absorption. For absorption, materials must have electric dipole or magnetic dipole to interact with the EM fields. Materials with a high dielectric constant such as $BaTiO_3$, has high electric dipoles whereas materials with high magnetic permeability, such as a Fe_2O_3 and Fe_3O_4 have high magnetic dipoles. (Im et al., 2010b; Kang et al., n.d.; Moon et al., 2013) As already mentioned, traditionally, copper, aluminium, and other conductive metals were the first choice for EMI shielding materials due to their capability for effective reflection of EM radiation. For reflecting the EM waves, the materials must have free movable charge carriers since free movable charge carriers can interact with an electric field and reflect the EM waves. Most of the metals such as Ag, Cu, and Ni have free movable charge carriers. However, these metals

have problems related to processability, corrosion, and high weight. Towards solving these drawbacks, polymer composites have emerged as alternative (Bhattacharjee et al., 2018; Ji et al., 2018; L. Wang et al., 2019). Different strategies investigated for preparing electrospun composite fibers with metal, metal NPs, and metal oxide as fillers for EMI shielding are discussed in the following sections.

1.3.4.3 (a) Metal NPs

Electrical conductivity and magnetism are two factors that directly influence EMI shielding performance. Both Ni and Co are magnetic metals with great absorption attenuation in the EM wave band. The magnetic metal nanoparticles have a high surface area, and the presence of a large number of nanoparticles on the surface allows them to effectively absorb EM waves. Lightweight and flexible Ni-Co NPs coated on electrospun PAN PU fiber membrane (P@Ni-Co) was prepared by Hu et al. through a combination of electrospinning and electroless deposition process. The hybrid membrane exhibited excellent EMI SE of >68 dB in the range of 8- 26.5 GHz (X, Ku, and K-band) and an average EMI SE of 77.8 dB with a thickness of 0.180 mm and a density of 0.59 g cm^{-3}. The absolute EMI SE (SSE_T) was found to be 7325.8 dB cm^2 g^{-1}. The high EMI SE was explained to be due to its remarkable electrical conductivity of 1139.6 S cm^{-1} and the reasonable saturation magnetization value of 49.6 emu g^{-1}. The EMI SE of the P@Ni-Co hybrid membrane increased with an increase in the deposition time because it also increased the electrical conductivity and thickness of the P@Ni-Co hybrid membrane. The Ni-Co alloy NP-coated PAN PU nanofibers would be promising for applications as thin and light EMI shielding materials (Y. Hu et al., 2019).

Silver (Ag) and Ag NPs possess high thermal and electrical conductivities due to which these are widely used in nanocomposites for their broad applications in integrated circuits and EMI SE. Copper (Cu) and Cu NPs also show high electrical and thermal conductivities and are cheaper than Ag and Ag NPs. Copper tape and copper foil are widely used for EMI shielding due to their high electrical conductivity. But the disadvantage of Cu and Ag metal, copper tape, and Cu foil is their susceptibility to corrosion. Reflection is found to be the dominant mechanism responsible for EMI shielding in these materials (Y. Chen et al., 2020; H.-R. Kim et al., 2012; J. Lee et al., 2017). When metal NPs are incorporated into the polymer composites, EMI shielding is improved due to enhancement in absorption mechanism. Ji et al. investigated EMI SE of metal NPs decorated cross-linked electrospun PAN (CPAN) nanofiber in X, Ku, and K–band. An efficient and facile approach to prepare freestanding, lightweight, and flexible

cross-linked PAN NF/ metal NPs (CPAN NF/MNP) with high efficiency and reasonable strength via electrospinning followed by an electroless deposition process was demonstrated.

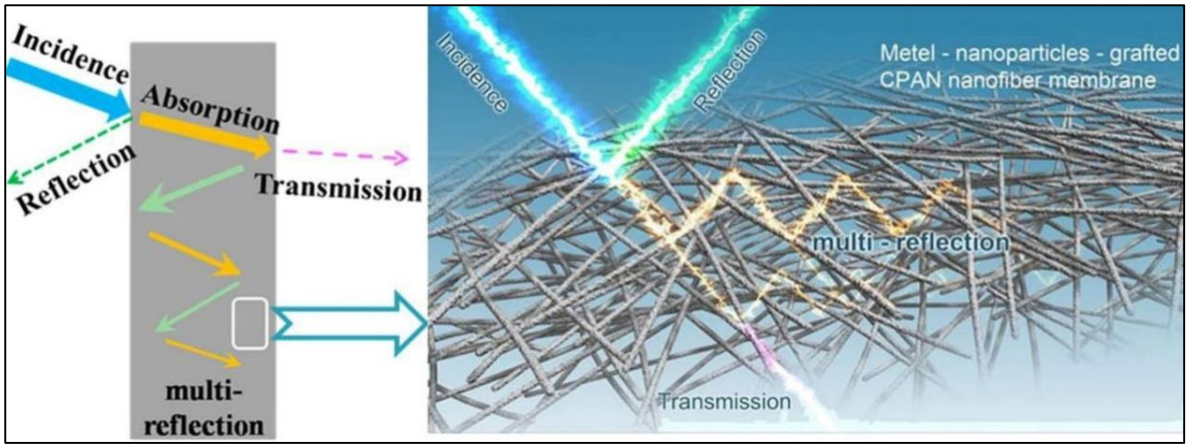

Figure 1.10: EMI shielding mechanism of CPAN NF/metals NP hybrid membrane. Reproduced from (Ji et al., 2018) *copyright 2018, Springer nature.*

The CPAN NF/MNP hybrid membrane exhibited high mechanical strength and excellent electrical conductivity with a small thickness of the hybrid membrane. A 53 µm thick CPAN NF/Ag NPs hybrid membrane exhibited excellent EMI SE of 90 dB, which is equal to the pure metal as it exhibited higher electrical conductivity compared to CPAN NF/Cu NP and CPAN NF/Ni NP hybrid membranes. But, CPAN NF/Cu NP and CPAN NF/Ni NP possessed low values of electrical conductivity as compared to CPAN NF/Ag NP hybrid membrane due to the formation of an electrically insulating metal oxide layer on the surface of Cu and Ni. The cross-linked PAN NF has better absorption of EM wave, as shown in **Figure 1.10**. (Ji et al., 2018)

Kim et al. investigated the EMI SE of metal (Cu, Ni, and Ag) deposited PVA electrospun nanofibers composite mats prepared by electrospinning and metal deposition methods in the frequency range of 0.5 – 18 GHz. Here, PVA was used as the electrospun fiber instead of cross-linked PAN, and it exhibited lower EMI SE than CPAN NF/MNP hybrid membrane. The 200 nm Cu- deposited PVA nanofiber mats exhibited 30-33 dB EMI SE whereas 100 nm Cu-deposited showed 20 dB at 10 GHz. The contribution of absorption and reflection mechanism involved in EMI shielding was investigated for 50 nm Cu-deposited PVA nanofiber mats which exhibited ~60% - absorption coefficient, ~40 % transmittance coefficient, and 0% reflection coefficient. The EMI SE due to absorption was about 4 dB, and that due to reflection was about 0 dB at 10 GHz. It was suggested that the contribution of the absorption was dominant due to the increased thickness of the deposited metal layer, unique nanofibrous porous structure, and

formation of an interconnected metal deposited nanofibrous network throughout the insulating PVA matrix in the 50 nm Cu-deposited PVA NF mats (H. Kim et al., 2012). Kim et al. also investigated the EMI SE of Ag-deposited PVA nanofiber mats which always showed higher value than those of Cu & Ni- deposited PVA nanofiber mats in a frequency range of 0.5-18 GHz. The EMI SE of electrospun PVA nanofiber mats coated with Ag and Cu increased with an increase in the thickness of the metal layer. However, Ni-deposited PVA nanofiber mats exhibited almost zero EMI SE irrespective of the thickness of the deposited metal layer. The authors suggest that this can be probably due to higher resistivities of Ni deposition compared to Cu and Ag deposited nanofibers. The bi-metallic (Cu/Ni) deposited PVA nanofiber mats exhibited ~30 dB EMI SE with 0.25 fraction of Ni deposited on the outer layer and 0.75 fractions of Cu deposition. But, PVA nanofiber mats of the same thickness, with Cu deposition, showed EMI SE of ~17 dB (H. Kim et al., 2012). Kim et al., 2020 investigated the EMI shielding properties of Ag-deposited electrospun nylon 66. With a thickness of 100 μm, the composite exhibited an excellent EMI SE value of 60.6 dB in the X and Ku-band, because of the high thermal conductivity and alignment of electrospun fiber. The electrospinning methods improved the thermal conductivity, but they reduced the electrical conductivity of the Ag layer due to the porous morphology of the composite (Jaeyeon Kim et al., 2020). Carbon nanofibers (CNFs) containing ferromagnetic metal NPs were investigated for EMI shielding from C-band to Ku-band (4-18 GHz) by (Xiang et al., 2014). Fe/Co/Ni NPs were uniformly dispersed in the electrospinning solution, and the obtained fiber mats were carbonized. The highest reflection loss was -67.5, -63.1, and -61.0 dB for CNF-Fe, CNF-Co, and CNF-Ni at 16.6, 12.9, and 13.1 GHz with 1.3, 1.6-, and 1.7-mm thickness, respectively. The high reflection loss exhibited by CNF-Fe is due to the highest permeability resulting from the significant saturation magnetization (M_s) value of CNF-Fe.

1.3.4.3 (b) Metal oxide NPs

Different types of metal oxide NPs incorporated polymer composites have been investigated for EMI shielding applications by several researchers because of their high dielectric constants. Examples of metal oxide NPs used for the purpose include TiO_2, SiO_2, perovskites, and spinel particles (Dijith et al., 2017; Faisal & Khasim, 2013; Kuekha et al., 2022). Huang et al. demonstrated the EMI SE of lightweight and flexible electrospun TiO_2/SiO_2 (TS) nanofibers modified with polypyrrole (PPy) and r-GO sheets hybrid film in X-band. The sandwich-like structure of TiO_2/SiO_2@PPy@rGO (TSPG) hybrid film consisted of a double continuous conductive network. The EMI SE of TSPG film was 38 dB, and the specific EMI SE was ~

13829 dB cm^2 g^{-1}, with a thickness of 0.26 mm, which is superior to most metals and conductive composites. In this case, an absorption mechanism was dominant due to the double-continuous conductive network and sandwich structure in micro/nanoscale which was benefitted from the scattering and multiple reflections. When the EM waves were incident on TSPG film, a part of them is immediately reflected due to the skin effect of the highly conductive r-GO. High conductivity, dipoles, and interfaces were also found to be essential to attenuate EM waves by multiple reflections and scattering (L. Huang et al., 2019).

In another work, Nakhaei et al. prepared 1-D TiO_2/SiO_2 core-shell structured nanofibers with various concentrations of NPs via a single nozzle co-electrospinning method. Polyvinylpyrrolidone (PVP) and TiO_2 NPs formed the core, whereas PAN and SiO_2 NPs served as a shell. The TiO_2/SiO_2 core-shell nanofibers exhibited 150 dB EMI SE in the frequency range of 2-20 GHz. The excellent microwave absorption properties of the TiO_2/SiO_2 core-shell nanofibers are attributed to the special 1-D fibrous structure and the effective dielectric loss. The main mechanism of shielding is absorption, as the dipole of SiO_2 and TiO_2 NPs can interact with transverse electric (E) and magnetic (H) vectors of the incident EM waves to introduce losses into the system (Nakhaei et al., 2016).

Ferrite (Fe_3O_4) is one of the most common fillers for EMI shielding applications. Yuan et al. investigated the EMI shielding of lightweight, flexible, and a non-woven r-GO coated Fe_3O_4@SiO_2@PPy (FSPG) composite film with a core-shell and sandwich combined microstructure. A 0.27 µm thick FSPG composite film exhibited 32 dB EMI SE and a specific EMI SE of ~12608.4 dB cm^2 g^{-1} in the X- band. This high EMI shielding performance was originated due to the high electrical conductivity of FSPG films (0.71 S cm^{-1}). The unique multi-layer structure of the r-GO and conductive fibrous core-shell structure resulted in high electrical conductivity, which helped in attenuating the EM waves. In the core-shell structure layers, the PPy shell constructs a continuous conducting network. Silica has an extremely high transmission ratio, and Fe_3O_4 NPs in the fiber could contribute to magnetic loss and synergic shielding ability with PPy to further attenuate the EM waves (Yuan et al., 2018). Kim et al. studied the EMI shielding of Ag- decorated PVA electrospun nanofiber webs incorporating Fe_2O_3 NPs in the frequency range of 0.5 -18 GHz. The Ag- decorated PVA/Fe_2O_3 nanofiber composites were fabricated by electrospinning and metal deposition methods with various Ag thicknesses and different amounts of Fe_2O_3 NPs. The 200 nm Ag decorated PVA/10 wt%-Fe_2O_3 composite nanofiber exhibited EMI SE of ~42.5 dB at 10 GHz when prepared in a mixed solvent (DMSO/distilled water 80/20 by weight ratio). The interplay of reflection due to the

increased electrical conductivity and absorption due to the increase in the thickness of the deposited metal layers and the unique nanofibrous porous structure resulted in high EMI SE (H.-R. Kim et al., 2012).

PVDF is available in different crystalline forms such as α, β, and γ, and due to strong ferroelectric properties, β form has a high piezoelectric coefficient. Electrospinning techniques produce β-phase PVDF and also polarize the PVDF membrane making it to be ferro active. The ferroelectric properties of PVDF were improved by the addition of ferrite NPs (Revathi et al., 2015). Revathi et al. investigated the EMI SE of barium substituted magnesium ferrite ($Ba_{0.2}Mg_{0.8}Fe_2O_4$) (BFMO)-PVDF composite fibers in the frequency range of 2-3 GHz. The BFMO-PVDF composite fibers were prepared by electrospinning, and 3 mm BFMO-PVDF composite fibers exhibited EMI SE of 28 dB (Revathi et al., 2015). Zirconium oxide (ZrO_2) has been used as an additive due to its high permittivity, low thermal conductivity, chemical inertness, and hardness in EMI shielding applications. Im et al. studied the EMI SE of ZrO_2 -embedded graphite structured carbon fibers in the frequency range of 800-8500 MHz. The fibers were prepared by electrospinning and heat treatment methods. Heat treatment induced structural changes in the electrospun fibers and played an important role in improving the permittivity and EMI SE. The fibers exhibited 31.79 dB of EMI SE due to high permittivity. The permittivity and EMI SE increased with an increase in the amounts of ZrO_2 and heat treatment temperature (Im et al., 2011). Deeraj et al. also examined the EMI shielding properties of ZrO_2 incorporated PAN based CNFs reinforced epoxy composites (ZrO_2 @CNF mats) in the frequency range of 12-18 GHz (Ku- Band). With a thickness of 0.72 mm, the stacking of 8 layers of ZrO_2 @CNF mats exhibited 94 dB EMI SE (Deeraj et al., 2021).

Kowsari et al. studied the effect of ionic liquids on electrospinning and EMI shielding properties by addition of $Cr(NO_3)_2$/$Zn(CH_3COO)_2$/ionic liquid (IL) with electrospun PAN fibers. The influence of two different types of ionic liquids (ILs) $[C18(mim)]^+Br^-$ and $[C18(mim)]^+$ HSO_4^-, on electrospun fiber sizes were investigated. Zinc acetate/ chromium nitrate/IL/PAN composite nanofibers were dispersed as fillers in microwave-absorbing coating wherein epoxy resin acted as the polymer matrix. The fiber thickness and reflection attenuation could be controlled by the concentration of the IL. The spinel $ZnCr_2O_4$ nanofibers obtained after annealing at 600 ^oC for 3 hours exhibited maximum reflection loss of -38 dB in the frequency range of 5-12 GHz (Kowsari & Mallakmohamadi, 2012).

1.3.4.4 MXene incorporated electrospun fiber for EMI shielding.

MXene is a novel two-dimensional (2-D) material with early transition metal carbides and carbonitrides. The general formula of MXenes is $M_{n+1}X_nT_x$, where M represents early transition metals (e.g., Ti, V, Zr, Mo, or Ta), X represents carbon and/or nitrogen atoms, T_x represents the surface termination such as a mixture of -F, = O, and/or -OH groups, n represents 1,2 or 3 and x represents the number of terminating groups. MXene 2-D laminated nanocrystals show high specific surface area and high electrical conductivity similar to graphene. For example, $Ti_3C_2T_x$ possesses chemically active surfaces, coupled with the native defects and metallic character. These characteristics of $Ti_3C_2T_x$ make them suitable candidates for EMI shielding applications (**Figure 1.11**).

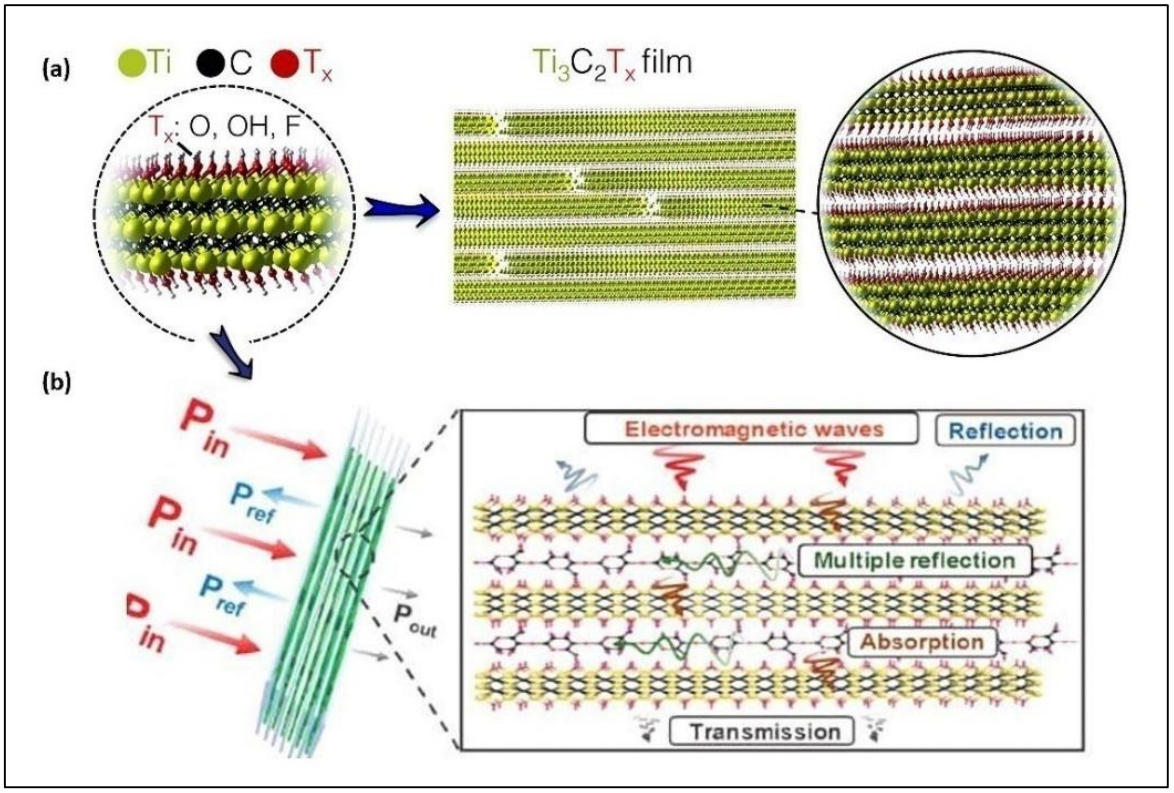

Figure 1.11: Schematic illustration of (a) structure of pristine MXene films and (b) EM wave transfer across the (MXene) d-$Ti_3C_2T_x$/CNF composite. Reproduced from (Shahzad et al., 2016) copyright 2016, Science.

But, pure $Ti_3C_2T_x$ film shows low mechanical properties and low flexibility. The mechanical properties and flexibility of MXene can be improved by making polymer-matrix composites and can be designed to have high processability, good flexibility, and low density. Excellent metallic conductivity and hydrophilicity of $Ti_3C_2T_x$ make them suitable components for polymer composites, with polymers such as cellulose, sodium alginate, PVA, and other

hydroxyl or oxygen or nitrogen-containing polymers. These polymers can form hydrogen bonds with terminating groups of $Ti_3C_2T_x$ which increase the mechanical property and flexibility of polymer composites. But as polymer loading increases, the electrical conductivity of composites decreases (W.-T. Cao et al., 2018; C. Cui et al., 2019; Shahzad et al., 2016; R. Sun et al., 2017).

Pure $Ti_3C_2T_x$ film with 45 µm thickness exhibits 92 dB EMI shielding effectiveness due to its excellent electrical conductivity (4600 S cm^{-1}). This high electric conductivity of $Ti_3C_2T_x$ film arises from the high electron density of states near the Fermi level as predicted from density functional theory (DFT). A film of $Ti_3C_2T_x$ of thickness 8 µm with 10 wt % loading of sodium alginate ($Ti_3C_2T_x$ – SA) exhibited 57 dB EMI SE (Shahzad et al., 2016).

The electrospun regenerated cellulose nanofiber (r-CNF) and MXenes (d-$Ti_3C_2T_x$/r-CNF) composite films were prepared by vacuum-assisted filtration method. Cellulose acetate (CA) electrospun fiber was prepared and d-$Ti_3C_2T_x$ flakes were continuously deposited on the surface of r-CNF by vacuum-assisted filtration method to form an overall electrical network. The high conductivity and specific surface area of $Ti_3C_2T_x$ produced more conductive paths for charge carriers, which is suitable for EMI shielding. The d-$Ti_3C_2T_x$/r-CNF composite films showed 46.3 S cm^{-1} electrical conductivity and exhibited 42.7 dB EMI SE with 15 µm thick-coated $Ti_3C_2T_x$ films. The $Ti_3C_2T_x$/r-CNF polymer composite showed good mechanical properties and better stability after being bent for 500 cycles confirming the flexibility of d-$Ti_3C_2T_x$/r-CNF composite films (C. Cui et al., 2019). The ultrathin and highly flexible MXenes/cellulose nanofiber (d-$Ti_3C_2T_x$/CNF) composite paper with nacre-like lamellar structure was fabricated via a vacuum filtration induced self-assembly process. The 47 µm thick $Ti_3C_2T_x$/CNF composite paper exhibited high electrical conductivity (739.4 S m^{-1}), excellent SSE/t (~ 2647 dB cm^2 g^{-1}), high tensile strength (135.4 MPa), good fracture strain up to 16.7 % and a high folding endurance up to 14,260 times (W.-T. Cao et al., 2018). The excellent EMI SE of MXene and their composites is due to the dominating effect of absorption mechanism rather than reflection. The absorption mechanism is dominant because of its high electrical conductivity and the layered structure of MXene ($Ti_3C_2T_x$) film. When EM wave strikes the surface of MXene films, some EM wave immediately gets reflected due to free electrons present at the conductive surface of the MXene. The remaining EM waves pass through the lattice structure or layered structure of MXene, where it interacts with a high electron density of MXene ($Ti_3C_2T_x$) that induces currents, which contributes to ohmic losses, resulting in a drop in the energy of the EM wave. The dipolar polarization caused by the surface

functional groups (T_x) of MXene, localized defects, and dangling bonds of MXene ($Ti_3C_2T_x$) plays an important role in the dielectric loss, which was similar to r-GO. The 2-D stacked layers of MXene ($Ti_3C_2T_x$) sheets can contribute to the formation of many interfaces, which increase the propagating path of EM waves (W.-T. Cao et al., 2018; C. Cui et al., 2019; Shahzad et al., 2016; R. Sun et al., 2017). The EMI SE of the MXene (d-$Ti_3C_2T_x$/r-CNF) composite increases with increasing thickness and loading of MXene. The d-$Ti_3C_2T_x$/r-CNF composite shows excellent flexibility and stability after 500 times of bending, and the retention rate of EMI SE was 92.9 %. The electrical conductivity of materials has great significance on EMI shielding. With increasing the content of $Ti_3C_2T_x$ in the MXene (d-$Ti_3C_2T_x$/r-CNF) composite, the electrical conductivity of the MXene (d-$Ti_3C_2T_x$/r-CNF) composite paper markedly increases. The 40 wt % of $Ti_3C_2T_x$ content in MXene (d-$Ti_3C_2T_x$/r-CNF) composite paper has an electrical conductivity of 0.6188 S $m^{-1,}$ which is 15 times greater than that of $Ti_3C_2T_x$ /PVA composite film. For practical application of EMI shielding, 1 S m^{-1} electrical conductivity of materials is required. The 50 wt % of $Ti_3C_2T_x$ has an electrical conductivity of 9.691 S m^{-1}, which is much higher than 1 S $m^{-1,}$ and 90 wt% of $Ti_3C_2T_x$ contents in MXene (d-$Ti_3C_2T_x$/r-CNF) composite paper shows 739.4 S m^{-1}. The directional alignment of 2-D $Ti_3C_2T_x$ nanosheet with cohesive action of CNFs results in the formation of conductive network (W.-T. Cao et al., 2018).

1.4 Summary

The demand for EMI shielding materials is increasing, and the development of lightweight, flexible materials with good EMI shielding qualities has become the priority. One-dimensional electrospun fibers have high potential as shielding materials, and the addition of fillers that generate magnetic or dielectric dipoles can enhance EMI shielding properties. Reflection, absorption, and multiple reflections are common EMI shielding mechanisms for all types of fillers, although electrical permittivity, magnetic permeability, dipole interaction, and interfacial polarization are other variables that increase reflection loss and absorption loss. The carbonic filler-based composite fibers have improved electrical conductivity and boost interfacial polarization, enhancing the EMI SE value. Metal NPs and metal oxide NPs based polymer composite fibers have increased electrical permittivity, dielectric loss, and transverse electric field, while metals such as iron, cobalt, and nickel exhibit high magnetic permeability and transverse magnetic field, which improves EMI SE. Electrospun SiC ceramic fibers are promising EMI shielding materials for high temperature applications. MXene based fiber composites are emerging as highly flexible and efficient EMI shielding materials. The layered

structure, high electron density, and dipolar polarization lead to high EMI shielding effectiveness.

Table 1.2 summarizes the EMI shielding performances of the different types of electrospun composite fibers.

Table 1.2: Performance of electrospun polymer composite fibers for EMI shielding applications- A summary.

S. No.	Composite fibers	Thickness	Frequency range	EMI SE (dB)
1.	Fluorinated CB (FCB)/PAN (Im et al., 2009)	-	800-4000 MHz	50
2.	GN/ CNF composites (Song et al., 2014)	0.27 mm	8-12 GHz	25-28
3.	GNPs/ PS composite fibers (Y. Guo et al., 2019)	3 mm	8.2- 12.4 GHz	33
4.	Fluorinated MWCNT-PANI/PEO (Im et al., 2010a)	-	800-4000 MHz	42
5	PVA/SDS/MWCNT (Salimbeygi et al., 2013)	1 mm	8-12 GHz	15
6	MWCNTs/PVA (Nasouri & Shoushtari, 2017a)	3 mm	12 GHz	31.5
7	PA6/SDS/MWCNTs (Nasouri & Valipour, 2015)	-	11.5 GHz	18
8	MWCNTs/PVP (Nasouri & Shoushtari, 2017b)	-	8.2-12.4 GHz	42
9	PANI/PAN/MWCNTs (Zhichun Zhang et al., 2014)	-		5.9
10	MWCNTs/PS (Qavamnia &	-	8.2-12.4 GHz	32

	Nasouri, 2016)			
11.	P@ Ni-Co hybrid membrane (Y. Hu et al., 2019)	0.180 mm	8-26.5 GHz	77.8
12.	TiO_2/SiO_2@PPy@rGO (TSPG) hybrid film (L. Huang et al., 2019)	0.26 mm	8-12 GHz	38
13.	CPAN NF/Ag NP (H. Kim et al., 2012)	35 µm	8-26.5 GHz	85.19
14.	CPAN NF/Cu NP (H. Kim et al., 2012)	36 µm	8-26.5 GHz	66.82
15.	CPAN NF/Ni NP (H. Kim et al., 2012)	35 µm	8-26.5 GHz	53.24
16.	200 nm Cu- deposited PVA nanofiber mats	-	0.5-18 GHz	30-33
18.	r-GO coated Fe_3O_4@SiO_2@PPy (FSPG) composite film (Yuan et al., 2018)	0.27 µm	8-12 GHz	32
19.	ZrO_2- embedded graphite structured carbon fibers (Im et al., 2011)		800-8500 MHz	31.79
20.	ZrO_2 @CNF mats/epoxy composite (Deeraj et al., 2021)	0.72 mm	12-18 GHz	94 dB
21.	Ag- decorated PVA/Fe_2O_3 nanofiber composites	-	10 GHz	45.2
22.	Ag-deposited electrospun nylon 66 (Jaeyeon Kim et	100 µm	8-18 GHz	60.6

	al., 2020)			
23.	Spinel $ZnCr_2O_4$ nanofibers (Kowsari & Mallakmohamadi, 2012)		5-12 GHz	-38 (R_L)
24.	$Ba_{0.2}Mg_{0.8}Fe_2O_4$ (BFMO)-PVDF composites fibers (Revathi et al., 2015)		2-3 GHz	28
25.	carbon composite nanofiber webs contained $BaTiO_3$ NPs (Kang et al., n.d.)	-	300 MHz-1.5 GHz	23
26.	carbon composite nanofiber webs contained Fe_3O_4 NPs (Kang et al., n.d.)	-	300 MHz-1.5 GHz	20
27.	Magnetic CNFs – Fe NPs (Xiang et al., 2014)	1.3 mm	4-18 GHz	67.5
28.	Magnetic CNFs – Co NPs(Xiang et al., 2014)	1.6 mm	4-18 GHz	63.1
29.	Magnetic CNFs – Ni NPs (Xiang et al., 2014)	1.7 mm	4-18 GHz	61.0
30.	MXenes (d-$Ti_3C_2T_x$/r-CNF) composite films (C. Cui et al., 2019)	15 µm	8-12 GHz	42.7

1.5 Conclusion

Over the last decade, advancements in the electronics sector have raised expectations for EMI shielding requirements. To meet this demand, recent research has focused on developing shielding materials that can give the same level of shielding effectiveness while eliminating all of the disadvantages of traditionally employed metallic shields. However, there is a significant

gap between laboratory-level preparation and industrial applications. Many, recent studies involve light-weight polymer composites with EMI shielding abilities. The EMI shielding performance of these composites is influenced by the matrix material and the fillers utilized in their fabrication. Conducting and non-conducting polymers are employed for EMI shielding with several benefits, although polymers have failed to produce high SE due to their limited electrical conductivity. As a result, numerous types of conductive fillers are utilised to improve the electrical conductivity of polymer composites. The electrospinning technique is a straightforward method to develop lightweight and flexible, high-performance EMI shielding materials with high value of SE_A. Because of the variety of composition options available, electrospun nanofibers can offer promising EMI shielding applications.

The electrical conductivity of a polymer fibre composite alone is insufficient for effective EMI shielding. Additional factors that contribute to a high EMI SE value include dielectric strength, magnetic permeability, and a good conductive network. Adding a small amount of carbon black, MWCNTs, and reduced graphene oxide (r-GO) produced improved results by forming a conductive network with a fibre matrix. The majority of the reported polymer fibre composites have EMI SE in the 20-50 dB range, which is still insufficient for industrial use. Even after incorporating metal nanoparticles and metal oxides, the produced electrospun composite fibers have an EMI SE value in the 40-80 dB range, which is lower than that of metals. These EMI shielding materials are still hard to use for real-world use.

1.6 Motivation

Polymer composites have been extensively explored for EMI shielding applications over the past two decades. Low conductive filler loading causes poor conductivity in polymer matrix composites, whereas high conductive filler loading usually results in lower mechanical properties and processibility due to filler agglomeration and weak interfacial polarization. Developing polymer matrix composites with uniformly dispersed conductive fillers and strong interfacial interaction is extremely desirable. Carbon foams with high porosity are becoming increasingly popular for EMI shielding due to their high specific shielding effectiveness (SSE) due to their low density. However, it is still challenging to develop EMI shielding materials with high SSE_t with low thickness. Flexible, lightweight, and hydrophobic EMI shielding materials are mandatory for real-world applications.

Electrospun fibers upon thermal treatment, might develop a 3-D interconnected conductive network suitable for high-performance EMI shielding with high SSE_t value. The 1-D CNF has

capability to induce multiple internal reflections inside the materials due to its fiber morphology which might enhance the SE_A value. Incorporation of conductive nano-fillers into CNF results in formation of hetero-interfaces, dipoles and defects. The synergistic effect of conductive nano fillers and CNF can aid in enhancing the EMI shielding performance. The post-treatment methods of CNF such as coating with ICPs and incorporation of conductive fillers into individual fibers can be employed to form interconnected 3-D conductive network for electron transport, resulting in high EMI shielding performance at smaller thickness.

1.7 Objective and scope of thesis

The main objective of the current research is development of lightweight, thin, hydrophobic, and flexible EMI shielding materials based on electrospun PAN fiber. Towards this, the following nanofiber composites were prepared and studied in detail.

- N-doped carbon nanofiber via carbonization of electrospun PAN fiber.
- PDMS composite of CNF to enhance ease of handling of CNF and for making it flexible for practical applications.
- Conductive CNF coated with PEDOT: PSS-PVP and PDMS composite for EMI shielding.
- Tellurium NPs incorporated CNF and PDMS composite for EMI shielding.
- Nb_2O_5 NPs embedded N-doped CNF and PDMS composite for EMI Shielding.
- $La_{0.85}Sr_{0.15}CoO_{3-\delta}$ NPs incorporated N-doped CNF and PDMS composite for EMI shielding.
- Aligned, $BaTiO_3$ NPs incorporated N-doped CNF and PDMS composite for EMI shielding.
- Carbon Black Incorporated N-doped CNF and PDMS composite for EMI shielding.

CHAPTER: 2

Experimental

Overview

This chapter provides details on the materials, methods for fabrication of nanofibers, post treatment of the nanofibers and preparation of composites. Description on various characterization methods employed are also included. In this work, carbon nanofibers (CNFs) are prepared from PAN and flexible composites of CNFs are made using polydimethylsiloxane (PDMS). Hence, the general method of fabrication of CNFs and PDMS composites are described in this chapter. Procedures for modification of CNFs by incorporation of different fillers are discussed in the respective chapters.

2.1 Materials

Polyacrylonitrile (PAN) (average Mw 150,000; CAS No. 25014-41-9), Poly(3,4-ethylenedioxythiophene): polystyrene sulfonate (PEDOT: PSS) (1.3 wt% dispersion in H_2O), (CAS: 9003-39-8), Tellurium (CAS: 13494-80-9), cobalt nitrate hexahydrate ($Co(NO_3)_2.6H_2O$), (CAS: 10026-22-9), strontium nitrate ($Sr(NO_3)_2$ (10042-76-9), and carbon black super P ((CBSP) CAS: 1333-86-4) were procured from Sigma Aldrich (Bangalore, India). Polyvinylpyrrolidone (PVP) (Average molecular weight: 30,000), lanthanum nitrate hexahydrate ($La(NO_3)_3.6H_2O$) (CAS: 10277-43-7), and N, N-dimethylformamide (DMF) (CAS: 66-12-2) were purchased from Spectrochem PVT. LTD. (Mumbai, India). The extrapure analytical reagent grade niobium pentoxide (CAS: 1313-96-8) was procured from Sisco Research Laboratories Pvt. Ltd. (Maharashtra, India). Polydimethylsiloxane (PDMS) kit of silicone resin and hardener (SLYGARD 184 kits) was purchased from "The Dow Chemical Company" (Mumbai, India).

2.2 Methods of preparation of Carbon Nanofiber (CNF)

2.2.1 Preparation of electrospun PAN fiber (EF)

A 10 mL of 10 wt% PAN solution in DMF was prepared. The above solution was transferred into a 12 mL syringe with a metallic needle, having diameter of 0.80 mm for electrospinning. The electrospinning machine was procured from Physics Instrument Co., Chennai, India as

shown in **Figure 2.1**. The metallic needle tip was subjected to a high voltage (13 kV) and a metallic rotatory drum collector was placed 13 centimeters away from the tip of the needle. Solution for electrospinning was pumped at a flow rate of 1.0 mL $h^{-1,}$ from the syringe to obtain electrospun fiber mat on aluminum foil adhered to the drum collector.

Figure 2. 1: The digital photograph of electrospinning set-up used for this thesis work.

2.2.2 Carbonization of electrospun PAN fiber (CNF)

The obtained electrospun PAN fiber (EF) mat was dried at room temperature for 12 h and then stabilized at 250 °C in air oven for 4 h, and then carbonized at 900 °C in argon atmosphere for 4 h, at a ramping rate of 2 °C min^{-1}. Carbonization was performed in high-temperature inert furnace procured from Vacuum Technologies Ltd. (Bangalore, India). A high vacuum was generated inside the furnace before carbonization and maintained a proper flow of Ar gas during carbonization of the electrospun mat. Upon carbonization, electrospun PAN fiber forms nitrogen-doped, interconnected, three dimensional (3-D) electrically conductive network that can directly influence the EMI shielding properties (S. Dong et al., 2022). The carbonized electrospun PAN fiber mat was termed as 1-D N-doped CNF (**abbreviated as CNF**). The CNF mat was cut into square pieces (4 cm x 4 cm) for EMI shielding testing and also for preparation of PDMS composites.

2.3 Fabrication of PDMS composite of CNF

SLYGARD 184 silicone resin and hardener were mixed in 10:1 ratio, as suggested by the manufacturer (Dow). The mixture was poured over the CNF mat in a mold after removing air bubbles by keeping in vacuum oven. Then the mold was kept in oven at 60 ^{o}C for 12 h to obtain flexible PDMS composite of CNF. **Figure 2.2** shows the schematic illustration of the fabrication procedure of CNF and its PDMS composite.

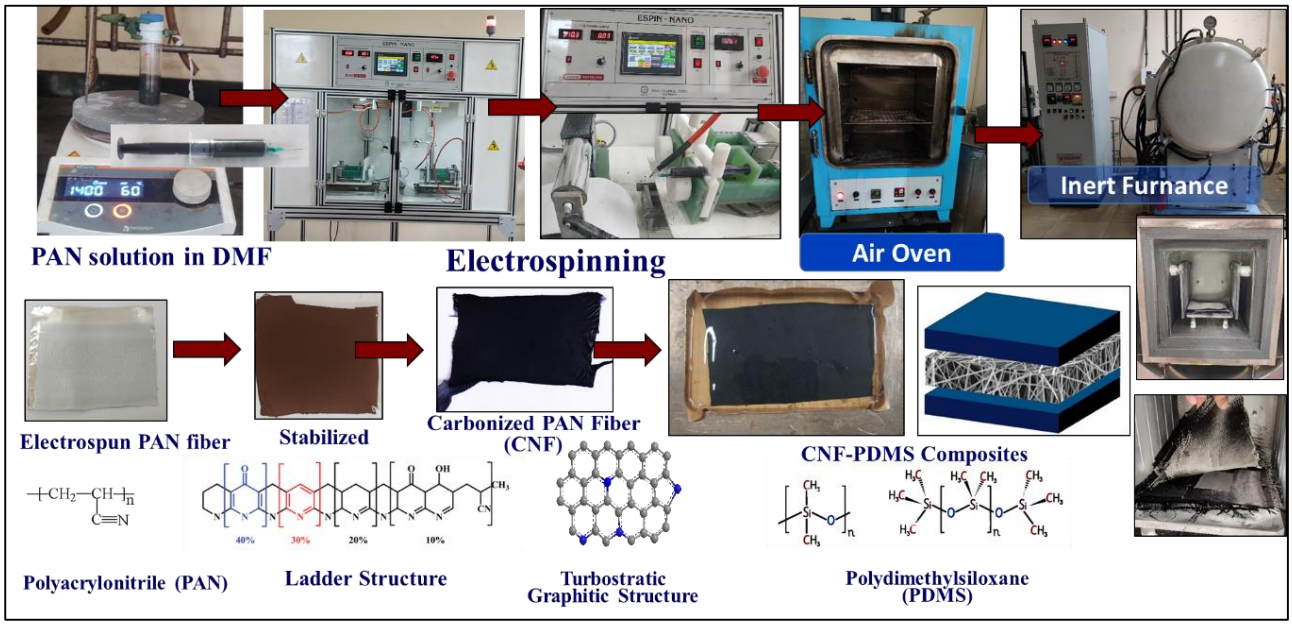

Figure 2. 2: Schematic illustration of the fabrication of CNF and its PDMS composite.

2.4 Characterization

2.4.1 Transmission electron microscopy (TEM) analysis

Microstructure of fillers (NPs) and morphology of electrospun fibers were analysed by TEM (JEOL microscope at 120 kV). Nanoparticles were dispersed in water and a small drop of colloidal suspension of NPs (usually about 5 µL) was pipetted onto the copper grid and allowed to dry at room temperature. The copper was directly examined in a TEM once the medium was evaporated. Solution of PAN or PAN solution containing homogeneously dispersed NPs was directly electrospun over the copper mesh grid with the optimized electrospinning parameters, for TEM analysis. The copper grid was pasted over aluminum foil wrapped over the drum collector, using tape.

2.4.2 Scanning electron microscopy (SEM) analysis

The fiber morphology and structure of the carbonized electrospun fibers and their PDMS composites were examined by scanning electron microscope (FE-SEM, Zeiss microscope). Prior to taking SEM images, the samples were sputter coated with gold. The fiber diameter was determined using SEM image of CNF mats and filler incorporated CNF mats at micrometer scale with imageJ software. At least 10 distinct fibers were used for the analysis.

2.4.3 Energy dispersive X-ray spectroscopy (EDS) analysis and elemental mapping

The elemental composition and elemental mapping of fibers were obtained from energy-dispersive X-ray spectrometer (EDS) equipped with the FESEM (Bruker, Zeiss microscope).

2.4.4 X-ray diffraction (XRD) pattern analysis

Powder XRD patterns of fillers (NPs), CNF, and fillers (NPs) incorporated-CNF were recorded using Cu Kα radiation (D8 Discover, Bruker, USA).

2.4.5 Raman spectra analysis

Raman spectra were obtained by employing argon ion excitation at a wavelength of 532 nm using Renishaw inVia Raman spectrometer in the range of 400-3200 cm^{-1}.

2.4.6 X-ray photoelectron spectroscopy (XPS)

Chemical composition and chemical bonding of CNF and fillers incorporated-CNF was checked by X-ray Photoelectron spectroscopy (XPS, PHI 5000 Versa Probe II, USA).

2.4.7 Universal testing machine (UTM)

The tensile strength of PDMS and PDMS composites of CNF was determined from the stress-strain measurements of rectangular samples of 30 mm x 10 mm x 0.84 mm using universal testing machine (UTM) (Instron5500, USA) with load cell of 250 N at an extension rate of 1 mm min^{-1}.

2.4.8 Dynamic mechanical analyzer (DMA)

Dynamic mechanical analysis (DMA) of PDMS and PDMS composite of CNF was performed in tensile mode using dynamic mechanical analyzer (Perkin-Elmer diamond from Seiko

instrument) using rectangular samples with dimensions of 10 mm x 6 mm x thickness (mm). The analysis was carried out at a frequency of 1 Hz with a heating rate of 2 $^{o}C\ min^{-1}$.

2.4.9 Contact angle measurement

Evaluation of the surface hydrophobicity of the CNF, fillers incorporated CNF, and its PDMS composites was performed by contact angle measurement using a Goniometer (Ram-hart Instrument Co., USA). According to the ASTM D5946 standard, the contact angle of water can be used to define the hydrophobicity of the samples. As stipulated in the standard, the water contact angle can be measured by capturing an image of a liquid drop sitting on a solid and subsequently analyzing it.

2.4.10 Thermogravimetric analysis

Thermogravimetric analysis (TGA) was carried out using a thermal analyser (Q-50, TA instruments) with heating rate 10 $^{o}C\ min^{-1}$ in the temperature range of 25 ^{o}C to 900 ^{o}C in N_2 atmosphere.

2.4.11 Sheet resistivity measurement

The four-probe method (ASTM F1529-97) was used to record the voltage with respect to the current applied, using Keithley SMU 2441. Current was applied from 0.1 mA to 3 mA to measure sheet resistance, resistivity, and electrical conductivity using the following equations (Im et al., 2009; Shahzad et al., 2016).

$$\text{Sheet resistance } (R_s) = 4.5324\ (V/I) \quad (18)$$

$$\text{Resistivity } (\rho) = R_s.\ t \quad (19)$$

$$\text{Electrical Conductivity } (\sigma) = 1/\rho \quad (20)$$

Where, t is the thickness of the samples.

2.4.12 EMI SE measurement

EMI SE was calculated using scattering (S) parameters obtained from two-port vector network analyser (VNA) (Agilent technologies, N5224A, USA) connected with rectangular waveguide adaptor (Vidyut Yantra Udyog, India) in the frequency range of 8 GHz- 26.5 GHz [X-band (8-12.4 GHz), Ku-band (12.4-18 GHz), and K-band (18-26.5 GHz)] as shown in **Figure 2.3(a and c)**. The VNA underwent proper calibration procedures prior to measurement of S-

parameters. **Figure 2.3(b and d)** demonstrate the VNA calibration procedure by using mechanical calibration kits that include open, short, & load (55 Ω) as well as electronic calibration module. The calibrated waveguide was connected with co-axial cable with proper connector and $SE_T$was measured using the relation $SE_T = 10 \log\left(\frac{1}{|S_{21}|^2}\right)$. When no sample is inserted, SE_T value exhibited should be 0 dB for X, Ku and K bands.

Figure 2. 3:Digital photograph of (a) two port VNA with waveguide adaptor (X-band), (b) mechanical calibration process, (c) rectangular waveguide adaptor ((X-band, Ku-band, and K-band) with sample holder, and (d) Mechanical calibration kits contains male and female open, short, and load (55 Ω).

The EMI shielding effectiveness (SE) was calculated by S-parameters using a waveguide transmission line equation. The reflection coefficient (R), transmission coefficient (T), and absorption coefficient (A) can be measured by $R= |S_{11}|^2 = |S_{22}|^2$, $T= |S_{12}|^2 = |S_{21}|^2$, and A= 1-R-T, respectively. The total EMI SE (SE_T) is calculated by summation of the contributions from shielding due to reflection (SE_R), absorption (SE_A), and multiple-reflection (SE_M) as shown in

Equations 5, 5, 10 and 11. (Chung, 2001, 2020; Ganguly et al., 2018; A. K. Singh et al., 2018; X. Y. Wang et al., 2022; Zahid et al., 2021b)

$$SE_T = SE_R + SE_A + SE_M \quad (5)$$

$$SE_T = SE_R + SE_A = 10\log\left(\frac{1}{T}\right) = 10\log\left(\frac{1}{|S_{21}|^2}\right) \quad (5)$$

$$SE_R = 10\log\left(\frac{1}{1-R}\right) = 10\log\left(\frac{1}{1-|S_{11}|^2}\right) \quad (10)$$

$$SE_A = 10\log\left(\frac{1-R}{T}\right) = 10\log\left(\frac{1-|S_{11}|^2}{|S_{21}|^2}\right) \quad (11)$$

Specific shielding effectiveness (SSE) = EMI SE/density (15)

Absolute shielding effectiveness (SSE_t) = SSE/thickness (16)

Effective absorption (A_{eff}) = $\frac{1-R-T}{1-R}\ X\ 100\ (\%)$ (17)

2.4.13 Complex dielectric permittivity

The complex relative dielectric permittivity ($\varepsilon_r^* = \varepsilon_r' - j\varepsilon_r''$) of PDMS composites of non-aligned CNF, aligned CNF, non-aligned $BaTiO_3$-CNF, and aligned $BaTiO_3$-CNF were measured using two port vector analyser (Keysight Technologies (N5234B)) via Keysight N1500A materials measurement software suit.

CHAPTER: 3

Carbon Nanofiber and Polydimethylsiloxane Composite for EMI Shielding

Overview

This chapter describes the morphology, structural analysis, chemical composition and chemical bonding of 1-D Nitrogen-doped carbon nanofibers (CNF). This chapter highlights the potential of CNF for EMI shielding in X-band, Ku-band, and K-band and also the need for further enhancing the EMI shielding performance. This chapter also describes the properties of PDMS composites of CNF

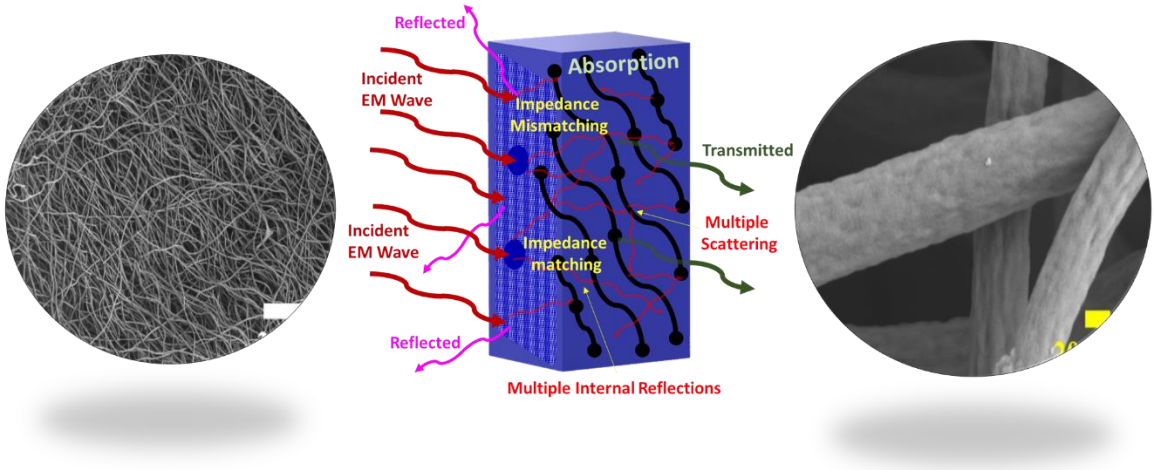

3.1 Introduction

PAN-based carbon fibers (CF) are leading high-performance fibers for composite materials, accounting for over 90% of global CF production. These fibers are used in structural applications, aerospace and sports industries due to their high tensile strength and stability.

One of the most effective ways for producing 1-D nanostructured fibers is electrospinning technique, which offers possibility of fabricating a wide range of fibrous materials. Electrospun fibers have unique features such as ultrafine diameter, a large surface area to volume ratio, a high length to diameter ratio, high porosity and good mechanical strength, processability, and cost effectiveness. Electrospun fiber composites provide a potentially effective platform for absorption and multi-reflection of incident EM waves inside

the materials due to 1-D fibrous structure, high porosity, and large surface area. (X. Lu et al., 2009) Mostly, electrospun fibers are insulating in nature and therefore, post-treatment is required to make them electrically conductive. One of the easy ways to make electrically conductive CNF is stabilization and carbonization of electrospun PAN fiber. Upon carbonization, electrospun PAN fiber forms nitrogen-doped, interconnected, 3-D electrically conductive network that can directly influence the EMI shielding properties (S. Dong et al., 2022; M. Kim et al., 2021; Mohan et al., 2021; Song et al., 2014; Liying Zhang et al., 2013; Zheng, Wang, et al., 2023). Conductive fillers are incorporated into the electrospun PAN fiber to further enhance the EMI shielding properties.

Herein, the CNF mats have been successfully fabricated by electrospinning followed by carbonization for EMI shielding. The 1-D N-doped CNF has turbostratic graphitic structure, and strong 3-D interconnected conductive network Porosity and high surface area allows multiple internal reflections for high performance EMI shielding. However, CNF is brittle and fragile and hence, difficult to be handled. Hence, PDMS composite of CNF was made which retained the EMI shielding property of CNF while improving the mechanical property of CNF. The PDMS composite of CNF is flexible and can be explored for applications under harsh environments.

3.2 Experimental

The methods for preparation of CNF and the PDMS composites are provided in Chapter 2 (section 2.2 - 2.4)

3.3 Results and discussions

The preparation of CNF involves heat treatment to convert electrospun PAN fiber (EF) into CNF having inherent nitrogen-doped into graphitic structure of CNF. The formation of CNF is a multi-stage procedure that involves varying temperature, using oxygen during stabilization process, and releasing other gases such as H_2, N_2, NH_3, CO_2 and HCN. Understanding the oxidative and thermal treatment throughout the conversion process of electrospun PAN fiber to CNF is critical for producing high carbon yield of CNF.

3.3.1 Thermogravimetric analysis

Thermogravimetric analysis (TGA) is an effective tool for studying the thermal stability of EF. TGA measures the variations in the weight loss of EF during carbonization process. **Figure 3.1(a)** represents the TGA plot of EF, which demonstrates the two main phases in the

conversion of EF into N-doped CNF. The first phase involves oxidative stabilization at temperatures ranging from 200 to 300 °C, which results in a ladder structure of heterocyclic six-membered rings. The formation of ladder structure was confirmed by Raman spectra (**Figure 3.4(a)**). This stabilized EF serves as precursor for carbonization process at 900 °C in inert atmosphere. In the second phase, the stabilized EF was carbonized at 900 °C in an inert atmosphere to remove all heteroatoms and generate N-doped graphitic structure, also known as turbostratic structure (haphazardly folded carbon sheets). After carbonization, the carbon yield is 31.4%, as shown in **Figure 3.1(a)**. As a result, we obtained CNF mats with an N-doped graphitic structure, also known as turbostratic structure, as confirmed by Raman spectra (**Figure 3.4(a)**) and XRD patterns (**Figure 3.4(b)**).

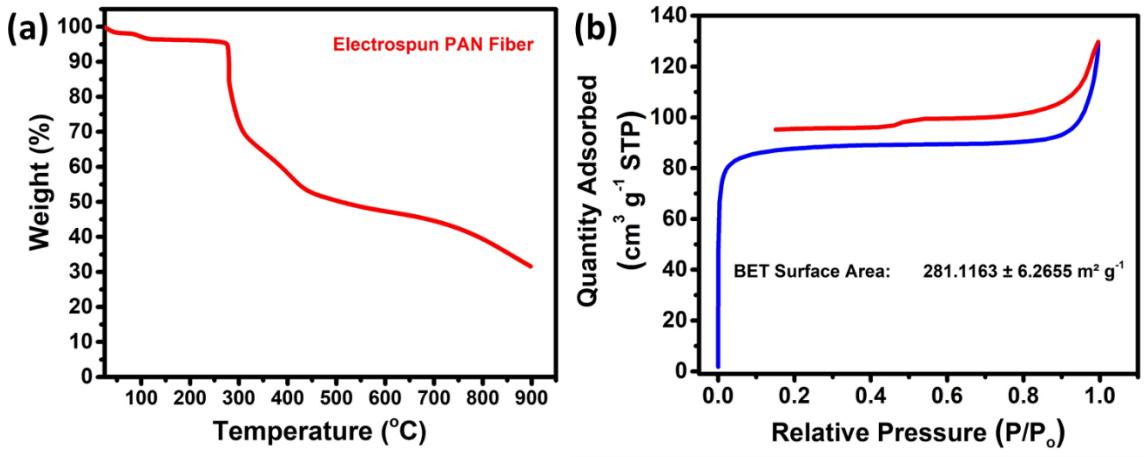

Figure 3. 1: (a) TGA plots of electrospun PAN fiber. (b) The N_2 adsorption-desorption isotherm of CNF.

3.3.2 Brunauer-Emmett-Teller (BET) surface area

Figure 3.1(b) shows the N_2 adsorption-desorption BET plot of CNF. The BET surface area obtained was 281 m^2 g^{-1} with pore volume of 0.188 cm^3 g^{-1} and average pore diameter of 2.68 nm. The porous structure of 1-D CNF with high surface area can cause polarization interface which allows multiple internal reflections based EMI shielding (Hou et al., 2021).

3.3.3 TEM image

TEM is an essential technique for examining the morphology of electrospun fibers. TEM images of PAN EF are displayed in **Figure 3.1**. **Figure 3.1** shows the TEM image of PAN EF.

The images show that there was no electrospraying and no bead formation during electrospinning.

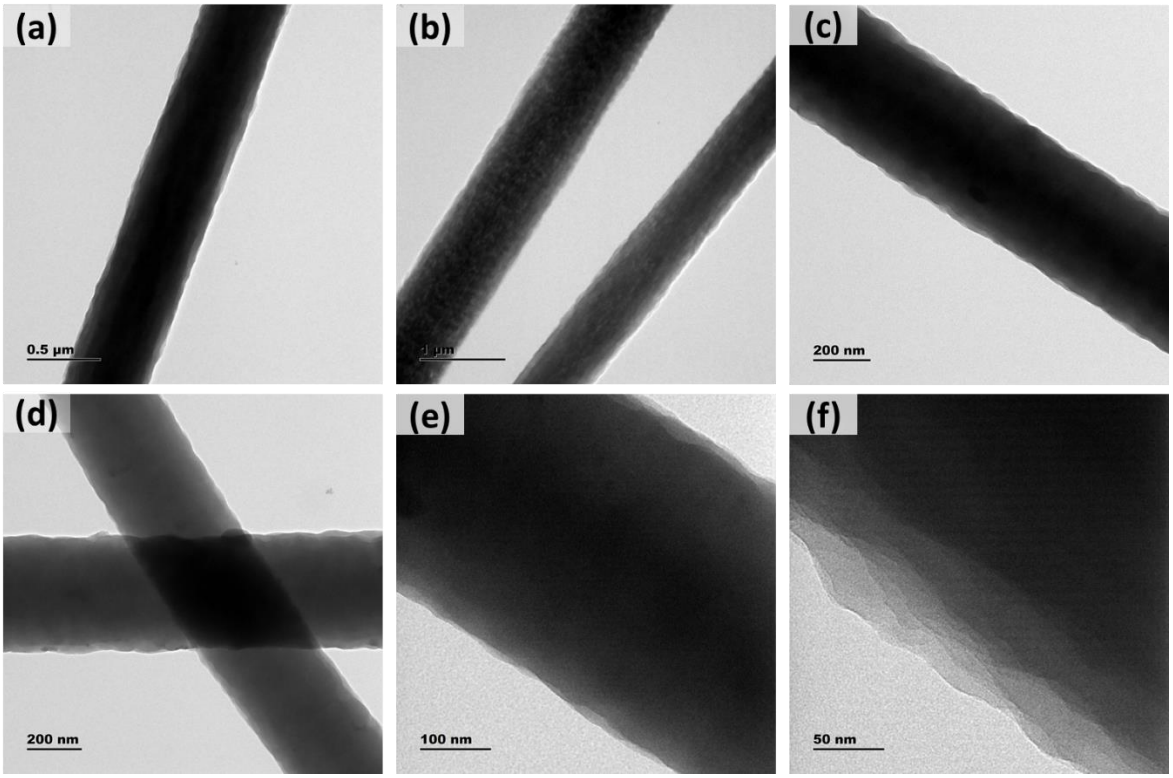

Figure 3. 2: (a-f) TEM images of electrospun PAN fiber.

3.3.4 SEM image

The SEM images of CNF, PDMS composites of CNF are presented in **Figure 3.2**. The images show that the fiber morphology of electrospun PAN fiber remains similar after carbonization. **Figure 3.2 (a-c)** presents the SEM images of CNF and shows that CNFs are continuous with a mean diameter of 462 ± 64 nm. It also shows that the fibers are continuous without bead formation. The SEM images of cross-section of CNF are presented in **Figure 3.2 (d-e)**, which show that CNFs have 1-D, layer-by-layer structure, and high porosity. **Figure 3.2 (g-h)** is the SEM image of PDMS composite of CNF and shows that PDMS composite has smooth surface. The SEM images of cross-section of PDMS composite of CNF are presented in **Figure 3.2 (j-l)**, and shows the tight bonding between CNF and PDMS and indicates that the fiber morphology remains intact in the composite.

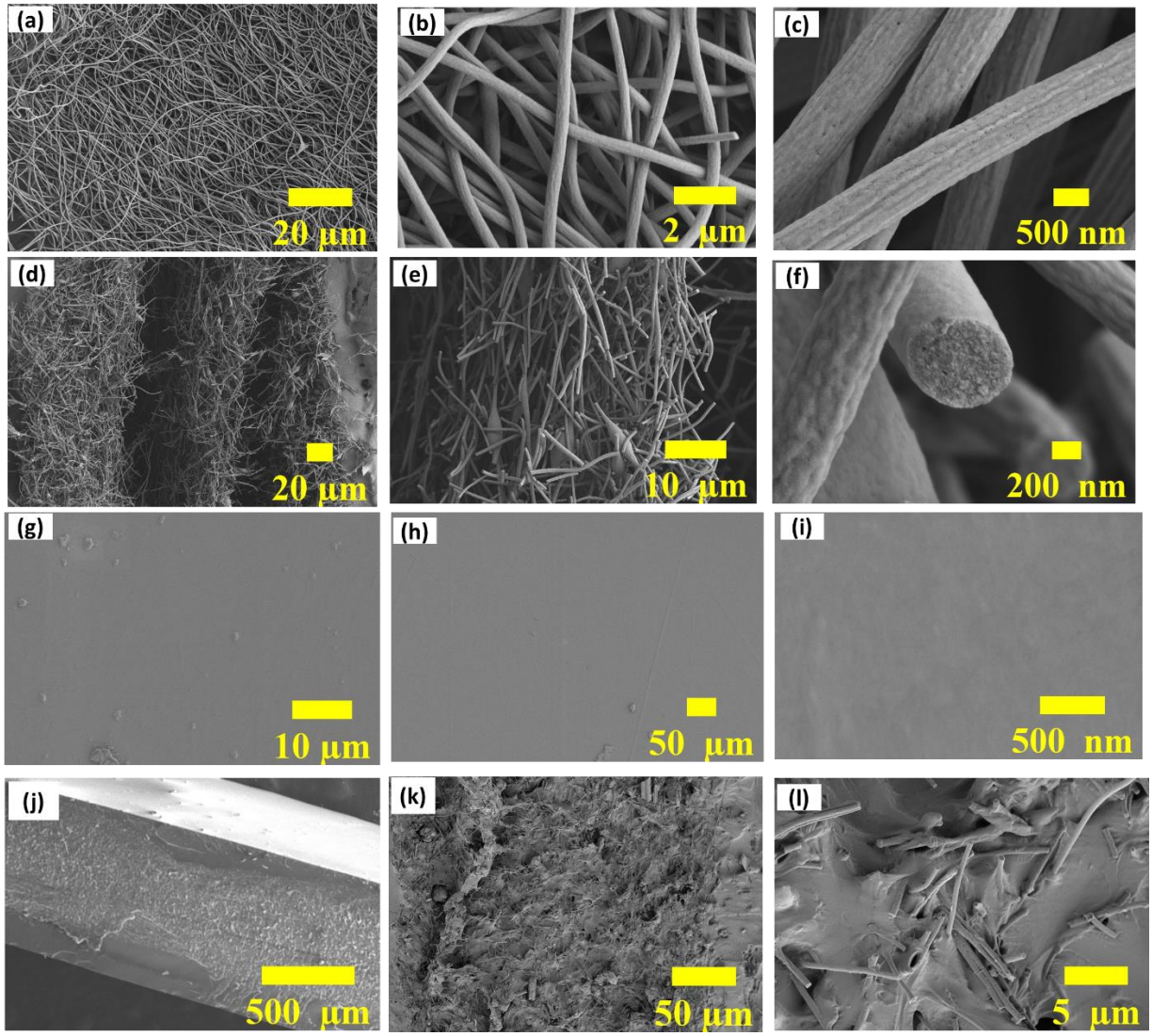

Figure 3. 3: SEM images of (a-c) CNF, (d-f) cross-sectional images of CNF, (g-i) PDMS composite of CNF, and (j-l) cross-sectional images of PDMS composite of CNF.

3.3.5 Raman Spectroscopy

The best way to determine the microstructure of carbon-based materials is Raman spectroscopy. The Raman spectra of electrospun PAN fiber, stabilized electrospun PAN fiber at 250 ^{o}C, and CNF are displayed in **Figure 3.4(a).** The G-band peak indicates graphitization and D-band peak represents the disordered graphitic structure of the sample. Formation of ladder structure in PAN EF is confirmed from the presence of D-band at 1352 cm^{-1} and G-band at 1595 cm^{-1}. The I_D/I_G ratios of the stabilized EF and CNF are 1.28 and 0.90 respectively. During stabilization of EFs at 250 ^{o}C, the nitrile groups present in the PAN fiber get cyclized to form aromatic structure known as ladder structure. (J. Li et al., 2013; Shokrani Havigh & Mahmoudi Chenari, 2022a; F. Zhang et al., 2014) Upon carbonization of EFs at 900 ^{o}C (CNFs),

the I_D/I_G ratio was decreased to 0.90. This indicates an increase in the extent of graphitization during carbonization. The graphitic and their hexagonal planes of CNF was further confirmed from XRD patterns.

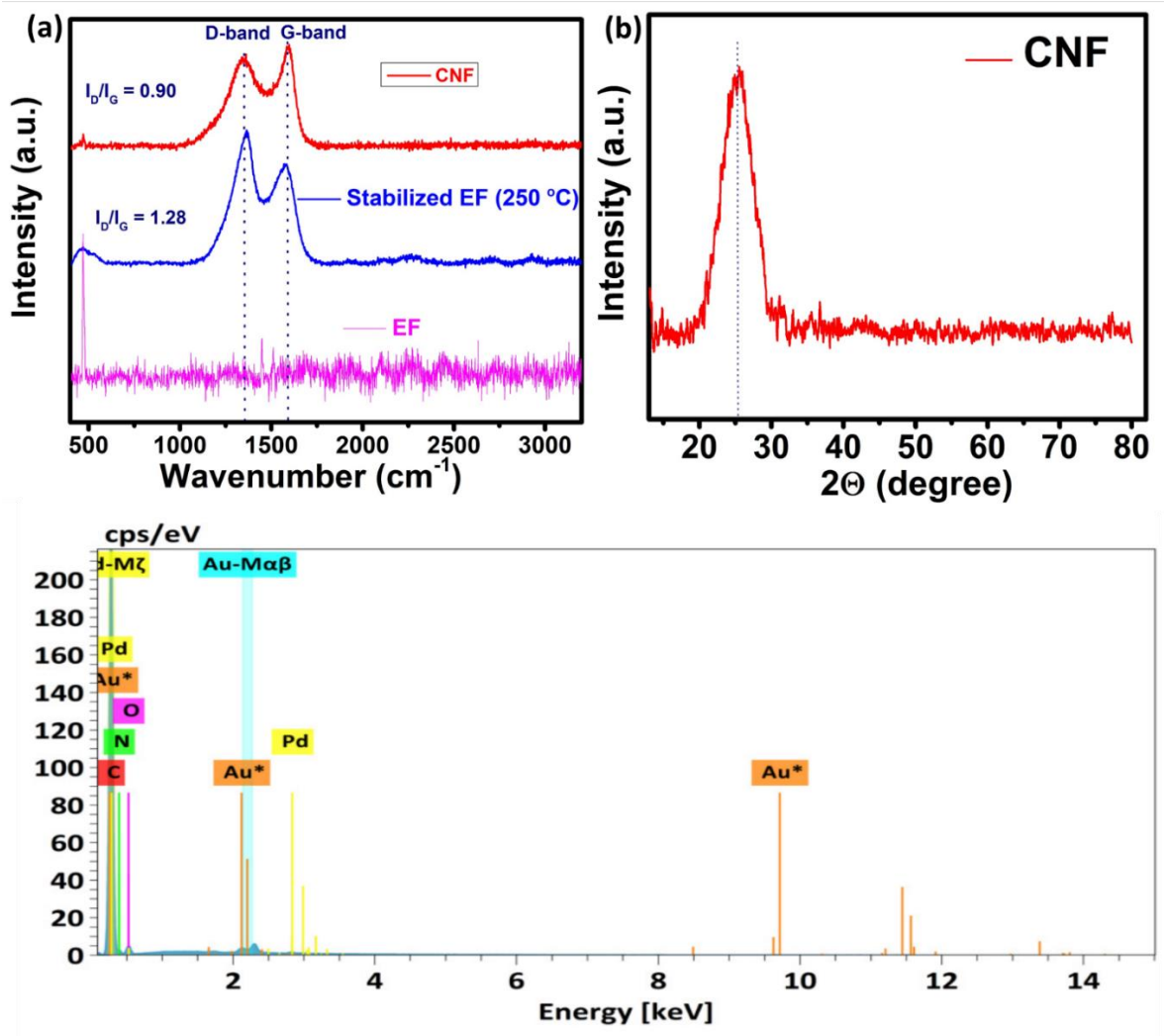

Figure 3. 4: (a) Raman spectra of electrospun PAN fiber, stabilized EF, and CNF. (b) XRD patterns of CNF, and (c) EDS Spectra of CNF.

3.3.6 XRD patterns

The crystallographic structure of carbonized PAN fiber (CNF)is examined by XRD patterns as demonstrated in **Figure 3.4(b)**. The broad peak centred at around 25.4^o in the XRD pattern of CNF belongs to the turbostratic carbon structure (JCPDS 41-1487). The broad peak at 25.4^o is relatively very low in intensity and indicates that carbonized PAN possesses turbostratic carbon structure and low crystallinity (Q. Y. Chen et al., 2014).

3.3.7 EDS analysis and elemental mapping

EDS provides information about the elements present in the CNF. The EDS spectra show strong peaks of carbon, nitrogen, and oxygen as shown in **Figure 3.4(c).**

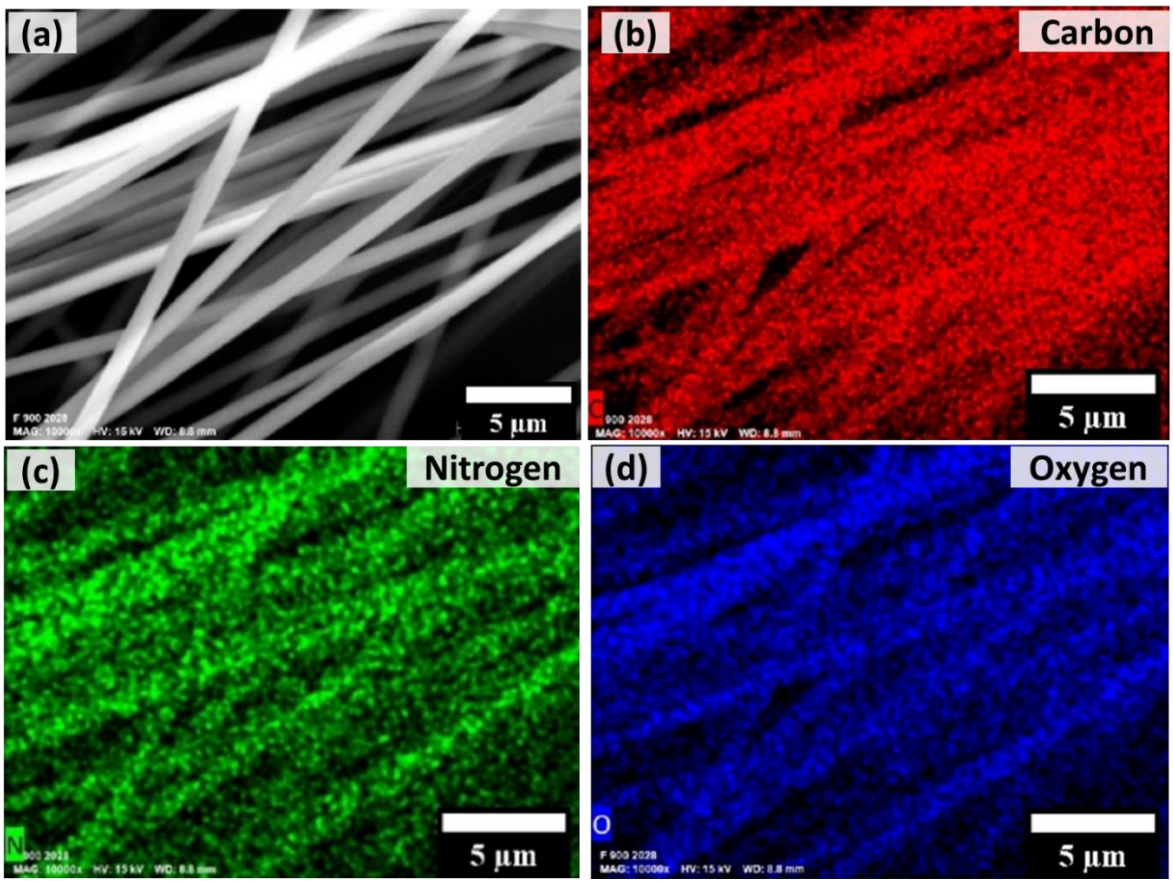

Figure 3. 5: (a) SEM image used for elemental mapping. (b-d) elemental mapping of carbon, nitrogen, and oxygen, respectively.

Elemental mapping is a technique which can be used to visualize and locate the distribution of elements into the CNF. **Figure 3.5(a)** shows the SEM image which was used for elemental mapping. The elemental mappings of carbon, nitrogen, and oxygen confirm the presence of these elements throughout the CNF which is evident from **Figure 3.5 (c-d)**.

3.3.8 XPS analysis

XPS analysis of CNF was carried out to understand the surface chemical compositions. The survey spectrum indicates the presence of carbon, nitrogen, and oxygen on the surface of the CNF as depicted in **Figure 3.6(a).**

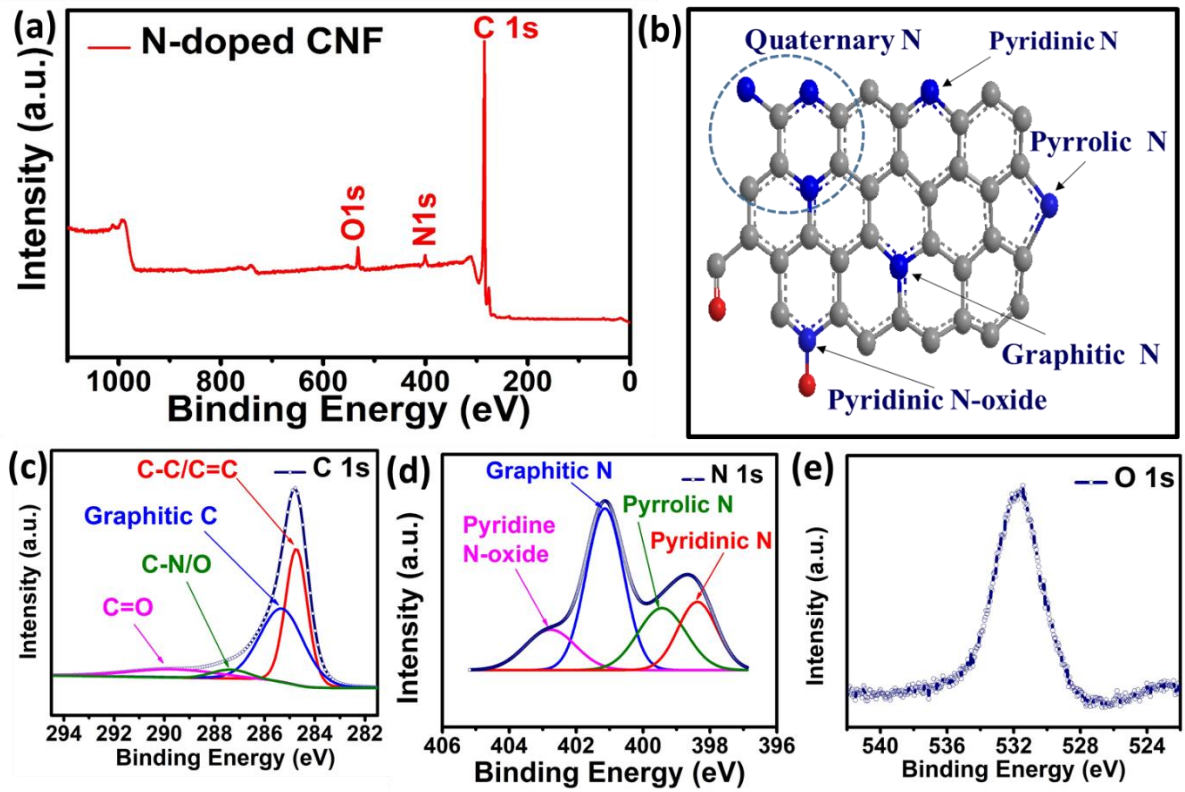

Figure 3. 6: (a) XPS survey scan of CNF, (b) molecular structure of N-doped CNF. (c-e) The high resolution elemental scans of (c) C 1s, (d) N 1s, and (e) O 1s.

The XPS survey scan of CNFs shows peaks at 285.0 eV, 401.7 eV, and 531.7 eV corresponding to C(1s), N(1s), and O(1s) species respectively. These peaks demonstrate the formation of N-doped CNF. The high-resolution elemental scans for the elements contained in CNF, such as C (1s), N (1s), and O (1s) are examined as displayed in **Figure 3.6(c-e),** respectively. The high resolution C 1s spectrum of CNF shows four peaks corresponding to carbonized PAN fiber at 284.8 eV (C=C), 285.7 eV (graphitic C), 288.8 eV (carbonyl carbon), and 285.5 eV (C-O/C-N). The strong peak at 284.8 eV belongs to SP^2 hybridized carbon due to cyclization and formation of graphitic structure (Jing et al., 2021; Meng et al., 2019; Su et al., 2023). The high resolution N 1s spectrum shows four peaks at 398.4 eV (pyridinic N), 400.0 eV (pyrrolic N), 401.1 eV (quaternary N), and 402.5 eV (pyridinic-N-oxide) which are attributed to carbonized PAN fiber as shown **Figure 3.6(b)**. This N 1s peak is due to cyclization of nitrile groups present in PAN, during carbonization. The high resolution O 1s spectrum exhibited two peaks at 531.1 eV and 532.9 eV belonging to carbonyl carbon.

3.3.9 Contact angle measurements

Contact angle measurement is a reliable technique for finding out a material's hydrophilic or hydrophobic nature by goniometry. When the contact angle between the materials surface and a drop of water is greater than 150^o, the material is super-hydrophobic, when it is between 90^o and 150^o, the material is hydrophobic, and when it is less than 90^o, the material is hydrophilic or moisture sensitive (Erbil, 2020). The contact angles of CNF and PDMS composite of CNF are 119^o as shown in **Figure 3.7(a-b)**. All these materials show contact angles greater than 90^o and imply that these materials are hydrophobic or moisture insensitive in nature and these may be used as waterproof shielding materials. CNF is hydrophobic due to turbostratic graphitic structure. PDMS composite of CNF is intrinsically hydrophobic due to the presence of hydrophobic methyl groups in its chemical structure (Ariati et al., 2021; Ji Park et al., 2014). The hydrophobicity of the shielding materials ensures their stability, reliability, and durability for long-term performance of electronic devices.

3.3.10 Mechanical Properties

Figure 3.7 (c) shows the load (100 g) bearing capacity of lightweight CNF. High mechanical strength, flexibility and straight forward fabrication methods adaptable for complicated structures of electronic devices are desirable properties for shielding materials. The PDMS composites of CNF fulfill all these requirements for shielding materials. The remarkable flexibility of the composites is demonstrated via twisting, rolling, and folding of PDMS composite of CNF as shown in **Figure 3.7(d-h)**. The PDMS composite of CNF can be twisted, folded, and rolled without sustaining any damage, and it can then regain its original shape.

DMA was carried out to investigate the viscoelastic properties and damping properties of PDMS and PDMS composite of CNF from -130 ^{o}C to 180 ^{o}C as shown in **Figure 3.7(i-k)**. Glass transition temperatures (T_g) of PDMS and PDMS composite of CNF are -116 and -113 ^{o}C respectively. The very low T_g is due to the chain flexibility arising from Si-O-Si bonds. (Zalewski et al., 2021) The F**igure 3.7(j)** shows that storage modulus of PDMS composite of CNF is more than that of pristine PDMS in the temperature range of 0 ^{o}C -180 ^{o}C. The damping properties (tan δ) of the PDMS and CNF PDMS composites are shown in **figure 3.7(k)**. The CNF PDMS composites exhibited a small shift in T_g determined at the maximum tan δ, towards higher temperature, due to the restriction of chain mobility in the composite. Surface of CNF is completely covered with PDMS and forms interface between PDMS and the layered, 1-D fibrous structure of CNF, as shown in the cross-sectional SEM images of CNF PDMS composite (**Figure 3.3(j-l)**).

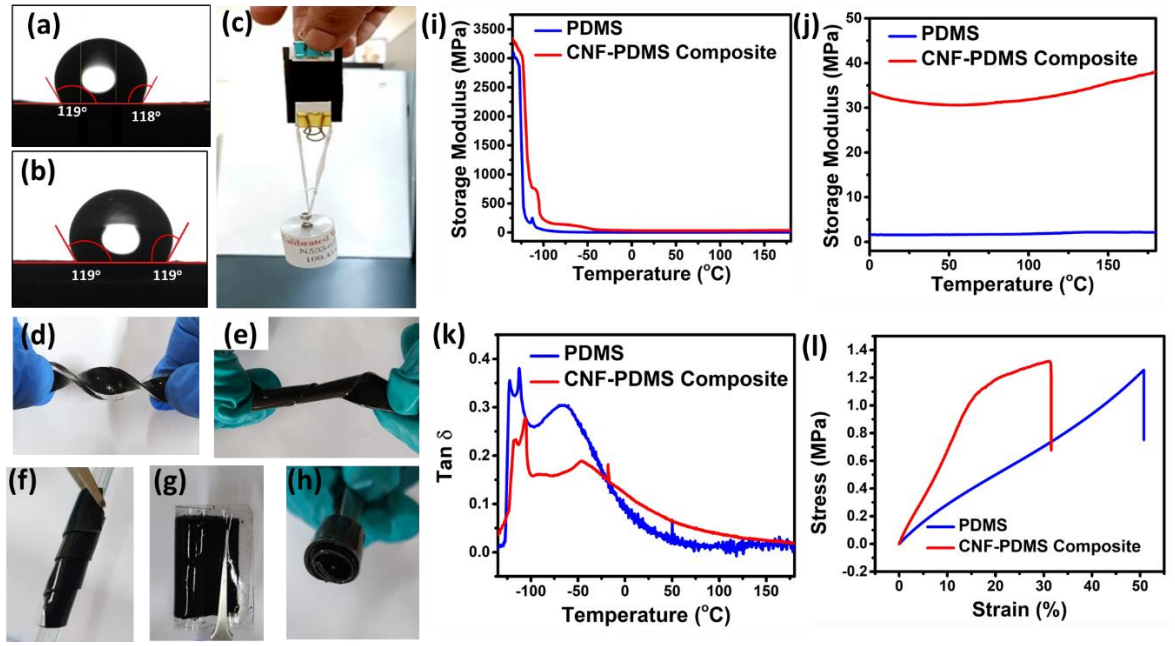

Figure 3. 7: (a-b) contact angle measurement of (a) CNF and (b) PDMS composite of CNF. (c-h) Digital photograph of (c) load (100 g) bearing capacity of CNF, (d-e) twisting, and (f-h) rolling and folding properties of PDMS composite of CNF. (i-k) DMA plots of PDMS and PDMS composite of CNF (i-j) storage modulus vs temperature range of (i) -130 °C to 180 °C, and (j) 0 °C to 180 °C), and (k) tan δ vs temperature. (l) stress-strain curve of PDMS and PDMS composite of CNF.

Incorporation of CNF into the PDMS matrix provides additional cross-linking due to post-curing effects, solid phase reaction and lead to lower macro-chain mobility in PDMS, which is also known as physical cross-linking. The post-curing, physical cross-linking and faster re-alignment and re-orientation of PDMS chains increased the stiffness at elevated temperatures, resulting in increased storage modulus. The dynamic stiffness effect might have increased due to faster re-alignment and re-orientation of PDMS chains in the temperature range of 150 °C to 180 °C. (Linlin Cao et al., 2016a; Placet & Delobelle, 2015) The tensile strength was determined from stress-strain curve as shown in **Figure 3.7(i).** The tensile strength of PDMS composite of CNF is 1.35 MPa which is higher that of pure PDMS (tensile strength = 1.25 MPa). The tensile strength of CNF PDMS composite was increased from the pure PDMS, because, incorporation of CNF into PDMS matrix led to the formation of strong chemical and physical hybrid crosslinks (Linlin Cao et al., 2016a).

3.3.11 Electrical Conductivity measurement

The electrical conductivity and formation of electrically conductive network can directly influence the properties of shielding materials. **Figure 3.8(a)** shows the formation of electrical

conductive network by using an electrical circuit and **Figure 3.8(b)** demonstrates current-voltage plot of CNF. The electrical conductivity of CNF is calculated to be 0.186 S cm^{-1}. The high electrical conductivity of CNF is due to SP^2 hybridized carbons present in CNF.

3.3.12 EMI SE

Metals, on account of their high electrical conductivity, are frequently utilised as shielding materials. However, metals are of heavy weight and low flexibility, susceptible to corrosion and may cause secondary EMI. N-doped CNF are suitable substitutes to metal based shields, because they are resistant to corrosion and can withstand high temperatures without deforming. The EMI SE of CNF was measured in X- band, Ku-band and K-band as displayed in **Figure 3.8(c)**.

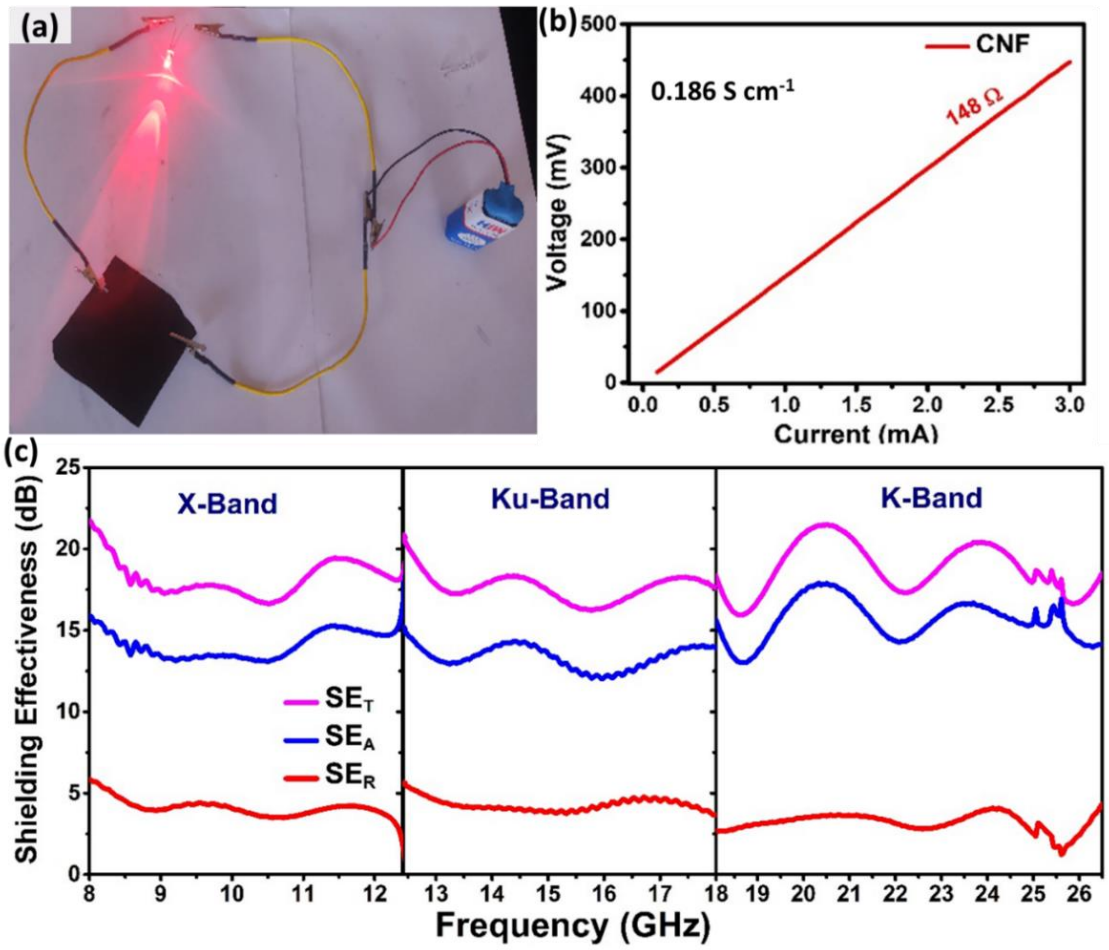

Figure 3. 8: (a) Digital photograph of electrical circuit of CNF connected with LED bulb and battery. (b) Voltage−current plots of CNF. (c) EMI SE properties of CNF in X, Ku, and K-band.

The pure PDMS is an insulator and does not exhibit EMI shielding properties. CNF exhibited average and highest EMI SE of 20 dB and 22 dB with thickness of 0.08 mm, which is above

than the commercial requirement for EMI shielding applications. For better understanding of the mechanism of EMI shielding, we further evaluated SE_A and SE_R. **Figure 3.8(c)** suggests that the SE_A contributes more than 80 % to the SE_T for the samples.

The high EMI SE values are due to 1-D nanostructure of N-doped CNF with formation of strong electrical conductive network between the individual CNF. The doping of nitrogen into CNF enhanced the charge density and mobility of electrons, because nitrogen has more valence electrons than carbon. The N-doped CNF increases the charge density and forms dipoles between carbon and nitrogen which helps in absorption of incident EM waves (Shahzad, Kumar, et al., 2015; W. D. Xue & Zhao, 2014). A portion of the incident EM waves on the CNF surface are reflected upon interaction with the mobile charge carriers present on the surface, while most of the EM waves are allowed to pass through the porous layers of the materials and get absorbed eventually.

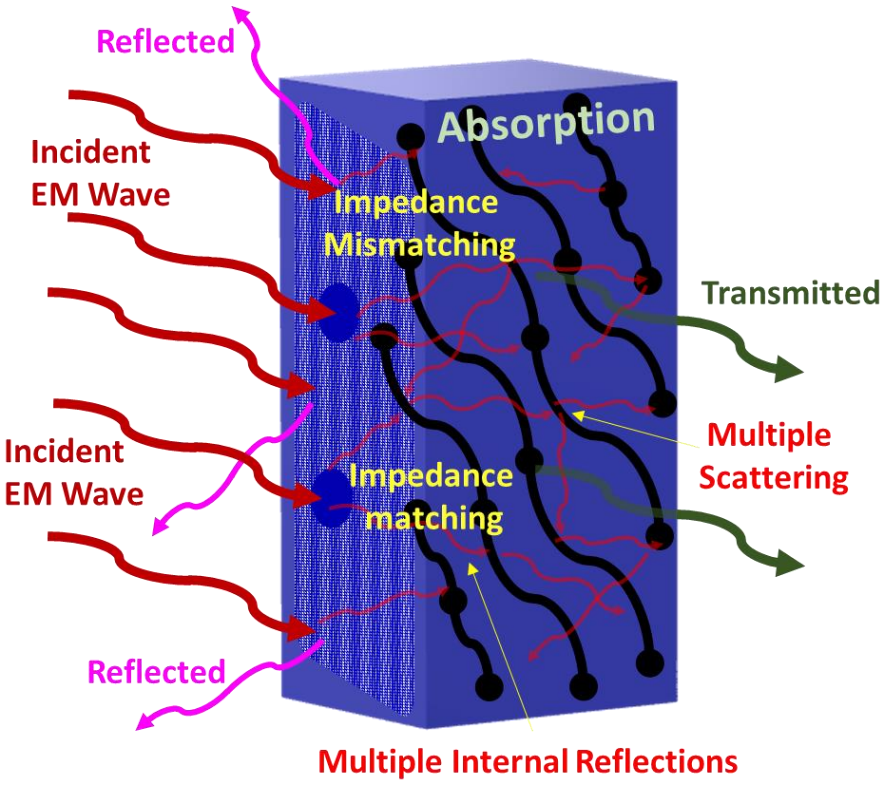

Figure 3. 9: Schematic illustration of EMI shielding mechanism of CNF.

Consequently, very few EM waves are transmitted resulting in high EMI SE value. The 1-D CNF facilitate dipole and interfacial polarization, leading to polarization losses. But, one-dimensional, fibrous, porous, and layer-by-layer structure of CNF can cause impedance matching, which would further enhance the multiple internal reflections. The contribution of

SE_A is more than 80 % of the total EMI SE for all the samples as illustrated in **Figure 3.9**. The effect of the microstructure of CNFs enhances dipole polarization, interfacial polarization and multiple internal reflections and make the shielding mechanism absorption dominant (Su et al., 2023; Ximing Zhang et al., 2022a).

The PDMS composites of CNF exhibited almost similar SE_T value. The PDMS composite of CNF provided high flexibility and make it easy to handle for practical applications. The EMI SE value of PDMS composites of CNF did not change after twisting, folding, bending, and rolling. But, SSE_t values vary due to the variations in the thickness and density.

3.4 Conclusion

This chapter described a simple method to prepare 1-D CNF by electrospinning followed by carbonization for EMI shielding in X-band, Ku-band, and K-band. The highest EMI SE of CNF was 22 dB with thickness of 0.08 mm due to their electrical conductivity and 3-D interconnected conductive network. The one-dimensional fibrous and porous structure of N doped CNF results in efficient shielding of EM waves.

CHAPTER: 4

PDMS Composite of Conductive PEDOT:PSS-PVP Film over CNF for EMI Shielding

Overview

This chapter reports fabrication of poly(3,4-ethylenedioxythiophene): polystyrene sulfonate (PEDOT:PSS) and polyvinylpyrrolidone (PVP) coated, carbonized electrospun PAN nanofiber (CNF) and their flexible PDMS composites. The material showed excellent EMI SE of 44 dB in the frequency range of 8-26.5 GHz with a thickness of 0.06 mm due to the synergetic effect of CNF matrix, PEDOT: PSS, and PVP. It also exhibited a high absolute EMI SE of 5678 dB cm^2 g^{-1} with low loading of PEDOT:PSS-PVP. Here, PEDOT:PSS-PVP/CNF shows higher SE_A than SE_R. These findings indicate the potential of these composites as thin, flexible, hydrophobic, and lightweight EMI shielding materials for practical applications.

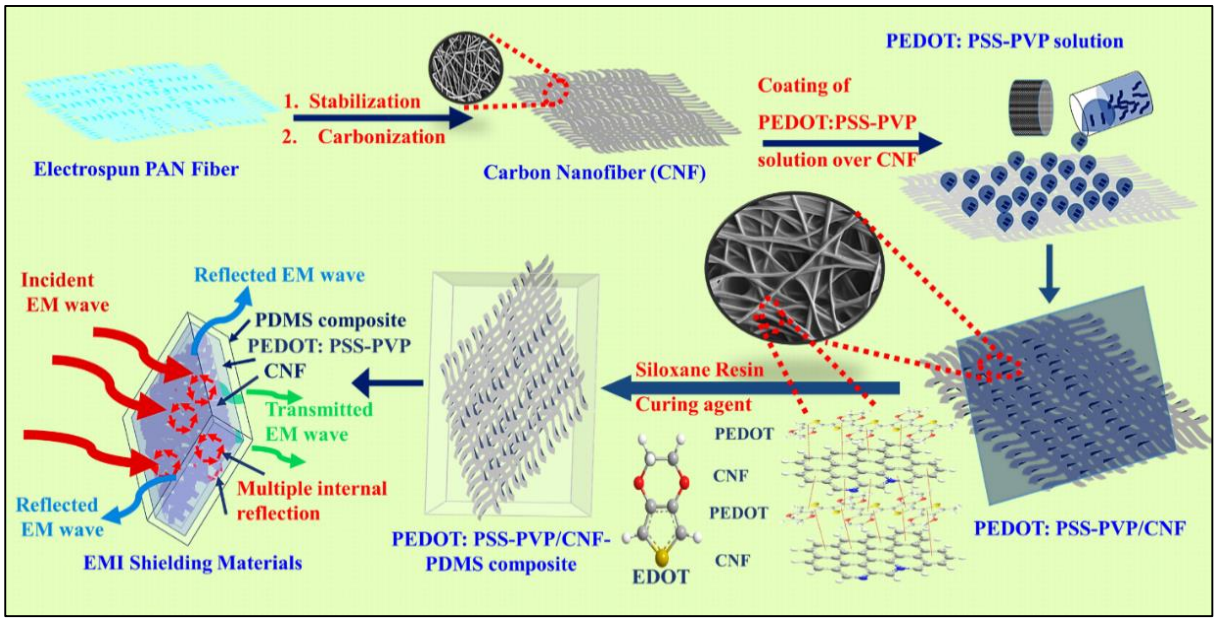

4.1 Introduction

As shown in the previous chapter, a single layer of CNF possesses low EMI SE of 18 dB and is insufficient to meet commercial EMI shielding requirements (20 dB). One way to enhance the performance of CNF is coating of ICPs over CNF. The coating of ICPs over CNF may fill the pores or voids present between the individual CNF and thus would allow formation of strong interconnected 3-D conductive network. ICPs such as polyaniline (PANI), polythiophene, polypyrrole, polyacetylene and poly(3,4-ethylenedioxythiophene): polystyrene sulfonate (PEDOT: PSS), and polyvinylpyrrolidone (PVP) show conductivity due to mobility of delocalized π electrons. ICPs have high potential to replace inorganic materials for shielding materials due to low density, processability, flexibility in design, and chemical functionalization capabilities (Iqbal & Ahmad, 2020; Soares et al., 2021).

PEDOT:PSS is a polyelectrolyte that consists of positively charged electrically conducting and conjugated PEDOT and negatively charged insulating PSS. PSS stabilizes the positively charged conjugated PEDOT in water and other polar solvents. PEDOT: PSS and its composites are used in various applications (Louwet et al., 2003; Yan Yang et al., 2020) such as flexible, conductive, or even stretchable and wearable electronic devices (Yan Yang et al., 2020), flexible electrodes (K. Sun et al., 2015), light-emitting diodes (Otieno et al., 2017b; Sharbati, 2016; H. Shi et al., 2015; Yan Yang et al., 2020), perovskite solar cells (Otieno et al., 2017a), bio-sensors (Yan Li et al., 2018), and thermoelectric devices(Yan Yang et al., 2020). Among the various conductive polymers, PEDOT:PSS exhibits superior EMI shielding due to its excellent electrical conductivity. Das et al. fabricated reduced graphene oxide- gallium / PEDOT:PSS (rGO- Ga/ PEDOT:PSS) nanocomposite, which was coated over cotton fabric by ultrasonic assisted fabrication for EMI shielding in X- band region (8.2-12.4 GHz). As number of coating cycles increased, the EMI SE also increased and the composite showed a high EMI SE of 34 dB for 18 cycles at a thickness of 0.36 µm (P. Das et al., 2022). Ghosh et al. developed a flexible, durable and conducting coating of polyethylene glycol (PEG) with PEDOT:PSS over cotton fabric (PEG/PEDOT:PSS@ cotton fabric), which showed excellent electrical conductivity and EMI shielding in X- band. The EMI SE was measured to be 46.8 dB with the thickness of 0.38 mm and 7.2 g filler deposition after 20 dipping cycles (Ghosh et al., 2019a). Both the above works utilized naturally occurring cotton fabric as a matrix for EMI shielding. Because, cotton fiber is usually insulating, it was treated with PEDOT:PSS to make it electrically conductive. The disadvantages of coating over cotton fiber include the need for a high concentration of the coating material, requirement for high coating thickness, in-

homogeneity of the coating, and the difficulty in forming continuous electrically conductive networks. Consequently, electrospinning may be considered as a straightforward and cost effective way to produce continuous fibers which after heat treatment forms continuous electrical conductive network that can directly influence the EMI shielding properties. Lai et al. reported PEDOT:PSS/electrospun glycerol-grafted PAN nanofibers (PEDOT:PSS/GPNF) composites for EMI shielding in X-band. PP/GPNF was prepared by electrospinning followed by dip-coating. PEDOT:PSS/GPNF composite film exhibited EMI SE of 30 dB at a thickness of 260 μm. The EMI SE was further improved to ~ 40 dB by deposition of PANI over PEDOT:PSS/GPNF (Lai et al., 2020a). The high EMI SE is due to the interconnected conductive network between the adjacent nanofibers. Coatings of conductive fillers over non-conductive substrates, such as cotton fabrics (W. Cheng et al., 2020; P. Das et al., 2022; Ghosh et al., 2018, 2019a; Rubeziene et al., 2021; Y. Wang et al., 2019), natural fiber (Yang Zhang, Yang, et al., 2020) , and polyethylene terephthalate (PET) fabric (H. J. Choi et al., 2019; Yang Zhang, Pan, et al., 2020), have been the subject of a number of recent studies. Non-conducting substrates have a number of drawbacks when it comes to EMI shielding, the most significant of which is that the effectiveness of the shielding may be limited or depend on the number of cycles, that the coating may not adhere well, and that, depending on environmental conditions, the coating may crack or peel over time. Cotton fabrics have poor conductivity and moisture absorption, and they can only be used to investigate EMI shielding in a limited frequency range (W. Cheng et al., 2020; P. Das et al., 2022; Ghosh et al., 2018, 2019a; Rubeziene et al., 2021; Y. Wang et al., 2019).

There have been several other studies concerning with utilisation of PEDOT:PSS for EMI shielding applications. EMI shielding materials were fabricated as thin film of PEDOT:PSS, in-situ polymerized PEDOT:PSS with metal NPs or composites of carbonic fillers with PEDOT:PSS. However, the practical applications of PEDOT:PSS for EMI shielding is not yet realised, because of the reasons like degradation of 3-D conductive network after removing the template or substrate, and poor dispersion of PEDOT:PSS in polymer matrix, the low flexibility, low mechanical strength, hydrophilic nature of PEDOT:PSS based materials and weak interfacial interactions. These issues limit commercial applications of shielding materials based on PEDOT:PSS.

This work concerns with fabrication of EMI shielding material with a combination of PEDOT:PSS and CNF and their flexible PDMS composites. PEDOT:PSS along with PVP was coated over CNF. Here, PVP acted effectively as a binder and an agent booster for phase

segregation in PEDOT:PSS (Jaewon Choi et al., 2010; S. Kim et al., 2020; Mendoza-Diaz et al., 2019; Sushma Devi et al., 2022; H.-D. Zhang et al., 2016). Upon coating with PEDOT:PSS, voids or pores in CNFs were reduced and a homogenous coating was formed on the surface of CNF (Jaewon Choi et al., 2010; S. Kim et al., 2020; Mendoza-Diaz et al., 2019; H.-D. Zhang et al., 2016). Combination of the ICPs and CNF significantly enhanced the electrical conductivity of the material. As a result, this combination would exhibit excellent EMI shielding properties with high absorption loss. Mechanical properties of CNF and CNF coated with PEDOT:PSS was found to be low. Therefore, PDMS composite was prepared in order to enhance the mechanical properties, flexibility, and hydrophobicity of CNF and PEDOT:PSS-PVP coated CNF for practical application in EMI shielding. The composite showed excellent EMI SE of 44 dB in X, Ku, and K-band regions with a thickness of 0.6 mm due to high electrical conductivity of CNF as well as PEDOT: PSS-PVP. Here, PEDOT:PSS-PVP coated CNF shows higher SE_A than SE_R.

4.2 Experimental Section

4.2.1 Materials

The specifications of PAN, PEDOT:PSS, PVP, and DMF are mentioned in chapter 2 (refer to section 2.1)

4.2.2 Preparation of CNF

The preparation of CNF is discussed in chapter 2 (refer to section 2.2).

4.2.3 Preparation of PEDOT:PSS-PVP coated CNF (PEDOT:PSS-PVP/CNF)

PEDOT:PSS (1.3 wt % dispersion in water) was lyophilized to obtain solid PEDOT:PSS. Solutions of PEDOT:PSS and PVP were prepared in water/DMF (2:1 v/v) in concentrations as shown in **Table 4.1.** The above solutions were kept under constant stirring for 8 h at 50 ℃ for complete dispersion of PEDOT:PSS and dissolution of PVP. The carbon nanofibers were cut into samples of 3 x 3 cm and kept immersed in 3 mL of the above solutions in stainless steel molds of 4 x 4 cm and dried at 50 ℃ for 2 h. The samples coated with different concentrations are referred to as PVP/CNF, PEDOT: PSS-PVP/CNF-1, PEDOT: PSS-PVP/CNF-2, and PEDOT: PSS-PVP/CNF-3, respectively as mentioned in **Table 4.1**. The above mentioned samples were cut according to the dimension of the waveguide adaptor for X, Ku, and K-band for EMI shielding measurement.

Table 4.1: Preparation of samples for EMI shielding

Sample	Concentration of PEDOT: PSS (wt.%)	Concentration of PVP (wt.%)
CNF	0	0
PVP/CNF	0	3.34
PEDOT: PSS-PVP/CNF-1	0.83	3.34
PEDOT: PSS-PVP/CNF-2	1.67	3.34
PEDOT: PSS-PVP/CNF-3	3.34	3.34

4.2.4 Preparation of PEDOT: PSS-PVP/CNF-PDMS composite

The PDMS composite of coated samples were prepared in the same methodology as mentioned in chapter 2 (section 2.3). **Figure 4.1** represents schematic illustration of the fabrication process of PEDOT: PSS-PVP/CNF-PDMS composites.

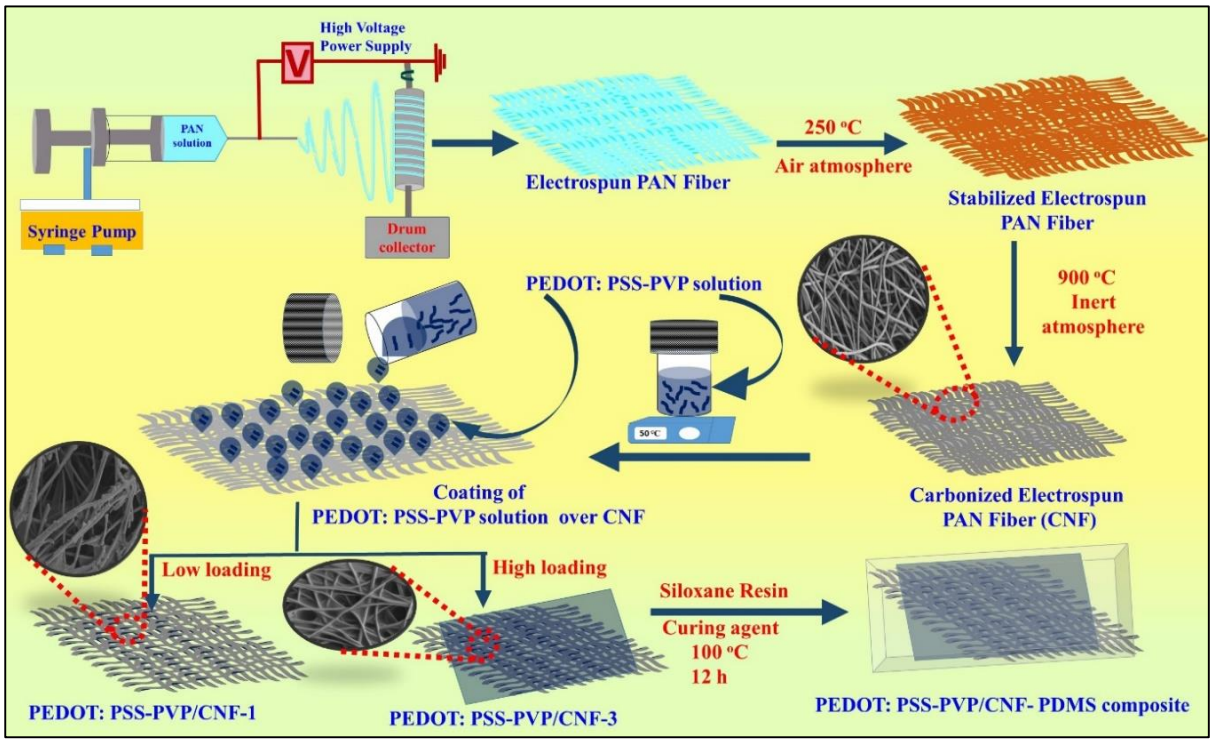

Figure 4. 1 Schematic illustration of fabrication of PEDOT:PSS-PVP/CNF-PDMS composite.

4.3 Results and discussion

4.3.1 SEM image

SEM images of CNF and PEDOT:PSS-PVP coated CNF with loading of 0, 0.83, 1.67, and 3.34 wt.% PEDOT:PSS and 3.34 wt.% of PVP are shown in **Figure 4.2**. **Figure 4.2(a)** shows SEM image of CNF are continuous without bead formation. **Figure 4.2(b-d)** show SEM images of PEDOT:PSS-PVP/CNF. When loading of PEDOT:PSS (0.83 wt.%) is low, the coating is not uniform and crack formation occurred (**Figure 4.2(b)**). When the loading of PEDOT: PSS is increased from 0.83 wt.% to 3.34 wt.%, CNFs get uniformly coated (**Figure 4.2(c-d)**).

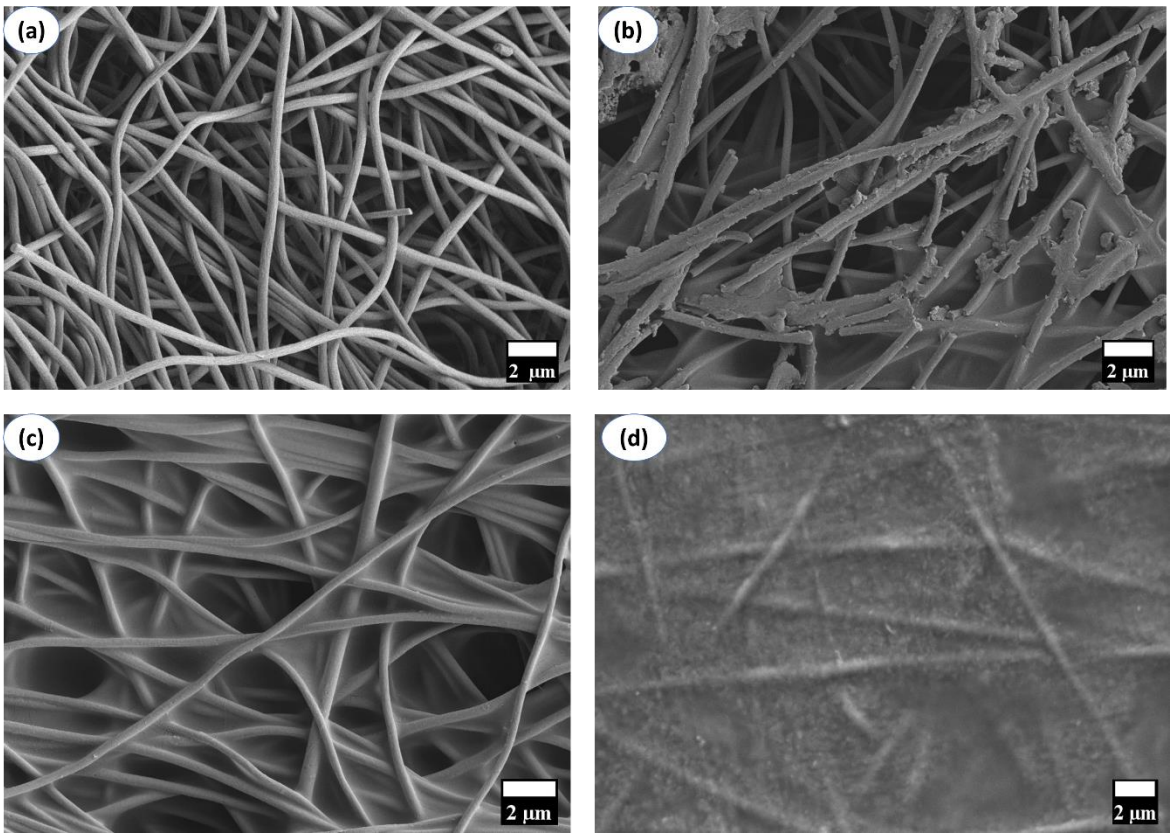

Figure 4.2: SEM image of (a) CNF , (b) PEDOT:PSS-PVP/CNF-1, (c) PEDOT:PSS-PVP/CNF-2, and (d) PEDOT:PSS-PVP/CNF-3.

The cross-sectional SEM images of CNF, PEDOT:PSS-PVP/CNF-1, PEDOT:PSS-PVP/CNF-2, and PEDOT:PSS-PVP/CNF-3 are shown in **Figure 4.3 (a-d)**, respectively. The cross-sectional SEM image of CNF without coating is shown in **Figure 4.3(a)** and demonstrates that CNF has layer-by-layer structure with space between the layers. However, after applying a PEDOT:PSS-PVP coating over CNF, it begins to bind these layers together and the space between them gets smaller, as seen in **Figure 4.3 (b-d)**. As PEDOT:PSS concentrations rise,

the binding characteristics get better. In PEDOT: PSS-PVP/CNF-3 all the layers are tightly bound as shown in **Figure 4.3(d).**

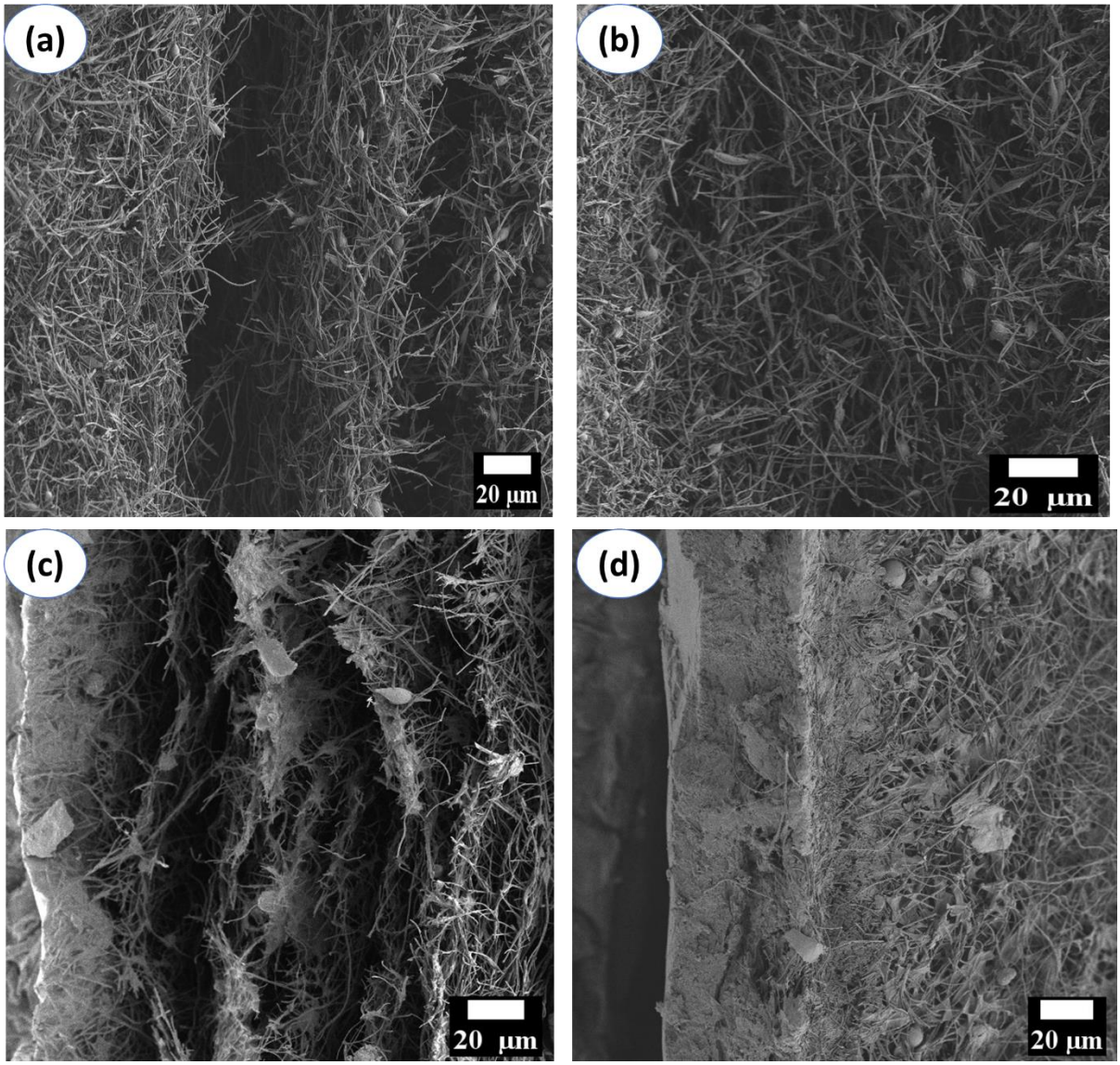

Figure 4.3: Cross-sectional SEM images of (a) CNF , (b) PEDOT:PSS-PVP/CNF-1, (c) PEDOT:PSS-PVP/CNF-2, and (d) PEDOT:PSS-PVP/CNF-3.

4.3.2 EDS analysis and elemental mapping

The uniform coating of PEDOT:PSS-PVP over CNF was further evidenced by the EDS elemental mapping. **Figure 4.4(b-e)** shows uniform distribution of carbon, oxygen, and nitrogen along the CNF. Sulfur atoms in PEDOT:PSS are uniformly present over the entire CNF. EDS spectrum of PEDOT:PSS-PVP/CNF-3 (**Figure 4.4(f))** confirms the presence of all the elements.

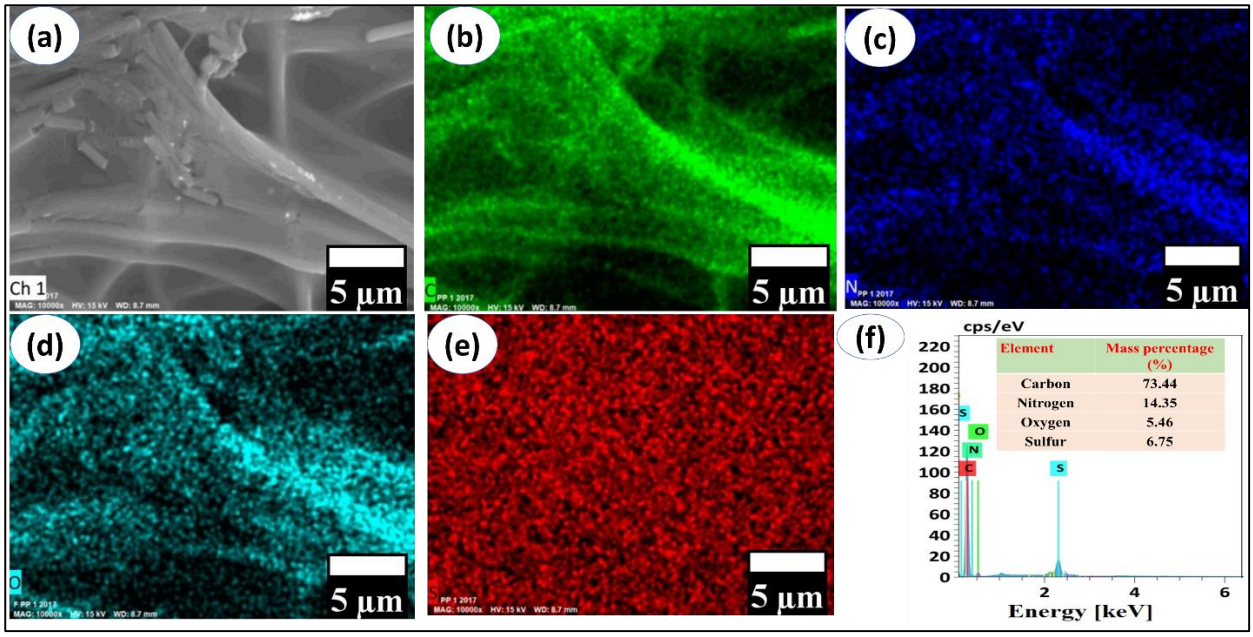

Figure 4.4: (a) SEM image used for EDS elemental mappings of PEDOT:PSS-PVP/CNF-3 (b-e) elemental maps of C, N, O, and S, respectively (f) EDS plot.

4.3.3 Raman Spectroscopy

Raman spectrum of the PEDOT:PSS-PVP/CNF-3 and CNF in wavenumber range of 200-3200 cm^{-1} are shown in **Figure 4.5 (a)**. The Raman spectrum of CNF exhibited two broad and intense peaks at 1344 and 1590 cm^{-1}. The peak at 1344 cm^{-1} is assigned to D-band whereas peak at 1590 cm^{-1} is assigned to G-band, similar to that found in nanostructured carbonaceous materials such as graphene and CNTs (Aadil, Zulfiqar, Shahid, Agboola, Al-Khalli, et al., 2021; Aadil, Zulfiqar, Shahid, Agboola, Haider, et al., 2021; Alazmi, 2022; K. Chaudhary et al., 2022). The D-band and G-band implies disordered and graphitic structure respectively. The ratio of intensity of the D-band and G-band (0.90) indicates turbostratic carbon structure of CNF. The most intense band in the Raman spectrum of PEDOT:PSS-PVP/CNF-3 appears at 1440 cm^{-1} and is attributed to symmetric $C_\alpha = C_\beta$ stretching mode of a thiophene ring. Meanwhile, two asymmetric $C_\alpha = C_\beta$ stretching peaks appear at 1564 and 1509 cm^{-1}. The additional peaks at 1365, 1260, and 988 cm^{-1} are assigned to C_β - C_β stretching, C_α - C_α inner ring bond, and C - O - C deformation, respectively. These peaks of PEDOT: PSS are similar to that reported in the literature (Funda et al., 2016; Otieno et al., 2017a). It is also worth mentioning that peaks corresponding to CNF is not seen, indicating the coverage of CNF with PEDOT:PSS layer.

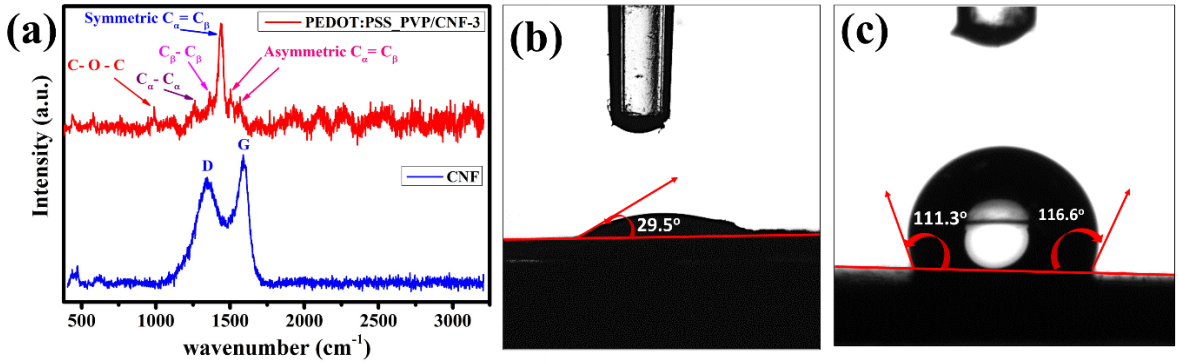

Figure 4.5: (a) Raman spectra of CNF and PEDOT:PSS-PVP/CNF-3. (b-c) contact angle measurement of PEDOT:PSS-PVP/CNF-3 and PEDOT:PSS-PVP/CNF-3 PDMS composite respectively.

4.3.4 Contact angle measurements

A reliable way of determining whether, a material is hydrophilic or hydrophobic is contact angle goniometry. In contrast to hydrophobic surfaces, which have contact angles larger than 90° and super-hydrophobic surfaces, which have contact angles more than 150°, hydrophilic surfaces have contact angles less than 90° (Erbil, 2020). Contact angle of 29.5° for PEDOT:PSS-PVP/CNF-3 (**Figure 4.5(b)**) indicates that PEDOT: PSS-PVP/CNF is highly hydrophilic in nature. Hydrophilic materials are not preferred for EMI shielding applications because they enable electrical current to flow through, potentially damaging the electronic equipment. So, PDMS composite of PEDOT: PSS-PVP/CNF-3 was also prepared for practical applications as effective EMI shielding materials with adequate mechanical properties. **Figure 4.5(c)** shows that the contact angle of PEDOT: PSS-PVP/CNF-3 PDMS composite is greater than 90° and confirms the hydrophobic nature of PDMS composite of PEDOT: PSS-PVP/CNF-3. The silicone elastomer PDMS is a polymer that contains siloxane and methyl groups. These ubiquitous methyl groups are essential for giving PDMS its hydrophobic characteristics (Ariati et al., 2021; Teixeira et al., 2021).

4.3.5 Mechanical Test

CNF is of very lightweight and has very low mechanical properties as shown in **Figure 4.6(a)**. CNF coated with PEDOT: PSS-PVP becomes brittle in nature as illustrated in **Figure 4.6(b)**. So, in order to improve their mechanical property and flexibility, PDMS composite was prepared as shown in **Figure 4.6(c)**. **Figure 4.6(d-f)** illustrate that PEDOT: PSS-PVP/CNF-3 PDMS composites exhibit high flexibility and good mechanical properties. A piece of PEDOT:PSS-PVP/CNF-3 PDMS composite was bent, folded, twisted, and then was returned

to its flat surface. The mat's structural integrity and EMI shielding were still intact, proving the mat's exceptional flexibility.

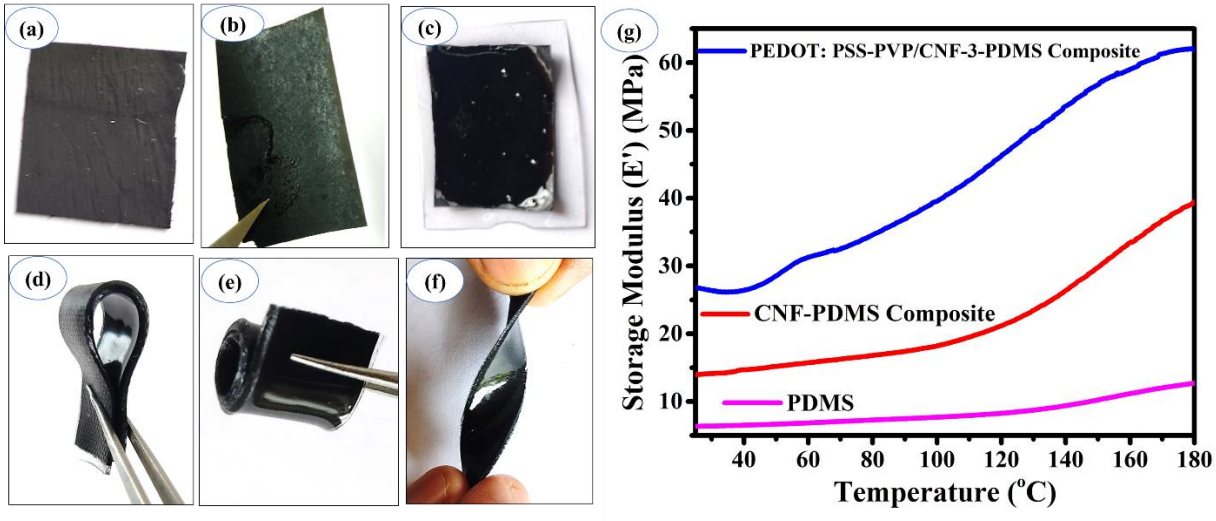

Figure 4.6: Photograph of (a) CNF, (b) PEDOT:PSS-PVP/CNF-3, (c) PEDOT:PSS-PVP/CNF-3 PDMS composite, (f-h) folding, rolling, and twisting of PEDOT: PSS-PVP/CNF- 3 PDMS composite. (g) change in storage modulus (E') with temperature.

The temperature-dependent mechanical properties of PDMS, CNF-PDMS composite, and PEDOT:PSS-PVP/CNF-3 PDMS composite were investigated using DMA. **Figure 4.6(g)** shows the overlay plots of storage modulus (E') versus temperature (T) for PDMS, CNF-PDMS composite, and PEDOT:PSS-PVP/CNF-3 PDMS composite. Here, the change of storage modulus (E') of the materials with temperature is measured, which refers to the elasticity or stiffness of the composites and is proportional to the energy stored during one period under load. It is seen that storage modulus of the pristine PDMS slightly rises with temperature as a result of slight possibilities of stiffening effect and chain mobility that comes from further curing at elevated temperature. The storage modulus of pristine PDMS is low and increases with adding of CNFs and PEDOT: PSS-PVP/CNF. The storage modulus of the composite is found to increase with temperature as shown in **Figure 4.6(g)**. The storage modulus of PDMS, CNF-PDMS composite, and PEDOT: PSS-PVP/CNF-3 PDMS composite are 6, 14, and 27 MPa at 25 ^{o}C, and 13, 40, and 62 MPa at 180 ^{o}C respectively. The E' of the polymeric materials directly depends on their cross-linking density and temperature as reported in literature (Linlin Cao et al., 2016b). At elevated temperatures, the stiffness might have enhanced due to post-curing effects, chemical cross-linking reactions, dynamic loading, diffusion, and solid-phase reaction in PDMS materials (Linlin Cao et al., 2016b; S. Lu et al., 2022; Placet & Delobelle, 2015; Y. C. Sun et al., 2019). The incorporation CNF enhanced the

chemical cross-linking network in the cured PDMS and the formation of interface/interphase due to the interaction with polymer chains that plays critical role in the dynamic stiffness effect. As a result, the storage modulus of the CNF-PDMS composite rises, and it increases further after coating with PEDOT:PSS-PVP due to the adhering of all CNF layers together as shown in **Figure 4.3**.

4.3.6 Electrical conductivity measurement

The current-voltage graphs of CNF, PVP/CNF, PEDOT:PSS-PVP/CNF-1, PEDOT:PSS-PVP/CNF-2and PEDOT:PSS-PVP/CNF-3 are shown in **Figure 4.7**. A straight line demonstrates that sheet resistance (R_s) does not vary when the current varies from 0.1 to 3 mA, as shown in **Figure 4.7**. The electrical conductivity (σ) and resistivity (ρ) of CNFs were determined using **Equations 18, 19,** and **20**. The R_s, ρ, and σ of the samples are shown in **Figure 4.7**.

The R_s and ρ of CNF increases upon coating with PVP and exhibited lower conductivity than CNF. But, after coating with PEDOT: PSS and PVP, the resistance decreased and electrical conductivity increased. **Table 4.2** indicates the variation of electrical conductivity of CNF and PEDOT: PSS-PVP/ CNF. The electrical conductivity of CNF is 0.13 S cm^{-1}; however, after coating of CNF with PVP the electrical conductivity is decreased from 0.13 S cm^{-1} to 0.048 S cm^{-1} due to low electrical conductivity of PVP. However, when 0.83 wt.% PEDOT: PSS is combined with PVP and coated over CNF, the electrical conductivity rises from 0.048 to 0.356 S cm^{-1}. With increasing the loading of PEDOT: PSS from 1.67 to 3.34 wt.%, the electrical conductivity

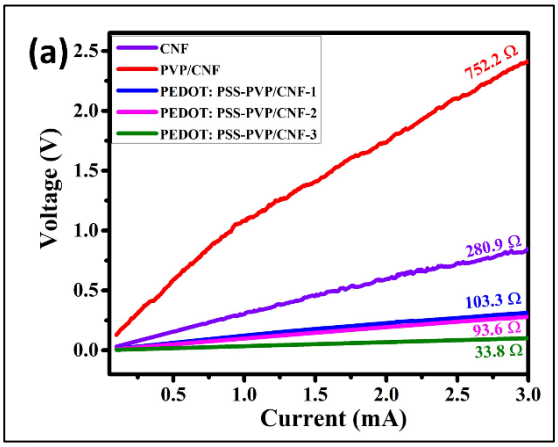

Figure 4.7: Current-voltage graph of CNF, PVP/CNF, PEDOT:PSS-PVP/CNF-1, PEDOT:PSS-PVP/CNF-2, and PEDOT:PSS-PVP/CNF-3.

of PEDOT: PSS-PVP/CNF increased from 0.392 to 1.08 S cm^{-1}. Hence, they are expected to exhibit high EMI shielding properties.

Table 4.2: Sheet resistance, Resistivity, and conductivity of samples.

Sample	**R_s (Ω)**	**ρ (Ω cm)**	**σ (S cm^{-1})**
CNF	1273	7.64	0.13
PVP/CNF	3412	20.4	0.04
PEDOT: PSS-PVP/CNF-1	468.2	2.81	0.35
PEDOT: PSS-PVP/CNF-2	424.2	2.54	0.392
PEDOT: PSS-PVP/CNF-3	153.2	0.92	1.09

4.3.7 EMI SE

The EMI SE strongly depend on formation of electrical conductive network or bridge between the matrix and the conducting filler. The EMI SE of PEDOT:PSS-PVP/CNF and their PDMS composites were measured over X, Ku, and K-band regions with thickness of 0.06 mm and 0.6 mm respectively. The EMI SE of the samples are shown in **Figure 4.8**. Pure CNF shows average EMI SE of 14.76 dB due to low electrical conductivity. PVP coated CNF also exhibited similar average EMI shielding due to low electrical conductivity of PVP. Hence, coating of CNF with PVP alone is not effective for improving EMI shielding. However, PVP may be utilized as binder as well as booster for phase segregation between conducting PEDOT and insulating PSS (Mendoza-Diaz et al., 2019). Therefore, PEDOT:PSS was uniformly coated over CNF using PVP. The coating decreased the void size and gap between the CNF layers as shown in SEM image (**Figure 4.3**), which facilitated the formation of 3-D conductive network and facilitated the interaction of PEDOT:PSS with CNF improving the charge transfer between PEDOT:PSS and CNF. The total EMI SE values of the CNF, PVP-CNF, PEDOT:PSS-PVP/CNF-1, PEDOT:PSS-PVP/CNF-2, and PEDOT:PSS-PVP/CNF-3, are presented in **Figure 4.8(a).** With increasing the loading of PEDOT:PSS, the EMI SE value of PEDOT:PSS-PVP/CNF increased significantly. As the loading of PEDOT:PSS increases from 0 to 3.34 wt.%, the total EMI SE increased from 17 dB to 44 dB as shown in **Figure 4.8(a)**. The increase in EMI SE is due to the formation of electrically conductive network upon uniform coating of

CNF with PEDOT:PSS. The formation of electrically conductive network is crucial to impart high EMI SE properties. A coating of PEDOT:PSS-PVP over CNF forms interconnected 3D-conductive network and π-π interaction of thiophene ring of backbone conjugated π-electron of PEDOT with turbostratic carbon structure of CNF and facilitates electron transport channels between the adjacent conductive nanofibers (Lai et al., 2020b; S. H. Lee et al., 2017; Sushma Devi et al., 2022) as proposed in **Figure 4.9(c).** Thus, the layer by layer structure of PEDOT:PSS coated CNF aided electron transfer between PEDOT:PSS and CNF. The incident EM waves directly interact with π-electrons of PEDOT:PSS and CNF and reflects the EM waves. The remaining EM waves pass through PEDOT:PSS-PVP/CNF and allows multiple internal reflections and multiple scattering at inhomogeneous interfaces inside the porous structure which also contribute to the EMI SE.

The overall reasons for high EMI shielding performance of PEDOT:PSS-PVP/CNF are: (1) formation of 3D electrically conductive network, (2) high π-electron density and ionic interaction of PEDOT:PSS leading to electric dipoles helping in ohmic losses, (3) interfacial polarization between (a) PEDOT:PSS and CNF, (b) CNF-CNF, (c) PEDOT-CNF, and (d) PSS-CNF leading to impedance matching (Bandar A. Al-Asbahi et al., 2021; Al Naim et al., 2021).

To further detect the fundamental mechanism behind the high EMI SE, we separately measured the contribution of SE_A and SE_R. **Figure 4.8(b-c)**, indicate that SE_A contributes more than 85% to the total EMI SE (EMI SE_T) in all the samples. Therefore, the dominant mechanism for EMI shielding is absorption for all the samples. The multi-reflections are included in the EM wave absorption mechanism since re-reflected waves would eventually dissipate as heat in the EMI shielding materials (Rajesh Kumar et al., 2021; X. Y. Wang et al., 2022). When the PEDOT: PSS loading is increased from 0 to 3.34 wt.%, the reflection contribution increases from 3 to 10 dB, while the absorption contribution increases from 12 to 41dB. The average contribution due to absorption, and reflection for all the samples are shown in **Figure 4.9(a)**. The proposed mechanism for EMI shielding property of PEDOT:PSS-PVP/CNF is shown in **Figure 4.9(c).** We calculated the R, T, and A using **Equations 6**, **7**, and **8**, respectively, to gain insight into the EMI shielding mechanism. The average R value and T value decreases from 0.4558 to 0.2500 and 8.1 x 10^{-3} to 4.1 x 10^{-5} with increasing the loading of PEDOT:PSS from 0.83 wt% to 3.34 wt%, while the A value rises from 0.5360 to 0.7497. These values are also indicative of a highly effective shielding mechanism based on absorption within the materials.

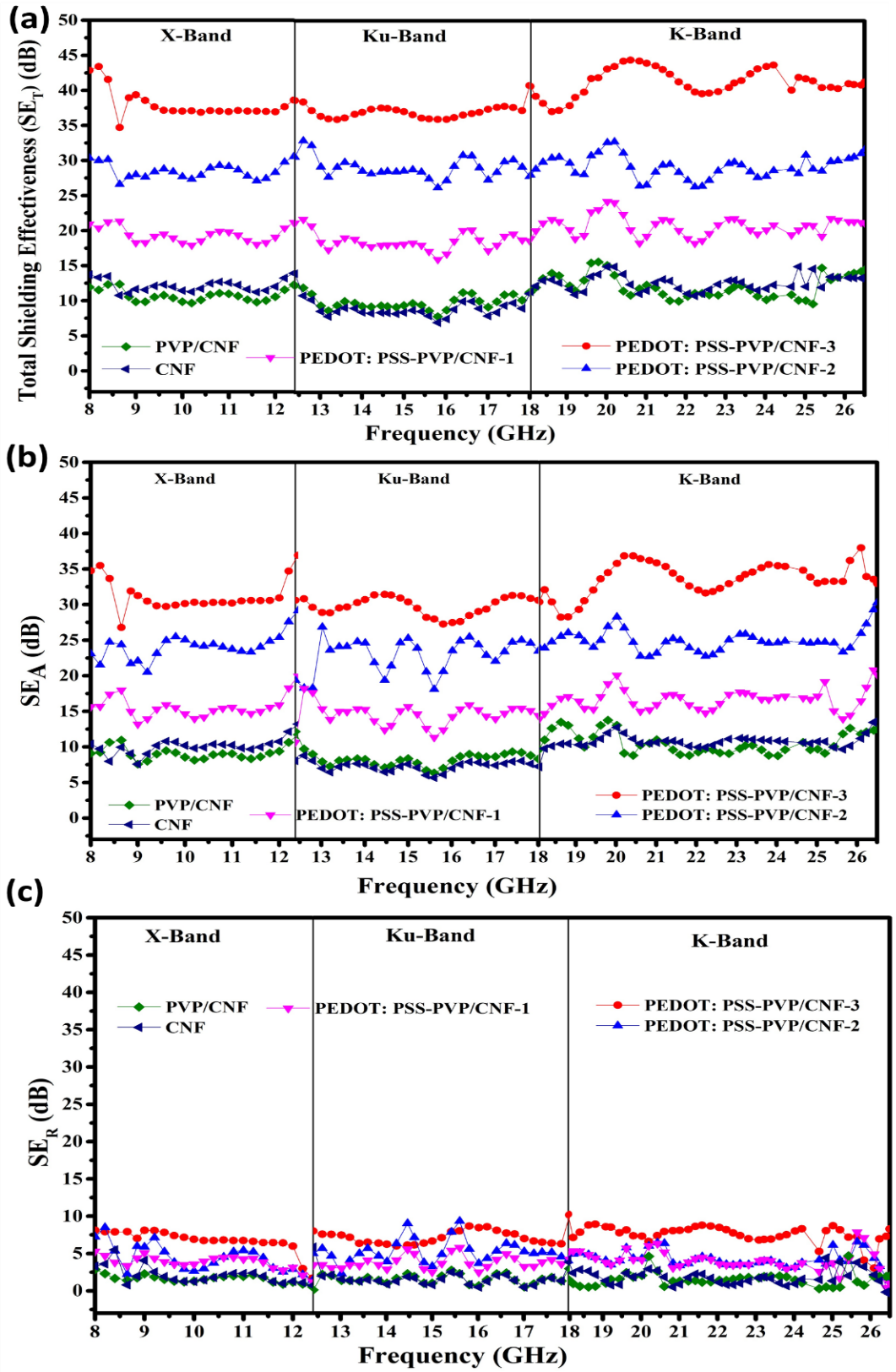

Figure 4.8: (a) Total EMI SE of CNF, PVP/CNF, PEDOT: PSS-PVP/CNF-1, PEDOT: PSS-PVP/CNF-2, and PEDOT: PSS-PVP/CNF-3, respectively. (b) EMI SE due to absorption, and (c) EMI SE due to reflection for X, Ku, and K- band frequency region.

To improve the mechanical properties, flexibility, and hydrophobicity, PEDOT: PSS-PVP/CNF-PDMS composites were fabricated. The pristine PDMS composite shows zero EMI SE. PDMS composite of PEDOT:PSS-PVP/CNF-3 exhibits average EMI SE of 40 dB which is almost similar to PEDOT:PSS-PVP/CNF-3. Bending test was performed as shown in **Figure 4.9(b)** (Y. Wang et al., 2019; Zhu Zhang et al., 2022). The EMI SE of PEDOT: PSS-PVP/CNF-PDMS composites, as shown in **Figure 4.9(b)**, is consistent after 100 cycles of bending.

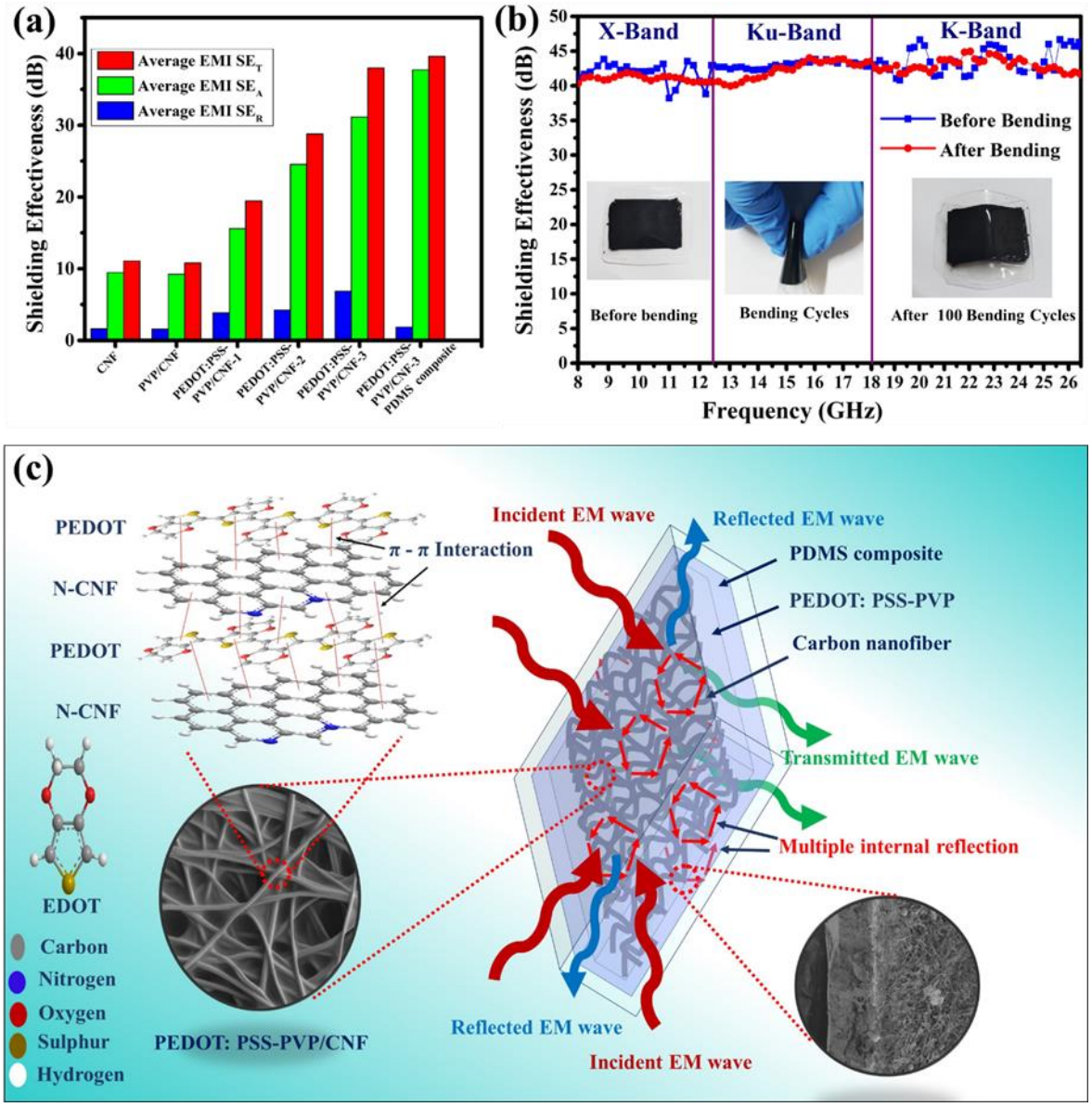

Figure 4.9: (a) The average EMI SE of the samples for X, Ku, and K- band frequency region. (b) EMI SE of PEDOT:PSS-PVP/CNF-3 PDMS composites before and after 100 cycles bending. (c) Schematic illustration of EMI shielding mechanism.

As is well known, the density and thickness of the materials have a significant impact on the practical applications of EMI shielding materials. Therefore, density, thickness, SSE, and SSE_t are important parameters for EMI shielding materials and these values are mentioned in **Table 4.3**. Both CNF and PVP coated CNF had significant SSE_t values, although neither sample exceeded the EMI SE (20 dB) limit for commercial use. As a result, these two materials are not suitable for commercial use. When 0.83 wt.% PEDOT: PSS is combined with PVP and coated over CNF, EMI SE limit for commercial use is exceeded and has a high SSE_t value of 5678 dB $cm^2 g^{-1}$. As the loading of PEDOT:PSS increased from 1.67 to 3.34 wt.%, the SSE_t of PEDOT: PSS-PVP/CNF reduced from 3907 to 2605 dB $cm^2 g^{-1}$owing to increase in the density.

A comparison of the results reported in closely related works is presented in **Table 4.3**. The results of the current study assume importance, because, the fabricated PEDOT:PSS-PVP/CNF PDMS composites exhibit several benefits such as high EMI SE (26-44 dB) in the wide frequency range (X, Ku, and K-band), low thickness, lightweight, flexibility, moisture insensitivity (hydrophobic) and simple processing method.

Table 4.3: The properties of samples related to EMI SE.

Sample	**Thickness (mm)**	**Density ($g\ cm^{-3}$)**	**Conductivity ($S\ cm^{-1}$)**	**Frequency Range**	**Highest EMI SE (dB)**	**SSE ($dB\ cm^3\ g^{-1}$)**	**SSE_t ($dB\ cm^2\ g^{-1}$)**	**Average EMI SE_T (dB)**
CNF	0.03	0.274	0.131	8.2-26.5 GHz	17.8	64.8	21603.3	11.0
PVP/CNF	0.04	1.130	0.049	8.2-26.5 GHz	16.5	14.5	3643.8	10.8
PEDOT:PSS-PVP/CNF-1	0.04	1.139	0.356	8.2-26.5 GHz	25.9	22.7	5678.2	19.4
PEDOT:PSS-PVP/CNF-2	0.05	1.766	0.392	8.2-26.5 GHz	34.5	19.5	3907.1	28.7

PEDOT:PSS-PVP/CNF-3	0.06	2.776	1.088	8.2-26.5 GHz	43.4	15.6	2605.0	39.0
PEDOT:PSS-PVP/CNF-3-PDMS composites	0.60	1.529	-	8.2-26.5 GHz	43.4	28.3	473.07	40.0
PEG/PEDOT:PSS @ cotton fabric(Ghosh et al., 2019b)	0.38	51		8.2-12.4 GHz	46.8	-	-	-
PEDOT:PSS/GPNF(Lai et al., 2020a)	0.26	0.017		8.2-12.4 GHz	30	-	-	-
PEDOT:PSS sponges (Sarkar et al., 2021)	0.1	0.0038		8.2-12.4 GHz	24	-	-	-
rGO/Ga/PEDOT:PSS(P. Das et al., 2022)	0.36 µm	38.41		8.2-12.4 GHz	34	-	-	-
Natural Bagasse fiber/PANI core-shell composite(Yang Zhang, Yang, et al., 2020)	0.4 mm		6.27	8.2-12.4 GHz	37.72			
Mulberry like PANI based flexible composite	0.78 mm		9.2 S m^{-1}	8.2-12.4 GHz	25.9			

fabrics (Pan et al., 2020)								

4.4 Conclusion

A lightweight, flexible, and hydrophobic material namely, PEDOT:PSS-PVP/CNF-PDMS composite was successfully fabricated for EMI shielding applications in X, Ku, and K-band. The conductive polymer PEDOT:PSS was coated over CNF where PVP acted as a binder and booster for phase segregation of conducting PEDOT from insulating PSS. With a 3.34 wt% loading of PEDOT:PSS over CNF,EMI SE of 43.4 dB was achieved for a 0.06 mm thick sample. The material exhibits a high SSE_t of 5678 dB cm^2 g^{-1} with low loading (0.83 wt%) of PEDOT:PSS-PVP. This high EMI shielding property of the material is due to the synergetic effect of the CNF matrix and the conductive coating. Thus, it is demonstrated that PEDOT:PSS-PVP/CNF and their PDMS composites are high performance EMI shielding materials, suitable for commercial applications with benefits such as ease of fabrication and environmental stability. These lightweight, flexible, and hydrophobic materials with high EMI shielding performance are promising in military/ aerospace applications and in wearable smart devices.

CHAPTER: 5

Tellurium Nanoparticles Incorporated CNF and PDMS Composites for EMI Shielding

Overview

The work presented in the previous chapter concerned with coating of PEDOT:PSS-PVP over CNF for enhancing the EMI shielding performance of CNF. This present work looks into the possibility of incorporation of a suitable filler into CNF for obtaining improvement in EMI shielding performance. Here, tellurium nanoparticles (Te NPs) incorporated N-doped carbon nanofiber (Te-CNF) is fabricated. Incorporation of Te NPs into CNF may improve the electrical conductivity of CNF and create hetero-interfaces that causes interfacial polarization, resulting in high EMI shielding property. This chapter provides a detailed analysis of the properties of Te-CNF, especially the EMI shielding properties in the X-band.

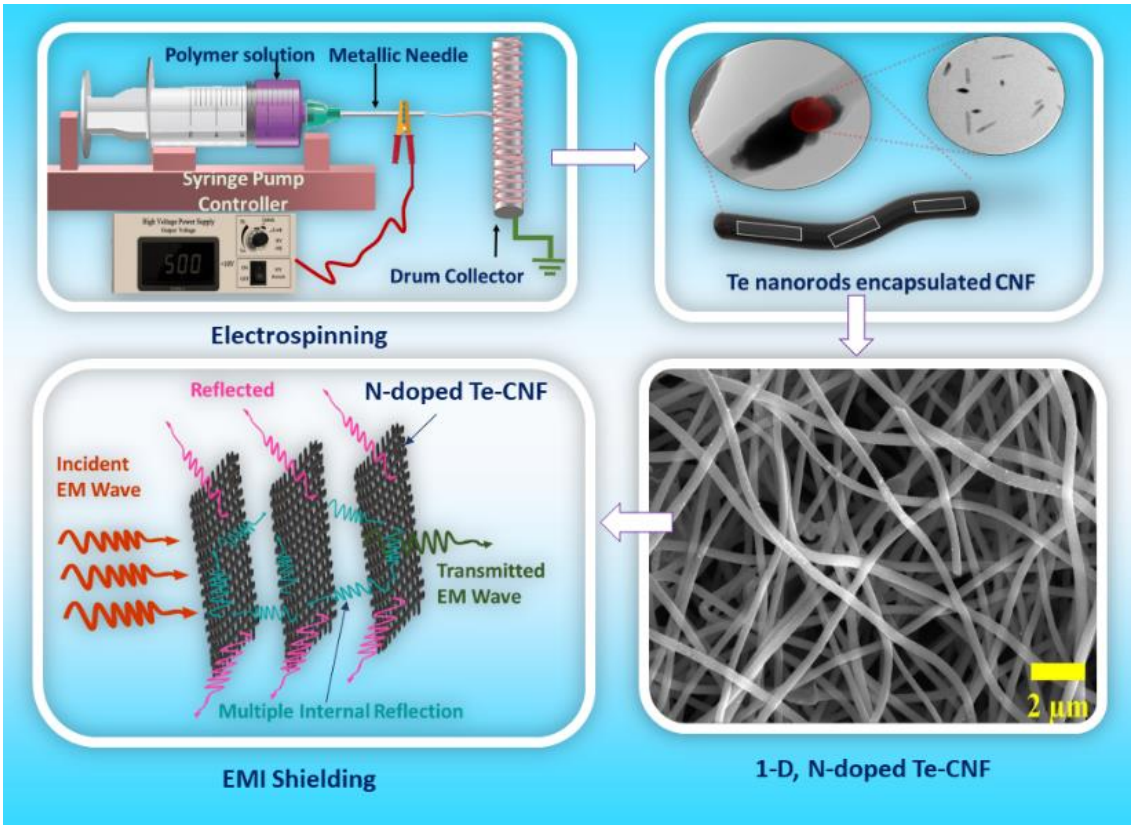

5.1 Introduction

In the work presented in the previous chapter, PEDOT:PSS-PVP coated on CNF showed 44 dB of EMI SE. Obtaining uniform and constant coating of PEDOT:PSS-PVP over CNF remains difficult for complex structures and large surfaces. In order to improve the EMI SE of PEDOT:PSS-PVP/CNF, a thicker coating of PEDOT:PSS-PVP over CNF is required, resulting in restrained adhesion between the PEDOT:PSS coating and CNF. As a result, poor adhesion might cause delamination.

Hence, the incorporation of fillers (metal and metal oxide NPs) into CNF is an effective way to produce high-performance EMI shielding materials. The incorporation of fillers into CNF is an easy way to produce hetero-interfaces and interconnected 3-D conductive networks and improve electrical conductivity, which leads to better EMI shielding performance. Introduction of chalcogen elements such as sulfur, selenium, and tellurium (Te) into carbon skeleton is an effective way to form 3-D conductive network which has been explored for EMI shielding materials also (F. Huang et al., 2021; Hung et al., 2022; Luxa et al., 2023). Jiang et al. fabricated nitrogen doped carbon nanofiber with sulfur (S-NCFs), through electrospinning and heat treatment with sublimed sulfur for microwave absorption in the frequency range of 2-18 GHz. S-NCFs exhibited minimum reflection loss of -48.67 dB with thickness of 1.39 mm with 15% loading of sulfur (Y. Jiang et al., 2020). Among the chalcogen elements, tellurium is a metalloid with a narrow band gap and tellurium has the most metallic characteristics and high electrical conductivity (Jaeyoo Choi et al., 2015; C. K. Kim et al., 2020a; S. Lee et al., 2019; Yue Zhang et al., 2021). Asbahi et al. reported, Te nanorods embedded PEDOT: PSS nanocomposite for EMI shielding, which exhibited a total EMI SE of 60.88 dB with 20 wt% in the X-band region (Bandar A. Al-Asbahi et al., 2021). Naim et al. fabricated carbon dots (C_{dots}) adorned telluride (Te) nanorods incorporated into PEDOT:PSS (C_{dots}Te/PEDOT:PSS) nanocomposite films which exhibited total EMI SE of 63.17 dB with a loading of 8 wt% C_{dots} and 2 wt% Te nanorods in X- band region (Al Naim et al., 2021). In another work, (B. A. Al-Asbahi et al., 2023) bismuth telluride nanorods (PEDOT: PSS/n- Bi_2Te_3) nanocomposite film was fabricated which exhibited total EMI SE of 42.08 dB with 16 wt% n- bismuth telluride nanorods in X-band region. In the above reports, Te nanorods were incorporated along with PEDOT: PSS to obtain nanocomposite films. Since, the above-mentioned nanocomposites and films are based on PEDOT: PSS, these would be hydrophilic in nature or moisture sensitive, with low durability and low mechanical strength. The stability of metal NPs is a matter of concern, since there is, chances to form metal oxide which may deteriorate the properties of the nanoparticles. Te NPs are known to exhibit remarkable stability at high temperatures (L.

Xu et al., 2015). Even if Te NPs undergo oxidation and become TeO_2 NPs, the reduction, which would happen during carbonization at elevated temperatures in presence of carbon and in vacuum conditions would convert them back to Te NPs (Arab et al., 2016; L. Xu et al., 2015; Zambonino et al., 2021; H. Zhu et al., 2023). Hence, Te NPs may act as an efficient filler for enhancing the EMI shielding properties of carbon-based matrixes (J. He et al., 2017; Y. Liu et al., 2014; J. Xu et al., 2016). There are only a few reports available, where Te NPs are used as fillers for EMI shielding applications and the reported EMI SE values are low.

Te NPs are semiconductors with narrow band gap (Jaeyoo Choi et al., 2014, 2015) and are effective fillers which can be incorporated into electrospun PAN fiber and can form 3-D conductive network after carbonization. Here, we fabricated Te NPs incorporated N-doped carbon nanofiber (Te-CNF) via electrospinning followed by carbonization. The Te-CNF exhibited high electrical conductivity of 1.4 S cm^{-1} and consequently high EMI SE. The highest EMI SE exhibited by Te-CNF is 38 dB with a low thickness of 0.08 mm. The formation of 3-D electrically conductive network and hetero-interfaces of Te NPs and 1-D N-CNF make it a facile system for high-performance EMI shielding material. The synergistic effect of Te NPs and 1-D N-CNF and Te-CNF may cause conduction loss, polarization loss, multiple internal reflections and interfacial polarization. The Te-CNF shows high SSE_t of 92580 dB cm^2 g^{-1}. However, Te-CNF is brittle and fragile and hence, difficult to be handled. Hence, PDMS composite of Te-CNF was made which retained the EMI shielding property of Te-CNF while improving the mechanical property of Te-CNF. The PDMS composite of Te-CNF is flexible and can be explored for applications under harsh environments.

5.2 Experimental Section

5.2.1 Materials

The specifications of PAN, Tellurium granules, and DMF are mentioned in chapter 2 (refer to section 2.1)

5.2.2 Preparation of Te NPs incorporated Te- CNF

Te NPs were obtained by grinding Te granules using mortar and pestle. The obtained Te NPs (250 mg) were homogeneously dispersed in 10 mL of 10 wt% PAN solution in DMF. The above solution was transferred into a 12 mL syringe with a metallic needle, having diameter of 0.80 mm for electrospinning. The metallic needle tip was subjected to a high voltage (13 kV) and a metallic rotatory drum collector was placed 13 cm away from the tip of the needle.

Solution for electrospinning was pumped at a flow rate of 1.2 mL $h^{-1,}$ from the syringe to obtain electrospun fiber mat on aluminum foil adhered to the drum collector. The obtained Te NPs incorporated electrospun PAN fiber (Te-EF) mat was dried at room temperature for 12 hours and then stabilized at 250 °C in air oven for 4 hours, and then carbonized at 900 °C in argon atmosphere for 5 hours, at a ramping rate of 2 °C min^{-1}. Carbonization was performed in high-temperature inert furnace procured from Vacuum Technologies Ltd. (Bangalore, India). A high vacuum was generated inside the furnace before carbonization and maintained a proper flow of Ar gas during carbonization of the electrospun mat. The carbonized Te NPs incorporated electrospun PAN fiber mat was termed as **Te-CNF**. Te-CNF mat was cut into square pieces (4 cm x 4 cm) for EMI shielding testing and also for preparation of PDMS composites.

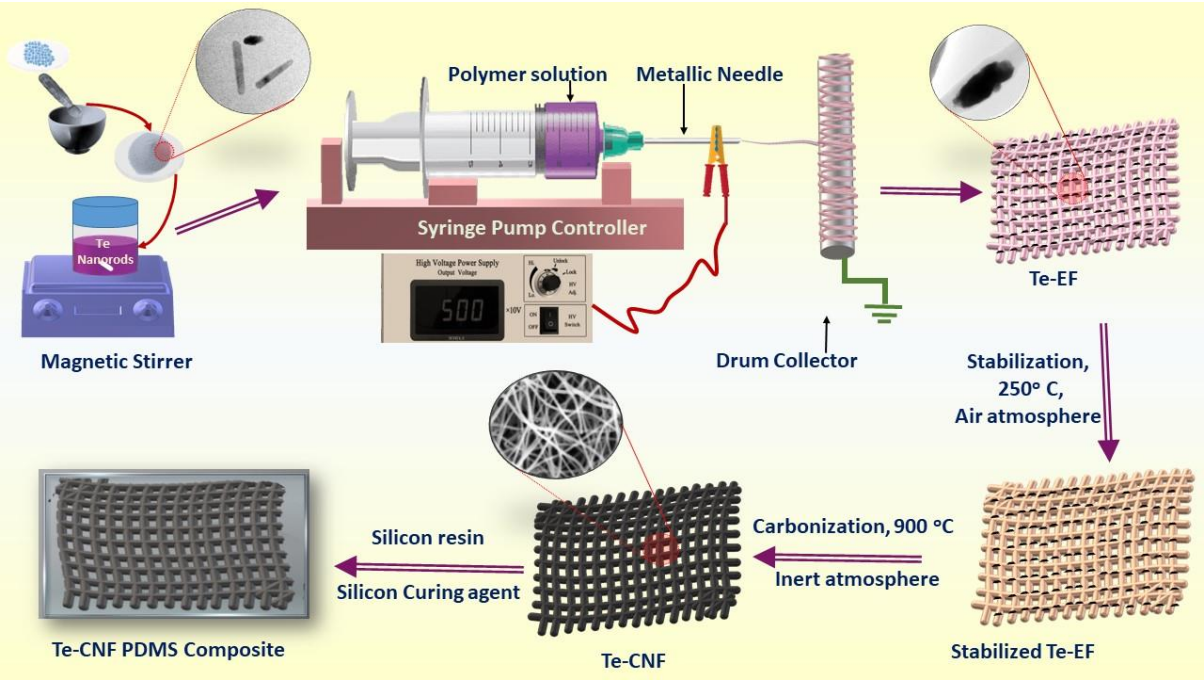

Figure 5.1: Schematic illustration of fabrication of PDMS composite of Te NPs incorporated N-doped CNF.

5.2.3 Preparation of PDMS composites of Te-CNF

The PDMS composite of coated samples were prepared in the same methodology as mentioned in chapter 2 (section 2.3). **Figure 5.1** shows the schematic illustration of the fabrication of Te NPs incorporated N-doped CNF and its PDMS composite.

5.3 Results and Discussion

5.3.1 TEM image

TEM images provide information about the crystalline nature and dimension of Te NPs and incorporation of Te NPs into electrospun PAN fibers. The TEM images of Te NPs demonstrate the polycrystalline nature and cylindrical shapes as shown in **Figure 5.2(a-e)**. The lattice space, average diameter and average length of Te NPs are, 0.6 nm, 10.8 ± 1.6 nm and 44.1 ± 19.2 nm respectively. The distribution and incorporation of Te NPs into electrospun PAN fibers can be seen in the TEM images (**Figure 5.2(f-h)**). **Figure 5.2(f-h)** reveals that Te-EFs are continuous without bead formation and electrospraying of Te NPs has not occurred. The average diameter of Te-EFs are 451 ± 58 nm. The distribution of Te NPs after carbonization of Te-EFs were further confirmed by EDS and elemental mapping of tellurium.

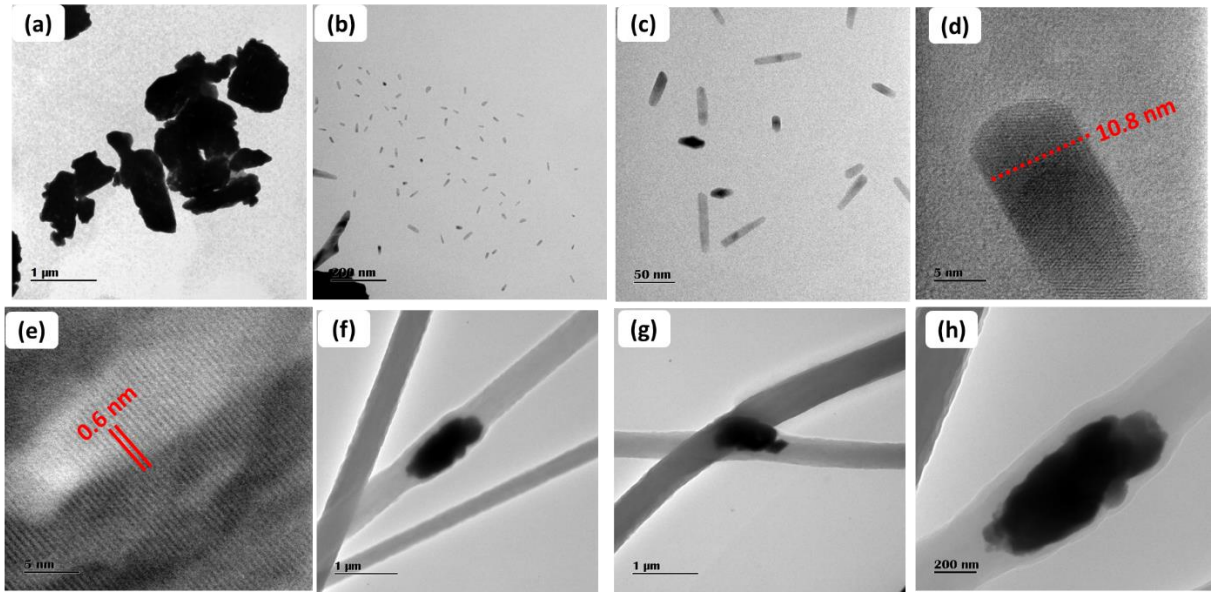

Figure 5.2: TEM images of (a-d) Te NPs and (e-h) Te NPs incorporated into electrospun PAN fiber.

5.3.2 SEM image

SEM images provide information of fiber morphology, porosity, and aspect ratio of fibers. The fiber morphology was retained after carbonization of Te-EFs as shown in **Figure 5.3**. The SEM image of Te-CNF shows high aspect ratio with average diameter of 352 ± 33 nm. The SEM images **(Figure 5.3(a-f))** of Te-CNF reveal the highly porous, 1-D fiber morphology with layered structure. Te NPs are seen to be successfully incorporated within the N-doped CNF as shown in **Figure 5.3(d-e)**. This was further confirmed with EDS and elemental mapping. The SEM images of Te-CNF PDMS composites are shown in **Figure 5.3(f-i)**. **Figure 5.3(f)** shows the smooth surface of PDMS composite and indicates that Te-CNF is completely covered with PDMS. The cross-sectional SEM images (**Figure 5.3(g-i))** of Te-CNF PDMS composite

exhibit the tight bonding between Te-CNF and PDMS and maintenance of the fiber morphology of Te-CNF.

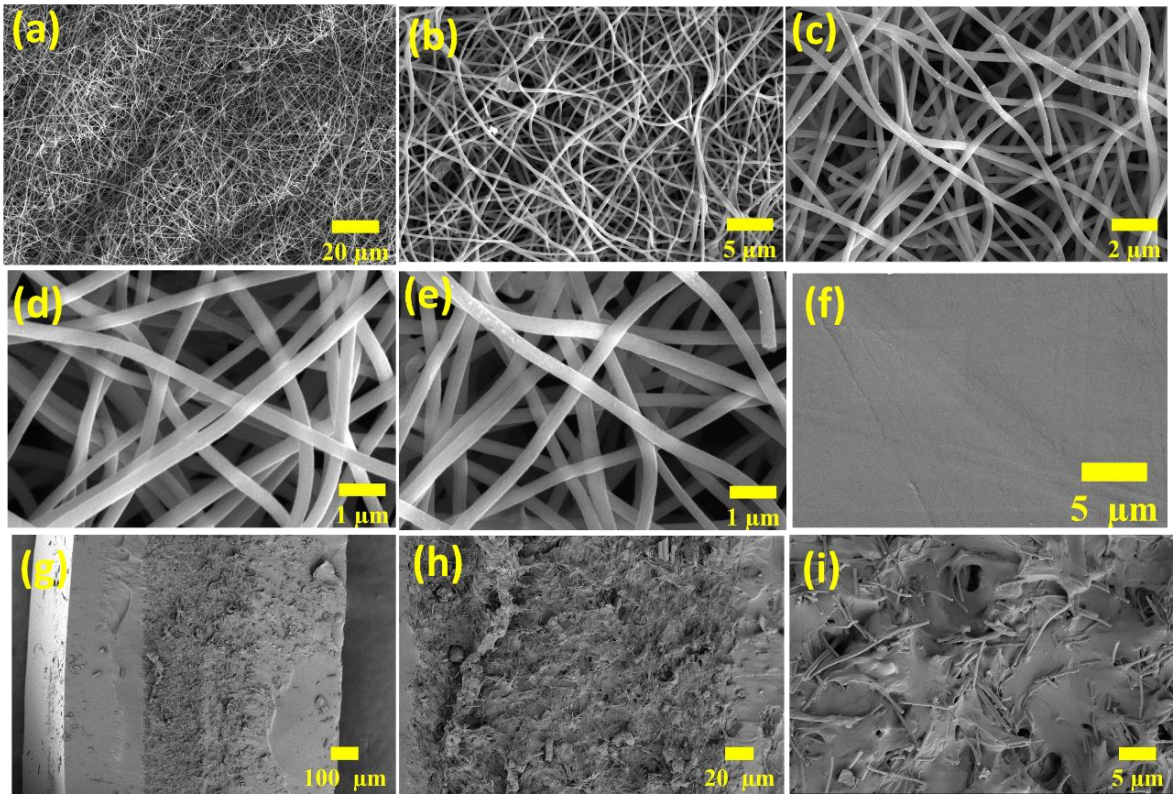

Figure 5.3: SEM images of (a-e) Te-CNF, (f) Te-CNF PDMS composite, and (g-i) Cross-section of Te-CNF PDMS composite.

5.3.3 EDS analysis and elemental mapping

EDS provides information about the elements present in the Te-CNF. The EDS spectra show strong peaks of tellurium, carbon, nitrogen, and oxygen as shown in **Figure 5.4(a). Figure 5.4(b)** shows the SEM image which was used for elemental mapping. Distribution of tellurium, carbon, nitrogen, and oxygen in Te-CNF was checked by elemental mapping as shown in **Figure 5.4(c-f).** Distribution of Te NPs is uniform throughout the fibers and confirms the incorporation of tellurium into N-doped CNF (**Figure 5.4(f)**).

5.3.4 Raman Spectroscopy

Raman spectroscopy is used to study the graphitic structure of carbon based materials. The Raman spectra of the stabilized Te-EFs at 250 ^{o}C and carbonized Te-EFs (Te-CNF) shown in **Figure 5.5(a)** exhibit peaks corresponding to D-band and G-band that belong to carbon-based materials. The G-band peak indicates graphitization and D-band peak represents the disordered graphitic structure of the sample. Formation of ladder structure in PAN EF is confirmed from

the presence of D-band at 1367 cm^{-1} and G-band at 1578 cm^{-1}. The I_D/I_G ratios of the stabilized Te-EFs and carbonized Te-EFs (Te-CNFs) are 1.31 and 0.82 respectively.

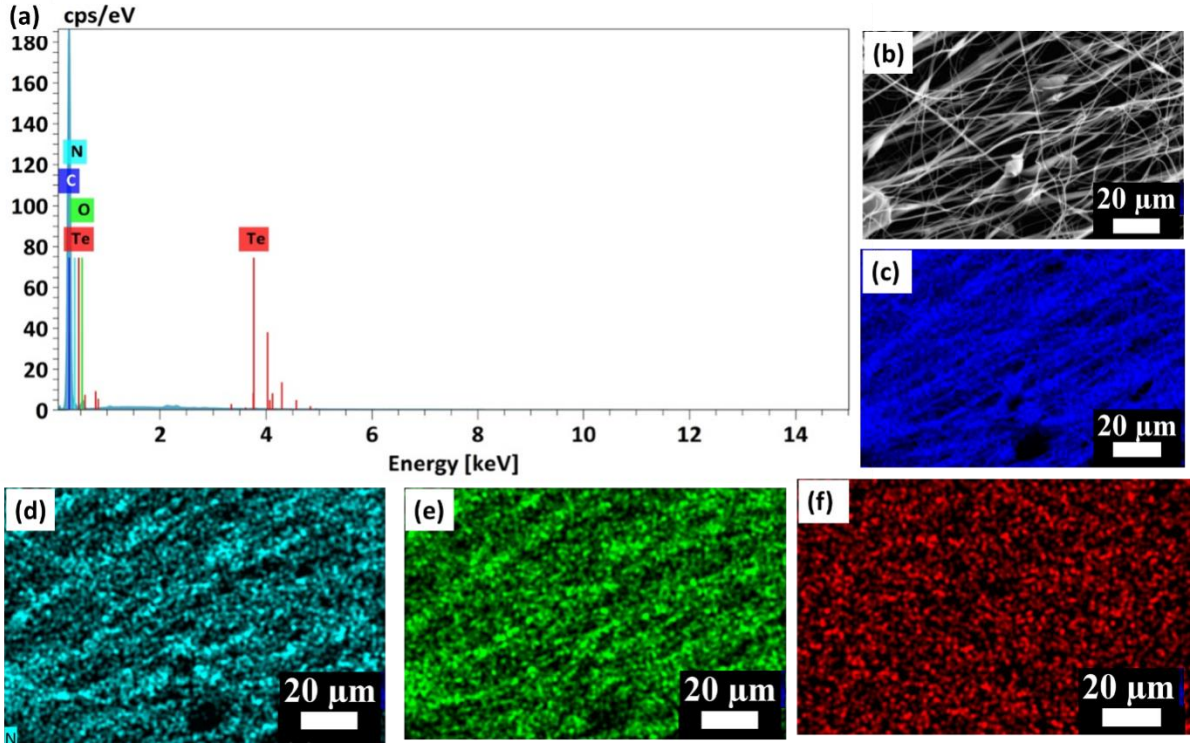

Figure 5.4: (a) EDS spectrum of Te-CNF. (b) SEM image used for elemental mapping of Te-CNF. (c-f) elemental mapping of carbon, nitrogen, oxygen, and tellurium respectively.

During stabilization of Te-EFs at 250 ^oC, the nitrile groups present in the PAN fiber get cyclized to form aromatic structure known as ladder structure (J. Li et al., 2013; Shokrani Havigh & Mahmoudi Chenari, 2022a; F. Zhang et al., 2014). Upon carbonization of Te-EFs at 900 ^oC (Te-CNFs), the I_D/I_G ratio was decreased to 0.82. This indicates an increase in the extent of graphitization during carbonization. The graphitic and their hexagonal planes of Te-CNF was further confirmed from XRD patterns.

5.3.5 XRD patterns

Powder XRD patterns of Te NPs and Te NPs incorporated N-doped CNF (Te-CNF) are shown in **Figure 5.5(b)**. The XRD pattern of Te NPs show strong peaks at 2Θ of 23^o, 27.5 ^{o}, 38.2 ^{o}, 40.4 ^{o}, 43.4 ^{o}, 46.8 ^{o}, 49.6 ^{o}, 56.9 ^{o}, 62.8 ^{o}, and 82.0 ^{o} which are assigned to hexagonal Te NPs (JCPDS No. 36-1452). The successful incorporation of hexagonal Te-NPs into N-doped CNF was confirmed from the XRD pattern. The XRD pattern of Te-CNF shows two broad diffraction peaks appearing at 2Θ = 24^o and 43^o which are assigned to the (002) and (100) crystallographic planes of graphite crystallites and the formation of turbostratic graphitic structure with randomly oriented graphitic carbon layers (C. K. Kim et al., 2020b; Shokrani

Havigh & Mahmoudi Chenari, 2022a). Thus, the pattern belongs to graphitic planes present in CNF (JCPDS No.41-1487). The XRD diffraction peaks of Te NPs are not at all visible, since Te NPs are incorporated in the CNF (Xi et al., 2008).

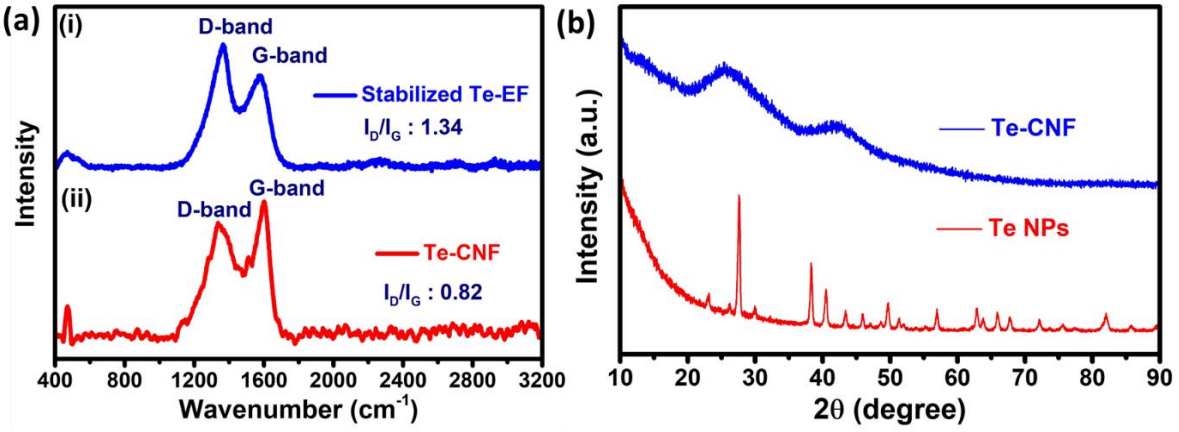

Figure 5.5: (a) Raman spectra of (i) Stabilized Te-EF at 250 °C and (ii) Te-CNF. (b) XRD pattern of Te-NPs and Te-CNF.

5.3.6 XPS Analysis

The elemental composition and chemical bonding of Te NPs and Te-CNF were analysed by XPS analysis. The XPS survey scans of Te NPs and Te-CNF are shown in **Figure 5.6(a)**. The XPS survey scan of Te-CNF confirmed that Te NPs were introduced into carbon structure of CNF after carbonization (C. K. Kim et al., 2020b). High-resolution XPS elemental spectra of Te (3d), C (1s), N 1s, and O 1s were analyzed to get better understanding of the chemical bonding in Te-CNF as shown in **Figure 5.6(b-e)**. The high-resolution spectrum of Te 3d present in Te NPs shows two peaks with binding energy of 575.7 eV and 586.2 eV, which are attributed to Te $3d_{5/2}$ and Te $3d_{3/2}$ as shown in **Figure 5.6(b).** The peaks of Te $3d_{5/2}$ and Te $3d_{3/2}$ were shifted to 576.6 eV and 587.0 eV after incorporation of Te NPs into N-doped CNF as shown in **Figure 5.6(b)** (C. K. Kim et al., 2020b; Ohkawa et al., 1992; Xi et al., 2008). The high-resolution C 1s spectrum was deconvoluted into four peaks at 284.5, 285.2, 286.1, and 287.7 eV corresponding to graphitic C=C (SP^2), graphitic C-C (SP^3), C-O/C-N, and C=O, respectively as shown in **Figure 5.6(c)**. The electrospun PAN fiber undergoes cyclization and forms ladder structure during stabilization, due to the presence of nitrile groups. The ladder structure has six membered rings which form pyridinic N, pyrrolic N, quaternary N, and pyridinic N-oxide during carbonization at 900 °C. The deconvoluted N 1s XPS spectrum exhibited four peaks at 398.1, 400.8, 401.4, and 402.3 eV belonging to pyridinic N, pyrrolic N, quaternary N, and pyridinic N-oxide, respectively due to the different forms of nitrogen in the carbonized PAN fiber (B. S. Lee et al., 2016) as shown in **Figure 5.6(d)**. The high-resolution

O 1s spectrum exhibited two major peaks at 531.9 and 533.3 eV that attributed to lattice oxygen of Te and carbonyl oxygen (C=O) as shown in **Figure 5.6(e)**.

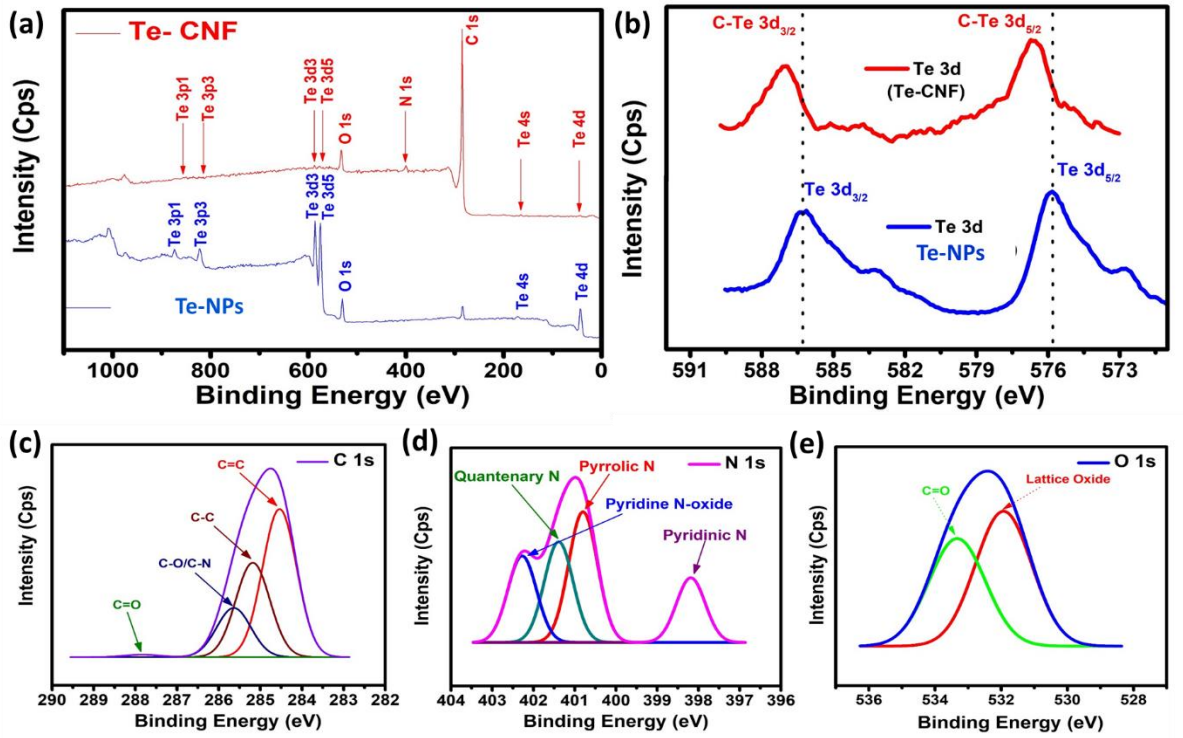

Figure 5.6: (a) XPS survey spectra of Te NPs and Te-CNF. (b) The XPS high-resolution elemental scanning of Te 3d present in Te NPs and Te-CNF. (c-e) XPS high-resolution elemental spectra of (c) C 1s, (d) N 1s, and (e) O 1s.

5.3.7 Contact angle measurement

Hydrophobicity is a desirable property for shielding materials. Hydrophobic shielding materials can protect electronic devices in harsh environmental conditions such as high humidity and corrosive environment. Contact angle is used to determine the hydrophilic and hydrophobic nature of shielding materials. Generally, surfaces with contact angle of more than 90^{o} are considered to be hydrophobic materials while surfaces with contact angles of less than 90^{o} are considered to be hydrophilic materials (Erbil, 2020). Both, Te-CNF and the PDMS composite show contact angles well above 90^{o} as shown in **Figure 5.7(a-b)** and hence, both the materials are hydrophobic in nature. The hydrophobicity of the shielding materials ensures their stability, reliability, and durability for long-term performance of electronic devices.

5.3.8 Mechanical Property

Since, Te-CNF mat is fragile in nature and for employing in practical applications, mechanical property has to be improved. Therefore, PDMS composite of Te-CNF was made as described already. PDMS composite of Te-CNF is expected to be thermally stable and flexible in a wide

temperature range. **Figure 5.7(c-f)** shows the photographs of PDMS composite of Te-CNF, subjected to twisting, folding and rolling. It was found that the composite retained its properties, after being twisted, folded, and rolled.

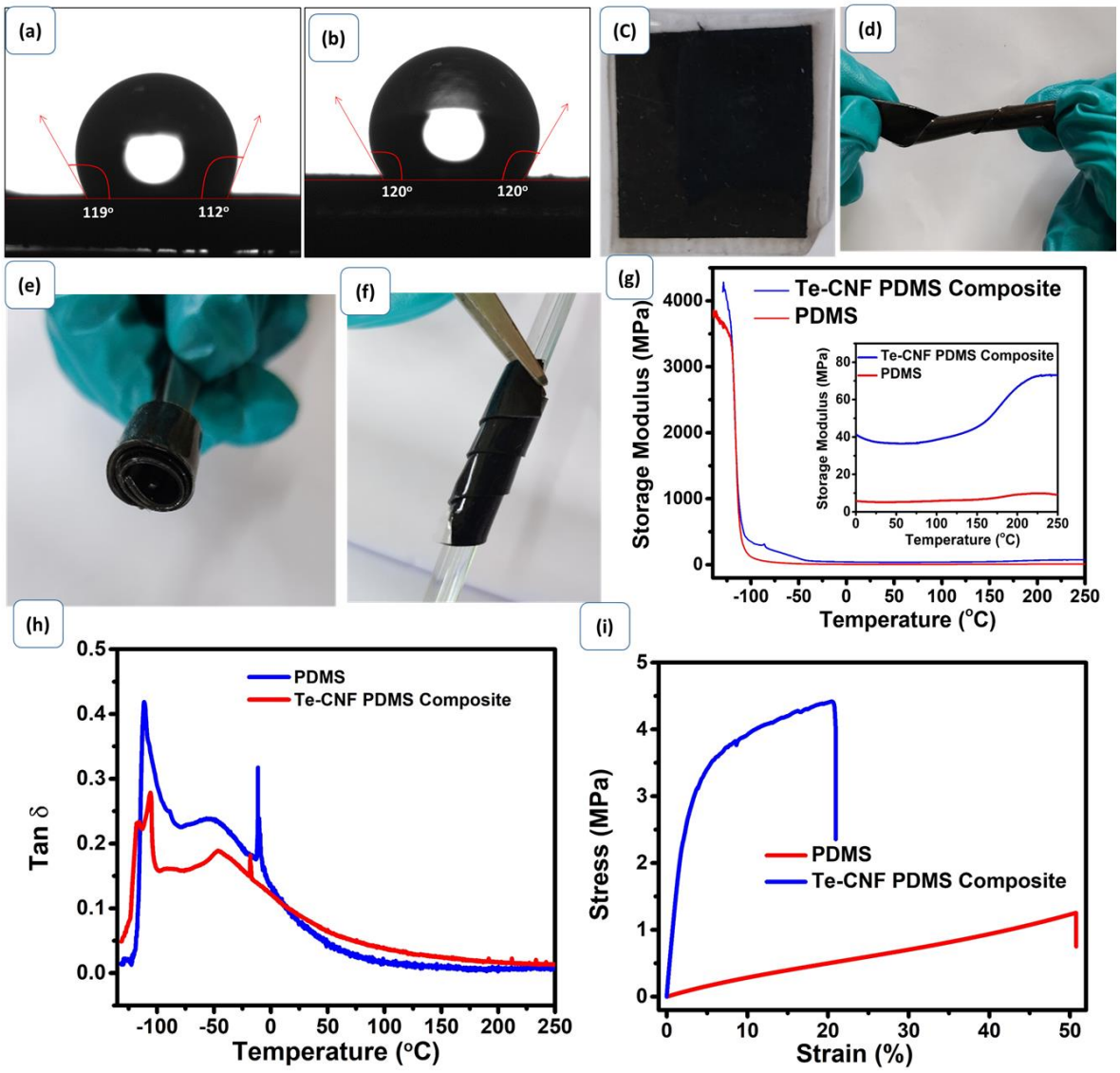

Figure 5.7: (a-b) Contact angle measurement of (a) Te-CNF and (b)Te-CNF PDMS composite. (c-f) Photographs of (c) PDMS composite of Te-CNF, (d) twisting, (e) folding, and (f) rolling of PDMS composites of CNF. (g-h) DMA plots of PDMS and PDMS composite of Te-CNF, (g) storage modulus vs temperature and (h) tan δ vs temperature. (i) stress-strain curve of PDMS and Te-CNF PDMS composites.

DMA was carried out to investigate the viscoelastic properties and damping properties of PDMS and PDMS composite of Te-CNF from -130 °C to 250 °C as shown in **Figure 5.7(g-h)**. Glass transition temperatures (T_g) of PDMS and PDMS composite of Te-CNF are -116 and -111 °C respectively. The very low T_g is due to the chain flexibility arising from Si-O-Si bonds (Zalewski et al., 2021). The **inset figure 5.7(g)** shows that storage modulus of PDMS

composite of Te-CNF is more than that of pristine PDMS in the temperature range of 0 ^{o}C - 250 ^{o}C. The damping properties (tan δ) of the PDMS and Te-CNF PDMS composites are shown in **figure 5.7(h)**. The Te-CNF PDMS composites exhibited a small shift in T_g determined at the maximum tan δ, towards higher temperature, due to the restriction of chain mobility in the composite. Surface of Te-CNF is completely covered with PDMS and forms interface between PDMS and the layered, 1-D fibrous structure of CNF, as shown in the cross-sectional SEM images of Te-CNF PDMS composite (**Figure 5.3(g-i)**). Incorporation of Te-CNF into the PDMS matrix provides additional cross-linking due to post-curing effects, solid phase reaction and lead to lower macro-chain mobility in PDMS, which is also known as physical cross-linking. The post-curing, physical cross-linking and faster re-alignment and re-orientation of PDMS chains increased the stiffness at elevated temperatures, resulting in increased storage modulus. The dynamic stiffness effect might have increased due to faster re-alignment and re-orientation of PDMS chains in the temperature range of 150 ^{o}C to 250 ^{o}C (Linlin Cao et al., 2016a; Placet & Delobelle, 2015). The Young's modulus and tensile strength were determined from stress-strain curve as shown in **Figure 5.7(i).** The tensile strength and Young's modulus of Te-CNF PDMS composite are 4 MPa and 62 MPa higher than that of pure PDMS (tensile strength = 1.27, Young's modulus = 2.28 MPa). The tensile strength of Te-CNF PDMS composite was increased 3.5 times than the pure PDMS, because, incorporation of Te-CNF into PDMS matrix led to the formation of strong chemical and physical hybrid crosslinks (Linlin Cao et al., 2016a).

5.3.9 Electrical Conductivity measurement

The electrical conductivity and formation of electrically conductive network can directly influence the properties of shielding materials. Te NPs are considered as inorganic semiconductors (Jaeyoo Choi et al., 2014, 2015). **Figure 5.8(a)** shows the current-voltage plot of Te-CNF and formation of electrical conductive network by using an electrical circuit **(inset Figure 5.8(a))**. The electrical conductivity of CNF is 0.186 S cm^{-1} whereas Te-CNF shows enhanced electrical conductivity of 0.684 S cm^{-1}. The high electrical conductivity of Te-CNF is due to the formation of conductive network between tellurium and SP^2 hybridized carbons present in CNF (Jaeyoo Choi et al., 2015; M. Han et al., 2021; Park et al., 2018; Shin et al., 2014; Xuefeng Zhang et al., 2021; Yue Zhang et al., 2021).

5.3.10 EMI SE

The EMI shielding performance of Te-CNF and its PDMS composites were measured in X-band with a thickness of 0.08 mm and 0.84 mm respectively. The pure PDMS is an insulator

and does not exhibit EMI shielding properties. The EMI shielding performance of Te-CNF and the contribution of SE_R and SE_A are shown in **Figure 5.8(b)**. CNF without any filler exhibited average EMI SE of 18 dB in X-band. Te-CNF exhibited an average EMI SE of 37.1 dB and contribution of SE_A and SE_R are 30.4 dB and 6.7 dB respectively in X-band. The high EMI shielding performance of Te-CNF is due to the high electrical conductivity and formation of interconnected 3-D conductive network which converts EM energy into current efficiently, leading to conduction loss. The presence of hetero atoms such as tellurium, nitrogen, and oxygen along with SP^2 hybridized carbon can produce structural defects which form dipoles in presence of EM waves and causes polarization loss (C. Han et al., 2021a; W. Li et al., 2012). The presence of nitrogen in the graphitic structure of PAN based CNF, developed inhomogeneity in electron density which led to polarization of C and N bonds and enhanced the polarization loss (C. Han et al., 2021a; Song et al., 2014; Xinci Zhang et al., 2019). Further, the presence of Te NPs into CNF forms small interfaces between Te NPs and CNF and develops impedance variation within the material. Layer-by layer structure of Te-CNF causes interfacial polarization. The Te-CNF exhibited a specific surface area of 221 m^2 g^{-1} as shown in **Figure 5.8(d).** The high surface area of Te-CNF allows interaction with the incident EM waves and consequently, the incident EM waves undergo multiple scattering and multiple-internal reflections (C. Han et al., 2021b; W. Li et al., 2012; M. Zhang et al., 2021).The scattered EM waves are absorbed by turbostratic graphitic structure of CNF via conduction loss and polarization loss. The synergistic effect of Te NPs and CNF leads to higher SE_A compared to SE_R.

The EMI shielding properties of Te-CNF mat as well as that of the PDMS composites of Te-CNF were measured. The pristine PDMS does not exhibit EMI shielding properties It is found that there is a slight increase in EMI SE (2-3 dB) in the composite, may be due to the introduction of polarization sites. However, when thickness of PDMS composite of Te-CNF was increased there was no increment in EMI SE. Therefore, the role of PDMS in the composite of Te-CNF is not significant compared to Te-CNF as far as EMI shielding is concerned. The schematic illustration of the EMI shielding mechanism of Te-CNF is shown in **Figure 5.8(e)**. The EMI shielding properties of Te-CNF was further evaluated by power coefficient (R, A, and T) determined by S_{22}, and S_{21} parameters as shown in **Figure 5.8(c)** (Oliveira et al., 2022). The average values are $R = 0.783$, $A = 0.223$, and $T = 2.03 \times 10^{-4}$.

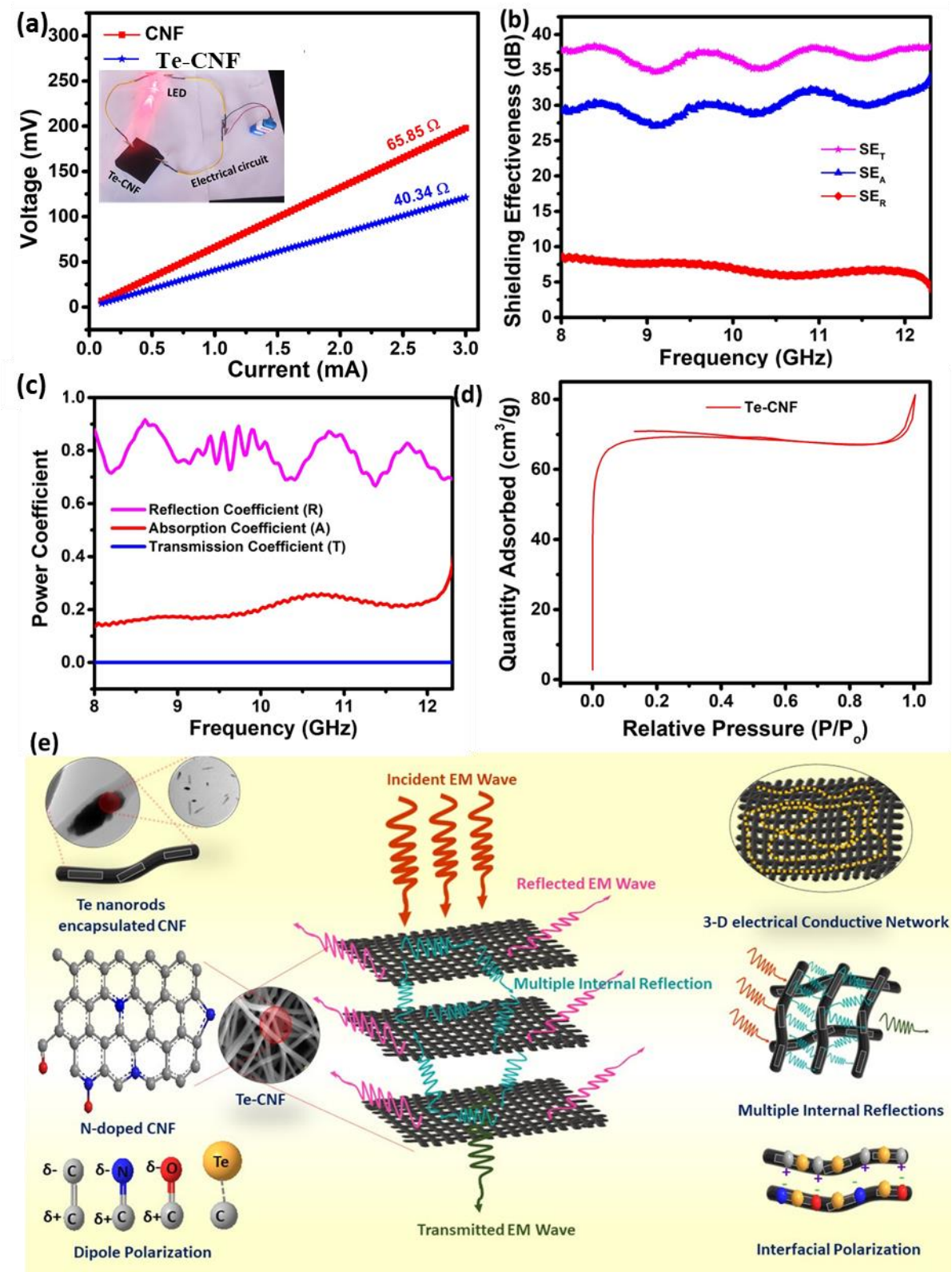

Figure 5.8: Voltage−current plots of Te-CNF. (b) EMI SE properties of Te-CNF. (c) power coefficient (R, A, and T) of Te-CNF in X-band region. (d) N_2 adsorption-desorption isotherm of Te-CNF. (e)) illustration of the EMI shielding mechanism of Te-CNF.

The high value of R may suggest reflection dominant shielding mechanism, due to high electrical conductivity, whereas, low value of T indicates low transmission of EM waves and high EMI SE of Te-CNF. The 1-D fibrous structure and hetero interfaces in Te-CNF attenuate the incident EM waves via continuous reflection or multiple scattering, until the total absorption of the incident EM waves occurs. The Te-CNF exhibited an average EMI SE of 37 dB which corresponds to 99.9998 % attenuation of the incident EM waves. Effective absorption (A_{eff}) was calculated using **Equation 9**, for better understanding of the EMI shielding based on absorption (Geetha et al., 2009). Te-CNF shows A_{eff} of 85.4 % which means that 85.4 % of the incident EM waves are absorbed by Te-CNF.

Lightweight, flexible, hydrophobic, and thin EMI shielding materials are required for commercial applications. Te-CNF is fragile and is difficult to be handled for applications in devices. PDMS composite of Te-CNF is highly flexible, has improved ease of handling and retains the EMI shielding property of Te-CNF. The normalized EMI SE values such as SSE and SSE_t are important for practical applications. The SSE and SSE_t value for Te-CNF are 74.24 dB cm^3 g^{-1} and 9280 dB cm^2 g^{-1} respectively with a density of 0.4997 g cm^{-3}. The SSE and SSE_t values of PDMS composite of Te-CNF are 29.53 dB cm^3 g^{-1} and 351 dB cm^2 g^{-1} respectively with thickness of 0.84 mm and density of 1.256 g cm^{-3}. Te-CNF and its PDMS composite exhibit high SSE_t values due to their lightweight and low thickness. **Table 5.1** compares the reported EMI SE values of composites, with similar kinds of fillers (metalloid and metal NPs).

Table 5.1: The EMI SE values reported in similar work.

Sample	**Thickness**	**Frequency Range**	**EMI SE (dB)**
Te-Polyvinyl alcohol (Yadav et al., 2023)	1 mm	8-12 GHz	4.19
Polyaniline/Te-polyvinyl alcohol(Yadav et al., 2023)	1 mm	8-12 GHz	4.0
Te/Polyaniline/Te/Ag-PVA (Yadav et al., 2023)	1 mm	8-12 GHz	10.19

Polypyrrole/Fe@TeO_2 (15 wt% TeO_2)(Basavaraja Patel et al., 2023)	1 mm	2-4 GHz	17
Nitrogen doped carbon nanofiber with sublimed sulfur (15 wt. % loading of sulfur) (Y. Jiang et al., 2020)	1.39 mm	2-18 GHz	-48.67 (R_L: Reflection loss)
Polyaniline-Antimony Oxide(Faisal & Khasim, 2013)		8-12.4 GHz	17.9 - 20.8
Liquid metal submicron particles films on glass and polyethylene terephthalate substrates. (Ye et al., 2022) Liquid metal: Ga In Sn alloys.	2 µm	2-18 GHz	33
Cobalt Particle-Embedded nitrogen doped Carbonaceous Nanostructures (Rajeev Kumar et al., 2019)	4 mm	2-18 GHz	33.1
Hexagonal Ni nanocrystals and Cubic Ni nanoflower assembled on graphene nanosheet(T. Chen et al., 2012)	5 mm	2-13GHz	-17.8 (R_L)
Te-CNF (This work)	**0.08 mm**	**8-12.4 GHz**	**38**

Previous studies (B. A. Al-Asbahi et al., 2023; Bandar A. Al-Asbahi et al., 2021; Al Naim et al., 2021) have reported fabrication of nanocomposite films of intrinsically conducting polymer PEDOT: PSS and Te nanorods for EMI shielding. However, the films are moisture sensitive and of low durability, and have inferior mechanical properties which may restrict their applications. The present work offers an effective strategy for achieving incorporation of chalcogen (Te) element into CNF to form 3-D conductive network which can be used as shielding materials in X-band. The PDMS composites of Te-CNF open new horizons for design of flexible, lightweight, and hydrophobic material with an absorption-dominant EMI shielding mechanism.

5.4 Conclusion

In summary, lightweight, thin, and hydrophobic tellurium nanoparticles incorporated, one-dimensional nitrogen-doped carbon nanofibers (Te-CNF) with high EMI shielding performance in X-band were prepared by electrospinning followed by carbonization. The Te-CNF exhibited an average EMI SE and SSE_t of 37.1 dB and 9280 dB cm^2 g^{-1} respectively, with a thickness of 0.08 mm. The Te-CNF shows higher SE_A values compared to SE_R due to the synergistic effects of incorporated Te NPs and N-doped CNF such as formation of conductive network, interfacial polarization, scattering, and multiple internal reflections. The PDMS composite of Te-CNF is flexibile and shows high storage modulus in wide temperature range. The combination of Te nanoparticles, CNF, and PDMS provides a simple method to prepare flexible, lightweight, thin, and hydrophobic EMI shielding material with absorption dominant shielding mechanism. The Te-CNF and its PDMS composite are promising candidates to be explored in flexible electronic devices and aerospace applications.

CHAPTER: 6

Nb_2O_5 Nanoparticles Embedded CNF and its PDMS Composite for EMI Shielding

Overview

The work presented in the previous chapter dealt with the inorganic semiconductor Te NPs incorporated CNF for EMI shielding. The current chapter concerns with investigation of EMI shielding properties of a semiconductor filler, namely Nb_2O_5 NPs (Nb_2O_5 NPs) incorporated CNF in X, Ku, and K-band. Here, Nb_2O_5 NPs improves the interfacial interaction with CNF and acts as an electron promoter to enhance the electrical conductivity of CNF resulting in high EMI shielding performance.

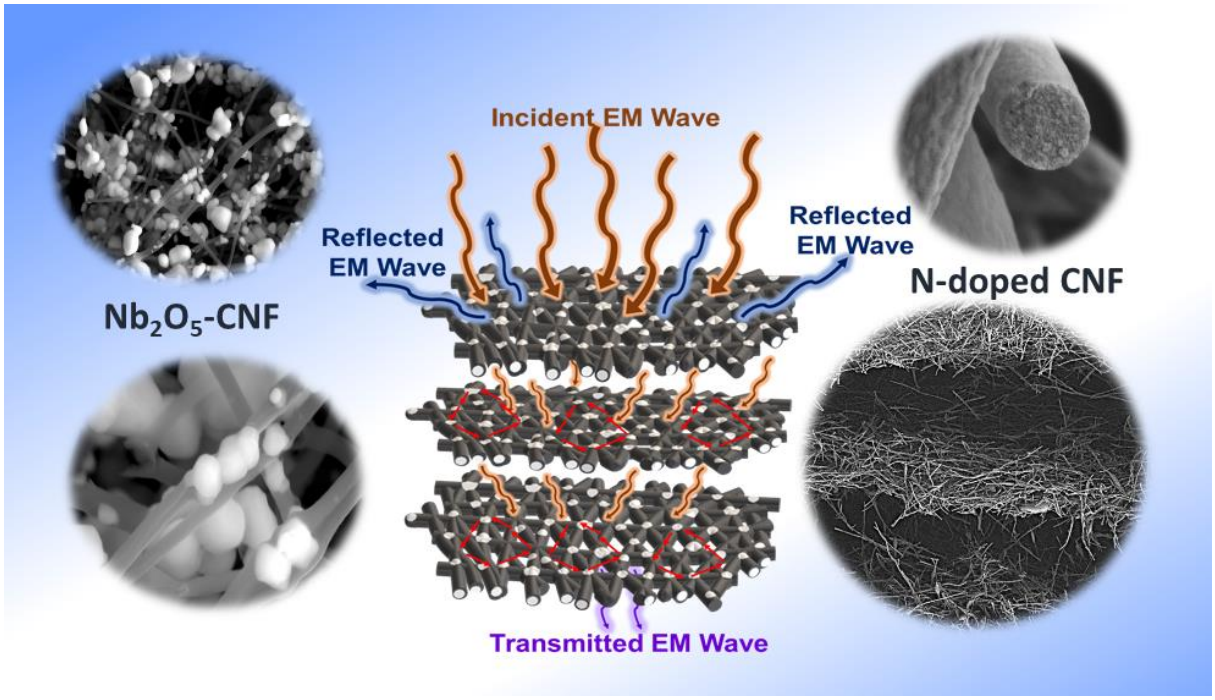

6.1 Introduction

Incorporation of metal oxide NPs into CNF can introduce dipole polarization and can form hetero-interfaces that cause interfacial polarization which may lead to polarization loss. Hence, incorporation of metal oxides with semiconductor properties as fillers into electrically conductive CNF is a good strategy for improving the EMI shielding performance. Electrical conductivity of semiconductors falls between a conductor and an insulator. The conventional semiconductors have a band gap between 1 and 1.5 eV, whereas wide band semiconductors have a band gap between 2 and 4 eV. Band gap of semiconductors is dependent on particle size and phase of the materials. Conductivity as well as dielectric properties of semiconductors are important factors which would affect their EMI shielding properties. Numerous semiconducting materials, including ZnO, TiO_2, MoS_2, CoO, $BaTiO_3$, $SrTiO_3$, and others, are known to possess good dielectric properties, which might play a significant role in the losses. EMI shielding property of these semiconducting fillers may be attributed to ohmic, conduction, eddy current losses, and polarization losses (Sushmita et al., 2020). Sushmita et al. reviewed the articles that discussed about semiconductor fillers-based polymer nanocomposites as advanced materials for EMI shielding (Sushmita et al., 2020). Zhang et al. investigated Nb_2O_5/NbO_2/Co/porous carbon nanocomposites for microwave absorption in the frequency range 8.2-18 GHz. The nanocomposite exhibited a minimum reflection loss of -64.68 dB with 0.37 mmol of Nb_2O_5 with thickness of 2.00 mm at 11.76 GHz (Ximing Zhang et al., 2022b). Raghavendra et al. reported EMI SE of polyaniline coated Nb_2O_5 nanocomposites with anticorrosion behavior. It exhibited EMI SE of 28.8 dB in the frequency range of 12-18 GHz (Maruthi, Faisal, Raghavendra, et al., 2021). Wang et al. fabricated flexible tantalum carbide (TaC)/C electrospun non-woven fabrics for EMI shielding in the frequency range of 8.2-12.4 GHz (H. Guo, Wang, et al., 2021).

Design and structure of the shielding materials can greatly influence absorption of EM waves. CNF with uniformly distributed conductive fillers provide low percolation threshold, large surface area, a wider porosity, and high aspect ratio of CNF, resulting in a longer EM dissipation path in the axial direction (J. H. Lee et al., 2022; C. Wang et al., 2023a; B. Yang et al., 2022). The layer-by-layer structure of 1-D CNF and its fibrous structure help to form numerous hetero-interfaces and enable interfacial polarization (Su et al., 2023). Nb_2O_5 is a semiconductor and their electrical conductivity can be enhanced by addition of carbonaceous materials such as carbon nanosheets, graphene, and MWCNT (Jing et al., 2021; Yang Li et al., 2020; Lim et al., 2014; Jiande Lin et al., 2018; Meng et al., 2019; H. Sun et al., 2017; S. Zhu

et al., 2020). Uniform distribution of Nb_2O_5 NPs in 1 D N-doped CNF may increase dielectric loss and sites for polarisation loss, interfacial polarization, and multiple internal reflections. The absorption-based shielding mechanism can be strengthened by these dielectric losses (Su et al., 2023).

The present study reports, 1-D nanostructured N-doped CNF containing Nb_2O_5 NPs with absorption dominant EMI shielding mechanism in wide frequency range (8.2 -26.5 GHz). Nb_2O_5 is an n-type semiconductor that has a bandgap of 3.4 eV and it possesses a high refractive index, great chemical stability, and good corrosion resistance. Nb_2O_5 improves the interfacial interaction with CNF and acts as an electron promoter to enhance the electrical conductivity of CNF (Jing et al., 2021; Yang Li et al., 2020; Lim et al., 2014; Jiande Lin et al., 2018; Meng et al., 2019; Morais et al., 2017; Shanmugapriya et al., 2019; H. Sun et al., 2017; Umeshbabu & Ranga Rao, 2017; Li Zhang et al., 2010; S. Zhu et al., 2020). Here, Nb_2O_5 NPs incorporated N-doped CNF (Nb_2O_5-CNF) was prepared through electrospinning, followed by heat treatment. Nb_2O_5-CNF exhibited high electrical conductivity and formed strong conductive network between Nb_2O_5 and CNF. Due to this, Nb_2O_5-CNF and their PDMS composites exhibited excellent EMI SE of 67 dB with thickness of 0.08 mm and 0.72 mm, respectively. Nb_2O_5-CNF PDMS composites are promising EMI shielding materials for application in flexible and wearable electronic devices.

6.2 Experimental Section

6.2.1 Materials

The specifications of PAN, Nb_2O_5 NPs, and DMF are mentioned in chapter 2 (refer to section 2.1.)

6.2.2 Preparation of Nb_2O_5 NPs incorporated CNF (Nb_2O_5-CNF)

10 mL of PAN solution (10 wt%) was prepared in DMF. Nb_2O_5 NPs (1g) were added to the PAN solution and stirred at 60 °C for 12 h to get homogeneous dispersion of Nb_2O_5 in PAN solution. The dispersion contained PAN and Nb_2O_5 in 1:1 weight ratio. Similarly, dispersion with PAN and Nb_2O_5 in 2:1 weight ratio also was prepared. The Nb_2O_5-PAN dispersion was filled into a 10 mL syringe having a needle diameter of 0.80 mm and was pumped into electrospinning chamber with a uniform flow rate of 1.2 mL h^{-1}. The distance between the needle and rotating drum collector was set to 13 cm. The rotating drum collector was covered with hard Al foil and its rotation speed was set to 1000 rpm. The temperature in the spinning

chamber was 25 ^{o}C with a relative humidity of 40%. A high voltage (13 kV) was applied on the needle to obtain Nb_2O_5 NPs embedded PAN electrospun fiber (EF). The terms PAN EF, Nb_2O_5-EF-33, and Nb_2O_5-EF-50 are referred to electrospun fibers prepared from pure PAN solution, containing PAN and Nb_2O_5 in 2:1 and 1:1 weight ratio respectively. The obtained electrospun fibers were stabilized in air oven at 250 ^{o}C in oxygen environment for overnight. Then carbonization was carried out in an inert (argon) environment in high temperature-inert furnace at 900 ^{o}C for 3 h. Heating rate employed was 1^{o}C min^{-1}. The carbonized electrospun PAN fiber and Nb_2O_5 incorporated electrospun PAN fiber were termed as CNF, Nb_2O_5-CNF-33, and Nb_2O_5-CNF-50.

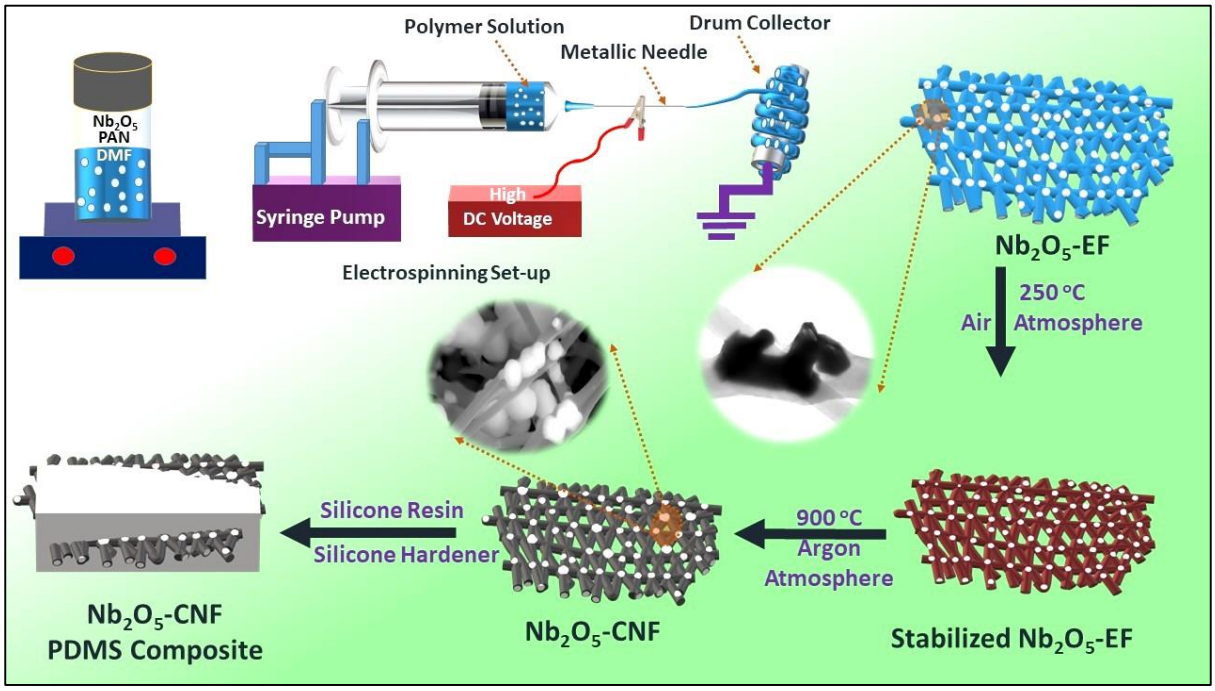

Figure 6.1: Schematic illustration of fabrication of PDMS composite of Nb_2O_5-CNF.

6.2.3 Fabrication of PDMS composite of Nb_2O_5-CNF

PDMS composite of Nb_2O_5-CNF was prepared following the procedure mentioned in Chapter 2 (section 2.3). The preparation and fabrication of Nb_2O_5-CNF and its PDMS composites are schematically represented in **Figure 6.1.** Development of entanglements of PDMS along with CNF results in formation of the flexible Nb_2O_5-CNF PDMS composite.

6.3 Results and Discussion

6.3.1 TEM image

TEM is an essential technique for examining the internal structure and morphology of nanofibers. TEM images of Nb_2O_5 NPs, PAN EF and Nb_2O_5-EFs are displayed in **Figure 6.2**. **Figure 6.2 (a-b)** shows that Nb_2O_5 NPs have a mean particle size of 37 ± 4 nm.

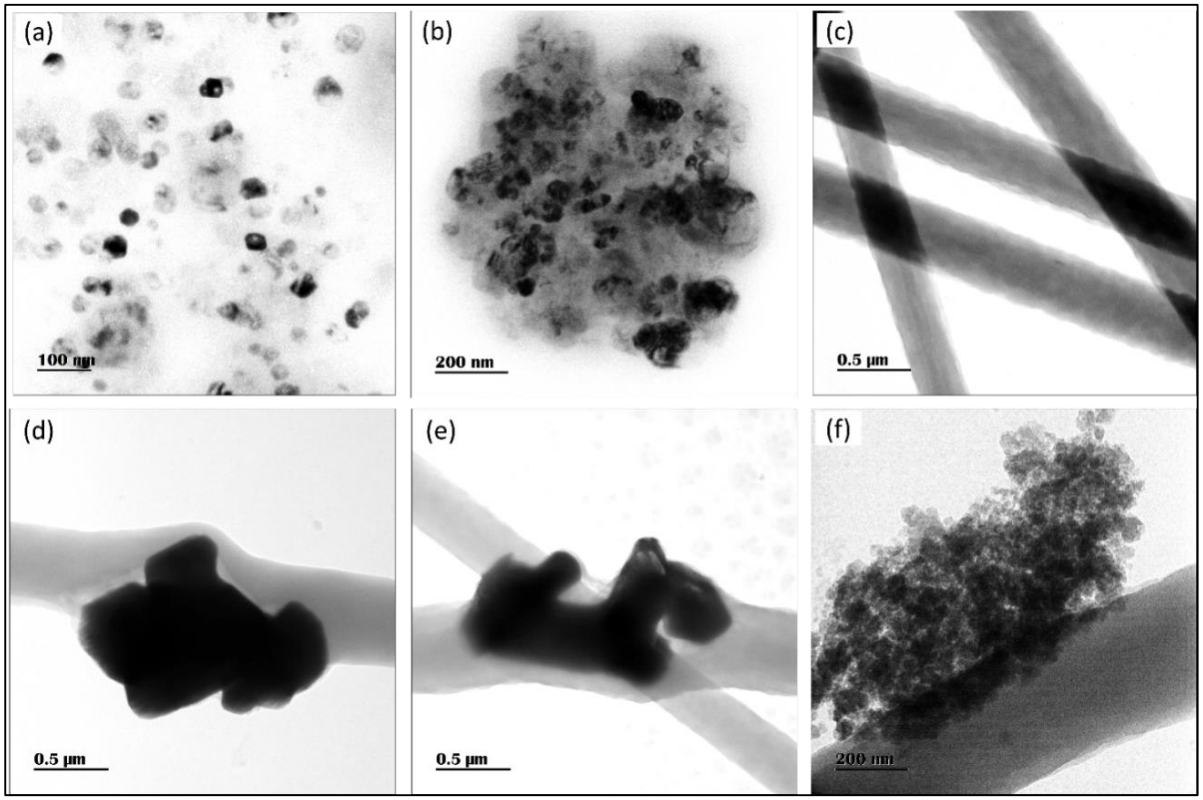

Figure 6.2: TEM image of (a-b) Nb_2O_5 NPs, (c) PAN EF, and (d-f) Nb_2O_5 NPs embedded PAN EF.

Figure 6.2(c) shows the TEM image of PAN EF and **Figures 6.2(d-f)** show the TEM images of Nb_2O_5 NPs embedded PAN EF. The image shows that Nb_2O_5 NPs are embedded and distributed along the EF. The images also indicate that there was no electrospraying and no bead formation during electrospinning. The Nb_2O_5-EF has a high aspect ratio. The mean diameter of PAN EF and Nb_2O_5 NPs embedded PAN EF are 496 ± 21 nm and 602 ± 46 nm, respectively based on **Figures 6.2(d-f)**.

6.3.2 SEM image

The SEM images of CNF, Nb_2O_5-CNF-33, and Nb_2O_5-CNF-50 are presented in **Figure 6.3**. The images show that the fiber morphology of electrospun PAN fiber and Nb_2O_5 nanoparticles incorporated electrospun PAN fiber remains similar after carbonization with high aspect ratio.

Figure 6.3(a) is the SEM image of CNF, it shows that carbon nanofibers are continuous with a mean diameter of CNF is 453 ± 42 nm. **Figure 6.3 (b-c)** gives SEM images of Nb_2O_5-CNF-33 and Nb_2O_5-CNF-50 and shows that the fibers are continuous without bead formation. It shows that Nb_2O_5 NPs are distributed along and embedded within the fibers. As the loading of Nb_2O_5 NPs increases, the distribution of Nb_2O_5 NPs becomes denser as seen in **Figure 6.3 (c)** (Nb_2O_5-CNF-50). The mean diameter of Nb_2O_5-CNF-33 and Nb_2O_5-CNF-50 are 362 ± 33 nm and 375 ± 74 nm, respectively.

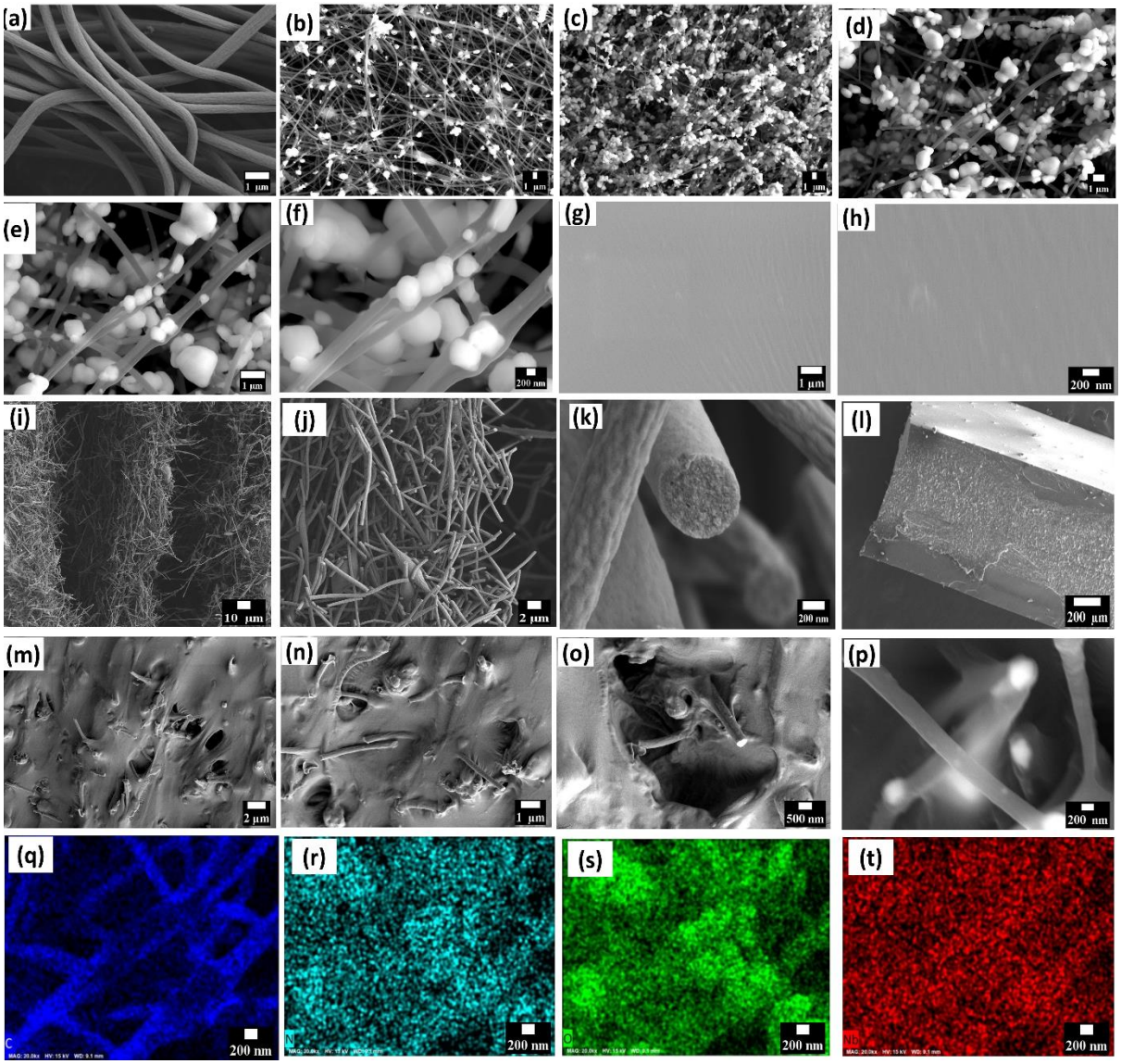

Figure 6.3: SEM images of (a) CNF, (b) Nb_2O_5-CNF-33, (c-f) Nb_2O_5-CNF-50, (g-h) Nb_2O_5-CNF-50 PDMS composites. Cross-sectional SEM image of (i-k) CNF and (l-P) Nb_2O_5-CNF-50 PDMS composites. (f) SEM image of Nb_2O_5-CNF-50 used for elemental mapping. (q-t) elemental mapping of (q) carbon, (r) nitrogen, (s) oxygen, and (t) niobium.

Figure 6.3(i-k) displays the cross-sectional SEM images of CNF. It shows that CNFs have layer-by-layer structure and fibrous structure with high porosity (**Figure 6.3(i-j))** and clearly shows the 1-D nanostructure of CNF **(Figure 6.3(k)].** The SEM images of the PDMS composite of Nb_2O_5-CNF-50 are shown in **Figure 6.3(g–h)**. It is seen that smooth surface is formed due to uniform covering of Nb_2O_5-CNF with PDMS. The cross-sectional SEM image of the PDMS composite demonstrated tight bonding between PDMS and Nb_2O_5-CNF without changing the fiber morphology as shown in **Figure 6.3(l-p).**

6.3.3 Elemental mapping

Elemental mapping is a technique which can be used to visualize and locate the distribution of elements into the CNF. The elemental mappings of carbon, nitrogen, oxygen, and niobium confirm the presence and distribution of Nb_2O_5 NPs throughout the CNF which is evident from **Figure 6.3 (q-t)**.

6.3.4 XRD patterns

The crystallographic structure of carbonized PAN fiber incorporated Nb_2O_5 NPs is examined by XRD patterns as demonstrated in **Figure 6.4(a)**. The broad peak centred at around 25.4^o in the XRD pattern of CNF belongs to the turbostratic carbon structure (JCPDS 41-1487). The broad peak at 25.4^o is relatively very low in intensity and indicates that carbonized PAN possesses turbostratic carbon structure and low crystallinity (Q. Y. Chen et al., 2014). The XRD patterns of commercial Nb_2O_5 NPs are shown in **Figure 6.4(a)**. The XRD peaks of Nb_2O_5 NPs embedded CNF can be assigned to the crystalline orthorhombic structure with peaks resolved at $2\Theta = 22.3^o$, 29.6^o, 31.9^o, 37.3^o, and 45.7^o (JCPDS card 00-030-0873) (Kumari et al., 2020; S. Li et al., 2016; Morais et al., 2017; Raba et al., 2016; Triani et al., 2019). The XRD patterns of Nb_2O_5-CNF confirms the presence and incorporation of Nb_2O_5 NPs into CNF.

6.3.5 Raman Spectroscopy

The best way to determine the microstructure of carbon-based materials is Raman spectroscopy. The Raman spectra of CNF, Nb_2O_5-CNF-33, and Nb_2O_5-CNF-50 are displayed in **Figure 6.4(b).** These samples exhibit peaks at 1363 cm^{-1} and 1596 cm^{-1}, which correspond to the D-band and G-band, respectively. The G-band is attributed to the crystalline graphitic structure, whereas D-band belongs to structural disorder (Björkman, 1969; Caņado et al., 2006). These peaks are very similar to those observed in nanostructured carbonaceous materials such as graphene and CNTs (Q. Dong et al., 2013; T. Li et al., 2018). The ratio of the intensities

of the D-band and the G-band, also known as I_D/I_G, are 0.90, 0.96, and 1.02 for CNF, Nb_2O_5-CNF-33, and Nb_2O_5-CNF-50, respectively. As the loading of Nb_2O_5 NPs increases, the ratio of I_D/I_G also increase indicating the decrease in degree of graphitization due to the increase in structural disorder in the crystalline graphitic structure of CNF (Björkman, 1969; Caņado et al., 2006; Shanmugapriya et al., 2019). All these samples have I_D/I_G value near to 1 that belongs to turbostratic carbon structure.

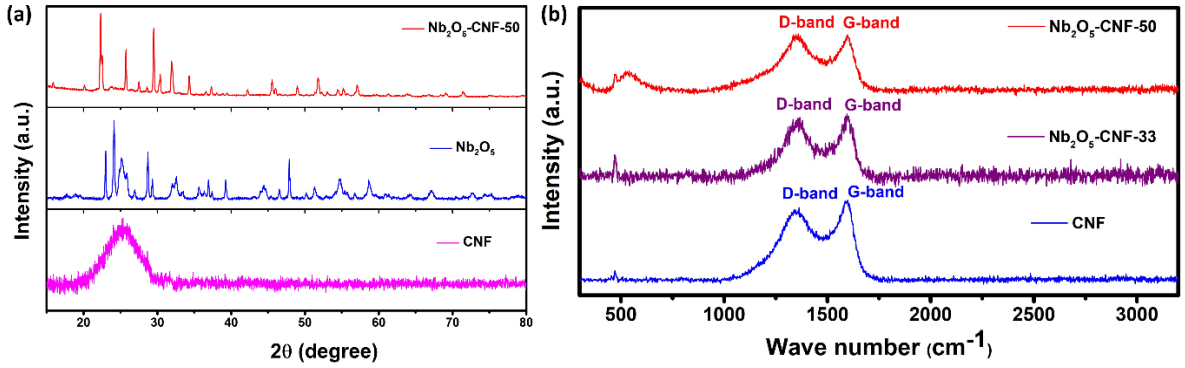

Figure 6.4: (a) XRD patterns of CNF, Nb_2O_5 NPs, and Nb_2O_5-CNF-50. (b) Raman spectra of CNF, Nb_2O_5-CNF-33, and Nb_2O_5-CNF-50.

6.3.6 XPS analysis

XPS analysis of Nb_2O_5-CNF was carried out to understand the surface chemical compositions. The survey spectrum validates the presence of niobium, oxygen, nitrogen, and carbon on the surface of the CNF as depicted in **Figure 6.5(a).** The survey scan of CNFs shows peaks at 285.0 eV, 401.7 eV, and 531.7 eV corresponding to C(1s), N(1s), and O(1s) species respectively. These peaks demonstrate the formation of N-doped CNF. The survey scan of commercially available Nb_2O_5 NPs shows peaks at 207.9 eV, 284.2 eV, 365.9 eV, 380.5 eV, and 530.8 eV belonging to Nb (3d), C (1s), Nb (3p3), Nb (3p1), and O (1s) species respectively. The survey scan of Nb_2O_5-CNF-50 exhibits collective peaks of CNF and Nb_2O_5 NPs detected at 209.1 eV, 284.2 eV, 366.4 eV, 382.0 eV, 400.2 eV, and 531.2 eV belonging to Nb (3d), C (1s), Nb (3p3), Nb (3p1), N (1s) and O (1s) species respectively. The high-resolution elemental scans for the elements contained in Nb_2O_5-CNF-50, such as Nb (3d), C (1s), N (1s), and O (1s) are examined as displayed in **Figure 6.5(b-e),** respectively. The high resolution spectrum of Nb 3d exhibited two strong peaks at 207.9 eV and 210.6 eV corresponding to Nb $3d_{5/2}$ and Nb $3d_{3/2}$, respectively (Jing et al., 2021; Qamar et al., 2015; Su et al., 2023). The high resolution C 1s spectrum of Nb_2O_5-CNF shows four peaks corresponding to carbonized PAN fiber at 284.8 eV (C=C), 285.7 eV (graphitic C), 288.8 eV (carbonyl carbon), and 285.5 eV (C-O/C-

N). The strong peak at 284.8 eV belongs to SP^2 hybridized carbon due to cyclization and formation of graphitic structure (Jing et al., 2021; Meng et al., 2019; Su et al., 2023).

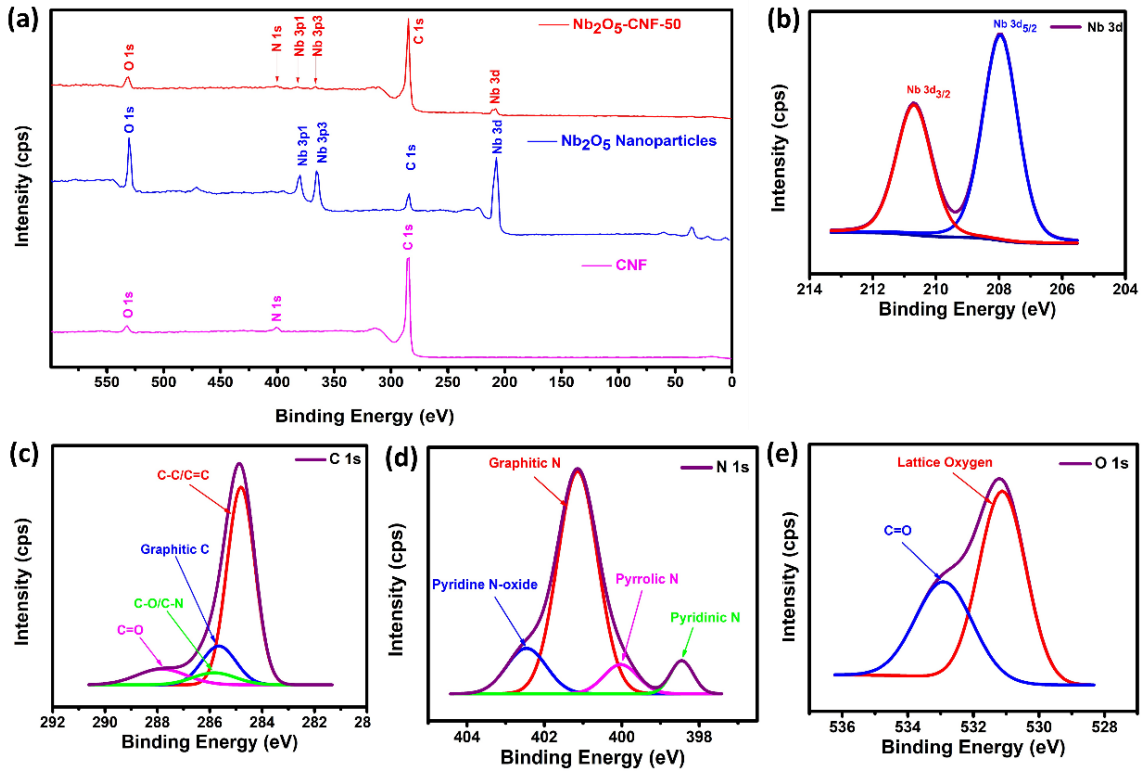

Figure 6.5: (a) XPS survey scan of CNF, Nb_2O_5 NPs, and Nb_2O_5-CNF-50. High resolution elemental and deconvoluted peaks of (b) Nb 3d, (c) C 1s, (d) N 1s, and (e) O 1s.

The high resolution N 1s spectrum shows four peaks at 398.4 eV (pyridinic N), 400.0 eV (pyrrolic N), 401.1 eV (quaternary N), and 402.5 eV (pyridinic-N-oxide) which are attributed to carbonized PAN fiber. This N 1s peak is due to cyclization of nitrile groups present in PAN, during carbonization. The high resolution O 1s spectrum exhibited two peaks at 531.1 eV and 532.9 eV belonging to carbonyl carbon and lattice oxygen of Nb_2O_5. The broader peak of O 1s attributed to chemical interaction between CNF and Nb_2O_5 and formation of Nb-O-C bonds (Nagaraju et al., 2020; Qamar et al., 2015; Su et al., 2023; Tang et al., 2018).

6.3.7 Contact angle measurements

The contact angles of CNF, Nb_2O_5-CNF-33, and Nb_2O_5-CNFs-50 PDMS composites are 130 ^{o}, 129 ^{o}, and 120^o respectively as shown in **Figure 6.6(a-c)**. All these materials show contact angles greater than 120^o and imply that these materials are hydrophobic or moisture insensitive in nature and these may be used as waterproof shielding materials.

6.3.8 Mechanical Properties

Figure 6.6 (d) shows the load (100 g) bearing capacity of lightweight Nb_2O_5-CNF. High mechanical strength, flexibility and straight forward fabrication methods adaptable for complicated structures of electronic devices are desirable properties for shielding materials. The PDMS composites of Nb_2O_5-CNF fulfill all these requirements for shielding materials. The digital photographs of Nb_2O_5-CNF PDMS composites are presented in **Figure 6.6(e)**.

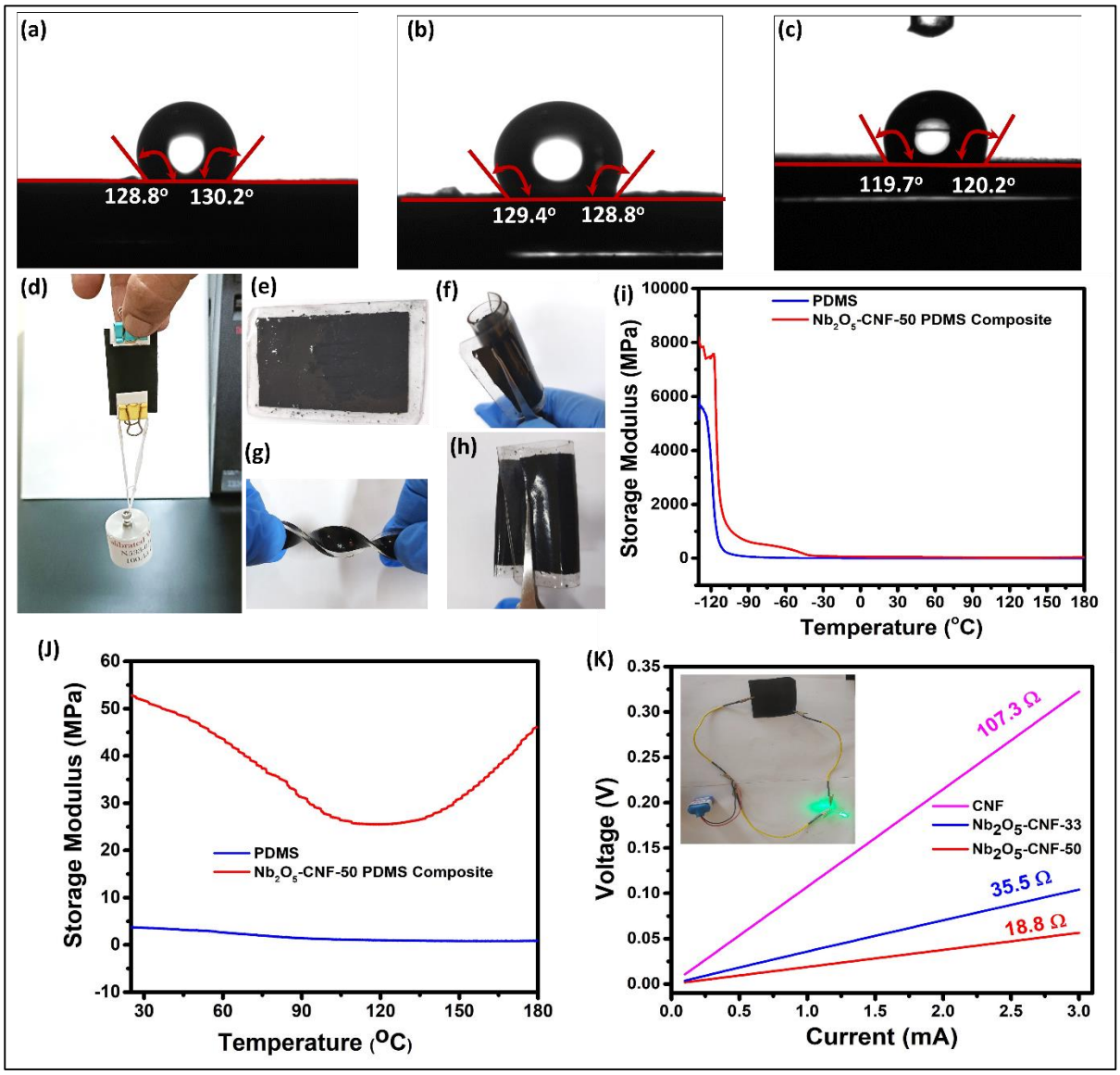

Figure 6.6: (a-c) Contact angle of (a) CNF, (b) Nb_2O_5-CNF-50, and (c) Nb_2O_5-CNF-50 PDMS composite. (d) Load (100 g) bearing capacity of Nb_2O_5-CNF. (e-h) digital photograph of (e) Nb_2O_5-CNF-50 PDMS composite, (f) rolling, (g) twisting, and (h) folding of properties Nb_2O_5-CNF-50 PDMS composite. (i-j) DMA plots of PDMS and Nb_2O_5-CNF-50 PDMS composite, (i) in the temperature range of -130 °C to 180 °C, and (j) room temperature (25 °C to 180 °C) (k) Current-voltage plot of CNF, Nb_2O_5-CNF-33, and Nb_2O_5-CNF-50.

The remarkable flexibility of the composites are demonstrated via twisting, rolling, and folding of Nb_2O_5-CNF PDMS composites as shown in **Figure 6.6(f-h)**. The Nb_2O_5-CNF PDMS composite can be twisted, folded, and rolled without sustaining any damage, and it can then regain its original shape.

6.3.8.1 Dynamic mechanical analysis

DMA is used to study the viscoelastic behavior of PDMS composites. **Figure 6.6 (i)** shows the viscoelastic properties of pure PDMS and Nb_2O_5-CNF-50 PDMS composite in the temperature range -130 ^oC to 180 ^oC. A DMA plot of storage modulus (G') as a function of temperature is shown in **Figure 6.6(i)** for pure PDMS and Nb_2O_5-CNF-50 PDMS composite. This plot shows that after incorporation of Nb_2O_5-CNF-50 into PDMS composite, glass transition temperature (Tg) increases from -124 ^oC to -117 ^oC. The low Tg of PDMS is due to the flexible nature of the Si-O-Si backbone and the weak intermolecular forces between the polymer chains. At low temperature (-130 ^oC), PDMS and Nb_2O_5-CNF-50 PDMS composite exhibit storage modulus of 5.65 GPa and 7.85 GPa, respectively. DMA plots of PDMS and Nb_2O_5-CNF-50 PDMS composite indicate that they exist in rubbery state in the temperature range of -50 to 100 ^oC due to low glass transition temperature arising from Si-O-Si backbone. The storage modulus of Nb_2O_5-CNF-50 PDMS composite is higher than the pure PDMS, since CNF acts as reinforcement in the PDMS composite. **Figure 6.6(j)** indicates the behavior of PDMS and Nb_2O_5-CNF-50 in the range 25 ^oC to 180 ^oC. It implies that the storage modulus and stiffness of Nb_2O_5-CNF-50 PDMS composites increase with increasing temperature due to post-curing effects, chemical cross-linking reactions, diffusion, and solid phase reaction (Linlin Cao et al., 2016b; S. Lu et al., 2022; Placet & Delobelle, 2015).

6.3.9 Electrical Conductivity measurements

Electrical conductivity is an essential property for EMI shielding materials. When electromagnetic waves encounter a conductive material, the electric field induces a current in the material, which in turn generates an opposing electric field that cancels out the incident wave. The higher the electrical conductivity of the material, the more effectively it can reflect the incident EM waves and provide high EMI shielding effectiveness. The current-voltage plots are displayed in **Figure 6.6(k)**. It demonstrates that voltage increases linearly as current changes from 0.1 mA to 3 mA with constant slope or resistance. The straight line or slope of current-voltage plots demonstrate that electrical conductivity is consistent throughout the CNF. The electrical conductivity of CNF, Nb_2O_5-CNF-33, and Nb_2O_5-CNF-50 were calculated using

the **Equations 18, 19**, and **20**. The electrical conductivity of CNF, Nb_2O_5-CNF-33, and Nb_2O_5-CNF-50 are 0.257, 0.781, and 1.470 S cm^{-1}, respectively. Hence, these materials are appropriate to be used for EMI shielding. The electrical conductivity depends on the mobility of charge carriers, specifically the electrons. The electron mobility is enhanced when electrons are de-localized. In the case of carbonized PAN fiber, large number of conjugated double bonds (SP^2 hybridized) are present which allow $\pi \rightarrow \pi^*$ transitions (Gehring et al., 2019) . Nb_2O_5 is semi-conductor with an energy gap of 3.4 eV between valence band and conduction band. As the loading of Nb_2O_5 increases, the electrical conductivity increases because Nb_2O_5 acts as electron promotor and that improves the formation of electrical conductive network and helps to enhance the $\pi \rightarrow \pi^*$ transitions in Nb_2O_5-CNF (Jing et al., 2021; Yang Li et al., 2020; Lim et al., 2014; Jiande Lin et al., 2018; Meng et al., 2019; Shanmugapriya et al., 2019; Su et al., 2023; H. Sun et al., 2017; Umeshbabu & Ranga Rao, 2017; Li Zhang et al., 2010; S. Zhu et al., 2020).

6.3.10 EMI SE

Metals, on account of their high electrical conductivity, are frequently utilised as shielding materials. However, metals are of heavy weight and low flexibility, susceptible to corrosion and may cause secondary EMI. Metal oxides incorporated N-doped CNF are suitable substitutes to metal based shields, because they are resistant to corrosion and can withstand high temperatures without deforming. But, most of the metal oxides are electrically insulating and high dielectric constant, restricts their use for EMI shielding in higher frequency range.

Nb_2O_5 NPs exhibit semiconductor properties and has a bandgap of 3.4 eV. Nb_2O_5 nanoparticles embedded N-doped CNF may perform as good EMI shielding materials due to 1-D nanostructure of CNF, action of Nb_2O_5 as electron promotor, and formation of 3D conductive network. The uniform distribution of Nb_2O_5 NPs along the N-doped CNF and the formation of electrical conductive network between Nb_2O_5 NPs and CNF may make them suitable materials for EMI shielding. **Figure 6.7** demonstrates the EMI shielding capabilities of Nb_2O_5-CNFs. The EMI SE of CNF, Nb_2O_5-CNF-33, and Nb_2O_5-CNF-50 were measured in X- band, Ku-band and K-band as displayed in **Figure 6.7**. Thickness of the carbonized nanofibers and their PDMS composites used for EMI SE are 0.08 mm and 0.72 mm respectively.

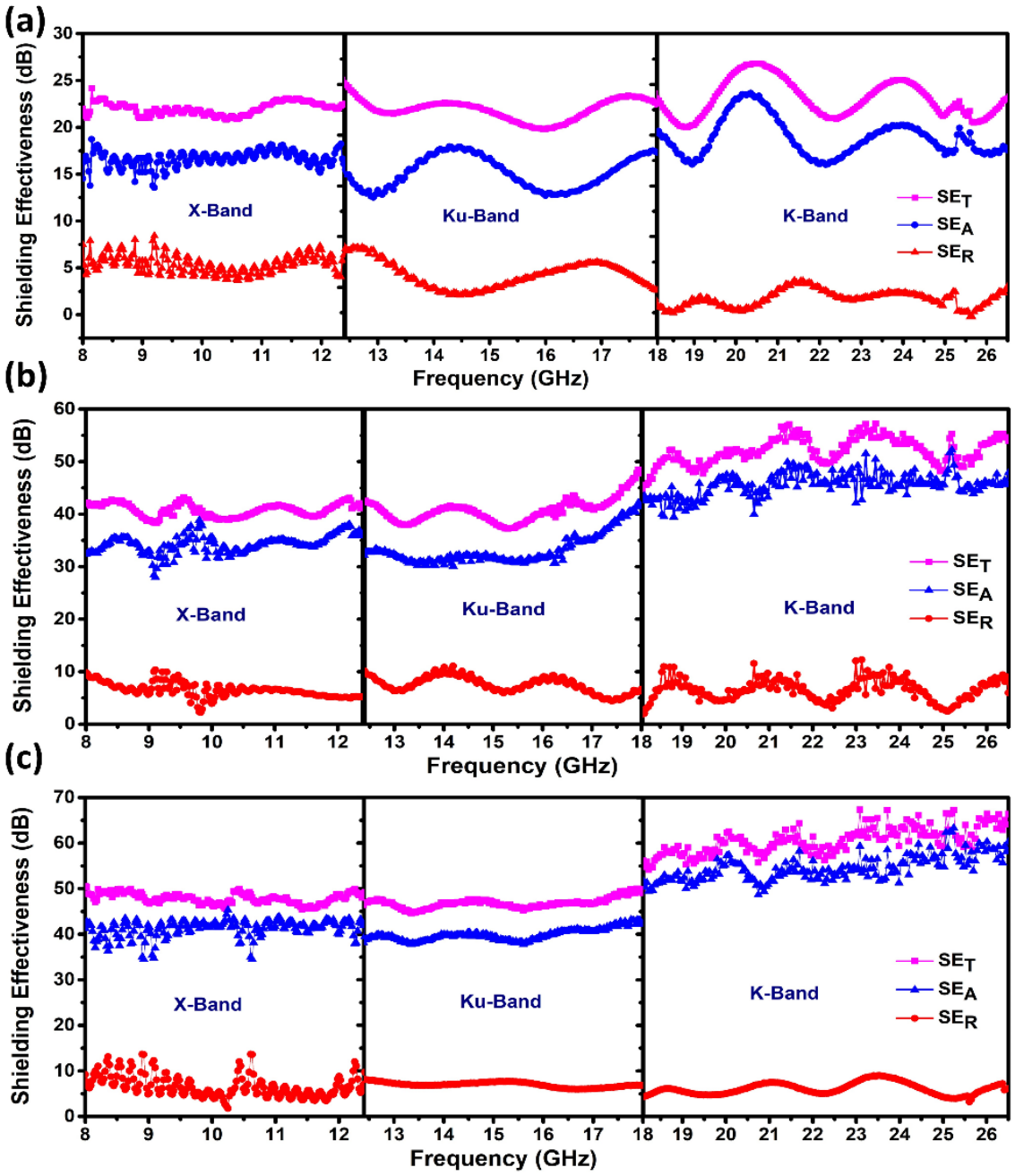

Figure 6.7: EMI SE of (a) CNF, (b) Nb_2O_5-CNF-33, and Nb_2O_5-CNF-50.

The pure PDMS exhibited almost zero EMI SE. The use of PDMS composites of CNF, Nb_2O_5-CNF-33, and Nb_2O_5-CNF-50 ensures ease of handling and accurate measurement of EMI SE by eliminating air gaps during testing. PDMS composites possess mechanical strength and flexibility required for EMI shielding applications. Pure CNF exhibited average and highest EMI SE of 22.7 dB and 26 dB which is above than the commercial requirement for EMI shielding application. After incorporation of Nb_2O_5 NPs (33.3 wt%) into CNF, the average and highest EMI SE were increased to 44.5 dB and 57.2 dB respectively. The average and highest

EMI SE was further improved to 51.6 dB and 67.3 dB with increase in the loading of Nb_2O_5 (50 wt%). For better understanding of the mechanism of EMI shielding, we further evaluated SE_A and SE_R. **Figure 6.7** suggests that the SE_A contributes more than 80 % to the SE_T for all the samples.

The high EMI SE values exhibited by these materials are due to 1-D nanostructure of N-doped CNF with formation of strong electrical conductive network between the Nb_2O_5 NPs and CNF. The doping of nitrogen into CNF enhanced the charge density and mobility of electrons, because nitrogen has more valence electrons than carbon. The N-doped CNF increases the charge density and forms dipoles between carbon and nitrogen which helps in absorption of incident EM waves (Shahzad, Kumar, et al., 2015; Shahzad, Yu, et al., 2015; W. D. Xue & Zhao, 2014). The incorporation and uniform distribution of Nb_2O_5 NPs into CNF enabled formation of strong electrical conductive network with CNF that improved the conductivity of the samples. The formation of strong electrical conductive network is an essential requirement for achieving high value of EMI SE. CNFs have conjugated SP^2 hybridized graphitic structure which allows $\pi \rightarrow \pi^*$ transitions and Nb_2O_5 NPs has band gap of 3.4 eV which helps to delocalize the electrons from SP^2 hybridized carbon to Nb_2O_5 and facilitates the formation of Nb_2O_5-carbon hetero-interface that enhances the interfacial polarization (Shanmugapriya et al., 2019; Su et al., 2023; Ximing Zhang et al., 2022a). A portion of the incident EM waves on the Nb_2O_5-CNF surface are reflected upon interaction with the mobile charge carriers present on the surface, while most of the EM waves are allowed to pass through the porous layers of the materials and get absorbed eventually.

Consequently, very few EM waves are transmitted resulting in high EMI SE value. The presence of Nb_2O_5 NPs in CNF form Nb_2O_5-carbon hetero-interfaces and facilitate dipole and interfacial polarization, leading to polarization losses. As the loading of Nb_2O_5 increases, the electrical conductivity increases and this enhances the total shielding effectiveness. The interaction of incident EM waves with the material, increases with increasing the electrical conductivity and SE_R should be increased. But, one-dimensional, fibrous, porous, and layer-by-layer structure of Nb_2O_5-CNF can cause impedance matching, which would further enhance the multiple internal reflections. The contribution of SE_A is more than 80 % of the total EMI SE for all the samples as illustrated in **Figure 6.8**. The synergetic effect of the microstructure of CNFs and the presence of Nb_2O_5 NPs enhances dipole polarization, interfacial polarization and multiple internal reflections and make the higher SE_A value compared to SE_R. (Su et al., 2023; Ximing Zhang et al., 2022a).

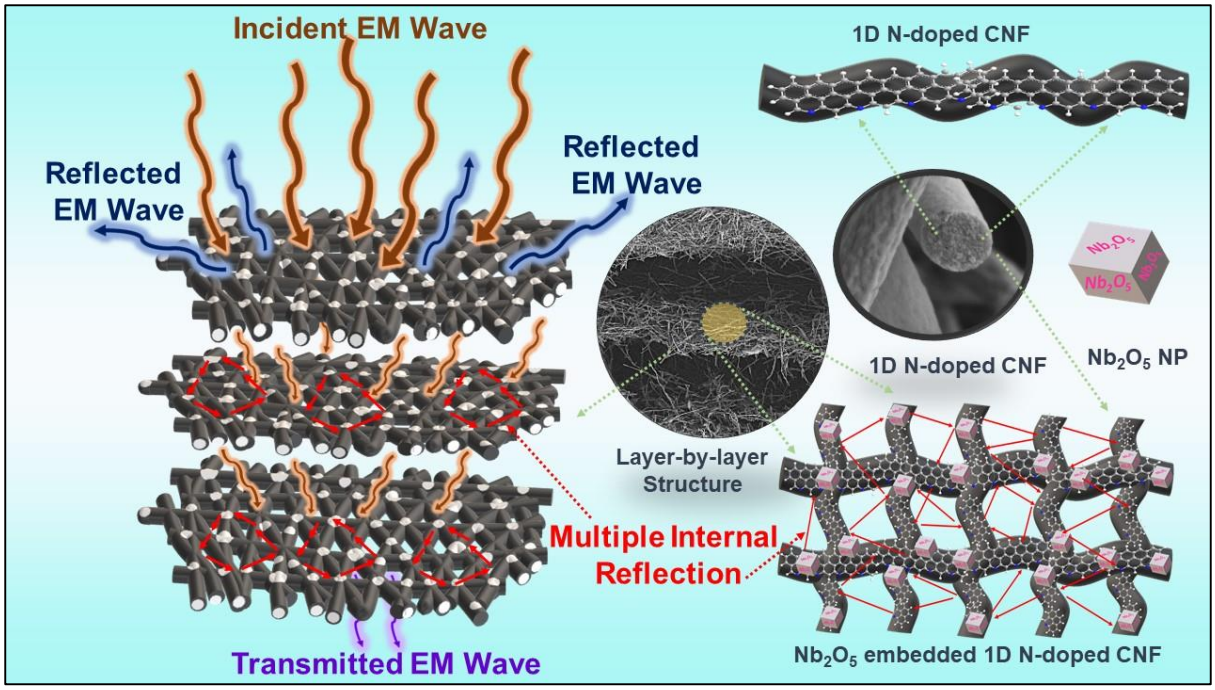

Figure 6.8: Schematic representation of EMI shielding mechanism of Nb_2O_5-CNF.

Normalized shielding effectiveness values help researchers, engineers, and industrial manufactures to choose and design EMI shielding materials based on industrial requirements for applications in flexible electronic devices, medical devices and aerospace. Density and thickness are crucial parameters for normalized SE for deciding the feasibility of practical applications of the shielding materials. The high value of SSE_t implies that Nb_2O_5-CNF can be explored for applications in aerospace and flexible electronic devices. Generally, fiber composites have high SSE_t due to their lightweight and low thickness. The Nb_2O_5-CNF-33 and Nb_2O_5-CNF-50 exhibited high SSE_t value of 3295.5 dB cm^2 g^{-1} and 2569.8 dB cm^2 g^{-1}, respectively. As the incorporation of Nb_2O_5 NPs increases the density of CNF increases and the resultant SSE_t value decreases. The PDMS composites of CNF, Nb_2O_5-CNF-33 and Nb_2O_5-CNF-50 exhibited almost similar SE_T value. The PDMS composites provided high flexibility and make it easy to handle for practical applications. The EMI SE value of PDMS composites of CNF, Nb_2O_5-CNF-33 and Nb_2O_5-CNF-50 did not change after twisting, folding, bending, and rolling. But, SSE_t values vary due to the variations in the thickness and density. **Table 6.1** summarizes the EMI shielding properties of Nb_2O_5-CNF and their PDMS composites.

Table 6.1: EMI shielding properties of Nb_2O_5-CNF and their PDMS composites.

Sample	**Thickness (mm)**	**Density ($g\ cm^{-3}$)**	**Conductivity ($S\ cm^{-1}$)**	**Frequency Range (GHz)**	**EMI SE (dB)**	**SSE ($dB\ cm^3\ g^{-1}$)**	**SSE_t**
CNF	0.08	0.202	0.257	8.2 -26.5	26	128.7	16089.1
Nb_2O_5-CNF-33	0.08	2.162	0.781	8.2 -26.5	57	26.36	3295.5
Nb_2O_5-CNF-50	0.08	3.259	1.470	8.2 -26.5	67	20.55	2569.8
CNF-PDMS composite	0.72	1.321	-	8.2 -26.5	26	19.68	27.33
Nb_2O_5-CNF-33 PDMS Composite	0.72	1.425	-	8.2 -26.5	57	40	55.55
Nb_2O_5-CNF-50 PDMS Composite	0.72	1.624	-	8.2 -26.5	67	41.25	57.30

6.4 Conclusion

This work describes a simple and facile method for fabrication of waterproof, lightweight, thin, and flexible EMI shielding materials for X-band, Ku-band, and K-band. Electrospinning and carbonization were used to obtain Nb_2O_5 NPs incorporated N-doped CNF. The EMI SE of the resulting Nb_2O_5-CNF improved from 57 dB to 67 dB as the loading of Nb_2O_5 NPs increased from 33 wt.% to 50 wt.%. The thickness of the material was 0.08 mm and more than 80 percent

of SE_T was contributed by SE_A. Nb_2O_5-CNF exhibited high SSE_t value of 3295 dB cm^2 g^{-1} with 33 wt% loading of Nb_2O_5 NPs in CNFs. The excellent EMI shielding performance of Nb_2O_5-CNF can be attributed to their high electrical conductivity due to the formation of conductive paths with CNF and Nb_2O_5, as well as interfacial and dipole polarization due to the presence of Nb_2O_5. The one-dimensional fibrous and porous structure of Nb_2O_5-CNF further enhances their ability to absorb EM waves through multiple internal reflection. The PDMS composite of Nb_2O_5-CNF is flexible and may find applications as efficient EMI shielding materials in flexible electronics.

CHAPTER: 7

$La_{0.85}Sr_{0.15}CoO_{3-\delta}$ Nanoparticles Incorporated CNF and PDMS composite for EMI Shielding

Overview

The work presented in the previous chapter dealt with semiconductor Nb_2O_5 NPs incorporated CNF with enhanced EMI shielding performance. This chapter presents the work on conducting perovskite type metal oxide NPs incorporated CNF for EMI shielding. Perovskite type metal oxide ($La_{0.85}Sr_{0.15}CoO_{3-\delta}$ (LSCO)) NPs was synthesized via sol-gel method followed by calcination at 900 ^oC. The synthesized LSCO NPs were incorporated into CNF (LSCO-CNFs) to investigate the EMI shielding properties in X, Ku, and K-band. The LSCO-CNFs shows excellent EMI shielding properties because of their high electrical conductivity leading to the formation of conductive paths with CNFs, interfacial polarization as well as dipole polarization due to the multicomponent heterogeneous interfaces and the dielectric loss due to the defects produced by Sr doping in $LaCoO_3$. The LSCO-CNFs-PDMS composites are ideal for fabricating lightweight, thin, waterproof, flexible and high-performance EMI shielding materials.

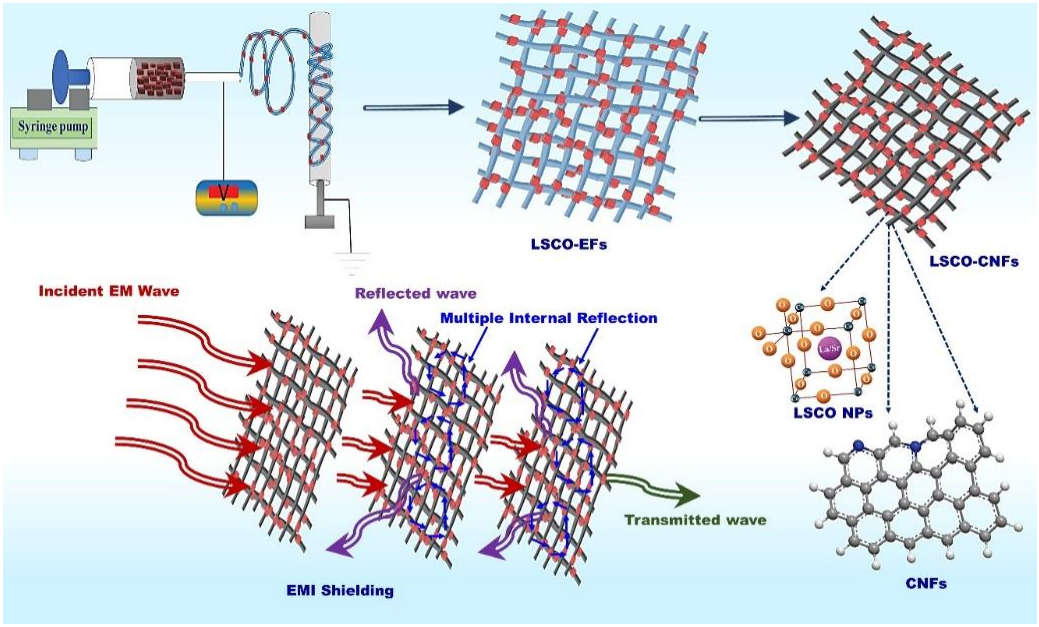

7.1 Introduction

The previous chapter concerned with semiconductor Nb_2O_5 NPs incorporated CNF for enhanced the EMI shielding properties. Nb_2O_5 acts as electron promotor and improves the formation of electrical conductive network and helps to enhance the $\pi \rightarrow \pi^*$ transitions in Nb_2O_5-CNF. The incorporation of Nb_2O_5 NPs into CNF forms hetero-interfaces which cause interfacial polarization. Incorporation of a conducting perovskite namely, $La_{0.85}Sr_{0.15}CoO_{3-\delta}$ (LSCO) NPs with several elements (La, Sr, Co, O, N, and C) into CNF may create multi-hetero interfaces and may increase interfacial polarisation, resulting in increased polarisation loss and enhanced EMI shielding ability.

Metal oxides, with perovskite structure have several characteristics, such as high ionic, electronic, or mixed conductivity and chemical and structural stability at high temperatures. Because of these properties, $LaCoO_3$ with perovskite structure is used as electrode for fuel cells (Ashok et al., 2018; Seo et al., 2015; Shingange et al., 2020). Perovskite-type compounds $LaCoO_3$ and $SrCoO_3$ can form solid solutions in every ratio to each other. The notation (La, Sr) CoO_3, or $La_{(1-x)}$ $Sr_xCoO_{3-\delta}$ (LSCO) means that some lanthanum (La^{3+}) ions are substituted by (Sr^{2+}) strontium ions at A site. Substitution of strontium ions for lanthanum ions in the system alters its electrical conductivity (Bisht et al., 2021; Mefford et al., 2016; Seo et al., 2015; Singhal et al., 2018; Stoerzinger et al., 2018; Suen et al., 2017; X. Wang et al., 2018; Zhen et al., 2017). LSCO NPs possess dielectric properties that can aid the EMI shielding properties (Deepa et al., 2014). Dijith et al. investigated EMI shielding properties of sintered $La_{0.5}Sr_{0.5}CoO_{3-\delta}$ (LSCO) sheets in X and Ku-band. The material exhibited EMI SE value of 35-42 dB with a thickness of 2 mm. However, the LSCO epoxy composite showed EMI SE value of 10 dB. In terms of practical applications, this number is relatively low (Dijith et al., 2017).

CNF incorporated with LSCO NPs is a potential candidate for a light weight, flexible and porous EMI shielding material with absorption as the dominant mechanism for shielding. One of the effective ways to incorporate metal oxide NPs into 1-D CNF is electrospinning. Electrospinning is a fiber-spinning method that employs electrostatic forces to make long and continuous fibers of diameters in nm to μm range (S. Dong et al., 2022; M. Kim et al., 2021; Mohan et al., 2021; Song et al., 2014; Liying Zhang et al., 2013; Zheng, Wang, et al., 2023). Nanofibers from polymer solutions or melts can be conveniently produced using this technique. Metal and metal oxide NPs can be incorporated into the nanofibers through electrospinning.

Due to their combined electrical conductivity, magnetic characteristics, and in particular, 1-D Nano-fibrous composites can be used as effective EMI shields (S. Dong et al., 2022). However, only a few studies have reported the use of such materials as EMI shields (Bayat et al., 2014). (Im et al., 2009) achieved maximum overall EMI SE of 50 dB for fluorinated CB/CNF composite with 0.5 mm thick samples in the frequency range of 800 MHz- 4 GHz. It is reported that a maximum EMI SE of 31 dB can be attained for 0.5 mm thick ZrO_2/CNF composite in the frequency range of 800 MHz - 8.5 GHz with 88 percent absorption. The EMI shielding property is presumed to be due to the high permittivity of graphite-structured carbon and tetragonal-structured ZrO_2 achieved through heat treatment (Im et al., 2011). Zhang et al. found a minimum reflection loss of 45 dB at 8 GHz for a 5 mm thick Fe_3O_4/CNF composite. Instead of directly dispersing Fe_3O_4 NPs into the PAN/DMF solution, they synthesized the composite using Fe_3O_4 precursor (T. Zhang et al., 2013).

The goal of the current work is to fabricate lightweight 1-D CNFs structure with significant absorption-based EMI shielding property. The multi-layer, porous nanostructure with low loading of conductive filler is expected to exhibit absorption-dominated EMI shielding. The work reports a facile and straightforward method to fabricate lightweight and flexible LSCO NPs incorporated N-doped CNF and its PDMS composite with excellent EMI shielding property in the wide frequency range of 8.2- 26.5 GHz. The N-doped CNFs were fabricated via electrospinning followed by heat treatment to obtain LSCO NPs incorporated N-doped CNF (LSCO-CNFs). PDMS composites were prepared by hand lay-up methods. The LSCO-CNFs exhibited high EMI SE of 43 dB with 80% absorption mechanism with thickness of 0.08 mm. The dominance of absorption mechanism is because of the electrically conductive network, porous morphology, and layer-by-layer structure of LSCO-CNFs.

7.2 Experimental Section

7.2.1 Materials

The specifications of PAN, $La(NO_3)_3.6H_2O$, $Co(NO_3)_2.6H_2O$, and $Sr(NO_3)_2$, and DMF are mentioned in chapter 2 (refer to section 2.1)

7.2.2 Synthesis of $La_{0.85}Sr_{0.15}CoO_{3-\delta}$ NPs (LSCO NPs)

Synthesis of $La_{0.85}Sr_{0.15}CoO_{3-\delta}$ NPs (LSCO NPs) was carried out according to a reported procedure (Somalu, 2016; J. Wang et al., 2008). Metal nitrates, namely, $La(NO_3)_3 \cdot 6H_2O$ (2.309 mmol), $Sr(NO_3)_2$ (0.4 mmol), and $Co(NO_3)_2 \cdot 6H_2O$ (2.716 mmol) were dissolved in 5

mL of deionized water in a beaker to obtain a pink colored solution. After the metal nitrates had completely dissolved, 2 mL of ethylene glycol and 8.148 mmol of citric acid were added to the solution to form citrate gel through the Pechini process (Galceran et al., 2007; Jun Lin et al., 2007). The above solution was heated to 70°C for 8 h with magnetic stirring for solvent evaporation, and then dried in an oven at 150°C for 12 h. Following drying, the sample was pre-calcined at 450°C for 2 h and calcined at 900°C for 4 h in air at a heating rate of 1°C min^{-1} to obtain black-coloured perovskite oxide.

7.2.3 Preparation of LSCO NPs incorporated N-doped CNF (LSCO-CNFs)

Electrospinning solution was prepared by adding LSCO NPs (10 and 25 wt %) in 10 mL of 10 wt% of PAN solution in DMF with constant stirring at 60 ^{o}C for 10 h. The uniformly dispersed solution was taken in a syringe (10 mL) for electrospinning. A voltage (12 kV) was applied on the spinneret and nanofibers were deposited on aluminium foil wrapped on the rotating drum collector which was placed 13 cm away from the tip of the spinneret. The feed rate of the polymer solution was 1 mL h^{-1}. The obtained electrospun fiber was dried at 80 ^{o}C in oven for 4 h to obtain 10 and 25 wt% LSCO NPs incorporated electrospun nanofiber (LSCO-EFs) mat. The electrospun nanofiber mat was stabilized in an air atmosphere at 250 ^{o}C for 12 h and then carbonized for 2 h at 900 ^{o}C with 2 ^{o}C min^{-1} ramping rate in an argon atmosphere. The terms CNFs, LSCO-CNFs-10, and LSCO-CNFs-25 refer to the obtained carbonized PAN fiber and carbonized PAN fiber with loadings of 10 and 25 wt% of LSCO NPs, respectively. The carbonized LSCO NPs incorporated CNF (LSCO-CNFs) were cut according to the size of the waveguide adaptors for EMI shielding measurements.

7.2.4 Fabrication of flexible PDMS composites of LSCO-CNFs

The PDMS composite of coated samples were prepared in the similar methodology as mentioned in chapter 2. The schematic illustration of fabrication of LSCO-CNFs and the composite are shown in **Figure 7.1**.

7.2.5 Characterization

The characterization methods are described in chapter 2. The doping composition of the LSCO-CNFs was estimated using Inductively coupled plasma mass spectrometry (ICP-MS) ((ICP-MS, 7500ce, Agilent Technologies).

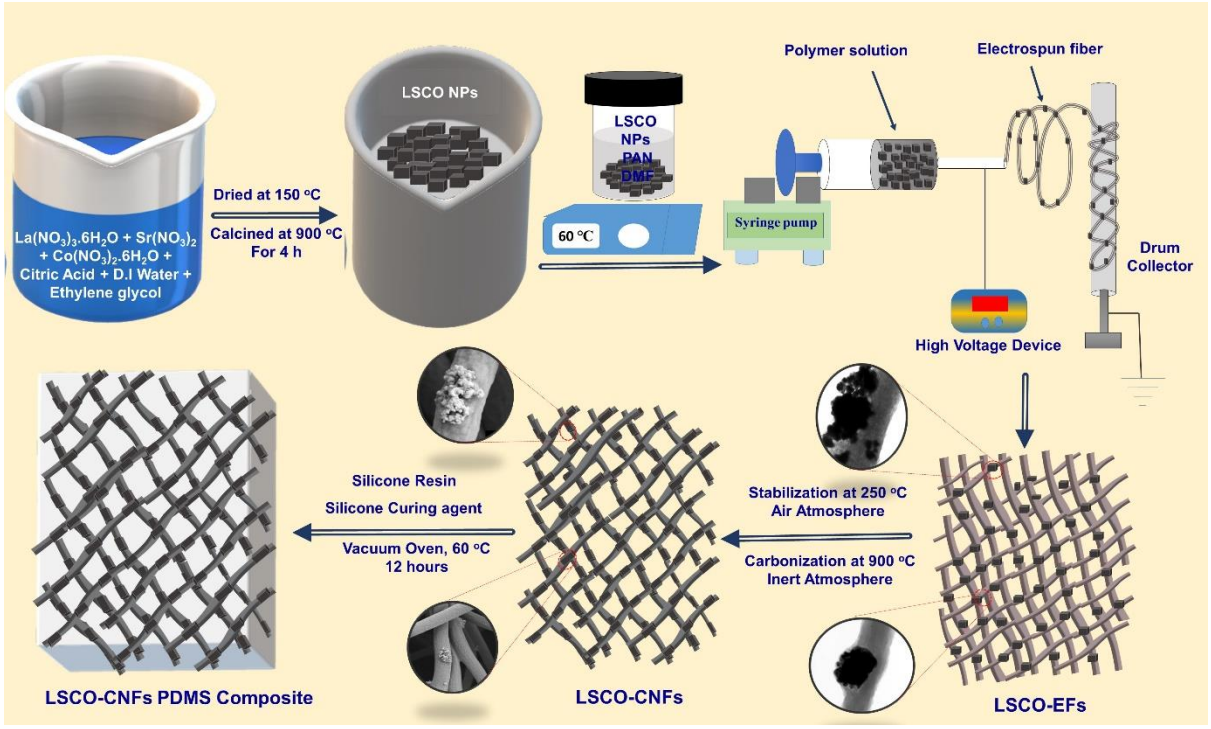

Figure 7.1: Illustration of fabrication of LSCO-CNFs PDMS composite.

7.3 Results and discussion

7.3.1 TEM image

TEM images of LSCO NPs, PAN electrospun fiber and LSCO NPs incorporated PAN electrospun fiber are shown in **Figure 7.2**. From **Figure 7.2(a-b)** LSCO NPs appear to be polydispersed and crystalline with an average particle size of 67.7 ± 12 nm. LSCO NPs are agglomerated and tend to stack on to each other. **Figure 7.2(c)** shows TEM image of electrospun PAN nanofiber and **Figures 7.2(d-f)** show the TEM images of LSCO NPs incorporated electrospun PAN nanofibers. The images indicate that the fiber is continuous and there is no bead formation. **Figures 7.2(d-f)** demonstrate that agglomerated LSCO NPs are embedded as well as distributed along the fiber. The mean diameter of electrospun PAN nanofiber and LSCO NPs incorporated electrospun PAN nanofiber are 406 nm and 557 nm, respectively based on **Figures 7.2(d-f).**

7.3.2 SEM image

Figure 7.3 shows the SEM images of **(a-b)** CNFs and **(c-f)** LSCO-CNFs and demonstrates the continuous nanofiber formation. The average fiber diameters are 437 ± 42 nm and 643 ± 58 nm, respectively, for CNFs and LSCO-CNFs. Both SEM and TEM images show that the average fiber diameter tends to increase with the addition of LSCO NPs.

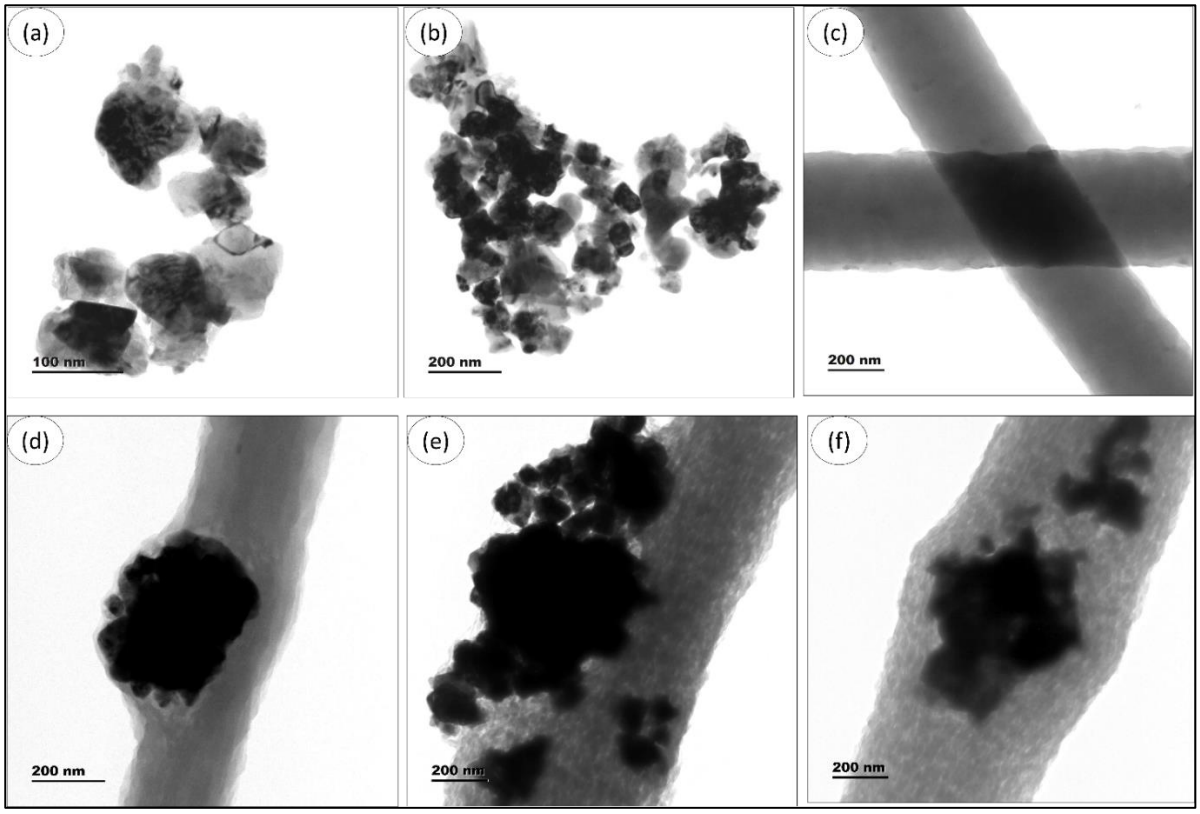

Figure 7.2: TEM images of (a-b) LSCO NPs, (c) electrospun PAN fiber, (d-f) electrospun PAN fiber with 25 wt% loading of LSCO NPs.

The TEM images of LSCO-CNFs show that the LSCO NPs are distributed along the fiber, with sporadic agglomeration of particles. The agglomeration of the particles is evident from the SEM images also. The reason for the observed agglomeration may be the difference in the charge accumulation behaviour of PAN and LSCO NPs during electrospinning.

7.3.3 Raman spectroscopy

Raman spectroscopy is the best method to determine the microstructure of carbonaceous materials. **Figure 7.4(a)** shows the Raman spectra of CNFs and LSCO-CNFs. Both the samples show peaks at 1349 cm^{-1} and 1593 cm^{-1} corresponding to D-band and G-band, respectively similar to nanostructured carbonaceous materials such as graphene and CNTs (Aadil, Zulfiqar, Shahid, Agboola, Al-Khalli, et al., 2021; Aadil, Zulfiqar, Shahid, Agboola, Haider, et al., 2021; Alazmi, 2022; K. Chaudhary et al., 2022). The D-band is associated with disordered turbostratic structures, whereas G-band is attributed to the graphitic structures. The ratio of intensity of D-band and G-band (I_D/I_G) of CNFs and LSCO-CNFs is 0.90 and indicates the turbostratic carbon structure of both the samples.

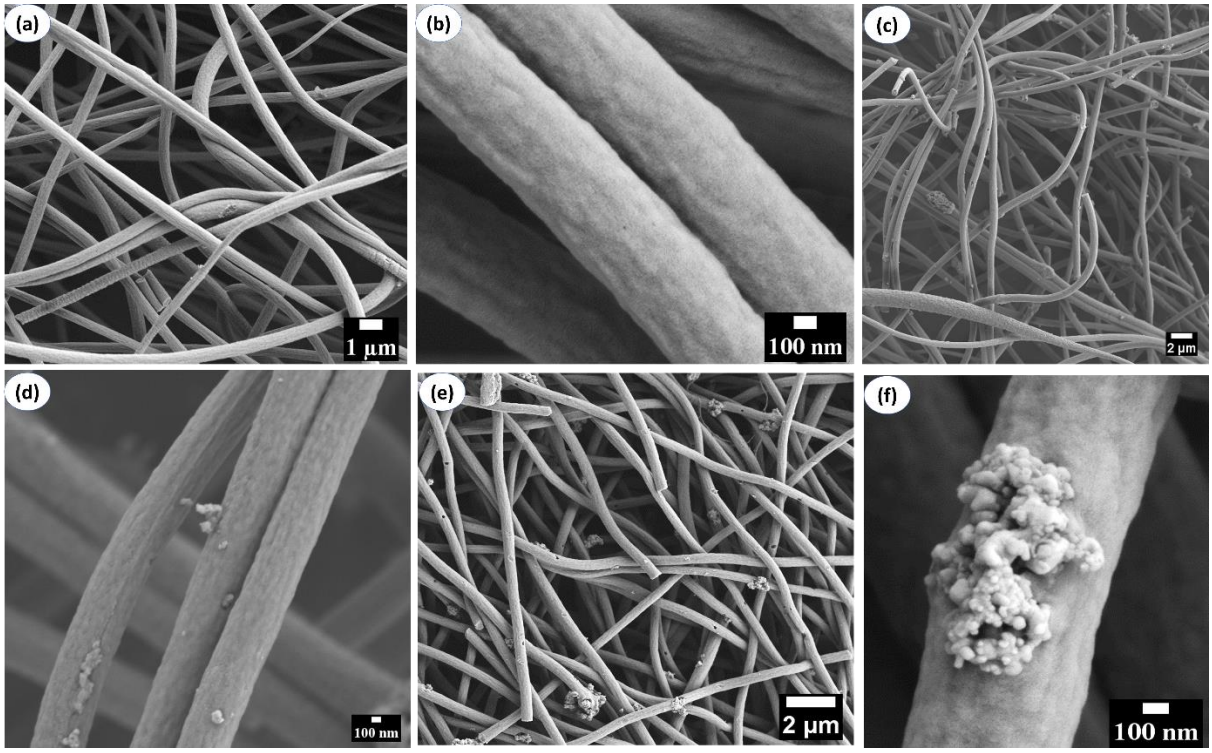

Figure 7.3: SEM images of (a-b) CNFs, (c-d) LSCO-CNFs-10, and (e-f) LSCO-CNFs-25.

7.3.4 XRD patterns

The XRD patterns of CNFs, LSCO NPs, and LSCO-CNFs are displayed in **Figure 7.4 (b).** The broad peak centred at around 25.4^{o} in the XRD pattern of CNFs belongs to the turbostratic carbon structure (JCPDS 41-1487). The broad peak at 25.4^{o} is relatively low in intensity and indicates that carbonized PAN possess turbostractic carbon structure and low crystallinity (Q. Y. Chen et al., 2014). The XRD pattern of LSCO NPs shows strong peaks of a perovskite phase which are similar to that reported in literature (Bisht et al., 2018; Bisht & Sharma, 2018; Nishio et al., 2015). The XRD pattern of LSCO-CNFs shows sharp peaks at 20.4^{o}, 25.2^{o}, 26.3^{o}, 28.2^{o}, 30.4^{o}, 35.1^{o}, 36.9^{o},44.3^{o}, 47.2 ^{o}, 48.6 ^{o}, and 51.5 ^{o}. The strongest peak at 25.2^{o} belongs to pure orthorhombic strontianite (JCPDS : 05-418) (Long Chen et al., 2013; P. Lu et al., 2018). The pattern indicates the presence of LSCO NPs in CNFs and also the formation of $SrCO_3$ on the surface of CNFs. During carbonization, in inert atmosphere, formation of $SrCO_3$ is favoured by the high reactivity of Sr with CO_2 and this may be embedded in CNFs or may be present at the surface. The formation of $SrCO_3$ was further confirmed by XPS data.

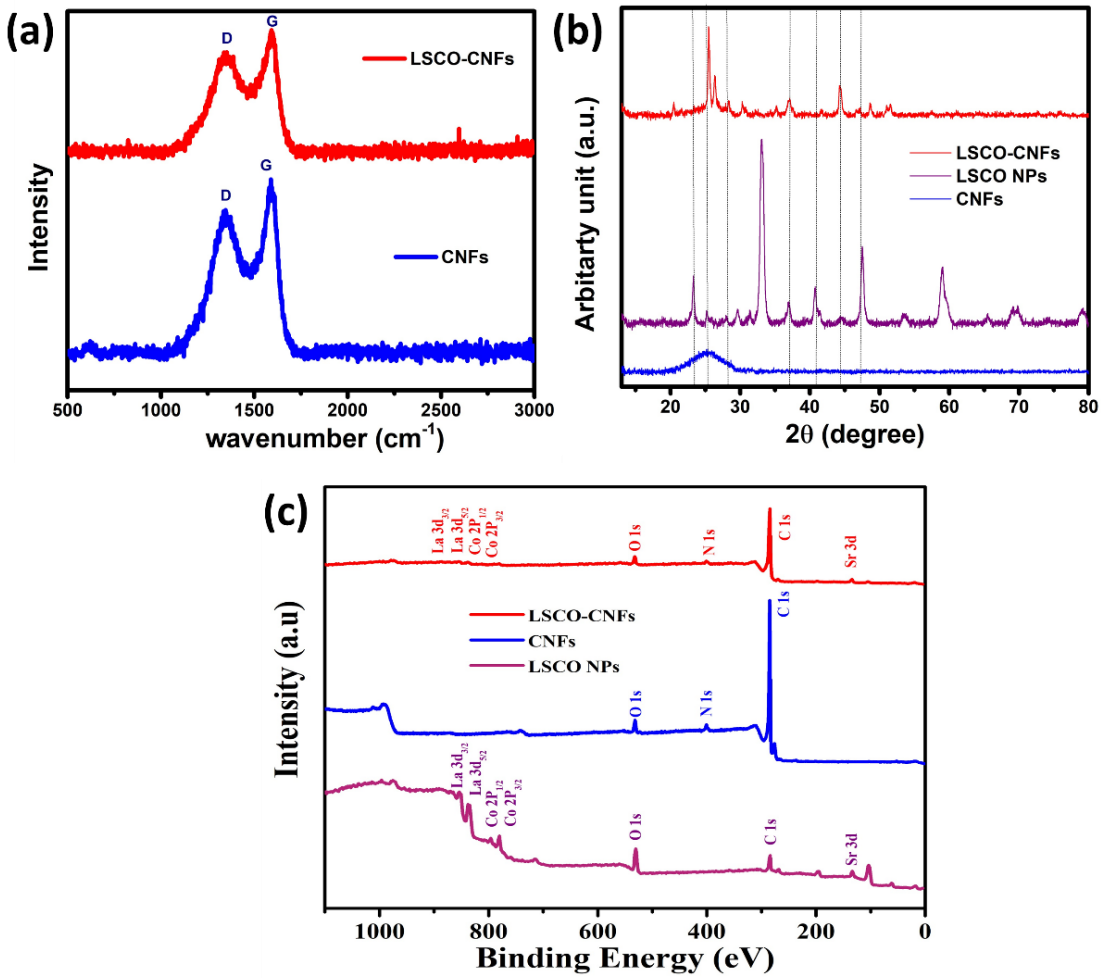

Figure 7.4: (a) Raman Spectra of CNFs and LSCO-CNFs. (b) XRD patterns of LSCO NPs, CNFs, and LSCO-CNFs. (c) XPS survey scans of LSCO NPs, CNFs, and LSCO-CNFs.

7.3.5 XPS analysis

XPS was used to examine the chemical composition and elemental analysis of CNFs, LSCO NPs and LSCO-CNFs. The survey spectrum of CNFs, LSCO NPs, and LSCO-CNFs are shown in **Figure 7.4(c)**. The survey scan of CNFs shows peaks at 285.0 eV, 401.7 eV, and 531.7 eV corresponding to C(1s), N(1s), and O(1s) species respectively. These peaks confirm the formation of N-doped carbon nanofibers. The survey scan of LSCO NPs shows peaks at 134.9 eV, 778.6 eV, 795.9 eV, 833.4 eV, 854.9 eV, 285.0 eV, and 531.7 eV corresponding to Sr (3d), Co ($2p_{3/2}$), Co ($2p_{1/2}$), La ($3d_{5/2}$), La ($3d_{3/2}$), C (1s) and O (1s) species respectively, and confirms the formation of LSCO NPs (X. Wang et al., 2018). Citrate gel method was used to prepare LSCO NPs. The C 1s peak seen at 285.0 eV in the survey scan of LSCO NPs is due to the citrate residues. **Figure 7.5** displays the high-resolution elemental scan of LSCO NPs. The

binding energy (BE) peaks of La 3d in **Figure 7.5(a)** centred at 851.2 and 834.1 eV can be assigned to La $3d_{5/2}$ and $3d_{3/2}$, respectively.

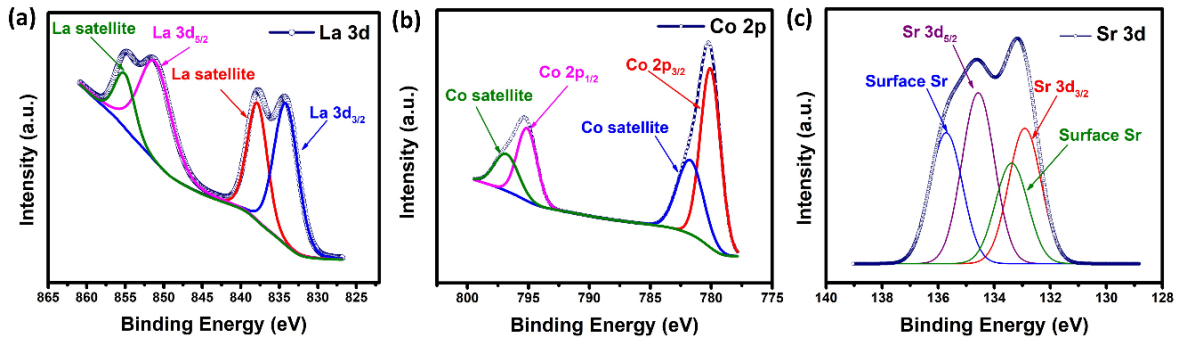

Figure 7.5: High-resolution XPS elemental scan of elements present in LSCO-NPs, (a)La 3d, (b) Co 2p, and (c) Sr 3d.

Two satellites peaks at 855.29 and 838.0 eV observed for La 3d are due to electron transition from the O 2p valence band to La 4f orbitals (Feng et al., 2022). The high elemental scan of Co 2p, which contains Co $2p_{1/2}$ peaks located at 795.0 and 780.07 eV is shown in **Figure 7.5(b)**.

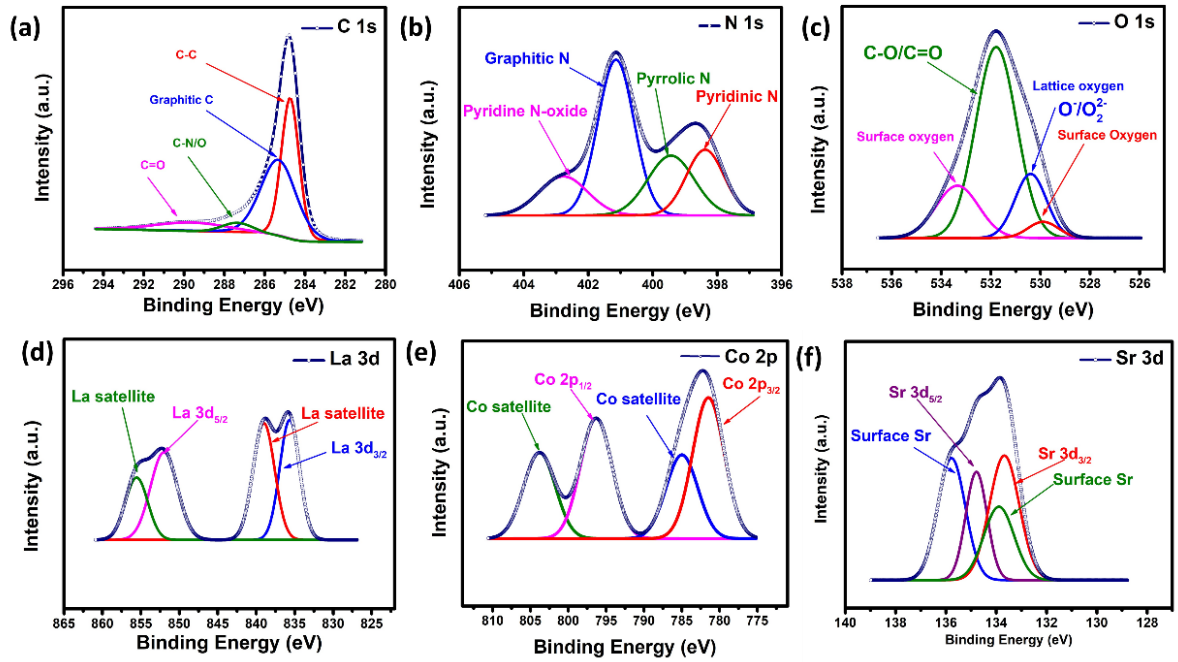

Figure 7.6: High resolution XPS elemental scan of elements present in LSCO-CNFs (a) C 1s, (b) N 1s, (c) O 1s, (d)La 3d, (e) Co 2p, and (f) Sr 3d.

The high elemental scan of Sr 3d is shown in **Figure 7.5(c)** and includes four peaks at 134.5, 132.9, 135.7, and 133.9 eV. The first two peaks are assigned to Sr $3d_{5/2}$, $3d_{3/2}$, and other two peaks at 135.7, and 133.9 belong to surface Sr (Baek et al., 2020).

After incorporation of LSCO NPs into CNFs, the combined peaks of CNFs and LSCO NPs, are seen in the spectrum as shown in **Figure 7.4(c).**

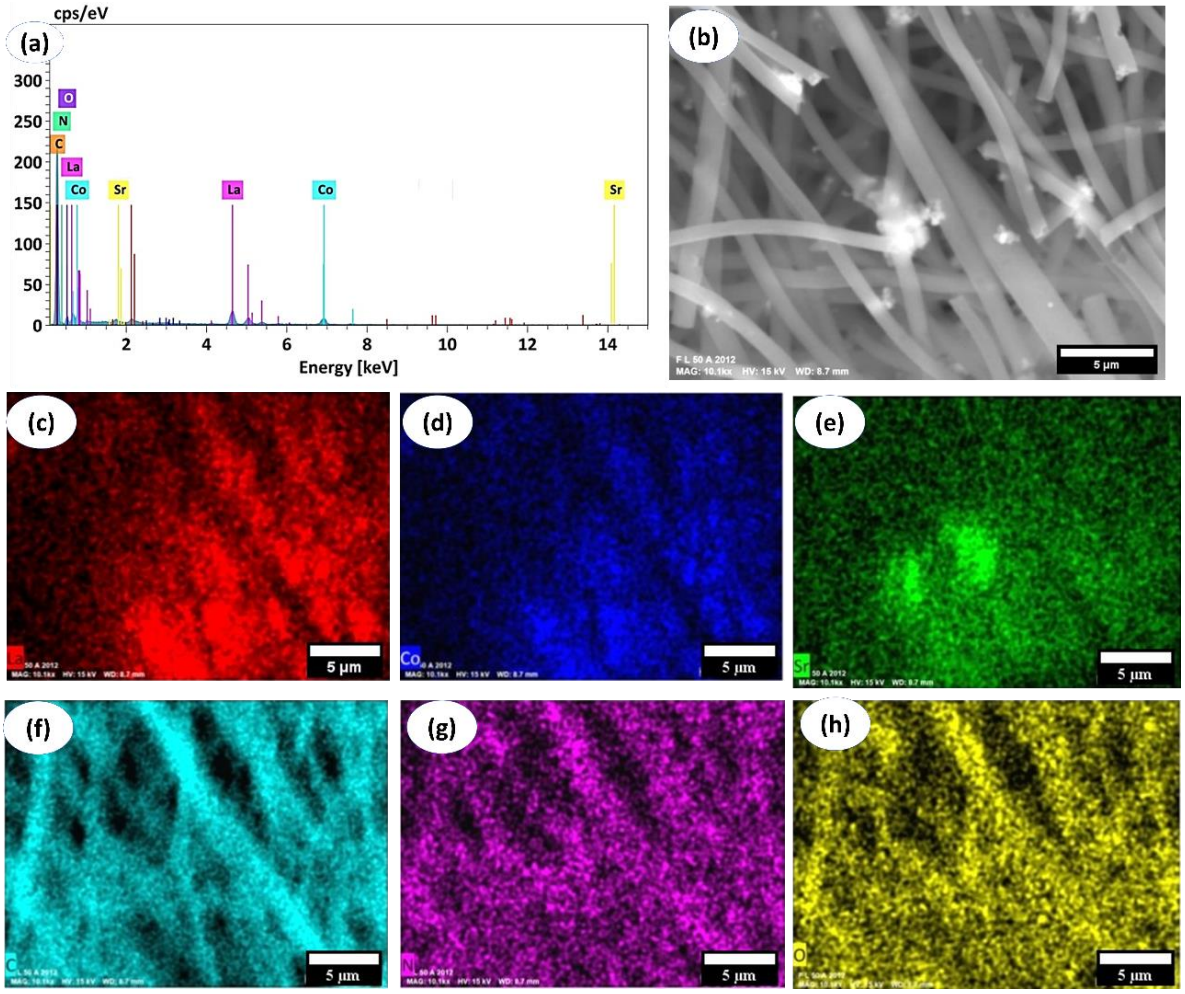

Figure 7.7: (a) EDS spectra of LSCO-CNFs; (b-h) elemental mapping analysis of LSCO-CNFs; (b) SEM image of spot used for the elemental mapping, (c) lanthanum, (d) cobalt, (e) strontium, (f) carbon, (g) nitrogen, and (h) oxygen.

Even though the loading of Sr is only 15 % in $LaCoO_3$, very strong peaks of Sr are seen in the survey scan of LSCO-CNFs as well as in the elemental scan of Sr (3d). This is due to the formation of $SrCO_3$ on the surface of CNFs during carbonization in inert atmosphere. High-resolution elemental scans for the elements present in LSCO-CNFs, such as C(1s), N (1s), O (1s), Sr(3d), Co (2p), and La (3d) are examined as shown in **Figure 7.6 (a-f**) respectively. It can be seen that La (3d), Co (2p) and Sr (3d) peaks in LSCO-CNFs are identical to the peaks in high- resolution spectra of LSCO NPs **(figure 7.5)**. The doping concentration of LSCO NPs was determined by inductive coupled plasma mass spectroscopy (ICP-MS) which confirmed

15% doping of Sr. The presence of all these elements are confirmed by XPS data and EDS data also.

7.3.6 EDS analysis and elemental mapping

The composition of LSCO-CNFs is further validated by energy dispersive X-ray spectroscopy (EDS) and elemental mapping analysis, as illustrated in **Figure 7.7**. The EDS spectra show peaks of carbon, nitrogen, oxygen, lanthanum, cobalt, and strontium present in LSCO-CNFs (**figure 7.7(a)**). The presence and distribution of La, Co, and Sr along the fiber is evident in **Figure 7.7 (c-e).**

7.3.7 Contact angle measurement

According to **Figure 7.8(a-c),** the contact angles of CNFs, LSCO-CNFs, and LSCO-CNFs-PDMS composites are around 119^{o}. It implies that these materials are hydrophobic and are suitable for waterproof EMI shielding applications. CNFs and LSCO-CNFs have hydrophobic surface due to its sp^2-hybridized carbon structure, which reduces the surface energy and makes it difficult for water molecules to adhere to the surface as shown in **figure 7.8(a-b).** However, the hydrophobicity of LSCO-CNFs can be further improved by making a PDMS composite as shown in **Figure 7.8(c)**. PDMS is inherently hydrophobic due to its chemical structure, which is distinguished by the presence of hydrophobic methyl groups (Ariati et al., 2021; Ji Park et al., 2014) .

7.3.8 Mechanical property

LSCO-CNFs and CNFs are extremely lightweight and have minimal mechanical strength. During carbonization, electrospun fibers, undergoes a sequence of chemical and physical transformations that increase the stiffness, heat resistance, and chemical inertness. But carbonization increases brittleness and this restricts their applications. Hence, PDMS composites of CNFs and LSCO-CNFs were fabricated to enhance their mechanical performance and flexibility. The PDMS composite of LSCO-CNFs and CNFs exhibited high flexibility and ability to withstand folding, bending, twisting, and rolling as shown in **Figure 7.8(d–h).** The PDMS composite returns to its original flat surface after being folded, bent, twisted, and rolled without undergoing any damage.

DMA was used to examine the temperature dependent mechanical properties of PDMS, CNFs-PDMS composite, LSCO-CNFs-10 PDMS composite, and LSCO-CNFs-25 PDMS composite.

Figure 7.8(i) shows the plots of storage modulus (E') versus temperature (T) for PDMS, CNFs-PDMS composite, LSCO-CNFs-10 PDMS composite, and LSCO-CNFs-25 PDMS composite.

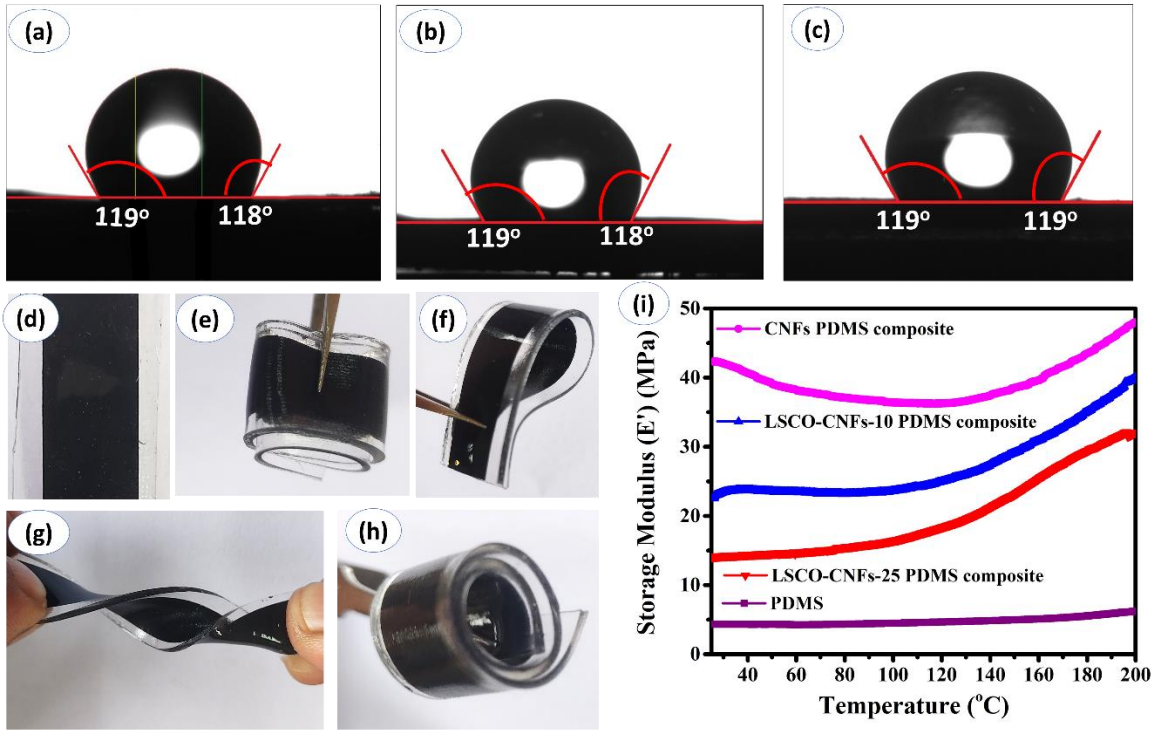

Figure 7.8: Contact angle of (a) CNFs, (b) LSCO-CNFs, and (c) LSCO-CNFs PDMS composite. Photograph of (d) LSCO-CNFs PDMS composites upon(e) folding, (f) bending, (g) twisting, and (h) rolling. (i) Plot of storage modulus Vs temperature.

Here, the change in E' of the materials with temperature is measured, which relates to the elasticity or stiffness of the composites and is the function of energy stored during one period under load. The storage modulus of the pristine PDMS slightly rises with temperature as a result of slight possibilities of stiffening that comes from further curing at elevated temperature. The E' of pristine PDMS is low and increases with adding of CNFs and LSCO-CNFs. The E' is found to increase with temperature as shown in **Figure 7.8(i)**. The E' of PDMS, CNFs-PDMS composite, LSCO-CNFs-10 PDMS composite, and LSCO-CNFs-25 PDMS composite are 4.4, 42.6, 22.3, and 13.9 MPa at 25 °C, and 5.9, 48.0, 40.2 and 31.8 MPa at 200°C respectively. Due to post-curing effects and faster re-alignment and re-orientation of PDMS chains brought on by the increased mobility of the polymer chains at higher temperatures, the stiffness might have increased at the elevated temperature. The addition of CNFs improved the PDMS's cured chemical cross-linking network and the formation of the interface/interphase was realised as a result of their contact with polymer chains, which is responsible for the dynamic stiffness effect (Linlin Cao et al., 2016b). The storage modulus of the CNF-PDMS

composite is higher in comparison to PDMS, however, the storage modulus decreased after incorporation of LSCO NPs into CNFs due to the decreased aspect ratio of LSCO-CNFs. With increase in the loading of LSCO NPs into CNFs, the aspect ratio of CNFs decreased further and consequently, their storage modulus also decreased. Thus PDMS composites have enhanced mechanical performance and flexibility in comparison to CNFs and LSCO-CNFs.

7.3.9 Electrical conductivity measurement

Figure 7.9(a) shows the voltage-current graphs of LSCO-CNFs and CNFs. The linearity of both the curves shows that the resistance does not vary with current variation up to 3 mA. The resistance of LSCO-CNFs is lower than the CNFs as shown in **Figure 7.9(a)**. The electrical conductivity (σ) was measured using the **Equations 18, 19,** and **20**. The electrical conductivity of CNFs, LSCO-CNFs-10, and LSCO-CNFs-25 are 1.07, 1.40, and 2.01 S cm^{-1} respectively. Both LSCO-CNFs-10 and LSCO-CNFs-25 are appropriate for use in EMI shielding because of their high electrical conductivity.

7.3.10 EMI SE

Metals are often employed as shielding materials, despite their susceptibility to oxidation and corrosion. As a result, metal oxides (conducting or magnetic) may be interesting choices due to oxidation resistance and endurance at high temperatures. In spite of the fact that perovskite metal oxides are the best fillers for high conductivity oxide, there have been only few prominent attempts to study their EMI shielding properties. In this present work, LSCO NPs are used as conducting fillers incorporated into N-doped CNFs (LSCO-CNFs) using electrospinning techniques. LSCO NPs possess high electrical conductivity for their cubic phase (Mefford et al., 2016). The electrospinning technique is an effective way to disperse LSCO NPs along the fibers. After carbonization of the electrospun fiber, LSCO NPs easily formed conductive path with N-doped CNFs. The formation of conductive path enhances the electrical conductivity, and EMI shielding performances. The EMI shielding properties of LSCO-CNFs are shown in **Figure 7.9(b-d)**.

Figure 7.9(b-d) shows EMI shielding performance of PDMS composites of CNFs, LSCO-CNFs-10, and LSCO-CNFs-25. The pristine PDMS sheets show zero EMI SE in X, Ku, and K-band. The active EMI shielding materials are CNFs and LSCO-CNFs. The PDMS composites allow easy handling and accurate measurement of EMI SE by avoiding air gap

during the measurement. The thickness of CNFs, LSCO-CNFs, and LSCO-CNFs- PDMS composite are 0.06 mm, 0.06 mm, and 0.62 mm, respectively.

The high electrical conductivity of CNFs is an important factor leading to high EMI SE. When perovskite LSCO NPs (25 wt%) are loaded into CNFs, the electrical conductivity rises from 1.07 S cm^{-1} to 2.01 S cm^{-1}. The EMI SE has a remarkable connection with the layer-by-layer structure and porosity of CNFs, in addition to the electrical conductivity. CNFs alone can meet the industry needs of EMI SE (20 dB) with 99 percent EM wave attenuation. The highest and average EMI SE of CNFs were 21.74 dB and 18.26 dB, respectively. With 10 wt% loading of LSCO NPs into CNFs (LSCO-CNFs-10), the highest and average EMI SE values were dramatically increased, and their values were 34.89 dB and 30.50 dB, respectively. When loading of LSCO NPs was 25 wt% the highest and average EMI SE of LSCO-CNFs-25 were 45.65dB and 37.32 dB respectively. The PDMS composite of CNFs and LSCO-CNFs improved the mechanical properties while EMI shielding effectiveness was not affected. EMI SE performance of CNFs and LSCO-CNFs are elucidated in **Figure 7.9(b-d)**. It can be seen that absorption loss contributes higher than reflection loss to the EMI SE for all the samples. SE_A is the dominant factor, that contributes more than 85 % to the total EMI SE for all the samples. The high EMI SE with higher SE_A value compared to SE_R may be attributed to the following factors. The incorporation of LSCO NPs with CNFs results in the formation of electrically conductive network, extending the transmission path of the incident EM waves which promotes multiple scattering, further enhancing the conduction loss.

The presence of multicomponent heterogeneous interfaces causes interfacial polarization as well as dipole polarization. Synergistic effect of the dipole polarization caused by the metal oxides (LSCO NPs) and the defects produced by Sr doping in $LaCoO_3$, increases the dielectric loss in LSCO-CNFs (C. Wang et al., 2023a, 2023b; Shuo Zhang & Jia, 1998). Porosity and fibrous layer-by-layer structure of LSCO-CNFs can cause impedance matching which further increases the multiple internal scattering of EM waves. Thus, the formation of conductive network and synergetic effects of various EM loss mechanisms lead to the excellent EM absorption properties of LSCO-CNFs. The proposed EMI shielding mechanism of LSCO-CNFs is illustrated in **Figure 7.9(e).** The power coefficient (R, T, and A) are calculated using the **Equations (6), (7), and (8)**. CNFs, LSCO-CNFs-10, and LSCO-CNFs-25 have average R of 0.0154, 0.600, and 0.743, respectively and the minimum R values are 0.003, 0.010, and 0.066, respectively. CNFs, LSCO-CNFs-10, and LSCO-CNFs-25 have average A value of 0.968, 0.398, and 0.256 respectively and have highest A values are 0.993, 0.989, and 0.996

respectively. CNFs, LSCO-CNFs-10, and LSCO-CNFs-25 have average T value of 0.0155, 0.0010, and 0.00179, respectively.

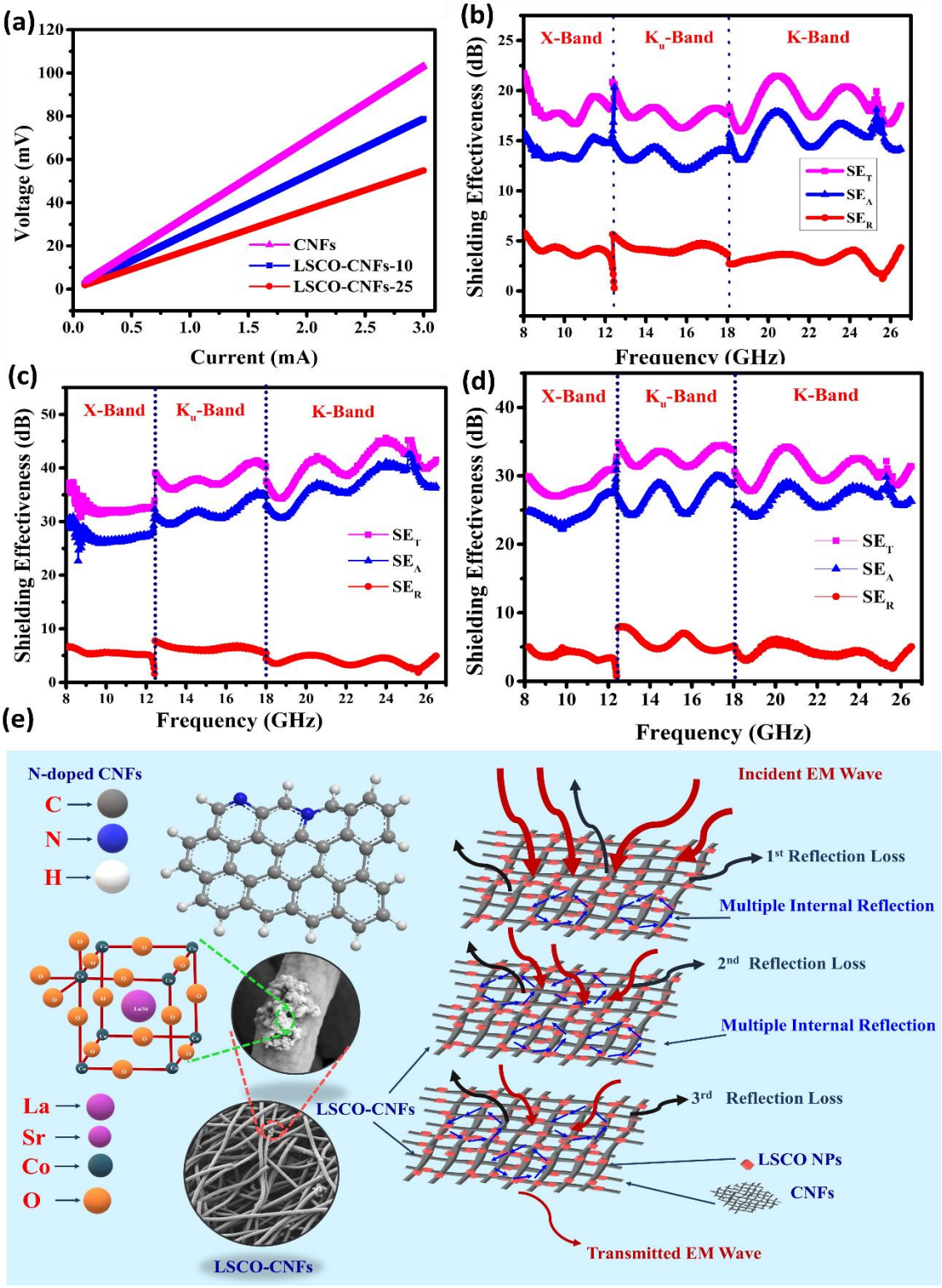

Figure 7.9: (a) Voltage-current plots of CNFs, LSCO-CNFs-10, and LSCO-CNFs-25. (b-d) EMI SE properties of (b) CNFs, (c) LSCO-CNFs-10, and (d) LSCO-CNFs-25. (e) Illustration of EMI shielding mechanism of LSCO-CNFs.

The CNFs shows low R value and high value of 'A' due to layer-by layer and highly porous structure. As the loading of LSCO NPs into CNFs increase, the average R value increases and average 'A' value decreases due to presence of free electrons on the surface of LSCO-CNFs. The contribution of SE_R is less than 15 % of the SE_T for CNFs, LSCO-CNFs-10, and LSCO-CNFs-25 as shown in **Figure 7.9(b-d).** Hence, CNFs and LSCO-CNFs can be considered as absorption dominant EMI shielding materials due to the low SE_R value and high contribution of SE_A (more than 80 %) towards SE_T.

The influence of weight and thickness of the shielding materials can be presented by SSE and SSE_t. These two values are critical parameters for electrospun polymer fiber composites when comparing with other shielding materials. Electrospun fiber composites in general, have a higher SSE and SSE_t values due to their lightweight and thinness. The density of CNFs rises as LSCO is loaded into CNFs, and the SSE value goes down from 175.3 to 75.08 dB cm^3 g^{-1} as mentioned in the **Table 7.1**. LSCO-CNFs shows excellent absolute EMI SE (SSE_t) value due to low thickness of CNFs. The SSE_t value of LSCO-CNFs-10 and LSCO-CNFs-25 are 9125 dB cm^2 g^{-1} and 7672 dB cm^2 g^{-1}, respectively. SSE and SSE_t values decreased upon addition of LSCONPs, because density and thickness were increased. The values for PDMS composites further decreased due to the still higher density and thickness. **Table 7.1** provides all the data related to EMI SE.

Summary

Table 7.1: EMI shielding properties of CNFs, LSCO-CNFs-10, and LSCO-CNFs-25.

Sample	**Thickness (mm)**	**Density (g cm^{-3})**	**σ (S cm^{-1})**	**Frequency (GHz)**	**EMI SE (dB)**		**SSE (dB cm^3 g^{-1})**		**SSE_t (dB cm^2 g^{-1})**	
					Highest	**Average**	**highest**	**average**	**highest**	**average**
CNFs	0.08	0.13	1.07	8.2-26.5	21.74	18.26	175.3	147.2	21915	18407
LSCO-CNFs-10	0.08	0.42	1.40	8.2-26.5	34.89	30.50	83.50	73.00	10438	9125
LSCO-CNFs-25	0.08	0.61	2.01	8.2-26.5	45.65	37.32	75.08	61.38	9385	7672

CNFs-PDMS composite	0.62	1.62	-	8.2-26.5	21.74	18.26	13.42	11.27	223.6	187.8
LSCO-CNFs-10-PDMS composite	0.62	1.76	-	8.2-26.5	34.89	30.50	19.82	17.32	330.4	288.8
LSCO-CNFs-25-PDMS composite	0.62	1.82	-	8.2-26.5	45.65	37.32	25.08	20.50	418.0	341.7

7.4 Conclusion

Here, an easy and facile method for fabrication of lightweight, flexible, and hydrophobic EMI shielding materials in X, Ku, and K-band in microwave region is demonstrated. Perovskite metal oxide (LSCO) was successfully prepared by sol-gel method. LSCO NPs were incorporated into CNFs through electrospinning, followed by heat treatment. As the loading of LSCO NPs in CNFs increases from 10 wt% to 25 wt%, the EMI SE increases from 34 dB to 45 dB with a thickness of 0.08 mm. The SE_A contributes more than 85 percent to the total SE_T. LSCO-CNFs exhibited high SSE_t value of 7672 dB cm^2 g^{-1} with 25 wt% loading of LSCO NPs in CNFs. The LSCO-CNFs shows excellent EMI shielding properties because of their high electrical conductivity leading to the formation of conductive paths with CNFs, interfacial polarization as well as dipole polarization due to the multicomponent heterogeneous interfaces and the dielectric loss due to the defects produced by Sr doping in $LaCoO_3$. Porosity and fibrous layer-by-layer structure of LSCO-CNFs increases the multiple internal scattering, further aiding the absorption of EM waves. PDMS composite of LSCO-CNFs with improved mechanical properties can be used to create flexible EMI materials. The performance of these materials may be further improved by modifying the architecture and also by incorporating fillers with magnetic properties.

CHAPTER: 8

Aligned $BaTiO_3$ Nanoparticles incorporated CNF and their PDMS Composite for EMI shielding

Overview

The work presented in the previous chapter dealt with conducting perovskite metal oxide $La_{0.85}Sr_{0.15}CoO_3$ NPs incorporated CNF for EMI shielding. The current chapter concerns with investigation of EMI shielding properties of aligned and non-aligned CNF incorporated with barium titanate ($BaTiO_3$) NPs ($BaTiO_3$-CNF) in X, Ku, and K-band. According to the reports, aligned $BaTiO_3$ NPs demonstrated high dielectric properties, including piezoelectric and ferroelectric properties and aligned carbonized electrospun PAN fiber (CNF) exhibited high electrical conductivity. Therefore, in this work we attempted to design high performance EMI shielding material by taking advantage of the dielectric properties of aligned $BaTiO_3$ NPs and the high electrical conductivity of aligned CNF. The alignment improved multiple internal reflections and interfacial polarization in the layered structure of the CNF. Alignment of suitably doped CNF may open up new opportunities for industrial-scale production of shielding materials that are waterproof, lightweight, and flexible.

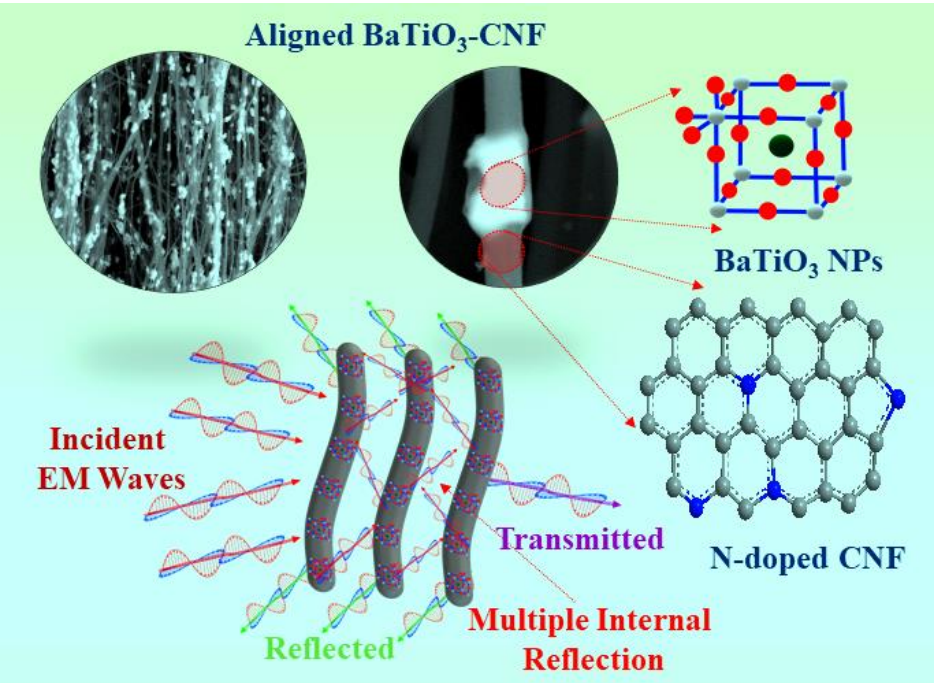

8.1 Introduction

Uniform distribution, high loading and alignment of conductive nano fillers are crucial to form conductive network for high EMI shielding performance. However, high loading of nano-fillers may deteriorate mechanical properties of the composites. Therefore, uniform distribution and alignment of the conductive nano-fillers are preferred for achieving high EMI SE (Huo et al., 2023; Qian et al., 2023; M. Zhou et al., 2023).

Electrospinning is one of the efficient methods to form 1-D nanostructured fibers with uniform distribution of fillers. By suitably optimizing the spinning conditions, it is possible to fabricate aligned nanofibers containing conductive nano-fillers along the fibers (S. Dong et al., 2022; M. Kim et al., 2021; Mohan et al., 2021; Song et al., 2014; Liying Zhang et al., 2013; Zheng, Wang, et al., 2023). Electrospun fibers have high surface area, porous structure and can form interconnected network with embedded or distributed conductive fillers within the fibrous structure. Electrospun fibers with conductive fillers can form an electrically conductive network for electron transport that reflects the EM waves. It is reported that aligned electrospun fibers with oriented polymer chains lead to increased mechanical properties and dielectric losses (Isaac et al., 2021). Lan et al. investigated axial alignment of CNT on fibers for EMI shielding in X and Ku-bands. The several micron-thick coating of aligned CNT microarchitecture exhibited 81 times better conductivity than that of the disordered CNT structure and exhibited EMI SE of 21.5 dB (Lan et al., 2020). Kumar et al. fabricated self-aligned graphene/polymer composite films with EMI SE of ~30 dB in the frequency range of 8.2-12 GHz (P. Kumar et al., 2017). Song et al. investigated alignment of graphene sheets in wax composites for EMI shielding (Song et al., 2013). The alignment produced anisotropic properties that improved the absorption and reflection properties of shielding materials (Isaac et al., 2021). Carbonization of electrospun PAN fiber can form interconnected 3-D electrically conductive network with high EMI shielding properties (S. Dong et al., 2022; M. Kim et al., 2021; Mohan et al., 2021; Song et al., 2014; Liying Zhang et al., 2013; Zheng, Wang, et al., 2023). Im et al. fabricated electrospun PAN based carbon fibers involving Fe_2O_3/$BaTiO_3$/MWCNT additives for EMI shielding in the frequency range of 800 MHz- 4 GHz. The EMI SE of Fe_2O_3 and $BaTiO_3$ NPs incorporated carbon fibers was 32 dB and it was further improved to 37 dB by addition of MWCNTs (Im et al., 2010b). Chen et al. fabricated biomass-based aligned carbon nanostructure by heat treatment of commercial cotton pads for tunable EMI shielding in X-band. As the pyrolysis temperature increased from 700 to 1000 ^{o}C

for the double layer carbon networks, the EMI SE also rose to 49 dB from 38 dB (J. Chen et al., 2022). Yousefi et al. fabricated highly aligned graphene/polymer nanocomposites with EMI SE of 38 dB with 2 wt% loading of rGO (Yousefi et al., 2014).

Among the various conductive fillers, ABO_3-type perovskite oxides such as $LaCoO_3$, $PbTiO_3$, and $BaTiO_3$ have received attention for developing absorption-based shielding materials. Composites containing $BaTiO_3$ NPs exhibited high piezoelectric, ferroelectric, and dielectric properties (J. J. Jiang et al., 2015; Saini et al., 2013; Jing Yan & Jeong, 2017; Jun Yan et al., 2023). $BaTiO_3$ NPs induced internal charges at the interface, in presence of carbon matrix which improved dielectric losses (J. J. Jiang et al., 2015; Saini et al., 2013). Goel et al. reported CQD@$BaTiO_3$/$BaFe_{12}O_{19}$ which showed a reflection loss of -25.38 dB with a thickness of 2.75 mm in the X band (Goel et al., 2021). Qing et al. reported reflection loss of carbonyl iron/$BaTiO_3$ composite with 20 wt% $BaTiO_3$ and 60 wt% carbonyl iron particles at 2.0 mm to be -42 dB in X-band region (Qing et al., 2011). Ran et al. fabricated $BaTiO_3$/rGO composite, which showed a reflection loss of -44.9 dB with a thickness of 2.5 mm in an adsorption bandwidth of 5.4 GHz (Ran et al., 2019). Saini et al. reported polyaniline– tetragonal $BaTiO_3$ nanocomposite, with EMI SE of 71.5 dB in Ku-band (Saini et al., 2013). As already mentioned, it is desirable to use EMI shielding materials which show absorption dominated EMI shielding. Absorption of EM waves by shielding materials are influenced by the design and structure of the shielding materials and alignment of nano-fillers in the structure.

The uniformly incorporated or embedded conductive fillers into 1-D CNF have several desirable properties. 1-D CNF provides a large surface to interact with EM waves and high porosity allows EM waves to enter inside the materials and undergo multiple scattering and multiple internal reflections. These properties contribute to an extended EM dissipation route in the axial direction of CNF. Fibrous morphology and alignment of CNF in a layer-by-layer fashion facilitates development of multiple hetero-interfaces and promotes multiple internal reflections and interfacial polarization (J. H. Lee et al., 2022; Qian et al., 2023; C. Wang et al., 2023a; B. Yang et al., 2022; M. Zhou et al., 2023) resulting in attenuation of EM waves, thereby promoting absorption-dominated EMI shielding.

1-D N-doped CNF along with $BaTiO_3$ NPs is a potential system to be explored as absorption-based shielding materials. The dielectric and electrical properties of $BaTiO_3$ NPs may get modified when present along with CNF (Im et al., 2010b). The aligned $BaTiO_3$ NPs and Nanowires demonstrated high piezoelectric and ferroelectric capabilities for various

applications such as sensing, energy harvesting, fibrous scaffolds, bone tissue engineering, and microelectronics (Khatkhatay et al., 2013; Koka, Zhou, & Sodano, 2014; Koka, Zhou, Tang, et al., 2014; Z. Zhou et al., 2013). Electrospinning is an easy strategy to align $BaTiO_3$ NPs along fibers. There are several reports related to alignment of $BaTiO_3$ NPs along with electrospun fibers (Bauer et al., 2016; D. Li et al., 2003; Yiping Li et al., 2017; McCann et al., 2006). Li et al. used electrospinning to fabricate uniaxial aligned nanofibers based on organic polymers, ceramics, and polymer/ceramics composites (D. Li et al., 2003). Bauer et al. studied the structure property relation of aligned electrospun $BaTiO_3$ nanofibers for piezoelectric properties (Bauer et al., 2016). McCann et al. reported the preparation of polycrystalline $BaTiO_3$-nanofibers with controllable aspect ratio using electrospinning (McCann et al., 2006). Li et al. fabricated composite fibrous scaffolds with randomly orientated and aligned electrospun poly-(L-lactic acid) containing $BaTiO_3$ NPs using electrospinning (Yiping Li et al., 2017). According to the reports, aligned $BaTiO_3$ NPs demonstrated higher dielectric properties, including piezoelectric and ferroelectric properties and aligned CNF exhibited high electrical conductivity (Bauer et al., 2016; D. Li et al., 2003; Yiping Li et al., 2017; McCann et al., 2006). Therefore, by combining electrical conductivity of aligned CNF and dielectric properties of aligned $BaTiO_3$ NPs, materials with high performance EMI shielding performance may be designed. The carbonized electrospun fiber mats are fragile and brittle in nature. PDMS is widely recognized as the most flexible polymer derived from silicone, particularly at room temperature. Hence, fabrication of flexible and stretchable EMI shielding materials can be achieved by the use of a PDMS composite containing $BaTiO_3$ NPs along with 1-D N-doped CNF.

Under this frame work, we fabricated aligned and non-aligned N-doped CNF containing $BaTiO_3$ NPs through electrospinning followed by carbonization. Aligned N-doped CNF ($BaTiO_3$-CNF) with a 60 wt% loading of $BaTiO_3$ NPs exhibited maximum EMI SE of 60, 65, and 81 dB in X, Ku, and K-band respectively, with a thickness of 0.24 mm. The alignment of CNF improved electrical conductivity and also enhanced multiple internal reflections. The presence of $BaTiO_3$ NPs in one-dimensional, layer-by-layer fibrous structure of CNF induced high interfacial polarization. The synergistic effect of $BaTiO_3$ NPs and CNF resulted in higher SE_A compared to SE_R. PDMS composite of $BaTiO_3$-CNF was prepared by hand lay-up method to improve flexibility and mechanical properties of the CNF. The $BaTiO_3$-CNF PDMS composites with thickness of 0.84 mm exhibited EMI SE similar to that of $BaTiO_3$-CNF. The composite material has low thickness, excellent flexibility and is waterproof and lightweight.

These characteristics make them suitable for use in wearable electronics, and in electronic packaging applications in civil, military, and space applications.

8.2 Experimental

8.2.1 Materials

The specifications of PAN, Barium titanate, and DMF are mentioned in chapter 2 (refer to section 2.1.)

8.2.2 Preparation of aligned, N-doped CNF containing $BaTiO_3$ NPs ($BaTiO_3$-CNF)

The solution for electrospinning was obtained by dispersing $BaTiO_3$ NPs in PAN solution. A 10 ml of 10 wt% PAN solution in DMF was prepared in a 15 mL vial and 1.5 g of $BaTiO_3$ NPs was added to the solution. The mixture was kept on hot plate with constant stirring at 60 ^oC for 24 h to obtain a uniform dispersion of $BaTiO_3$ NPs in PAN solution. The solution was then poured into a 10 mL syringe with a 0.80 mm diameter of metallic needle for electrospinning. Electrospinning was performed using an electrospinning set-up designed by Physics Instrument Co. Ltd, India. The syringe was placed in a syringe pump holder and was connected to positive electrode of a high voltage power supply. The negative electrode of the power supply was connected to aluminium foil wrapped metallic rotatory drum collector. High voltage of 12-14 kV was applied to the electrospinning solution which was fed at a rate of 1.2 mL h^{-1}. The metallic drum collector was placed 15 cm away from the tip of the needle of the syringe and speed of the drum collector was in the range of 800-1000 rpm to obtain non-aligned electrospun PAN fibers as well as non-aligned electrospun PAN fiber containing $BaTiO_3$ NPs ($BaTiO_3$-EFs). Aligned electrospun PAN fibers were obtained after optimizing the distance of the collector (10 cm) and speed of the drum collector (1300-1500 rpm). Similarly, the aligned electrospun PAN fiber containing $BaTiO_3$ NPs ($BaTiO_3$-EFs) was also prepared. The electrospun mats were put in air oven at 250 ^oC for 5 h for stabilization. During stabilization, conjugated ladder structure will be formed in the electrospun PAN fiber (Shokrani Havigh & Mahmoudi Chenari, 2022b). Then, the stabilized electrospun mats were kept in high-temperature inert furnace (Vacuum Technologies, India) at 900 ^oC with 2 ^oC min^{-1} heating rate for 4 h in an argon atmosphere to obtain non-aligned and aligned N-doped CNF containing $BaTiO_3$ NPs ($BaTiO_3$-CNF). The term, $BaTiO_3$-CNF refers to N-doped CNF containing $BaTiO_3$ NPs.

8.2.3 Preparation of PDMS composites of $BaTiO_3$-CNF

The PDMS composite of coated samples were prepared in a similar methodology as mentioned in chapter 2 (section 2.3). The uniform and tight bonding between N- doped CNFs and PDMS was confirmed by SEM images, EDS, and elemental mapping. Schematic illustration of preparation of $BaTiO_3$-CNF and their PDMS composite is shown in **Figure 8.1**.

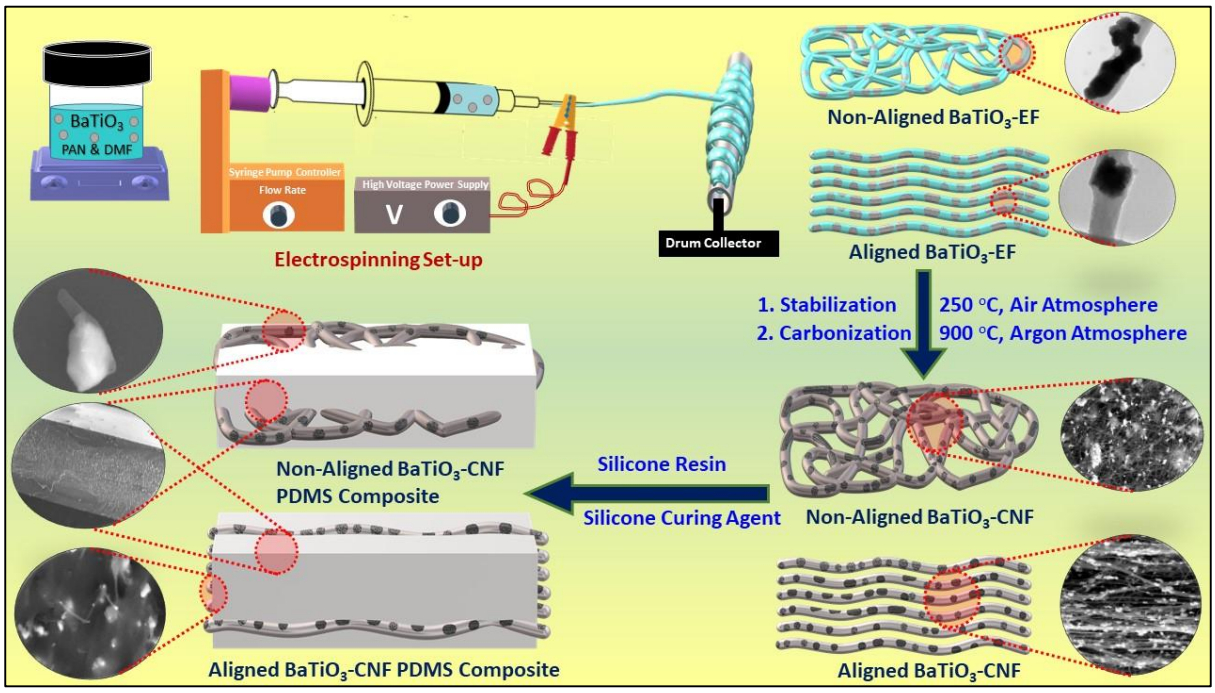

Figure 8.1: Schematic illustration of preparation of non-aligned and aligned $BaTiO_3$-CNF and their PDMS composites.

8.2.4 Characterization

Details of the characterization techniques employed have already been discussed in chapter 2. The complex relative dielectric permittivity ($\varepsilon_r^* = \varepsilon_r' - j\varepsilon_r''$) of PDMS composites of non-aligned CNF, aligned CNF, non-aligned $BaTiO_3$-CNF, and aligned $BaTiO_3$-CNF were measured using two port vector analyser (Keysight Technologies (N5234B)) via Keysight N1500A materials measurement software suit.

8.3 Results and discussion

Highly aligned CNFs have significance in the field of carbon fiber-reinforced nanocomposites. Alignment of CNF can improve electrical conductivity as well as dielectric properties along the fiber axis. (Lan et al., 2020) . Morvan et al. described that the electric field generated during the electrospinning process can align the $BaTiO_3$ NPs along with electrospun fiber. During the

initial stage of the electrospinning process, the $BaTiO_3$ NPs can easily rotate before the solvent gets completely evaporated (Morvan et al., 2012). The orientation of the polarization of $BaTiO_3$ NPs are locked around the polymer matrix (PAN) during solidification that happens after the solvent evaporates. The $BaTiO_3$ NPs would be aligned with electrospun PAN fiber due to electric polarization of $BaTiO_3$ NPs during electrospinning. (Yiping Li et al., 2017; Morvan et al., 2012) Aligned electrospun fiber was obtained by optimizing the applied voltage, flow rate of polymer solution, distance between the needle tip and collector, and speed of the rotatory drum collector. High speed of the rotating drum collector and short distance between tip and collector are crucial to obtain aligned fibers. (Robinson et al., 2021; Shao et al., 2021) The optimal speed of rotatory drum collector can cause the maximum alignment of fibers. (Isaac et al., 2021) The schematic illustration of the electrospinning set-up and preparation of aligned and non-aligned $BaTiO_3$-CNF and their PDMS composites is shown in **Figure 8.1**. The rotation of drum collector controls the fiber deposition. The distance between the needle tip should be appropriate, so that fibers would deposit on the drum collector without further modification. If the distance between the tip and collector is too large, then there is chance of breakage or disintegration of the fibers before they reach the collector which may decrease the aspect ratio. If the distance between the tip and collector is too small, then there are chances for bead formation. (Z.-M. Huang et al., 2003; Robinson et al., 2021; Schiffman & Schauer, 2008) If the speed of the drum collector is low, then the fiber would deposit as randomly orientated fibers. At very high rotation speed of the drum collector, the fiber aspect ratio decreases and would fail to deposit on the collector due to breakage of the fibers and formation of continuous fiber would be impossible. Therefore, rotation speed of the collector and distance between the tip of the needle and the collector should be optimal to form continuous, aligned fibers (Isaac et al., 2021).

In the present study, when the drum collector was placed 15 cm away from the tip of the needle of the syringe and speed of the drum collector was in the range of 800-1000 rpm, non-aligned electrospun fibers as well as non-aligned electrospun fiber containing $BaTiO_3$ NPs ($BaTiO_3$-EF) were obtained. Aligned electrospun fibers and aligned electrospun fiber containing $BaTiO_3$ NPs ($BaTiO_3$-EF) were obtained, when the distance of the collector was 10 cm and speed of the collector was in the range of 1300-1500 rpm. SEM images of these fibers after carbonization are displayed in **Figure 8.3**. It is seen that, the fiber structure is maintained after carbonization also.

8.3.1. TEM image

Figure 8.2 (a-b) shows TEM images of $BaTiO_3$ NPs. The average particle size of $BaTiO_3$ NPs is 192 ± 62 nm. **Figure 8.2(c-h)** shows that $BaTiO_3$ NPs are incorporated and are embedded in the continuous fibers. The average diameter of $BaTiO_3$-EFs is 517 ± 67 nm.

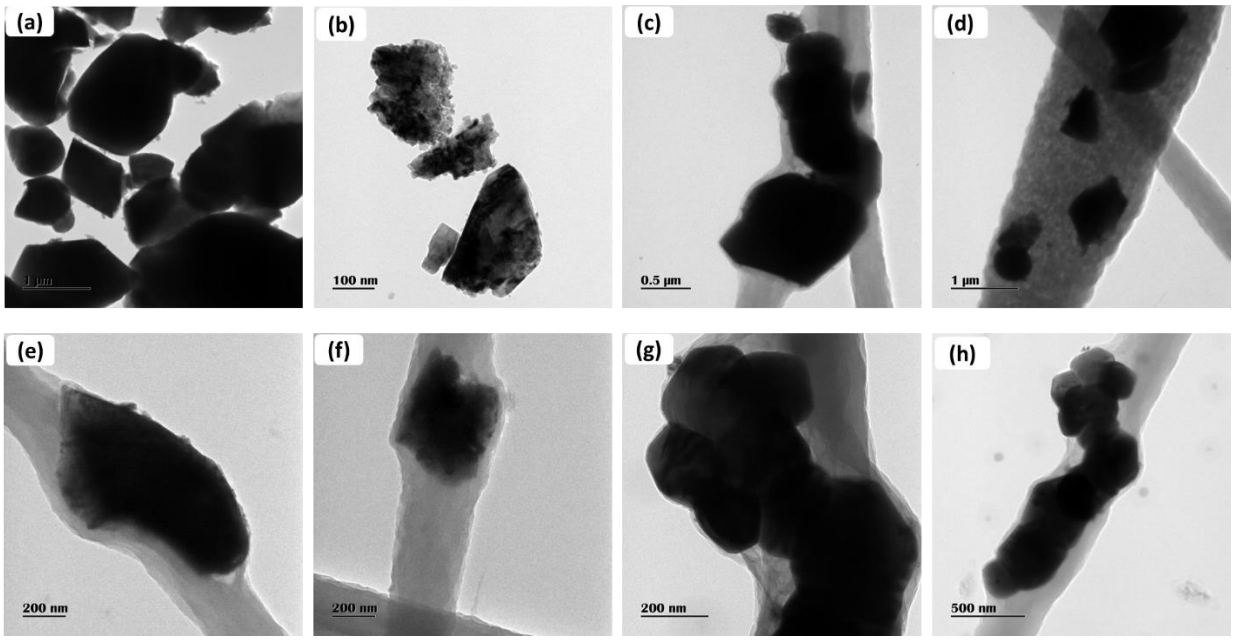

Figure 8.2: TEM images of (a-b) $BaTiO_3$ NPs and (c-h) $BaTiO_3$ NPs embedded PAN electrospun fiber.

8.3.2. SEM image

Figure 8.3 shows SEM images of CNF, $BaTiO_3$-CNF, PDMS composite of $BaTiO_3$-CNF and cross-sectional images of PDMS composites of $BaTiO_3$-CNF. The SEM images (**Figure 8.3(a-k)**) show that the carbonized fibers are continuous. **Figure 8.3(a-b)** shows the non-aligned CNF and **Figure 8.3(c-e)** shows the aligned CNF obtained by optimizing the electrospinning parameters. Similarly, **Figure 8.3(f-h)** shows the non-aligned $BaTiO_3$-CNF and **Figure 8.3(i-k)** shows the aligned $BaTiO_3$-CNF. The TEM and SEM images show that $BaTiO_3$ NPs are distributed all along the continuous fibers. The distribution of $BaTiO_3$ NPs was further confirmed by EDS and elemental mapping. The average diameters of non-aligned CNF, aligned CNF, non-aligned $BaTiO_3$-CNF, and aligned $BaTiO_3$-CNF were 485 ± 123 nm, 712 ± 67 nm, 261 ± 45 nm, and 437 ± 71 nm, respectively. **Figure 8.3(l-m)** displays the images of PDMS composites of $BaTiO_3$-CNF at low and high magnifications respectively and confirm the uniform cross-linking between silicone resin and curing agents resulting in a smooth solid matrix. **Figure 8.3(n-p)** shows cross-sectional SEM images of PDMS composites of $BaTiO_3$-

CNF. These images show the tight bonding between the $BaTiO_3$ NPs and CNF and preservation of the fiber morphology.

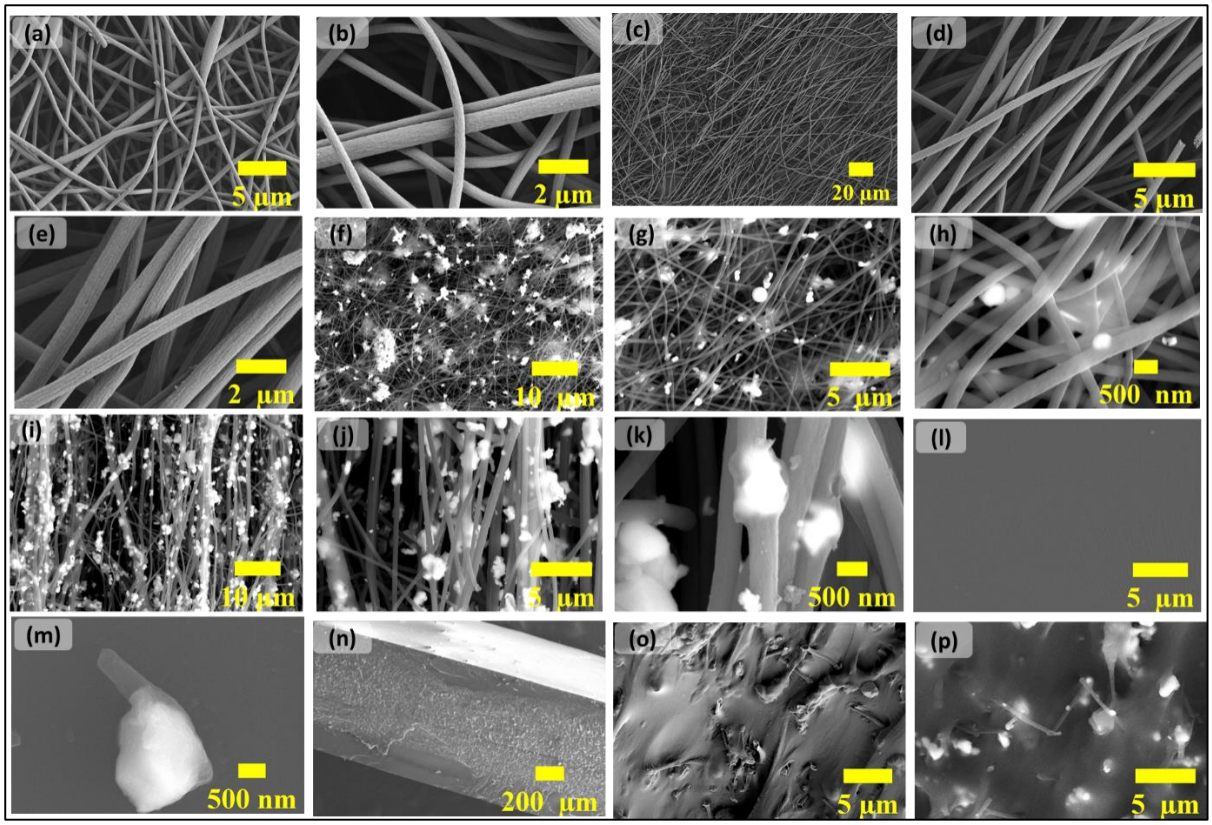

Figure 8.3: SEM images of carbonized PAN fiber (a-b) non-aligned CNF, (c-e) aligned CNF, (f-h) non-aligned $BaTiO_3$-CNF, (i-k) aligned $BaTiO_3$-CNF. SEM images of (l-p) PDMS composites of $BaTiO_3$-CNF, (l) at low magnification and (m) at high magnification. (n-p) cross-sectional SEM images of PDMS composites of $BaTiO_3$-CNF.

8.3.3. EDS analysis and Elemental Mapping

EDS and elemental mapping are used for determining presence of elements in CNF and $BaTiO_3$-CNF. The EDS spectra of CNF, $BaTiO_3$-CNF, and PDMS composite of $BaTiO_3$-CNF are shown respectively in **Figure 8.4(a-c)**. The SEM image used for elemental mapping of CNF, $BaTiO_3$-CNF, and cross-section of PDMS composite of $BaTiO_3$-CNF are shown in **Figure 8.4(d, h, and n)** respectively. The EDS spectra (**Figure 8.4(a))** and elemental mapping (**Figure 8.4 (e-g))** of CNF confirmed the presence of carbon, nitrogen, and oxygen throughout the fibers. The EDS spectra (**Figure 8.4(b))** and elemental mapping (**Figure 8.4(i-m))** of $BaTiO_3$-CNF confirmed the presence of Ba, Ti, C, O, and N throughout the fiber. The SEM image used for mapping of Ba, Ti, and O in N-doped CNF is shown in **Figure 8.4(h).**

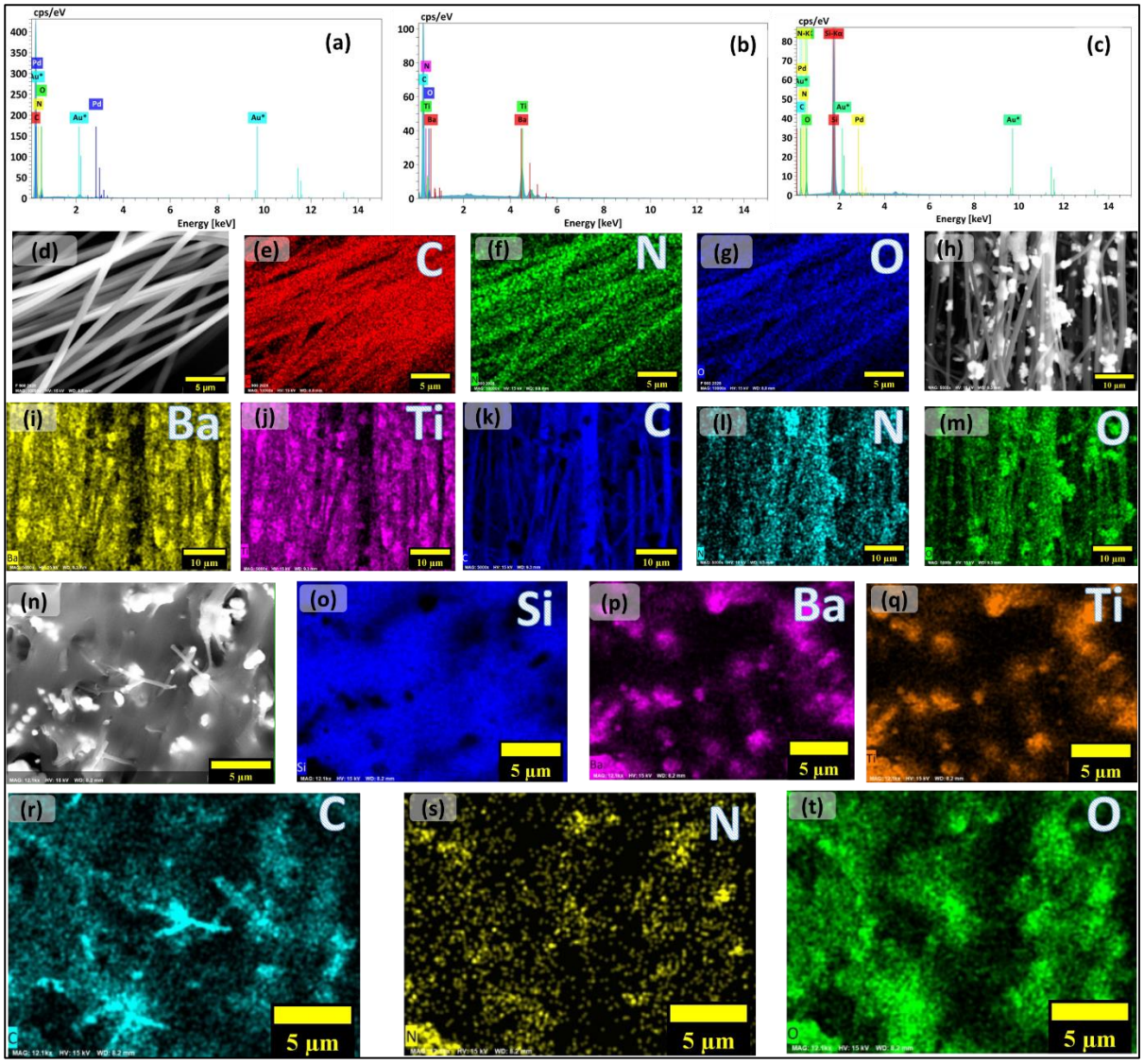

Figure 8.4: (a-c) EDS spectra of (a) aligned CNF, (b) aligned $BaTiO_3$-CNF, and (c) PDMS composites of aligned $BaTiO_3$-CNF. SEM image that was used for elemental mapping of (d) aligned CNF, (h) aligned $BaTiO_3$-CNF, and (n) cross-section of PDMS composites of aligned $BaTiO_3$-CNF. The elemental mapping of (e) carbon, (f) nitrogen, and (g) oxygen present in aligned N-doped CNF. The elemental mapping of (i) barium, (j) titanium, (k) carbon, (l) nitrogen, and (m) oxygen present in aligned $BaTiO_3$-CNF. The elemental mapping of (o) silicone, (p) barium, (q) titanium, (r) carbon, (s) nitrogen, and (t) oxygen present in PDMS composites (cross-section) of aligned $BaTiO_3$-CNF.

The EDS spectrum (**Figure 8.4(c)**) and elemental mapping (**Figure 8.4(o-t)**) of cross-section of PDMS composite of $BaTiO_3$-CNF confirm the presence of Si, Ba, Ti, C, N, and O and incorporation of $BaTiO_3$-CNF in the PDMS matrix. The SEM image used for elemental mapping (**Figure 8.4(n)**) also confirmed the packing of $BaTiO_3$-CNF in the PDMS matrix with preservation of fiber morphology.

8.3.4. Raman Spectroscopy

Raman spectra of CNF and $BaTiO_3$-CNF displayed in **Figure 8.5(a)**, exhibit D-band at 1350 cm^{-1} and G-band at 1594 cm^{-1} belonging to turbostratic graphitic structure. The spectra are similar to that of electrospun PAN fiber carbonized at 900 ^oC (Qanati et al., 2022; Ramlow et al., 2023; Y. X. Zhu et al., 2021). The D-band corresponds to amorphous carbon belonging to vibrations of SP^3 hybridized carbon atoms of disordered graphite representing the amorphization of carbon, whereas the G-band represents SP^2 hybridized graphitic carbon in 2-D hexagonal lattices attributed to the graphitization of carbon (Y. X. Zhu et al., 2021). The ratio of the intensity of D-band and G-band (R-value) indicates degree of graphitization. The degree of graphitization calculated for CNF, non-aligned $BaTiO_3$-CNF, and aligned $BaTiO_3$-CNF were 0.87, 0.99, and 0.96 respectively. It is observed that, after the incorporation of $BaTiO_3$ NPs into CNF, the intensity of D-band increases, implying a decrease in the graphitic structure due to the increase in structural disorder in CNF (Björkman, 1969; Caṇado et al., 2006; Shanmugapriya et al., 2019). Raman spectra and degree of graphitization of CNF, non-aligned and aligned $BaTiO_3$-CNF reveal the turbostratic carbon nanostructure of these materials.

8.3.5. XRD patterns

XRD patterns of commercial $BaTiO_3$ NPs and the carbonized nanofibers (CNF) are displayed in **Figure 8.5(b)**. The broad peak at 24.5^o in the diffraction pattern of CNF belongs to 002 hexagonal graphitic plane (JCPDS 41-1487) (G. Y. Cui et al., 2018; Ravindra & Badekai Ramachandra, 2011). The XRD diffraction patterns of commercial $BaTiO_3$ NPs, non-aligned and aligned $BaTiO_3$-CNF reveal that all these materials have similar 2Ɵ peaks at 22.1^o, 31.4 ^{o}, 38.8 ^{o}, 45.4^o, 51.0^o, 56.2^o, 65.7^o, and 75.1^o which correspond to the perovskite phase in the tetragonal structure (JCPDS 05-0626) (Biglar et al., 2017; Moreira et al., 2008; M. Singh et al., 2017; Zou et al., 2021). The similar diffraction patterns confirmed the incorporation of $BaTiO_3$ NPs in the CNF with unaltered crystal structure and phase. However, the XRD patterns of $BaTiO_3$-CNF (**Figure 8.5(c)**) exhibit slight shift in lattice space towards higher 2Ɵ for both the samples (non-aligned $BaTiO_3$-CNF and aligned $BaTiO_3$-CNF) compared to $BaTiO_3$ NPs. This may be due to the presence of hexagonal graphitic plane of CNF along with the $BaTiO_3$ NPs. The shift is slightly more for the aligned $BaTiO_3$-CNF because $BaTiO_3$ NPs are aligned more with the aligned hexagonal graphitic planes of CNF. The aligned $BaTiO_3$-CNF exhibited sharper peaks compared to the non-aligned $BaTiO_3$-CNF that further indicates the higher

degree of graphitization that is seen in Raman spectra also. However, more detailed investigation is required to discern this phenomenon clearly.

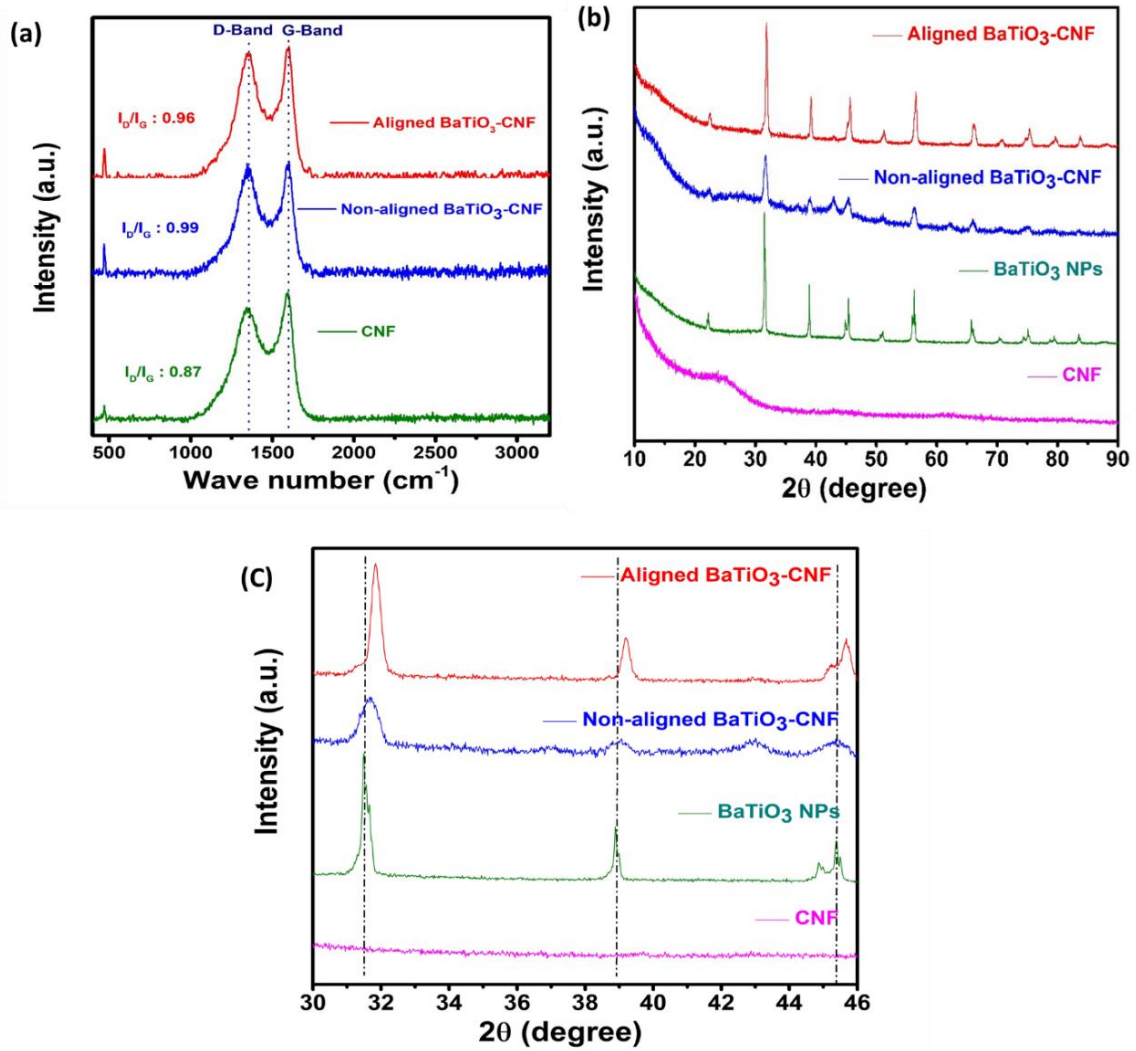

Figure 8.5: (a) Raman spectra of CNF, non-aligned and aligned $BaTiO_3$ CNF. (b) XRD pattern of CNF, $BaTiO_3$ NPs, non-aligned, and aligned $BaTiO_3$-CNF. (c) XRD pattern of CNF, $BaTiO_3$ NPs, non-aligned, and aligned $BaTiO_3$-CNF in 2Θ range of 30 to 46 degree.

8.3.6. XPS analysis

XPS was utilized for further confirming the chemical composition and oxidation states of elements present in $BaTiO_3$-CNF. **Figure 8.6(a)** provides XPS survey scans of $BaTiO_3$ NPs, CNF, and $BaTiO_3$-CNF. The survey scan of $BaTiO_3$-CNF shows combined peaks of $BaTiO_3$ NPs and CNF and confirms the incorporation of $BaTiO_3$ NPs into the N-doped CNF. **Figure 8.6(b-d)** shows the high-resolution XPS elemental scans of Ba 3d, Ti 2p, and O 1s present in $BaTiO_3$ NPs.

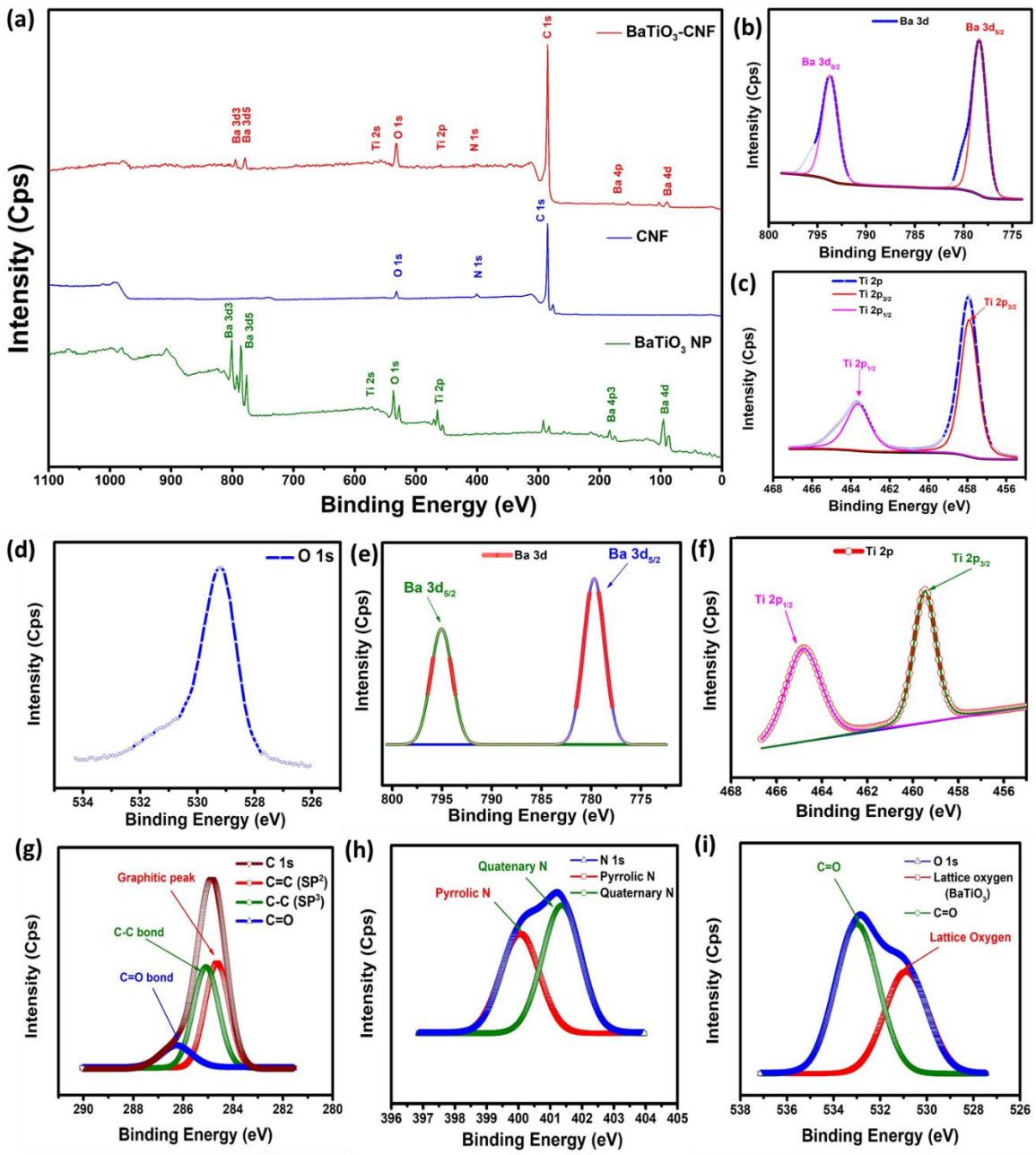

Figure 8.6: (a) XPS survey spectra of $BaTiO_3$ NPs, N-doped CNF, and $BaTiO_3$-CNF. The high-resolution XPS peaks of (b) Ba (3d), (c) Ti (2p), and (d) O (1s) present in $BaTiO_3$ NPs. The high-resolution XPS peaks of (e) Ba (3d), (f) Ti (2p), (g) C (1s), (h) N (1s), and (h) O (1s) present in $BaTiO_3$-CNF.

The Ba 3d XPS spectra shown in **Figures 8.6(b)** and **8.6(e)** for $BaTiO_3$ NPs and $BaTiO_3$-CNF exhibited two strong peaks located at 796 and 780 eV which are assigned to Ba $3d_{5/2}$ and Ba $3d_{3/2}$, respectively. The Ti 2p spectrum of $BaTiO_3$ NPs shows two strong peaks at 458.0 and 463.6 eV which are assigned to Ti $2p_{3/2}$ and Ti $2p_{1/2}$ as shown in **Figure 8.6(c)**, whereas Ti 2p spectrum of $BaTiO_3$-CNF shows that $2p_{3/2}$ and $2p_{1/2}$ are shifted to 459.4 eV and 464.8 eV due to presence of N-doped CNF as shown in **Figure 8.6(f)**. The curve-fitted C 1s core energy

level spectrum contains a strong peak at a binding energy of 284.6 eV which is assigned to SP^2 hybridized or graphitic C peak of C 1s as displayed in **Figure 8.6(g)**. The curve-fitted N 1s core energy level spectrum contains two strong peaks at 400.0 eV and 401.2 eV assigned to pyrrolic N and quaternary N that belongs to N-doped CNF as displayed in **Figure 8.6(h)**. The curve-fitted O 1s core energy level spectrum of $BaTiO_3$-CNF shows a strong peak at 530.5 eV similar to O 1s peak of $BaTiO_3$ NPs (**Figure 8.6(d**)) and peak at 533.3 eV is assigned to the formation of C=O, as displayed in **Figure 8.6(i)**.

8.3.7. Contact angle measurement

The contact angle of aligned CNF, non-aligned $BaTiO_3$-CNF, and aligned $BaTiO_3$-CNF are around 120^o as shown in **Figure 8.7(a-c),** due to the turbostratic graphitic structure. However, the fibrous and porous structure of non-aligned CNF, aligned CNF, non-aligned $BaTiO_3$-CNF, and aligned $BaTiO_3$-CNF enabled them to get wet when water droplet was placed over them.

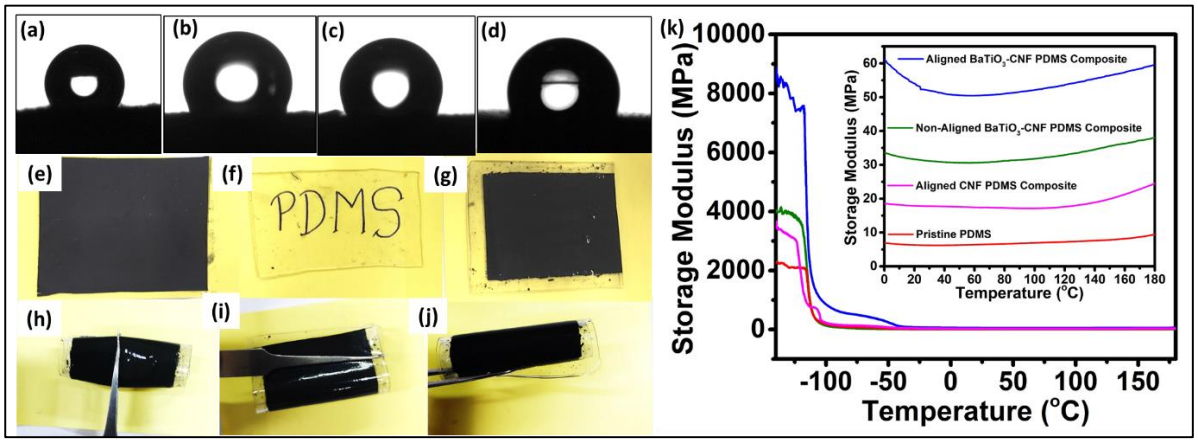

Figure 8.7: (a-d) Contact angle measurement of (a) aligned CNF, (b) non-aligned $BaTiO_3$-CNF, (c) aligned $BaTiO_3$-CNF, and (d) PDMS composite of aligned $BaTiO_3$-CNF. (e-g) Photograph of (e) $BaTiO_3$-CNF, (f) PDMS, and (g) PDMS composite of $BaTiO_3$-CNF. (h-J) photograph of (h) folding, (i) bending, and (j) rolling of PDMS composite of $BaTiO_3$-CNF. (k) DMA plots of storage modulus with respect to temperature.

Therefore, carbonized electrospun fibers can provide only partial protection from moisture or water. Hence, for achieving a hydrophobic surface it is essential that these CNFs are covered with a hydrophobic material. The contact angle of the PDMS composite of aligned $BaTiO_3$-CNF is around 118^o as shown in **Figure 8.7(d)**. Contact angle is greater than 90^o for all the samples and therefore, these samples can be considered as hydrophobic materials.

8.3.8. Mechanical Property

Figure 8.7(e-g) shows the photographs of CNF **(e)**, pristine PDMS **(f)**, and PDMS composite of $BaTiO_3$-CNF **(g)**. **Figure 8.7(h-j)** illustrates the ability of the aligned $BaTiO_3$-CNF PDMS composites to be folded **(h)**, bent **(i)**, and rolled **(j)** without causing damage to the samples. DMA was used to study the mechanical properties of PDMS composite of aligned CNF, non-aligned $BaTiO_3$-CNF, and aligned $BaTiO_3$-CNF in the temperature range of -135 ^oC to 180 ^oC. $BaTiO_3$ NPs acted as reinforcement material to improve the alignment of CNF and mechanical properties (Yiping Li et al., 2017). **Figure 8.7(k)** shows the DMA plots of storage modulus versus temperature for the PDMS composites. The glass transition temperature (T_g) is in the range of -120 ^oC to -115 ^oC. The low T_g is due to the chain flexibility of Si-O-Si bonds and presence of methyl groups (Zalewski et al., 2021). DMA plots show that the PDMS composites of CNF are in rubbery state at room temperature, and this would make the PDMS composites highly flexible at room temperature. The storage modulus was increased, when, CNF mat was incorporated into PDMS matrix in comparison to the pristine PDMS and it was further improved with loading of $BaTiO_3$ NPs into CNF. The loading of $BaTiO_3$ NPs into CNF provided additional mechanical strength compared to pure CNF. Alignment of $BaTiO_3$-CNF also improves the storage modulus in comparison to the composite with the non-aligned counterpart. Among the five samples analysed, the PDMS composite of aligned $BaTiO_3$-CNF shows the highest storage modulus in fiber direction **(Figure 8.7 k**). The alignment of CNF increases crystallinity of the CNF, due to which the storage modulus also increased (Khosla et al., 2018; Y. Shi et al., 2020).

8.3.9. Electrical Conductivity measurement

Electrically conductive materials reflect incident EM waves and provide EMI shielding properties. **Figure 8.8(a)** demonstrates that the voltage linearly increases with increasing the current from 0.1 mA to 3 mA and reveals the uniform sheet resistance throughout the fibers. The sheet resistance, sheet resistivity, and electrical conductivity of CNF, non-aligned and aligned $BaTiO_3$-CNF were calculated using **Equations 18, 19, and 20**. The uniform electrical conductivity throughout the fiber was further confirmed by the electrical circuit as displayed in **Figure 8.8(b).** Electrical conductivity of non-aligned CNF, aligned CNF, non-aligned $BaTiO_3$-CNF and aligned $BaTiO_3$-CNF are 0.18, 0.24, 0.28, and 0.32 S cm^{-1}. The aligned CNF exhibited higher electrical conductivity, since electron mobility tends to increase in the axial direction of fibers, compared to non-aligned CNF (Lan et al., 2020). The incorporation of

$BaTiO_3$ into CNF further improved the alignment of CNF and increased the electrical conductivity.

8.3.10. EMI SE

The EMI shielding performance of aligned CNF, non-aligned and aligned CNF containing $BaTiO_3$ NPs with thickness of 0.24 mm were calculated by the above-mentioned **Equations 5, 10, 11, and 12** in the frequency range of 8-26.5 GHz as displayed in **Figure 8.8(e-g)**. All these samples are brittle and fragile in nature and therefore to make it flexible and to improve their mechanical strength PDMS composites of non-aligned CNF, aligned CNF, non-aligned $BaTiO_3$-CNF, and aligned $BaTiO_3$-CNF were prepared. The pristine PDMS exhibited 1-2 dB of EMI SE since PDMS is insulator in nature and does not have EMI shielding property. PDMS composite of CNF preserved the fibrous structure of the CNF and the EMI shielding properties. The non-aligned CNF exhibited average EMI SE of 18-22 dB in X, Ku, and K-band. The EMI shielding properties and mechanism of EMI shielding in non-aligned CNF are already discussed in our previously work. The aligned N-doped CNF exhibited average EMI SE of 30 dB with thickness of 0.24 mm in X, Ku, and K- band as displayed in **Figure 8.8(e)**.

The aligned N-doped CNF exhibited EMI SE of 30 dB due to its high electrical conductivity and development of a 3-D electrically conductive network which facilitates conduction loss. Doping of nitrogen into CNF is crucial to the shielding mechanism. Presence of nitrogen atoms polarizes the conjugated carbon double bonds, since nitrogen is more electronegative than carbon and this causes polarization loss. Nitrogen atom which has one extra electron than carbon atom is present in pyrrolic and pyridinic structure in the CNF. This helps to improve electrical conductivity of the CNF (M. Zhang et al., 2021). The CNF's one-dimensional fibrous structure offers a large surface area to interact with incident EM waves. The Layer-by-Layer structure of CNF provides interfacial polarization. The high porosity of CNF improves the impedance matching that causes multiple internal reflections. The alignment of CNF directly improves the electrical conductivity.

Thus the synergistic effect of formation of conductive network, polarization of nitrogen-carbon double bond, interfacial polarization, and multiple internal reflections along the fiber axis in the aligned N-doped CNF results in higher SE_A compared to SE_R (Bctpsqujpo et al., 2022; Gao et al., 2018; F. Huang et al., 2021; Ramlow et al., 2023; Ziyu Zhang et al., 2022; Y. X. Zhu et al., 2021). Moreover, the incorporation of $BaTiO_3$ NPs in aligned and non-aligned N-doped CNF introduce piezoelectric, dielectric, ferroelectric, and electric properties. These properties

can help to enhance the EMI shielding properties (H. Hu et al., 2019; J. J. Jiang et al., 2015; B. S. Lee et al., 2016; Peidavosi et al., 2022; Saini et al., 2013; Jing Yan & Jeong, 2017; D. Yang et al., 2018).

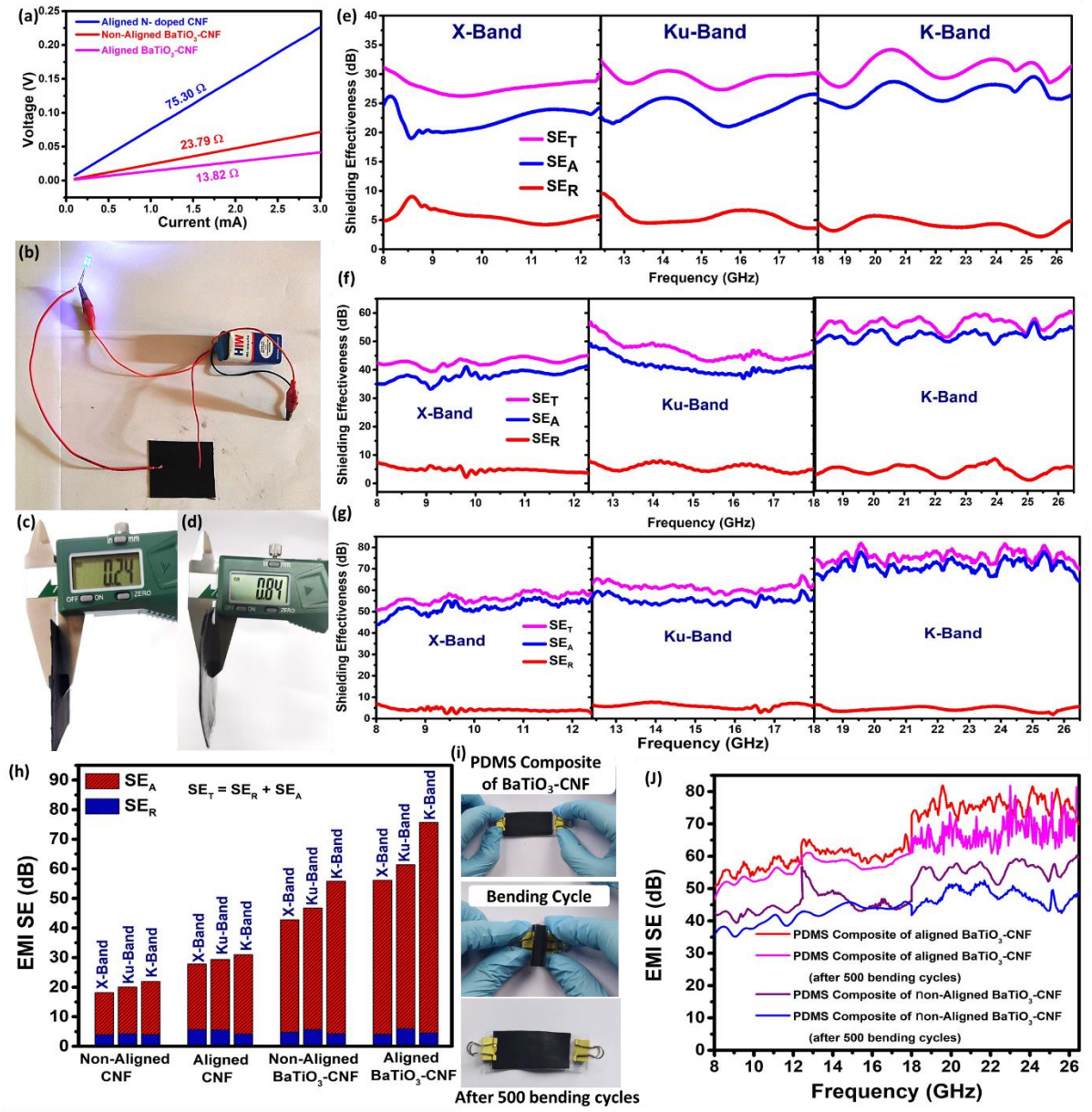

Figure 8.8: (a) Graph between current and voltage of aligned CNF, $BaTiO_3$ NPs containing aligned and non-aligned CNF. (b) electrical circuit of $BaTiO_3$-CNF, LED bulb, and DC battery. (c and d) The thickness of $BaTiO_3$-CNF and their PDMS composite measured using a digital caliper. (e-g) EMI SE of aligned CNF, non-aligned $BaTiO_3$-CNF, and aligned $BaTiO_3$-CNF, respectively in X-band, Ku-Band, and K-band. (h) the contribution of SE_A and SE_R in SE_T of non-aligned CNF, aligned CNF, non-aligned $BaTiO_3$-CNF, and aligned $BaTiO_3$-CNF, respectively in X-band, Ku-Band, and K-band. (i) photograph of bending cycles of PDMS composite of $BaTiO_3$-CNF. (j) The EMI SE of PDMS composite of non-aligned $BaTiO_3$-CNF, and aligned $BaTiO_3$-CNF before and after 500 bending cycles.

The average EMI SE value with 60 wt% loading of $BaTiO_3$ NPs into non-aligned CNF in X, Ku, and K-band are 42 dB, 50 dB, and 55 dB respectively as displayed in **Figure 8.8(f)**. The average EMI SE value of aligned $BaTiO_3$-CNF (60 wt % loading) are 55 dB, 60 dB, and 75 dB respectively in X, Ku, and K-band as shown in **Figure 8.8(g).** The highest EMI SE values obtained for non-aligned and aligned $BaTiO_3$-CNF are 61 dB and 81 dB respectively. The values of R, A, and T are shown in **Figure 8.9(a-d)**. The average R values of non-aligned CNF, aligned CNF, non-aligned $BaTiO_3$-CNF, and aligned $BaTiO_3$-CNF are 0.575, 0.687, 0.628, and 0.657, respectively. Due to high electrical conductivity of aligned CNF, it shows higher R values than non-aligned CNF.

The R-values are more than 0.5 suggesting that these samples exhibit reflection dominant shielding mechanism. All these carbonized electrospun PAN fibers are electrically conductive, form inter-connected 3-D conductive network, and 1-D fibrous structure with various internal interfaces and hetero-interfaces that augment the multiple internal reflection and internal scattering, which should result in absorption shielding (Fang et al., 2023; Zheng, Wang, et al., 2023). The average T values of non-aligned CNF, aligned CNF, non-aligned $BaTiO_3$-CNF, and aligned $BaTiO_3$-CNF are 1.80 $x10^{-2}$, 1.22 x 10^{-3}, 2.75 x 10^{-5}, and 1.97 x 10^{-6}, respectively. The aligned CNF have lower T values compared to the non-aligned and with loading of $BaTiO_3$ into CNF, T values further decrease. The average A values of non-aligned CNF, aligned CNF, non-aligned $BaTiO_3$-CNF, and aligned $BaTiO_3$-CNF are 0.405, 0.311, 0.0.370, and 0.343, respectively.

The average SE_R and SE_A values of non-aligned CNF, aligned CNF, non-aligned $BaTiO_3$-CNF, and aligned $BaTiO_3$-CNF are shown in **Figure 8.9(a)**. The SE_R value is low for all the samples and there is no enhancement in SE_R after the incorporation of $BaTiO_3$ NPs into CNF and this suggests that in $BaTiO_3$-CNF, EM waves undergo multiple internal reflections resulting in dielectric losses. These dielectric losses are induced by multiple polarization relaxations due to electronic polarization in covalent bonds of C-N, and C=N, interfacial polarization due to hetero-interfaces, and dipole polarization caused by $BaTiO_3$ NPs incorporated in CNF under the electric field (Ma et al., 2023).

The complex relative dielectric permittivity ($\varepsilon_r^* = \varepsilon_r' - j\varepsilon_r''$) of PDMS composites of non-aligned CNF, aligned CNF, non-aligned $BaTiO_3$-CNF, and aligned $BaTiO_3$-CNF were also investigated for better understanding of the shielding mechanism.

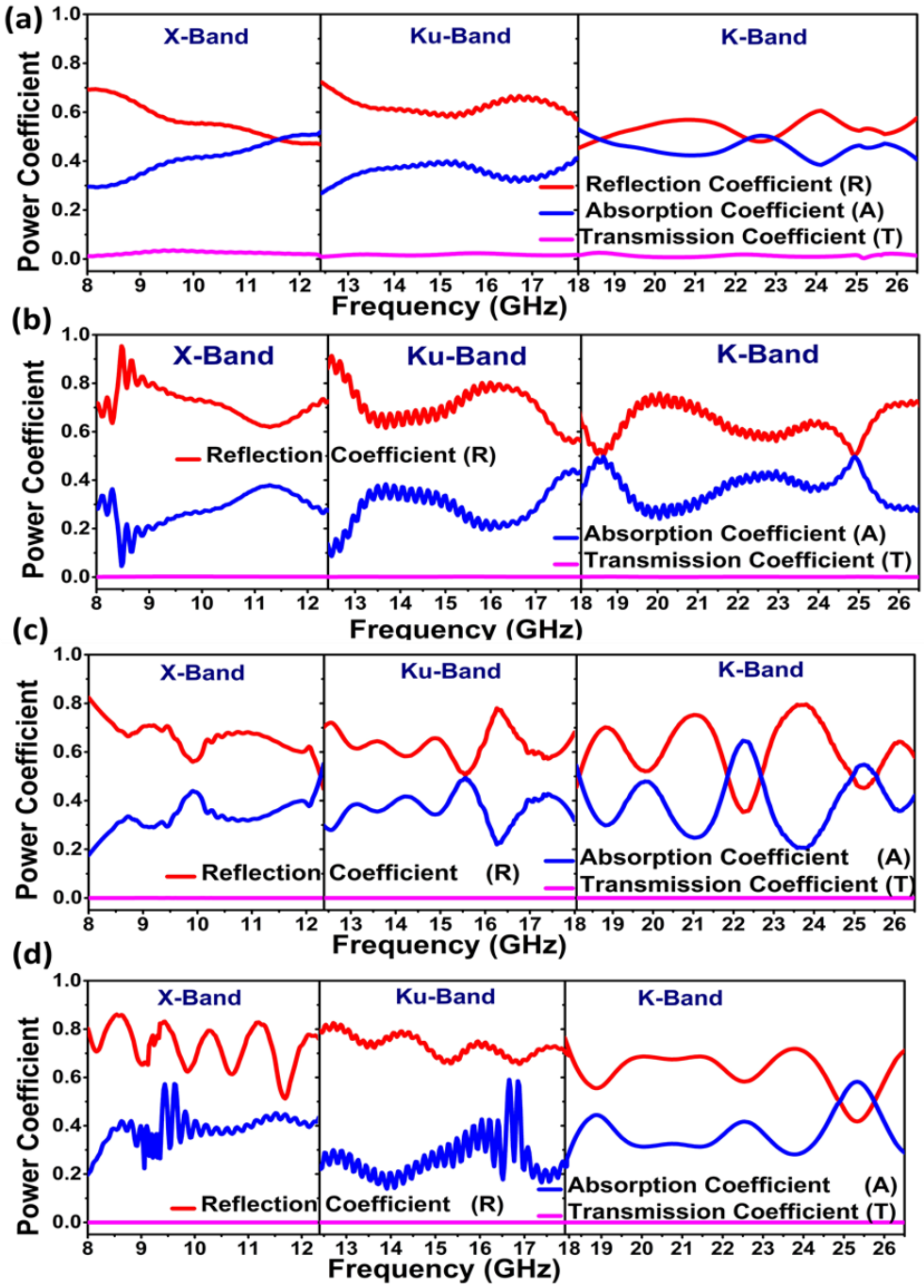

Figure 8.9: (a-d) Power coefficients of non-aligned CNF (h), aligned CNF (i), non-aligned $BaTiO_3$-CNF (j), and aligned $BaTiO_3$-CNF, respectively in X, Ku, and K-band.

The real part of complex permittivity (ε_r') is often associated with polarization, which is related to the separation and alignment of electric dipoles in materials caused by an electric field, while imaginary part (ε_r") denotes the dissipation of electrical energy. (Lv et al., 2017; Sajid et al., 2022) As can be seen in **Figure 8.10 (a-b)**, the pristine PDMS exhibited low ε' and ε" and the values increased for PDMS composite of non-aligned CNF and aligned CNF.

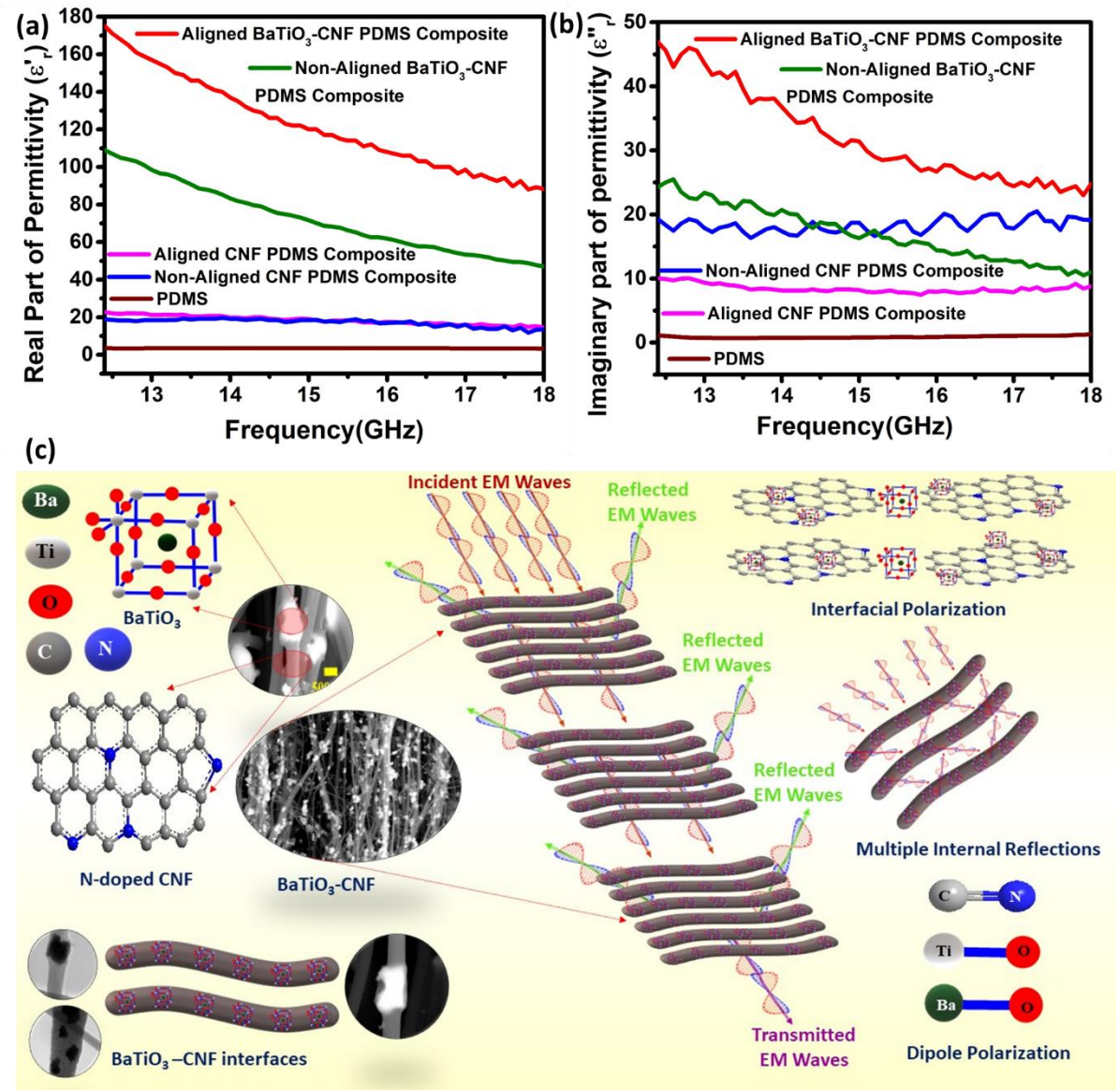

Figure 8.10: (a-b) Variation of real part (a) and imaginary part (b) of dielectric permittivity of pristine PDMS and PDMS composite of non-aligned CNF, aligned CNF, non-aligned $BaTiO_3$-CNF, and aligned $BaTiO_3$-CNF in the frequency range of 12.4-18 GHz (Ku-band). (c) Schematic Illustration of EMI shielding mechanism of $BaTiO_3$-CNF.

The values further increased for PDMS composite of non-aligned $BaTiO_3$-CNF, and aligned $BaTiO_3$-CNF due to formation of multiple hetero-interfaces between the $BaTiO_3$ NPs and CNF. The complex relative dielectric permittivity ($\varepsilon_r^* = \varepsilon_r' - j\varepsilon_r''$) is dependent on the frequency as seen in **Figure 8.10(a-b)**. The aligned $BaTiO_3$-CNF exhibited high dielectric properties due to alignment of $BaTiO_3$ NPs, which improve the interfacial polarization and EM wave attenuations. $BaTiO_3$-CNF has electrically conductive network with interfacial polarization between $BaTiO_3$ NPs and CNF. The hierarchical 3-D electrically conductive network, formation of hetero-interfaces between $BaTiO_3$ NPs and CNF, and 1-D fibrous structure of

$BaTiO_3$-CNF led to dielectric losses (conduction loss, polarization loss, interfacial polarization) and multiple internal reflections, resulting in higher SE_A (more than 80 %) compared to SE_R as shown in **Figure 8.8(h).** The EMI shielding mechanism of $BaTiO_3$-CNF is illustrated in **Figure 8.10(C)**. The bending cycle test was performed as shown in **Figure 8.8 (i)** (Y. Wang et al., 2019; Zhu Zhang et al., 2022). **Figure 8.8(j)** illustrate the EMI SE of PDMS composite of non-aligned $BaTiO_3$-CNF, and aligned $BaTiO_3$-CNF tested before and after 500 cycles of bending and releasing. The results indicate that all the samples retained their EMI SE value upto 90 % even after 500 cycles, suggesting the high flexibility of the PDMS composites.

Lightweight shielding materials are extremely important for aerospace applications. Density of shielding materials is a significant parameter to determine the SSE of different materials as mentioned in **Equation 15**. The highest SSE values of aligned CNF, non-aligned $BaTiO_3$-CNF, and aligned $BaTiO_3$-CNF are 86, 64, and 88 dB cm^3 g^{-1}, respectively. The SSE value of PDMS composite of aligned CNF, non-aligned $BaTiO_3$-CNF, and aligned $BaTiO_3$-CNF are 29, 36, and 49 dB cm^3 g^{-1}, respectively. SSE alone is not adequate criterion for assessment of of shielding materials, because high SSE can be attained by increasing the thickness, which will further raise the final weight of shielding materials. As a result, in comparison to SSE, SSE_t is a more realistic way to evaluate the shielding effectiveness of materials. The highest SSE_t values of aligned CNF, non-aligned $BaTiO_3$-CNF, and aligned $BaTiO_3$-CNF are 3583, 2678, and 3676 dB cm^2 g^{-1}, respectively. The SSE_t value of PDMS composite of aligned CNF, non-aligned $BaTiO_3$-CNF, and aligned $BaTiO_3$-CNF are 341, 426, and 585 dB cm^2 g^{-1}, respectively. These materials are promising for commercial applications because of high EMI SE, and high SSE_t. **Table 8.1** provides a comparison of the reported EMI SE values of the similar systems and the present work.

Table 8.1: Comparison of EMI shielding of similar kinds of composites.

Sample	**Thickness (mm)**	**Frequency Range**	**EMI SE (dB)**
Fe_2O_3/$BaTiO_3$/MWCNT additive (Im et al., 2010b)	-	800 MHz- 4 GHz	37
Axial alignment of CNT on fibers (Lan et al., 2020)	1.49 µm	8.2-18 GHz	21
Self-aligned/polymer composite films (P. Kumar et al., 2017)	Thin films	8.2-12.4 GHz	~30
Biomass-based aligned carbon nanostructure (J. Chen et al., 2022)	~ 0.3	8.2-12.4 GHz	49
CQD@$BaTiO_3$/$BaFe_{12}O_{19}$ (Goel et al., 2021)	2.75	8.2-12.4 GHz	25
Carbonyl Iron/$BaTiO_3$ composite (Qing et al., 2011)	2.00	8.2-12.4 GHz	42
$BaTiO_3$/rGO composite (Ran et al., 2019)	2.5	5.4 GHz	44
Polyaniline-Tetragonal $BaTiO_3$ nanocomposite (Saini et al., 2013)	-	Ku Band	71
Aligned CNF	**0.24**	**8.2-26.5 GHz**	**30 (This work)**
Non-aligned $BaTiO_3$-CNF	**0.24**	**8.2-26.5 GHz**	**61 (This work)**
Aligned $BaTiO_3$-CNF	**0.24**	**8.2-26.5 GHz**	**81 (This work)**

8.4 Conclusion

Herein, we have demonstrated the fabrication of flexible materials with EMI shielding property in X, Ku, and K-band. The effect of alignment of N-doped CNF and the presence of dielectric materials ($BaTiO_3$ NPs) in CNF on EMI SE have been analyzed. The aligned $BaTiO_3$-CNF exhibited a higher EMI SE of 81 dB compared to the non-aligned $BaTiO_3$-CNF (61 dB). The high EMI SE value is due to high dielectric properties of $BaTiO_3$ and formation of 3D electrically conductive network of N-doped CNF. The alignment of N-doped CNF enhanced the electrical conductivity along the fiber axis. The synergistic effect of $BaTiO_3$ NPs and N-doped CNF made the high-performance EMI shielding materials. The PDMS composites of $BaTiO_3$-CNFs were prepared to improve flexibility and ease of handling for industrial applications. The flexible and hydrophobic PDMS composite of $BaTiO_3$-CNFs have potential applications in flexible electronic devices as shielding materials for next-generation applications.

CHAPTER: 9

Carbon black incorporated CNF and PDMS Composite for EMI Shielding

Overview

The work presented in the previous chapters discussed the EMI shielding properties of CNF, PEDOT:PSS coated CNF, Te NPs incorporated CNF (Te-CNF), metal oxide NPs (Nb_2O_5, LSCO, and $BaTiO_3$) incorporated CNF. The current chapter concerns with investigation of EMI shielding properties of carbonic filler (carbon black super P (CBSP)) incorporated CNF (CBSP@CNFs) in X-band, Ku-band, and K-band. The highest and average values of EMI SE for 9 wt% and 16.6 wt% of CBSP NPs loaded in CNFs were 55.8 and 50.7 dB. The SSE_t values of 0.06 mm thick CBSP@CNFs) were 24,837 and 14741 dB cm^2 g^{-1} respectively. These values are remarkably higher than the most reported EMI shielding materials.

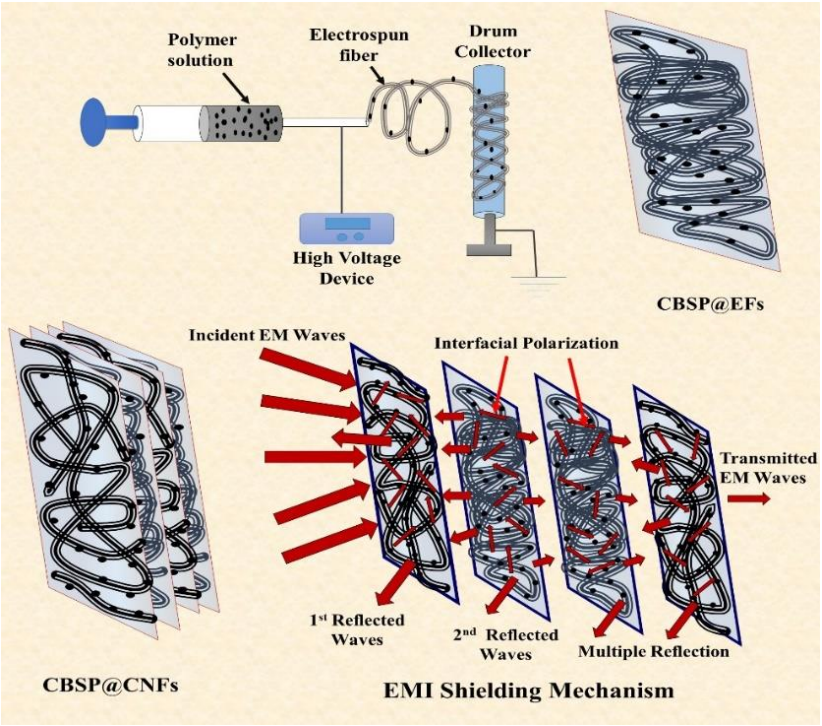

9.1 Introduction

Carbon black (CB) is a chemically stable, lightweight material that is extensively utilized to produce conductive polymer composites for the dissipation of electrostatic discharge. Compared to other conductive carbon materials such as CNTs and graphene, carbon black is a far less expensive solution. However, a high amount of carbon black (>40 wt%) is required to prepare a conducting polymer composite, limiting its economic applicability for EMI shielding (N. C. Das et al., 2001; Im et al., 2009; Jinyoung Kim et al., 2021; Rani et al., 2020). Im et al. employed electrospinning and heat treatment to fabricate Carbon black (CB) embedded carbon fibers(CFs) for EMI shielding. Fluorination was utilized to enhance dispersion of CB in the hydrophobic electrospinning solution. The fluorinated CB was dispersed in 10 wt% PAN solution in DMF. The fluorinated CB embedded carbon fiber showed an EMI SE value of 50 dB in the frequency range of 800-4000 MHz (Im et al., 2009). This frequency band is too narrow for practical use and is inadequate for satellite communication or military applications.

This chapter reports highly flexible carbon black super P (CBSP) incorporated CNFs (CBSP@CNFs) and its PDMS composite which exhibit excellent EMI shielding property in the frequency range of 8.2-26.5 GHz. CBSP@CNFs were fabricated via electrospinning method followed by heat treatment. Because of its good electrical conductivity, CBSP@CNFs exhibited 55.9 dB of EMI SE at a thickness of 0.06 mm. Carbon nanofibers (CNFs), as well as the filler CBSP, are of light weight, resulting in a material of very high absolute EMI SE value (24837 dB cm^2 g^{-1}) compared to the materials previously reported in literature for carbon based composites.

9.2 Experimental

9.2.1 Materials

The specifications of PAN, CBSP, DMF, and SLYGARD^{TM} 184 silicone elastomer kits are mentioned in chapter 2 (refer to section 2.1)

9.2.2 Preparation of CBSP incorporated CNF (CBSP@CNFs)

The electrospinning solution was prepared by mixing carbon black super P (CBSP) (0, 50 mg, and 100 mg (0, 9 and 16.6 wt %)) in 0.5 g of PAN in 5 mL of DMF by continuous stirring at 80 ℃ for 12 h. The homogenously dispersed solution was loaded into a 5 mL syringe for electrospinning. A high voltage (10 kV) was applied to the tips of the needle, and nanofiber was collected on aluminium foil pasted on a rotating drum collector.

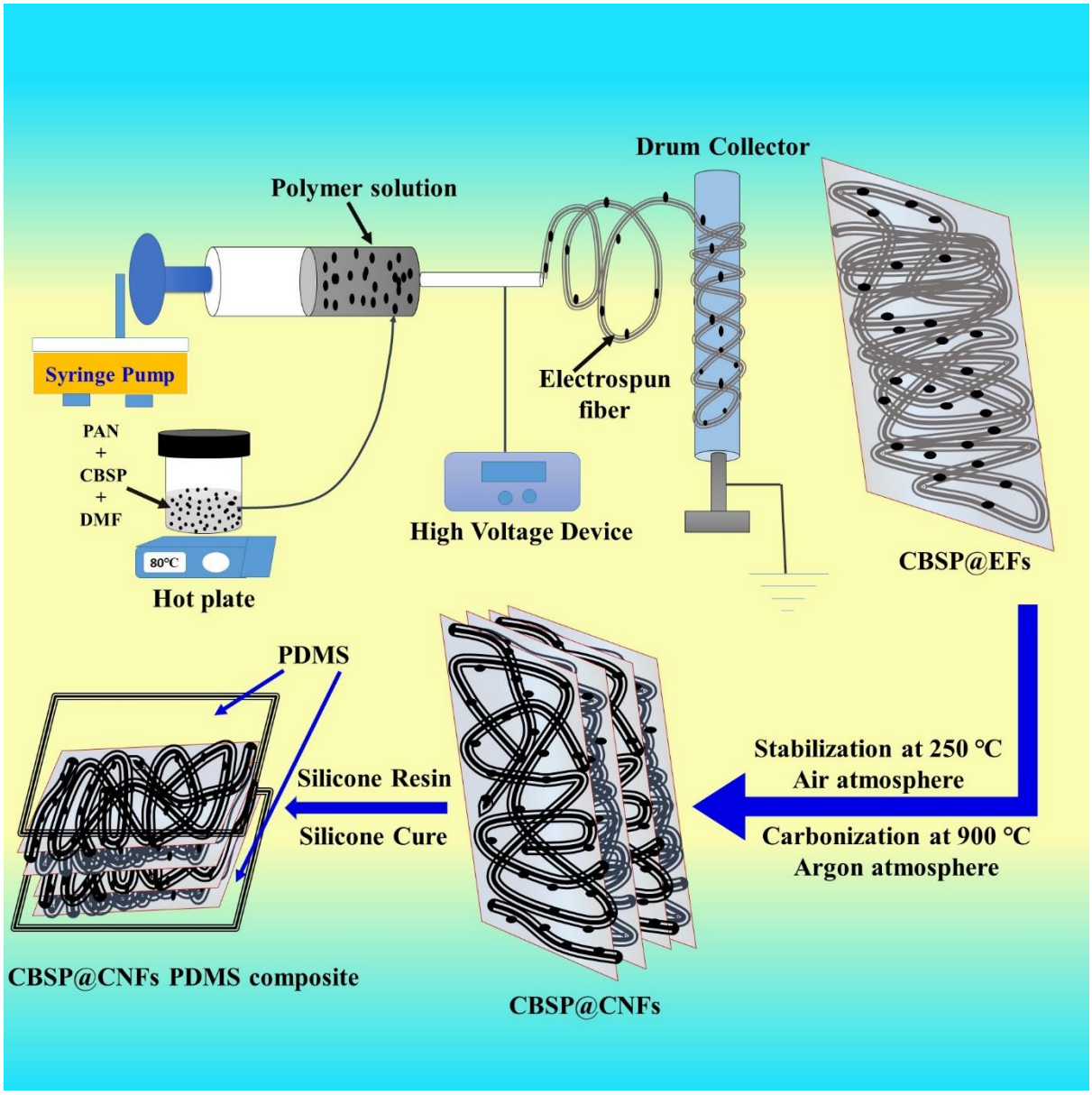

Figure 9.1: Fabrication process of CBSP@EFs, CBSP@CNFs, and CBSP@CNFs PDMS composite.

The drum collector was placed 13 cm away from the tip of the metallic needle. The flow rate of the electrospinning solution was 0.8 mL h^{-1}. The obtained fibers were dried at room temperature for 12 h to obtain CBSP NPs incorporated electrospun nanofiber (CBSP@EFs) mats. The CBSP@EFs mats were stabilized in an air environment at 250 °C for 6 h and then carbonized at 900 °C with the ramping rate of 3 °C min^{-1} for 2 h in an argon atmosphere. The CBSP incorporated carbon nanofibers (CBSP@CNFs) with 0, 50 mg, and 100 mg loading of the CBSP@CNFs are referred to as CNFs, CBSP@CNFs-50, and CBSP@CNFs-100, respectively. These mats were cut into particular dimensions according to the dimension of waveguide adaptor for X, Ku, and K- bands for EMI shielding measurements.

9.2.3 Fabrication of flexible PDMS composite of CBSP@CNFs

The PDMS composite of CBSP@CNFs were prepared in similar ways as mentioned in chapter 2 (section 2.3).

9.3 Results and discussion

Metal NPs are used to impart conductivity to polymer composites. However, high concentration of metal NPs is required to attain high electrical conductivity and EMI SE, and as a result, composites become heavy and inflexible. Carbon black (CB) is a conductive filler commonly used for making plastic materials conductive (Barkoula et al., 2008; Islam et al., 2018; Van Bellingen et al., 2002). The small particle size of CB provides more specific surface area for electron transfer (H. J. Choi et al., 2019). CBSP is a popular conductive additive which can enhance battery performance with addition of minimum amount of the additive (Kannan et al., 2021). This contains very light weight particles with moderate surface area (62 m^2 g^{-1}) which can provide more specific surface area for electron transfer. In this work, we have used CBSP as an additive in CNFs to enhance the electrical conductivity. CBSP@CNFs were fabricated by electrospinning methods, a stabilization process, and carbonization heat treatment in an argon atmosphere. The enhancement in conductivity upon addition of conductive fillers depends upon the continuity of the percolation path arising from the contact between the filler particles and the interaction of these particles with the matrix material. Here, CNFs containing CBSP was obtained by carbonization of electrospun PAN fiber. Thus, the conductive network of CNFs is influenced by the dispersion of CBSP into PAN solution used for electrospinning. Homogeneous dispersion of CBSP in PAN solution was achieved by constant stirring for 12 h and a stable jet for electrospinning was achieved by easily optimizing the electrospinning conditions. Effective dispersion of CBSP is presumed to reduce the distance between CBSP particles and enhance the formation of conductive paths. The electrospinning technique helps to improve the distribution of CBSP particles throughout the electrospun fiber. The fabrication process of CBSP@CNFs and their PDMS composite is illustrated in **Figure 9.1**.

9.3.1 TEM image

The TEM images of electrospun PAN nanofiber without and with CBSP are shown in **Figure 9.2(a-d)**. The TEM images of electrospun PAN nanofiber without CBSP **(a)** and CBSP **(b-d)** show that fiber is continuous without any bead formation. **Figure 9.2(c-d)** reveals that CBSP is distributed along with the fiber as well as embedded into the electrospun nanofiber. The

average diameter of electrospun PAN nanofiber without CBSP and CBSP is 319 ± 26 nm and 545 ± 34 nm, respectively.

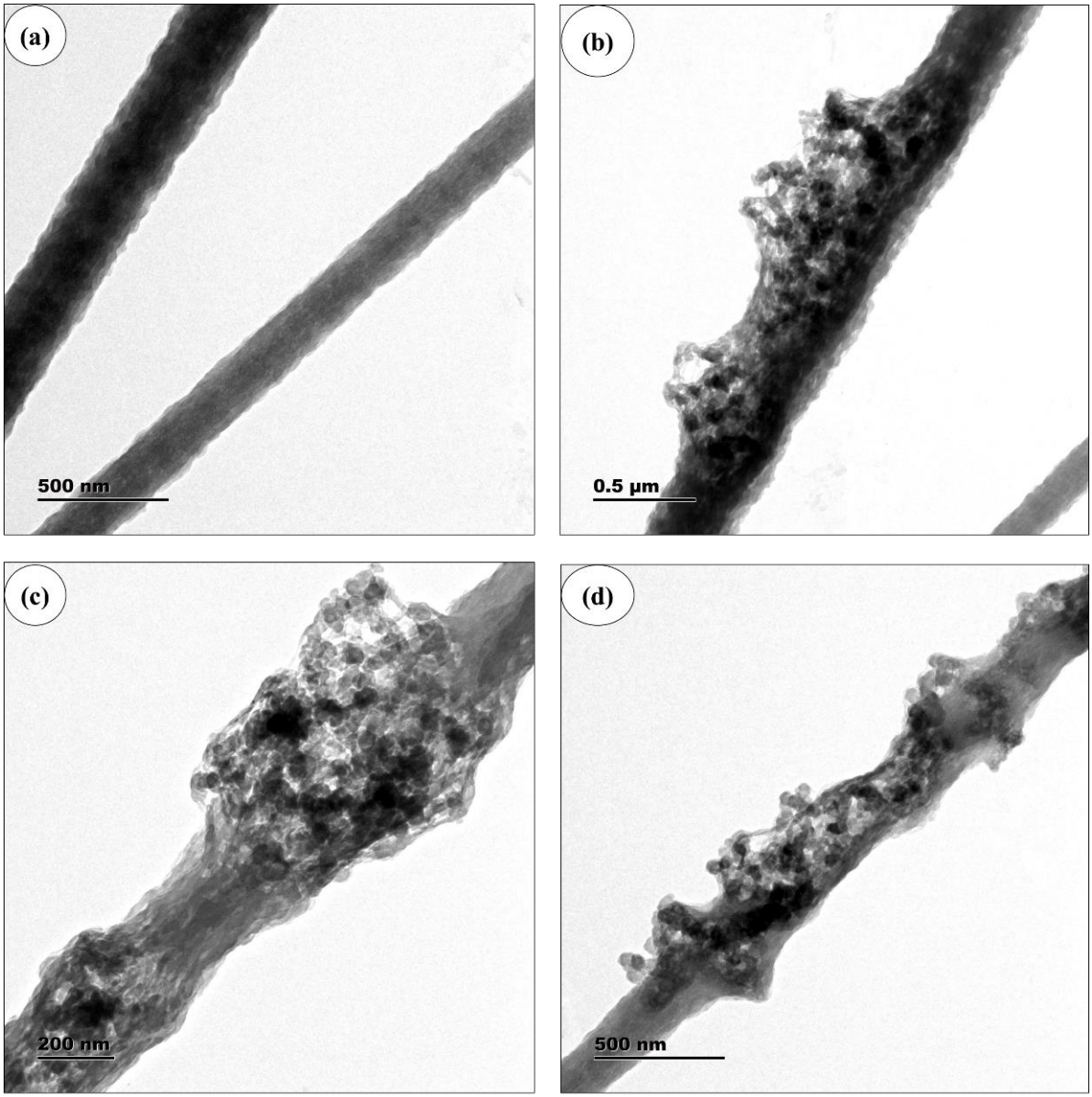

Figure 9.2: TEM image of electrospun fiber (a) PAN fiber and (b-d) CBSP@EF-100.

9.3.2 SEM image

The surface morphologies of the CNFs (**Figure 9.3(a-b))** and CBSP@CNFs (**Figure 9.3 (c-f**)) are shown in **Figure 9.3(a-f)**. The SEM image of CNFs (**Figure 9.3(a-b))** shows that the fiber is continuous and prolonged, whereas after incorporation of CBSP (**figure 9.3(c-f)**, the fiber becomes discontinuous and of shorter length. This may have effect on the mechanical properties of the fiber. CBSP@CNFs have wide ranges of diameter from 600 nm to 900 nm, with an average diameter of 790 ± 126 nm, whereas without CBSP, the average diameter of

the fiber is 378 ± 53 nm. It is evident from the images (**Figure 9.3(c-f))** that CBSP particles are aggregated continuously over the carbon fibers increasing the diameter and forming a conducting path. The formation of this conducting path is expected to enhance the conductivity and EMI shielding property of CBSP@CNFs.

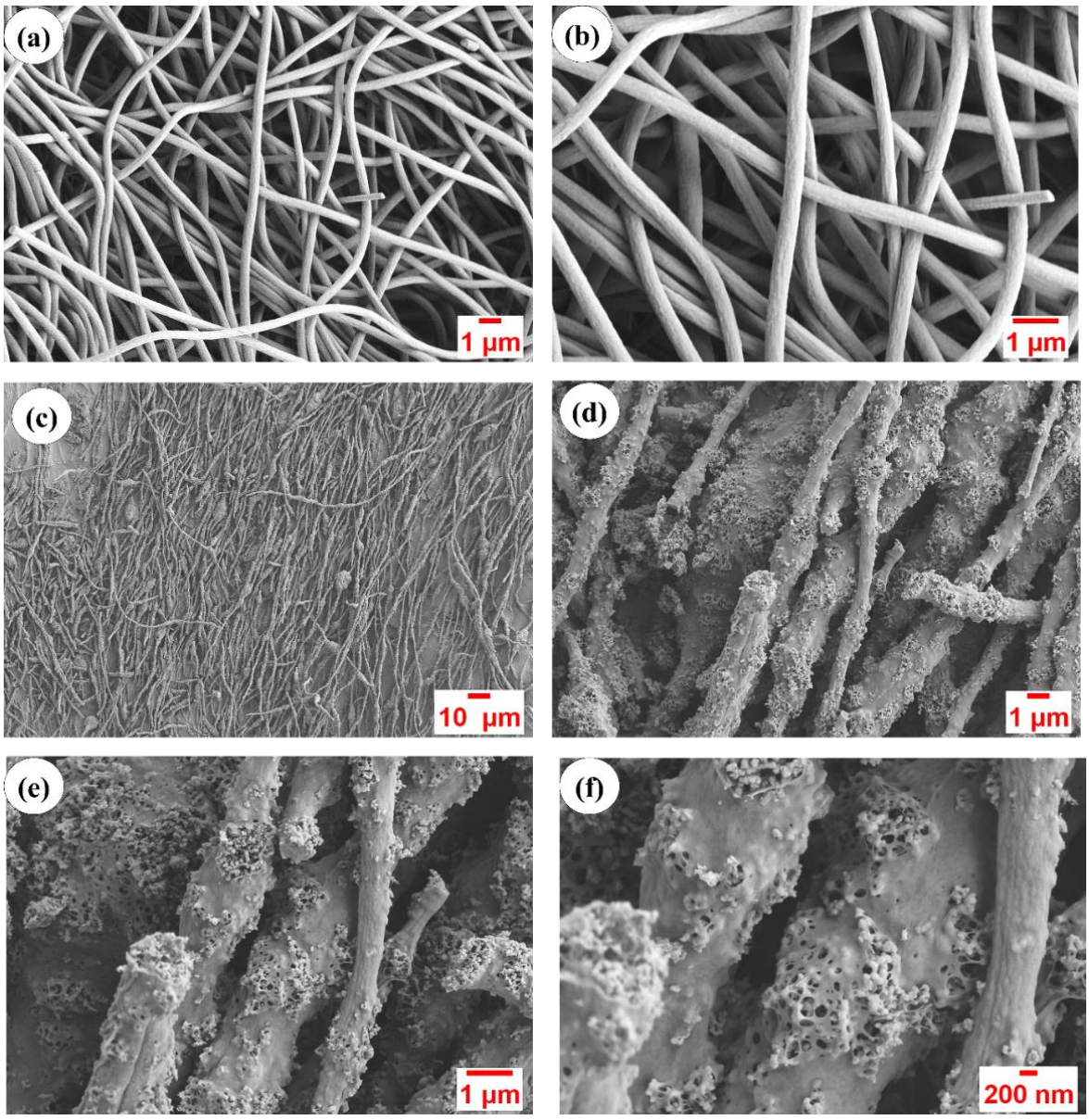

Figure 9.3: SEM images of (a-b) CNFs and (c-f) CBSP@CNFs-100.

9.3.3 Raman Spectroscopy

Raman spectroscopy is one of the most successful methods for determining the structural properties of carbon-based materials. **Figure 9.4(a)** shows Raman spectra of CNFs and CBSP@CNFs. The D- peaks around 1352 cm^{-1} imply a disordered structure, whereas the G peak near 1590 cm^{-1} indicates a graphitic structure of CBSP@CNFs and CNFs. The degree of

graphitization or the relative fraction of sp^2 hybrid carbon atoms in the carbon fiber was determined using the formula $R=I_D/I_G$ (I_D and I_G indicate integral intensities of the D and G peaks, respectively). The obtained R-value is 0.90 for both samples, suggesting the crystallinity and graphitization upon carbonization.

9.3.4 XRD patterns

The XRD patterns of CBSP@CNFs are shown in **Figure 9.4(b),** confirming the presence of CBSP and carbonization of PAN fiber. According to the literature, the broad peaks centered at 26.0° and 42.3° are related to (002) and (010) planes of the graphite carbon structure (JCPDS 41-1487), belonging to carbonized PAN fiber as well as for CBSP (Q. Y. Chen et al., 2014). The diffraction peak of CNFs without CBSP at 26.0° indicates the graphitic structure of carbonized PAN fiber. After incorporation of CBSP, the diffraction peaks at 26.0° and 42.3° have relatively high intensity and less broadening, indicating significant graphitization and crystallization in CBSP@CNFs.

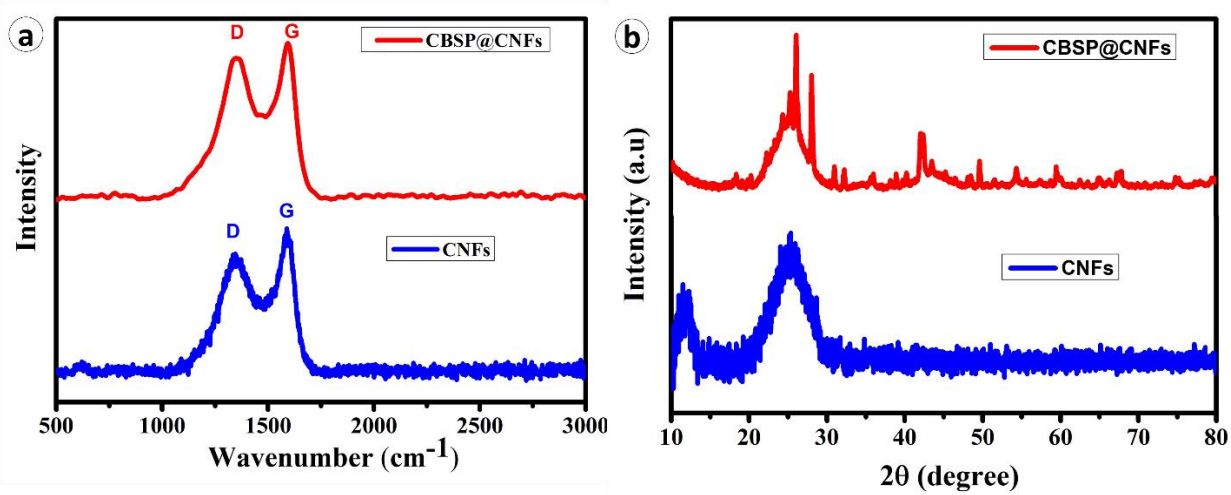

Figure 9.4:(a) Raman spectra and (b) XRD patterns of CNFs and CBSP@CNFs.

9.3.5 Contact angle measurements

The contact angle of CBSP@CNFs and CBSP@CNFs PDMS composite are 125° and 117°, respectively indicating the hydrophobic nature of CBSP@CNFs as well as the PDMS composite **(Figure 9.5).**

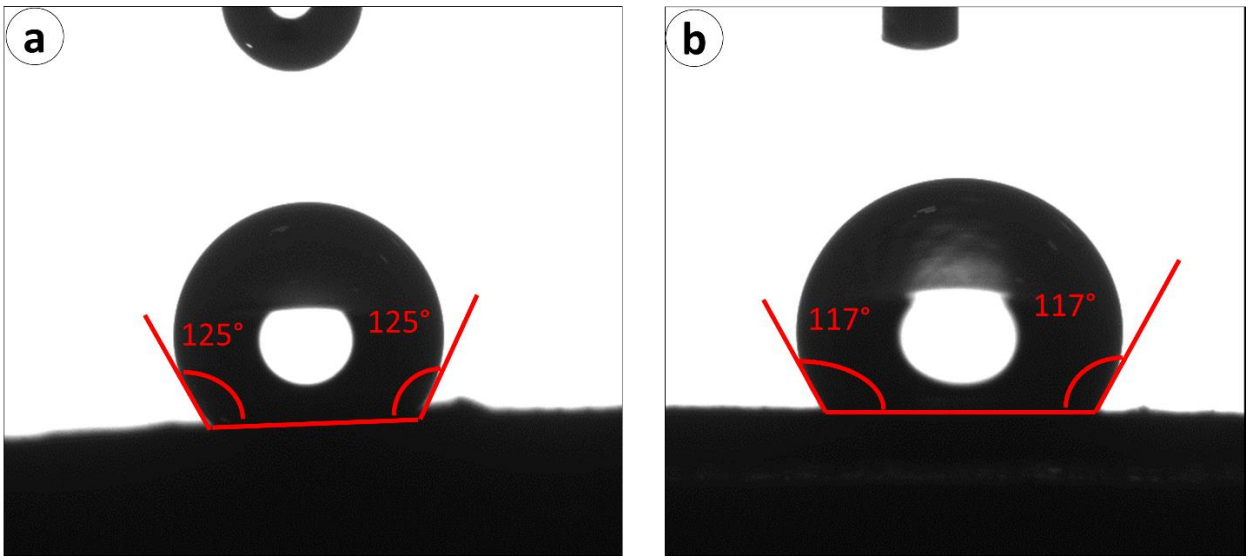

Figure 9.5: Contact angle measurement of (a) CBSP@CNFs and (b) CBSP@CNFs PDMS composites.

9.3.6 Mechanical test

As illustrated in **Figure 9.6**, CBSP@CNFs PDMS composites exhibit high flexibility and good mechanical properties. A piece of CBSP@CNFs PDMS composite was twisted into a roll, bent, folded, and then returned to its flat surface. The mat's structural integrity and EMI shielding were still intact, proving the mat's exceptional flexibility.

The temperature-dependent mechanical properties of composites of PDMS, CNFs PDMS, CBSP@CNFs-50 PDMS, and CBSP@CNFs-100 PDMS were investigated using DMA. **Figure 9.6(e)** shows the overlay plots of storage modulus versus temperature for PDMS and composites with CNFs, CBSP@CNFs-50, and CBSP@CNFs-100. Here, we measure the change of storage modulus (E') of the samples, which refers to the elasticity or stiffness the composites and is proportional to the energy stored during one period under load. The storage modulus of the composites increases with the incorporation of CNFs as expected, but decreases with loading of CBSP in CNFs. The storage modulus of PDMS and PDMS composites of CNFs, CBSP@CNFs-50, and CBSP@CNFs-100 are 16.1, 175.8, 135.0, and 29.7 MPa, respectively. Carbon nanofibers (CNFs) have a high aspect ratio (length to diameter ratio), but upon loading of CBSP, the fibers become discontinuous and shorter in length, as shown in SEM image (**Figure 9.3**). This may be the reason for the observed decrease in storage modulus of CBSP@CNFs PDMS composites in comparison to CNFs PDMS composite.

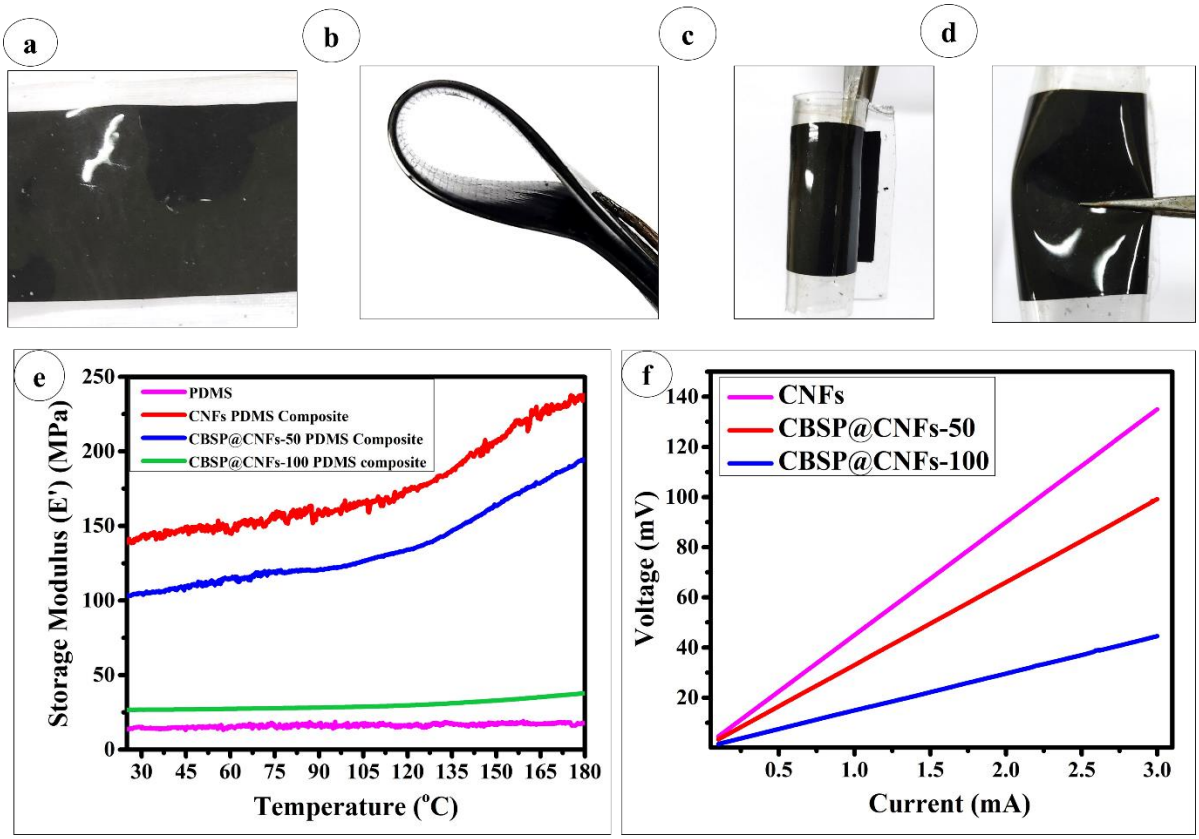

Figure 9.6: (a) Photograph of CBSP@CNFs PDMS composite. (b-d) Photographs of bending, rolling, and folding, of CBSP@CNFs PDMS composite, respectively. (e) Storage modulus vs. temperature curve. (f) Voltage-current graph of CNFs, CBSP@CNFs-50, and CBSP@CNFs-100.

9.3.7 Electrical conductivity measurement

The current-voltage graphs of CNFs, CBSP@CNFs-50, and CBSP@CNFs-100 are shown in **Figure 9.6(f).** A straight line demonstrates that resistance does not vary when the current varies from 0.1 to 3 mA, as shown in **Figure 9.6(f)**. The conductivity and resistivity of CNFs were determined using **Equations 18, 19, and 20**. Conductivities of CBSP@CNFs-100, CBSP@CNFs-50 and CNFs were 2.5, 1.2, and 0.8 S cm^{-1}, respectively. The resistance of CNFs decreases when CBSP is loaded, and their conductivity increases. Hence, they are expected to exhibit EMI shielding properties also.

9.3.8 EMI SE

Figure 9.7 (a-c) shows the EMI SE of the CNFs, CBSP@CNFs-50, and CBSP@CNFs-100. The samples used for the measurements were of 0.06 mm thickness. A significant increase in EMI SE with increase in loading of CBSP suggests that EMI SE is strongly correlated to the electrical conductivity, and EMI SE increases with increase in electrical conductivity. The

average EMI SE value of CNFs, CBSP@CNFs-50, and CBSP@CNFs-100 are 23.1 dB, 34.1 dB, and 43.6 dB, respectively, in X, Ku, and K-band. **Figure 9.7 (d-f)** shows the EMI SE of CNFs PDMS composite, CBSP@CNFs-50 PDMS composite, and CBSP@CNFs-100 PDMS composite. The samples used for the measurements were of 0.31 mm thickness. The average EMI SE is decreased after making the composites because the surface of the composite is an insulator and pure PDMS composite shows zero EMI SE. The average EMI SE value of CNFs PDMS composite, CBSP@CNFs-50 PDMS composite, and CBSP@CNFs-100 PDMS composite are 17.8 dB, 33.1 dB, and 45.2 dB, respectively, in X, Ku, and K-band. Commercial EMI shielding materials usually possess a large thickness (more than 1 mm) or high density to satisfy the commercial requirement of EMI shielding materials and usually, the reflection mechanism would be dominant. But, here, samples with low thickness and low density show high EMI shielding property. It can be seen from **Figure 9.7** that SE_A is dominant than SE_R and hence contributing more towards SE_T. It is shown that EMI shielding due to absorption is 85 percent more than that of reflection for all the samples over the entire frequency range. **Figure 9.8** illustrates the EMI shielding mechanism of CBSP@CNFs and their PDMS composites. The high EMI shielding property emanates from the high conductivity of CBSP@CNFs. The layer-by-layer structure of CNFs lead to dominance of SE_A.

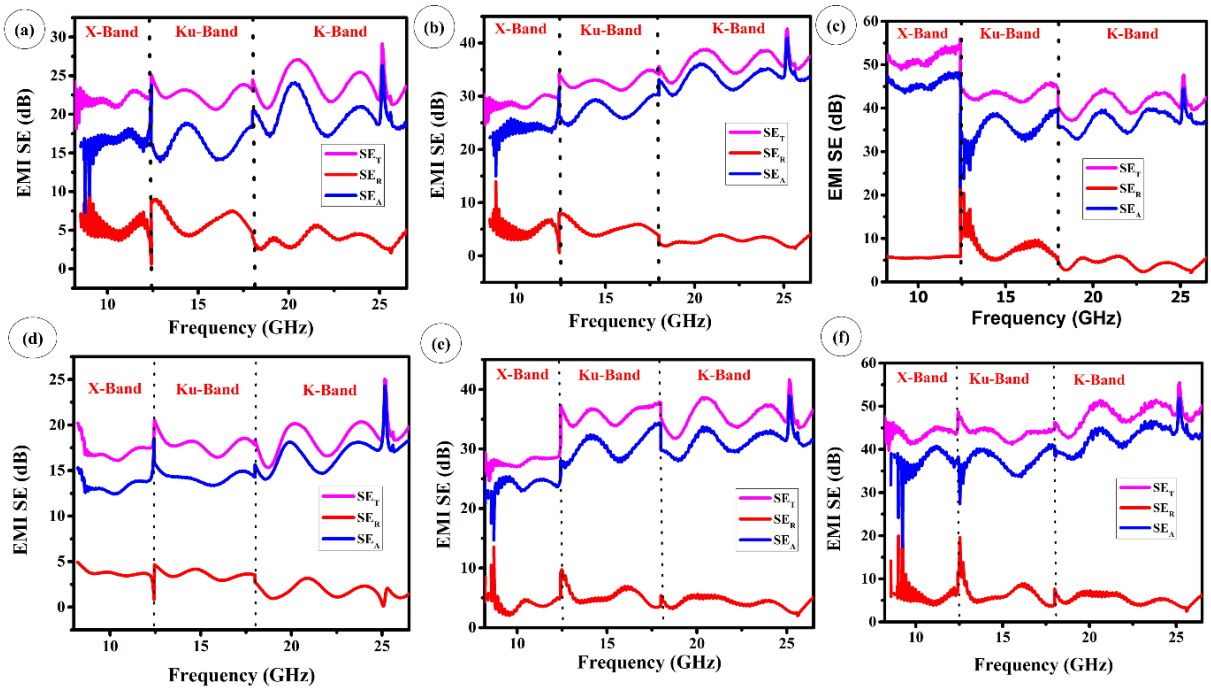

Figure 9.7: EMI SE of (a) CNFs, (b) CBSP@CNFs-50, (c) CBSP@CNFs-100, (d) CNFs PDMS composite, (e) CBSP@CNFs-50 PDMS composite, and (f) CBSP@CNFs-100 PDMS composite.

CBSP NPs are very light weight and as seen from the SEM images, the particles are distributed throughout the electrospun fiber. The continuous distribution of CBSP NPs, leads to the formation of a conductive network that enhances the polarization loss. It was observed that CNFs as well as CBSP@CNFs exhibit a significant increase in conductivity, because of graphitization and formation of conductive network upon carbonization. The effective interaction between CBSP and CNFs leads to high electrical conductivity and EMI shielding performance. The porous structure of CNFs allows the incident EM rays to pass through the layers and be reflected by the multiple layers of CNFs. Because of the layer-by-layer fibrous structure of CNFs, interfacial polarisation and multiple internal reflection increase, and due to this SE_A dominates. When the loading of CBSP NPs is increased CBSP NPs come closer increasing the continuity of the conductive network and interfacial polarization, and in turn enhances the electrical conductivity of CBSP@CNFs. The synergetic effect of all these factors help to improve the total EMI shielding performance of CBSP@CNFs as shown in **Figure 9.8.**

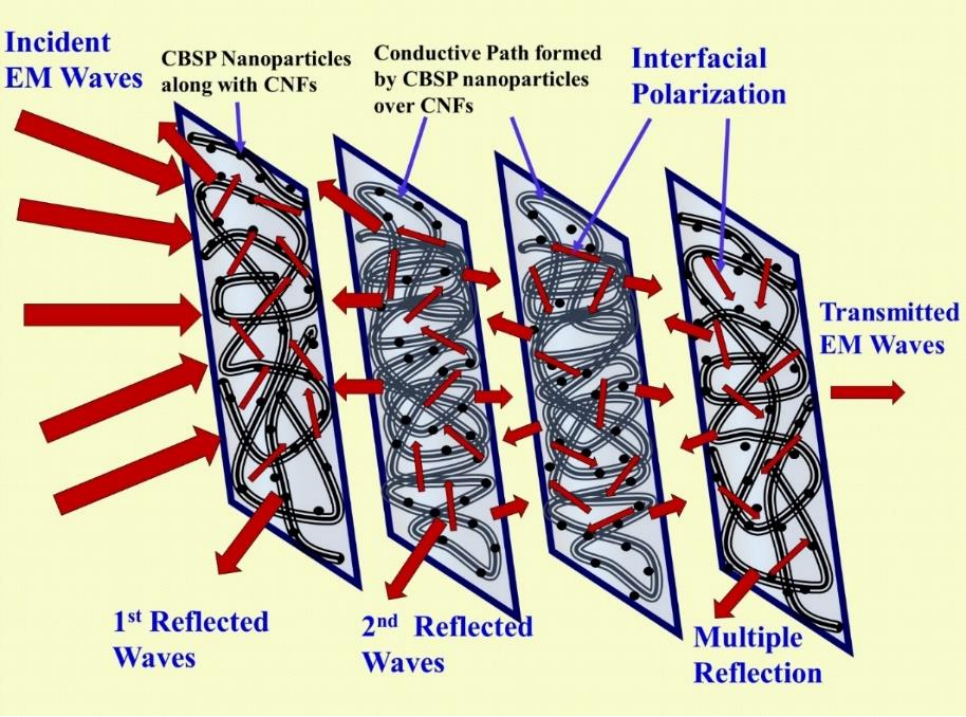

Figure 9.8: EMI shielding mechanism of CBSP@CNFs.

Flexibility, stretchability, hydrophobicity, thickness, and density are critical for EMI shielding performance of materials in practical applications. The electrospun fiber based composite shows very high SSE and SSE_t because of low thickness and low density. The density of CNFs, CBSP@CNFs-50, CBSP@CNFs-100, CNFs PDMS composite, CBSP@CNFs-50 PDMS composite, and CBSP@CNFs-100 PDMS composite are 0.159, 0.257, 0.632, 1.850, 1.970, and

2.12 g cm^{-3} respectively. The SSE and SSE_t are calculated using **Equation 15** and **16**, respectively. CBSP@CNFs have average SSE and SSE_t values of 132.8 dB cm^3 g^{-1} and 22140.0 dB cm^2 g^{-1}, respectively, higher than most other reported EMI shielding materials. The value of SSE and SSE_t of all the samples along with the corresponding values for the materials reported in the literature are mentioned in **Table 9.1**.

Table 9. 1: Summary and comparison of the EMI shielding performance of the materials.

Sample	**Conductivity (S cm^{-1})**	**Thickness (mm)**	**Frequency (GHz)**	**EMI SE_T (dB)**	**SSE (dB cm^3 g^{-1})**	**SSE_t (dBcm^2 g^{-1})**
CNFs	**0.81**	**0.06**	**8.2-26.5**	**24.2**	**151.5**	**252555.6**
CBSP@CNFs-50	**1.11**	**0.06**	**8.2-26.5**	**38.3**	**132.8**	**24837.8**
CBSP@CNFs-100	**2.493**	**0.06**	**8.2-26.5**	**55.9**	**68.9**	**14741.5**
CNFs PDMS composite	**-**	**0.31**	**8.2-26.5**	**20.1**	**9.6**	**350.3**
CBSP@CNFs-50 PDMS composite	**-**	**0.31**	**8.2-26.5**	**37.6**	**16.8**	**615.6**
CBSP@CNFs-100 PDMS composite	**-**	**0.31**	**8.2-26.5**	**50.7**	**21.3**	**770.7**
P@Ni-Co-120 hybrid membrane N. Zhang et al., 2019)	1139.6	0.180	8-26.5	77.8	131.9	7325.8
GO/WPU fiber (Hsiao et al., 2014)	0.168	1	8.2-12.4	34	-	-
Ag NW-coated cellulose papers	67.5	0.164	0.5-1	48.6	91.7	5591.5

(T.-W. Lee et al., 2016)						
Pd-CNT-Cu bucky paper (A. Kumar et al., 2015	11.64	0.2	12-18	35	109.4	5468.7
Ni-Co-B-coated carbon nanofibers hybrids (Xie et al., 2008)	-	1.2	8-18	20.1	-	-
Graphene/PDMS foam (Z. Chen et al., 2013)	2	1	8-12	30	500	5000
Graphene film (Shen et al., 2014)	1000	0.0084	8-12	20	-	-
Fluorinated Carbon black (FCB)/PAN fiber (Im et al., 2009)	38		800-4000 MHz	50	-	-
Ag- decorated PVA/Fe_2O_3 nanofiber composites (H. R. Kim et al., 2012)		-	10	45.2	-	-

9.4 Conclusion

Carbon black super p incorporated carbon nanofibers and their PDMS composites were successfully fabricated by electrospinning and heat treatment for EMI shielding applications. CBSP@CNFs show high electrical conductivity and high EMI SE with low thickness and low density. The CBSP@CNFs exhibited the highest EMI SE value of 55.9 dB in X, Ku, and K-

band. CBSP@CNFs have average SSE, and SSE_t values of 132.8 dB cm^3 g^{-1} and 22140.0 dB cm^2 g^{-1}, respectively, higher than most of the EMI shielding materials reported earlier. The results of this study are noteworthy in that the use of CBSP@CNFs and their PDMS composites for EMI shielding have several advantages for commercial applications such as simple production, high EMI SE, and environmental stability. This lightweight, flexible, and hydrophobic material with good EMI shielding performance may be explored as EMI shielding materials in a wide range of areas, including aerospace, military, and wearable smart devices.

CHAPTER: 10

Summary, Conclusion, and Scope for Future Work

Overview

This thesis reports effective strategies to enhance the EMI shielding properties of electrospun, PAN based nitrogen-doped, 1-D CNF. This chapter summarises the results of the investigations and presents the important conclusions. The scope for future work also is presented.

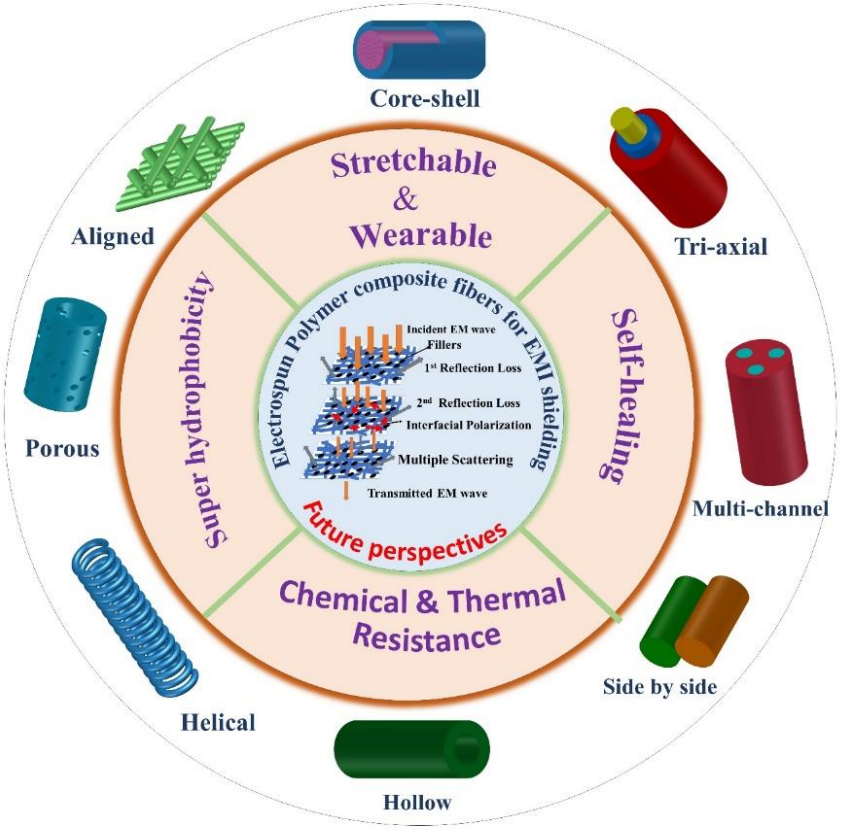

10.1 Summary

The development of lightweight, flexible, and hydrophobic materials with high EMI shielding properties has taken prominence due to the increasing demand for EMI shielding materials. The potential of 1-D electrospun fibers as shielding materials is great, and their EMI shielding qualities can be improved by post-treatment such as heat treatment, coating, and incorporation of fillers into electrospun fibers which produce dielectric or magnetic dipoles. Reflection, absorption, and multiple internal reflections are the common EMI shielding mechanisms. Electrical conductivity, interconnected 3-D conductive network, electrical permittivity, magnetic permeability, dipole interaction, and interfacial polarization are additional factors that influence reflection loss and absorption loss and modify the EMI shielding properties.

Chapter 3, discusses the preparation of CNF by electrospinning of PAN solution followed by carbonization. The carbonization of electrospun PAN fiber results in inherent doping of nitrogen into the graphitic structure of CNF. The graphitic structure of CNF led to high electrical conductivity and formed strong 3-D interconnected conductive network resulting in high conduction loss. The dipole formation in N-doped CNF due to difference in charge density of carbon and nitrogen led to dipole polarization. The 1-D N-doped CNF caused interfacial polarization and increased polarization loss. The CNF has 1-D fibrous, porous, and layer-by-layer structure making it suitable for absorption of EM waves (Shahzad, Kumar, et al., 2015; Shahzad, Yu, et al., 2015; W. D. Xue & Zhao, 2014).

Chapter 4 discusses PEDOT:PSS-PVP coated over CNF which formed interconnected 3-D conductive network and facilitated π-π interaction of thiophene ring of backbone conjugated π-electron of PEDOT with turbostratic carbon structure of CNF and formed electron transport channels between the adjacent CNFs (Lai et al., 2020b; S. H. Lee et al., 2017; Sushma Devi et al., 2022). Thus, the layer by layer structure of PEDOT:PSS coated CNF aided electron transfer between PEDOT:PSS and CNF. The incident EM waves directly interact with π-electrons of PEDOT:PSS and CNF and reflects the EM waves. The remaining EM waves pass through PEDOT:PSS-PVP/CNF and allows multiple internal reflections and multiple scattering at inhomogeneous interfaces inside the porous structure which also contribute to the EMI SE value. The overall reasons for high EMI shielding performance of PEDOT:PSS-PVP/CNF are: (1) formation of 3-D electrically conductive network, (2) high π-electron density and ionic interaction of PEDOT:PSS leading to electrical dipoles helping in ohmic losses, (3) interfacial

polarization between (a) PEDOT:PSS and CNF, (b) CNF-CNF, (c) PEDOT-CNF, and (d) PSS-CNF leading to impedance matching (Bandar A. Al-Asbahi et al., 2021; Al Naim et al., 2021).

Chapter 5 provides an effective strategy for achieving incorporation of chalcogen (Te) element into CNF to form 3-D conductive network which can be used as shielding materials in X-band. The presence of hetero atoms such as tellurium, nitrogen, and oxygen along with SP^2 hybridized carbon can produce structural defects which form dipoles in presence of EM waves and causes polarization loss.(C. Han et al., 2021a; W. Li et al., 2012) The presence of Te NPs into CNF forms small interfaces between Te NPs and CNF and develops impedance variation within the material. Layer-by layer structure of Te-CNF causes interfacial polarization. The high surface area of Te-CNF allows interaction with the incident EM waves and consequently, the incident EM waves undergo multiple scattering and multiple internal reflections (C. Han et al., 2021b; W. Li et al., 2012; M. Zhang et al., 2021). The scattered EM waves are absorbed by turbostratic graphitic structure of CNF via conduction loss and polarization loss. The synergistic effect of Te NPs and CNF leads to higher SE_A compared to SE_R.

Chapter 6 describes incorporation and uniform distribution of Nb_2O_5 NPs into CNF which enabled formation of strong electrical conductive network with CNF that improved the conductivity of the samples. The formation of strong electrical conductive network is an essential requirement for achieving high value of EMI SE. CNFs have conjugated SP^2 hybridized graphitic structure which allows $\pi \rightarrow \pi^*$ transitions and Nb_2O_5 NPs has band gap of 3.4 eV which helps to delocalise the electrons from SP^2 hybridized carbon to Nb_2O_5 and facilitates the formation of Nb_2O_5-carbon hetero-interface that enhances the interfacial polarization (Shanmugapriya et al., 2019; Su et al., 2023; Ximing Zhang et al., 2022a). The presence of Nb_2O_5 NPs in CNF form Nb_2O_5-carbon hetero-interfaces and facilitate dipole and interfacial polarization, leading to polarization losses. As the loading of Nb_2O_5 increases, the electrical conductivity increases and this enhances the SE_T.

The incorporation of LSCO NPs with CNFs results in the formation of electrically conductive network, extending the transmission path of the incident EM waves enhancing the conduction loss. This study is described in chapter 7. The presence of multicomponent heterogeneous interfaces causes interfacial polarization as well as dipole polarization which leads to polarization loss. Synergistic effect of the dipole polarization caused by the metal oxides (LSCO NPs) and the defects produced by Sr doping in $LaCoO_3$, increases the dielectric loss in LSCO-CNFs (C. Wang et al., 2023a, 2023b; Shuo Zhang & Jia, 1998). Porosity and fibrous

layer-by-layer structure of LSCO-CNFs can cause impedance matching which further increases the multiple internal reflections and multiple scattering of EM waves. Thus, the formation of conductive network and synergetic effects of various EM loss mechanisms lead to the excellent EM absorption properties of LSCO-CNFs.

Chapter 8 reports incorporation of $BaTiO_3$ NPs in aligned and non-aligned N-doped CNF and the resultant piezoelectric, dielectric, ferroelectric, and electric properties. These properties can help to enhance the EMI shielding properties. (H. Hu et al., 2019; J. J. Jiang et al., 2015; B. S. Lee et al., 2016; Peidavosi et al., 2022; Saini et al., 2013; Jing Yan & Jeong, 2017; D. Yang et al., 2018) The aligned $BaTiO_3$-CNF exhibited high dielectric properties due to alignment $BaTiO_3$ NPs, which improve the interfacial polarization and EM wave attenuations. The hierarchical 3-D electrically conductive network, formation of hetero-interfaces between $BaTiO_3$ NPs and CNF, and 1-D fibrous structure of $BaTiO_3$-CNF led to dielectric losses (conduction loss, polarization loss, interfacial polarization) and multiple internal reflections, resulting in higher SE_A (more than 80 %) compared to SE_R.

Chapter 9 discusses carbon black super P (CBSP) incorporated into CNFs with enhanced electrical conductivity and strong 3-D electrical conductive network. The continuous distribution of CBSP NPs, led to the formation of a conductive network that enhanced the polarization loss. The effective interaction between CBSP and CNFs resulted in high electrical conductivity and EMI shielding performance.

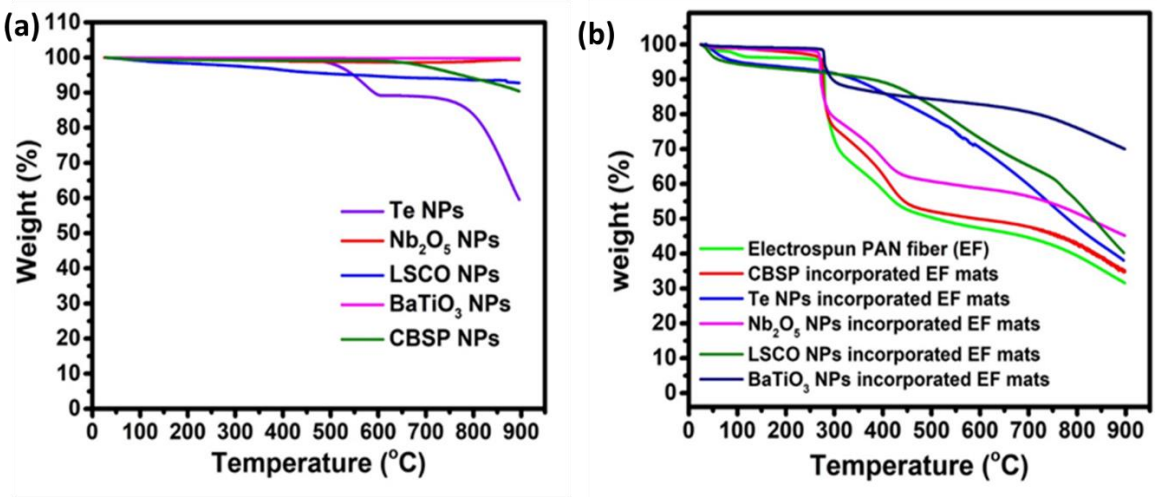

Figure 10.1: TGA thermogram of (a) fillers and (b) filler incorporated electrospun PAN fiber.

During carbonization of electrospun PAN fiber and fillers incorporated electrospun PAN fiber various of gases such as H_2, N_2, HCN would evolve with the formation of turbostratic graphitic

structure. TGA thermograms of fillers used in this work are shown in **Figure 10.1(a),** and demonstrate that there is no significant weight loss during carbonization except in case of Te NPs. Figure 10.1(b) shows the TGA thermograms of fillers incorporated electrospun PAN fibers. Pure electrospun PAN fiber gave residue of 31% which is equivalent to the carbon yield. As fillers are loaded into electrospun PAN fibers, the yield of the residue increased. The weight percentage of the fillers and CNF incorporated in PAN fiber based on the TGA analysis are given in **Table 10.1**.

Table 10.1: The weight percentage of fillers and CNF in PDMS composites of all the samples.

Sample	Weight ratio of fillers and PAN in 10 mL solution*	Residual mass (in %) from TGA*	Wt % of Fillers in CNF mat after carbonization at 900 ^{o}C*	Weight of filler incorporated CNF in PDMS composite (g)	Wt. % fillers incorporated CNF in PDMS composite
CNF	-	31.2	-	0.029 ± 0.005 g	1.16
PEDOT:PSS-PVP-CNF	-		3.34	0.048 ± 002	1.92
Te-CNF	0.25:1	38.0	17.8	0.033 ± 0.003	1.32
Nb_2O_5-CNF	1:1	45.7	32.0	0.038 ± 0.007	1.52
LSCO-CNF	0.25:1	40.4	22.7	0.0407± 0.004	1.62
$BaTiO_3$-CNF	1.2:1	70.3	55.6	0.044 ± 0.012	1.74
CBSP-CNF	0.1:1	34.8	10.3	0.035 ± 0.006	1.40

*(*calculations are based on the TGA analysis presented **Figure 10.1**)*

The carbonized electrospun fiber (CNF) mats are fragile and brittle in nature. PDMS is widely recognized as the most flexible polymer derived from silicone, particularly at room temperature. Hence, fabrication of flexible and stretchable EMI shielding materials can be achieved by the use of a PDMS along with CNF.(Gupta & Tai, 2019; Y. C. Sun et al., 2019)

The weight of CNF and fillers incorporated CNF (dimension: 40 mm x 40 mm x 0.08 mm) are given in **Table 10.1.** The total mass of the PDMS composite of fillers incorporated CNF mats is around 2.5 g. The loading of the CNF in the final PDMS composites is in the range of 1 wt % to 2 wt%.

The PDMS composite of CNF provides high mechanical strength as well as retains their EMI shielding properties. PDMS composite of CNF is ideal for tough environments such as high humidity, cold and hot regions. **Table 10.2** summarize the EMI shielding properties of all the samples related to this thesis work.

Table 10.2: The EMI shielding properties of all the samples related to this thesis work.

Sample Name		**Wt. %**	**Thickness (mm)**	**Conductivity (S cm^{-1})**	**EMI SE (dB)**	**SSEt (dB cm^2 g^{-1})**
CNF			0.08	0.18	24.2	16089
PEDOT:PSS-PVP/ CNF		3.34	0.06	1.08	43.4	2605.0
Te-CNF		20	0.08	0.68	37.1	9280
Nb_2O_5-CNF		50	0.08	1.47	67	2569
$La_{0.85}Sr_{0.15}CoO_3$-CNF		25	0.08	2.01	45.6	9385
$BaTiO_3$-CNF	Non-aligned	60	0.24	0.28	55	2678
	Aligned	60	0.24	0.32	**81**	3676
CBSP-CNF		10	0.06	2.49	55.9	**14741**

10.2 Conclusion

Over the last decade, advancements in the electronics sector have raised the bar for EMI shielding requirements. To meet this demand, recent research has focused on developing shielding materials that can give the same level of EMI SE value while eliminating all of the disadvantages of traditionally employed metallic shields. However, there is a significant gap between laboratory-level preparation and industrial applications. In this thesis work, we tried to fill this gap and have suggested simple strategies for preparing water-proof, lightweight, thin, and flexible shielding materials with high- performance EMI shielding in X, Ku, and K-band. Here, carbon nanofibers were produced from electrospun PAN by carbonization at 900°C. The obtained CNF mats have inherent nitrogen doping with graphitic structure and 1-D fibrous, porous, and layer-by- layer structure which make them capable of absorbing EM waves. The flexible and hydrophobic PDMS composite of these samples have potential applications in flexible electronic devices as shielding materials for next-generation applications.

However, the CNF alone do not provide sufficient EMI shielding for practical applications. In order to improve its EMI shielding properties, the CNF was coated with PEDOT:PSS-PVP and various fillers were incorporated into the CNF. By judiciously selecting the fillers and modifying the alignment of the fillers EMI shielding properties could be regulated. Fillers suitable for dispersing in PAN solution and which can retain their properties after carbonization at 900 °C were selected. During carbonization, the fillers incorporated electrospun PAN fiber mats shrink in both thickness as well as in diameter. PDMS is extensively used to develop flexible electronic devices, and PDMS coating can impart hydrophobicity and make materials water proof. Hence, PDMS composite of CNFs were prepared to make the CNF more flexible and mechanically strong while preserving the EMI shielding properties of CNF.

The hexagonal nanostructured semiconductor Te NPs were incorporated into CNF to improve the electrical conductivity which formed conductive network with hexagonal graphitic structure of CNF. These metal oxide NPs retained their properties after carbonization at 900 ^{o}C. A 20 wt% loading of Te NPs into CNF resulted in EMI SE of 38 dB. The electrical conductivity mainly contributed to reflection of the incident EM waves. Besides, the metal oxide NPs incorporated into the CNF enhanced the absorption of incident EM waves by dipole formation and dipole polarization by the metal oxide NPs.

Semiconductor metal oxide Nb_2O_5 NPs acted as electron promotor and facilitated formation of 3-D conductive network between Nb_2O_5 NP and CNF and made them appropriate materials for EMI shielding. Conducting perovskite metal oxide ($La_{0.85}Sr_{0.15}CoO_3$) (LSCO) NPs were also incorporated into CNF to improve the conductivity and formation of multi-hetero interfaces for superior EMI shielding properties. Additionally, EMI shielding properties were enhanced by alignment of dielectric perovskite metal oxide (BaTiO3 NPs) along with CNF. Finally, carbonic fillers (carbon black) were incorporated into CNF to enhance the EMI shielding properties. The carbon black NPs were present both inside and outside the CNF, hence CBSP@CNFs formed strong 3-D interconnected electric conductive network leading to excellent EMI shielding with low loading of CB.

Thus, in this work, we explored different types of fillers incorporated with CNF to improve the electric conductivity as well as EMI shielding properties. PDMS composite allows design of flexible EMI shielding materials for practical applications in different forms such as enclosures, gaskets, coatings over electronic circuits, and wrappers for electronic components.

10.3 Scope for future work

In this work, intrinsic conducting polymer (PEDOT:PSS), metal NPs (Te NPs), semiconductor metal oxide NPs (Nb_2O_5 NPs), conducting perovskite metal oxide NPs (LSCO NPs), dielectric perovskite metal oxide NPs ($BaTiO_3$ NPs) having piezoelectric and ferroelectric properties, and carbonic fillers (carbon black) are employed to improve the EMI shielding properties of CNF. $BaTiO_3$-CNF exhibited the highest EMI SE value of 81 dB with a thickness of 0.24 mm.

This EMI SE value is sufficient for practical applications; however, it can be further enhanced for better shielding. Magnetic fillers with high magnetic permeability are still remaining to explored. The lowest SE_R value obtained is greater than 3 dB, hence these materials can't be employed for stealth technology. So, further modification of CNF is required to reduce the SE_R value.

The continuous improvements and innovations in the design of electrospinning techniques such as co-axial, tri-axial with different types of metallic collectors to form random, aligned, core-shell, and interfacial fibrous structures hold great promise for designing high performing electrospun fibers for EMI shielding applications. Polymeric nanofibers with self-healing, fire retardant, super hydrophobic and improved thermal and mechanical properties also need to be

investigated. **Figure 10.1** depicts the possible future directions for electrospun polymer composites for EMI shielding applications.

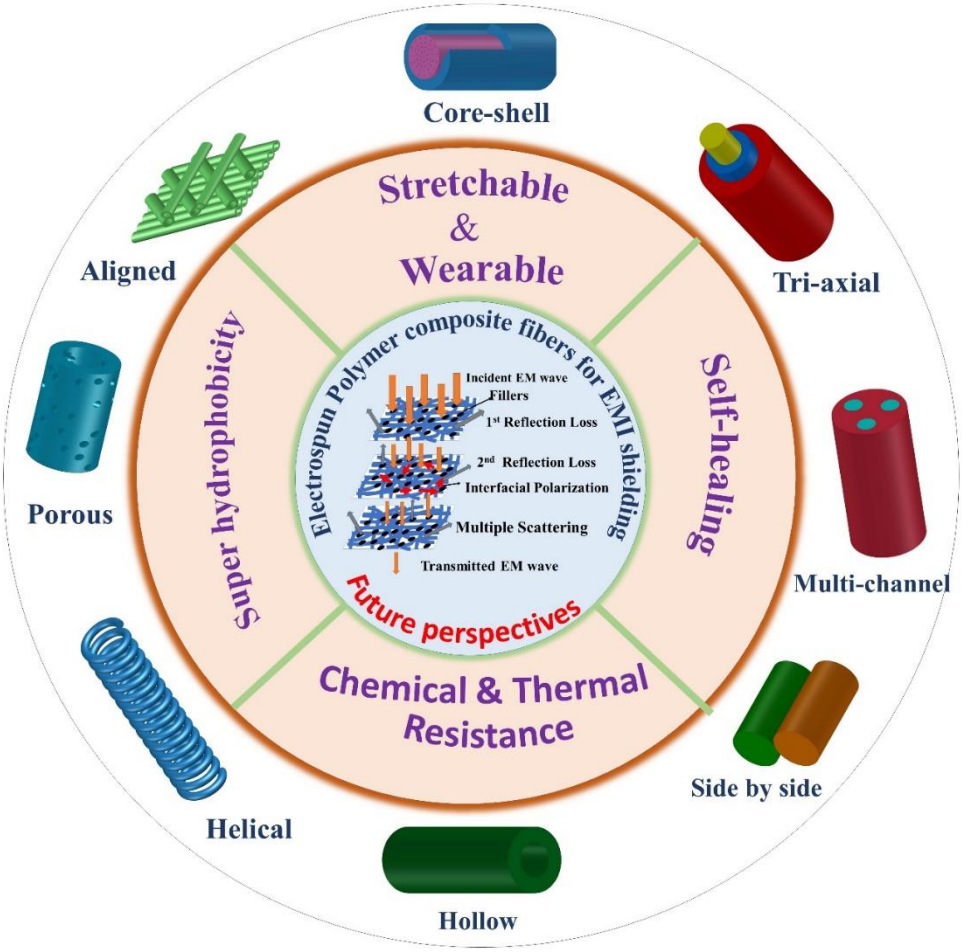

Figure 10.1: Future perspectives for nanofiber-based EMI shielding materials.

In this thesis work, only PDMS matrix is employed to enhance the flexibility of the CNF. There are several other polymer matrixes such as polyurethane and rubber which can be explored to improve the flexibility of CNF. The fabrication of these materials for practical applications are still pending. The PDMS composite of CNF with high performance can be explored for structural application, biomedical application, defense application, and high speed wireless communication systems. The institute in which (IIST Thiruvananthapuram) this work is carried out focuses on Space science and Technology and hence we would aim to develop EMI shielding materials for space applications.

REFERENCES

Aadil, M., Zulfiqar, S., Shahid, M., Agboola, P. O., Al-Khalli, N. F., Warsi, M. F., & Shakir, I. (2021). Fabrication of CNTs supported binary nanocomposite with multiple strategies to boost electrochemical activities. *Electrochimica Acta*, *383*, 138332.

Aadil, M., Zulfiqar, S., Shahid, M., Agboola, P. O., Haider, S., Warsi, M. F., & Shakir, I. (2021). Fabrication of rationally designed CNTs supported binary nanohybrid with multiple approaches to boost electrochemical performance. *Journal of Electroanalytical Chemistry*, *884*, 115070. https://doi.org/https://doi.org/10.1016/j.jelechem.2021.115070

Al-Asbahi, B. A., Qaid, S. M. H., Ahmed, A. A. A., & El-Shamy, A. G. (2023). Smart electromagnetic interference shields based on flexible PEDOT:PSS/Bi2Te3 films. *Materials Chemistry and Physics*, *293*(May 2022), 126922. https://doi.org/10.1016/j.matchemphys.2022.126922

Al-Asbahi, Bandar A., Qaid, S. M. H., & El-Shamy, A. G. (2021). Flexible conductive nanocomposite PEDOT:PSS/Te nanorod films for superior electromagnetic interference (EMI) shielding: A new exploration. *Journal of Industrial and Engineering Chemistry*, *100*(xxxx), 233–247. https://doi.org/10.1016/j.jiec.2021.05.019

Al Naim, A. F., Ibrahim, S. S., & El-Shamy, A. G. (2021). A new class of electromagnetic shields based on carbon dots adorning Te nanorods embedded into PEDOT:PSS for protection from electromagnetic (EM) pollutions. *Progress in Organic Coatings*, *161*(September), 106509. https://doi.org/10.1016/j.porgcoat.2021.106509

Alazmi, A. (2022). Synergistic effect of hydrothermal and physical activation approaches to fabricate activated carbon for energy storage applications. *Ceramics International*.

Arab, F., Mousavi-Kamazani, M., & Salavati-Niasari, M. (2016). Synthesis, characterization, and optical properties of Te, Te/TeO2 and TeO2 nanostructures via a one-pot hydrothermal method. *RSC Advances*, *6*(75), 71472–71480. https://doi.org/10.1039/C6RA10770B

Ariati, R., Sales, F., Souza, A., Lima, R. A., & Ribeiro, J. (2021). Polydimethylsiloxane composites characterization and its applications: A review. *Polymers*, *13*(23), 1–21. https://doi.org/10.3390/polym13234258

Ashok, A., Kumar, A., Bhosale, R. R., Almomani, F., Malik, S. S., Suslov, S., & Tarlochan, F. (2018). Combustion synthesis of bifunctional LaMO3 (M = Cr, Mn, Fe, Co, Ni) perovskites for oxygen reduction and oxygen evolution reaction in alkaline media. *Journal of Electroanalytical Chemistry*, *809*, 22–30. https://doi.org/10.1016/j.jelechem.2017.12.043

Baek, J. Y., Duy, L. T., Lee, S. Y., & Seo, H. (2020). Aluminum doping for optimization of ultrathin and high-k dielectric layer based on SrTiO3. *Journal of Materials Science and*

Technology, *42*(April), 28–37. https://doi.org/10.1016/j.jmst.2019.12.006

Barkoula, N. M., Alcock, B., Cabrera, N. O., & Peijs, T. (2008). Flame-Retardancy Properties of Intumescent Ammonium Poly(Phosphate) and Mineral Filler Magnesium Hydroxide in Combination with Graphene. *Polymers and Polymer Composites*, *16*(2), 101–113. https://doi.org/10.1002/pc

Basavaraja Patel, B. M., Revanasiddappa, M., Yallappa, S., & Rangaswamy, D. R. (2023). Iron nanoparticles embedded in polypyrrole and tellurium oxide ternary nanocomposites for electrical conductivity and electromagnetic interference shielding. *Journal of Materials Science: Materials in Electronics*, *34*(10), 1–16. https://doi.org/10.1007/s10854-023-10298-w

Bauer, M. J., Snyder, C. S., Bowland, C. C., Uhl, A. M., Budi, M. A. K., Villancio-Wolter, M., Sodano, H. A., & Andrew, J. S. (2016). Structure–Property Relationships in Aligned Electrospun Barium Titanate Nanofibers. *Journal of the American Ceramic Society*, *99*(12), 3902–3908. https://doi.org/10.1111/jace.14455

Bayat, M., Yang, H., Ko, F. K., Michelson, D., & Mei, A. (2014). Electromagnetic interference shielding effectiveness of hybrid multifunctional Fe3O4/carbon nanofiber composite. *Polymer*, *55*(3), 936–943. https://doi.org/10.1016/j.polymer.2013.12.042

Bctpsqujpo, X., Pg, Q., Epqfe, F., Obopgjcfst, D., Zhao, P., Wang, H., Cai, B., Sun, X., Hou, Z., Wu, J., Wang, G., & ƍ M. B. (2022). *&Mfdusptqjoojoh Gbcsjdbujpo Boe Vmusb Xjefcboe Fmfduspnbhofujd Xbwf Bctpsqujpo Qspqfsujft Pg $F0 / Epqfe Dbscpo Obopgjcfst*. *15*(9), 7788–7796.

Bhattacharjee, Y., Chatterjee, D., & Bose, S. (2018). Core-Multishell Heterostructure with Excellent Heat Dissipation for Electromagnetic Interference Shielding. *ACS Applied Materials and Interfaces*, *10*(36), 30762–30773. https://doi.org/10.1021/acsami.8b10819

Biglar, M., Gromada, M., Stachowicz, F., & Trzepieciński, T. (2017). Synthesis of barium titanate piezoelectric ceramics for multilayer actuators (MLAs). *Acta Mechanica et Automatica*, *11*(4), 275–279. https://doi.org/10.1515/ama-2017-0042

Bisht, A., Kumar Yadav, P., Dhakar, S., & Sharma, S. (2021). Pt4+ as an Active Site for Oxygen Evolution Reaction in La1–xSrxCo1–yPtyO3. *The Journal of Physical Chemistry C*, *125*(46), 25488–25496. https://doi.org/10.1021/acs.jpcc.1c06426

Bisht, A., & Sharma, S. (2018). Direct Formic Acid Electro-Oxidation on Pt Doped and Undoped La 1-x Sr x CoO 3 : Activity Suppression due to Proton Reduction Reaction . *Journal of The Electrochemical Society*, *165*(14), H927–H931. https://doi.org/10.1149/2.0011814jes

Bisht, A., Sihag, A., Satyaprasad, A., Mallajosyala, S. S., & Sharma, S. (2018). Pt Metal Supported and Pt4+ Doped La1−xSrxCoO3: Non-performance of Pt4+ and Reactivity Differences with Pt Metal. *Catalysis Letters*, *148*(7), 1965–1977.

https://doi.org/10.1007/s10562-018-2408-2

Björkman, Å. (1969). Thermische Klärschlammbehandlung. *Schweizerische Zeitschrift Für Hydrologie*, *31*(2), 632–645. https://doi.org/10.1007/BF02543692

Blachowicz, T., Hütten, A., & Ehrmann, A. (2022a). Electromagnetic Interference Shielding with Electrospun Nanofiber Mats—A Review of Production, Physical Properties and Performance. *Fibers*, *10*(6). https://doi.org/10.3390/fib10060047

Blachowicz, T., Hütten, A., & Ehrmann, A. (2022b). Electromagnetic Interference Shielding with Electrospun Nanofiber Mats—A Review of Production, Physical Properties and Performance. *Fibers*, *10*(6). https://doi.org/10.3390/fib10060047

Blachowicz, T., Hütten, A., & Ehrmann, A. (2022c). Electromagnetic Interference Shielding with Electrospun Nanofiber Mats—A Review of Production, Physical Properties and Performance. In *Fibers* (Vol. 10, Issue 6). https://doi.org/10.3390/fib10060047

Bonso, J. S., Kalaw, G. D., & Ferraris, J. P. (2014). *High surface area carbon nanofibers derived from electrospun PIM-1 for energy storage applications †*. https://doi.org/10.1039/c3ta13779a

Bredar, A. R. C., Chown, A. L., Burton, A. R., & Farnum, B. H. (2020). Electrochemical Impedance Spectroscopy of Metal Oxide Electrodes for Energy Applications. *ACS Applied Energy Materials*, *3*(1), 66–98. https://doi.org/10.1021/acsaem.9b01965

Brosha, E. L., Mukundan, R., Brown, D. R., Garzon, F. H., Visser, J. H., Zanini, M., Zhou, Z., & Logothetis, E. M. (2000). CO/HC sensors based on thin films of LaCoO3 and La0.8Sr0.2CoO3−δ metal oxides. *Sensors and Actuators B: Chemical*, *69*(1–2), 171–182. https://doi.org/10.1016/S0925-4005(00)00543-8

Caņado, L. G., Takai, K., Enoki, T., Endo, M., Kim, Y. A., Mizusaki, H., Jorio, A., Coelho, L. N., Magalhães-Paniago, R., & Pimenta, M. A. (2006). General equation for the determination of the crystallite size la of nanographite by Raman spectroscopy. *Applied Physics Letters*, *88*(16). https://doi.org/10.1063/1.2196057

Cao, Li, Su, D., Su, Z., & Chen, X. (2014). Fabrication of Multiwalled Carbon Nanotube/Polypropylene Conductive Fibrous Membranes by Melt Electrospinning. *Industrial & Engineering Chemistry Research*, *53*(6), 2308–2317. https://doi.org/10.1021/ie403746p

Cao, Linlin, Wang, Y., Dong, P., Vinod, S., Tijerina, J. T., Ajayan, P. M., Xu, Z., & Lou, J. (2016a). *Interphase Induced Dynamic Self-Stiffening in Graphene-Based Polydimethylsiloxane Nanocomposites*. https://doi.org/10.1002/smll.201600170

Cao, Linlin, Wang, Y., Dong, P., Vinod, S., Tijerina, J. T., Ajayan, P. M., Xu, Z., & Lou, J. (2016b). Interphase Induced Dynamic Self-Stiffening in Graphene-Based Polydimethylsiloxane Nanocomposites. *Small*, *12*(27), 3723–3731.

Cao, W.-T., Chen, F.-F., Zhu, Y.-J., Zhang, Y.-G., Jiang, Y.-Y., Ma, M.-G., & Chen, F. (2018). Binary Strengthening and Toughening of MXene/Cellulose Nanofiber Composite Paper with Nacre-Inspired Structure and Superior Electromagnetic Interference Shielding Properties. *ACS Nano*, *12*(5), 4583–4593. https://doi.org/10.1021/acsnano.8b00997

Chaudhary, A., Kumar, R., Teotia, S., Dhawan, S. K., Dhakate, S. R., & Kumari, S. (2017). Integration of MCMBs/MWCNTs with Fe3O4 in a flexible and light weight composite paper for promising EMI shielding applications. *Journal of Materials Chemistry C*, *5*(2), 322–332. https://doi.org/10.1039/c6tc03241a

Chaudhary, K., Zulfiqar, S., Somaily, H. H., Aadil, M., Warsi, M. F., & Shahid, M. (2022). Rationally designed multifunctional Ti3C2 MXene@Graphene composite aerogel integrated with bimetallic selenides for enhanced supercapacitor performance and overall water splitting. *Electrochimica Acta*, *431*, 141103. https://doi.org/https://doi.org/10.1016/j.electacta.2022.141103

Chen, J., Yi, D., Jia, X., Wang, G., Sun, Z., Zhang, L., Liu, Y., Shen, B., & Zheng, W. (2022). Biomass-based aligned carbon networks with double-layer construction for tunable electromagnetic shielding with ultra-low reflectivity. *Journal of Materials Science and Technology*, *103*, 98–104. https://doi.org/10.1016/j.jmst.2021.06.039

Chen, Li, Guo, K., Zeng, S.-L., Xu, L., Xing, C.-Y., Zhang, S., & Li, B.-J. (2020). Cross-stacking aligned non-woven fabrics with automatic self-healing properties for electromagnetic interference shielding. *Carbon*, *162*, 445–454. https://doi.org/https://doi.org/10.1016/j.carbon.2020.02.034

Chen, Long, Jiang, J., Bao, Z., Pan, J., Xu, W., Zhou, L., Wu, Z., & Chen, X. (2013). Synthesis of barium and strontium carbonate crystals with unusual morphologies using an organic additive. *Russian Journal of Physical Chemistry A*, *87*(13), 2239–2245. https://doi.org/10.1134/S0036024413130153

Chen, Q. Y., Liu, L., & Wang, Y. H. (2014). Preparation and characterization of novel Fe2O3-flaky coated carbon fiber by electrospinning and hydrothermal methods. *Advances in Condensed Matter Physics*, *2014*, 1–6. https://doi.org/10.1155/2014/938072

Chen, R., Wang, H. Y., Miao, J., Yang, H., & Liu, B. (2015). A flexible high-performance oxygen evolution electrode with three-dimensional NiCo2O4 core-shell nanowires. *Nano Energy*, *11*, 333–340. https://doi.org/10.1016/j.nanoen.2014.11.021

Chen, T., Deng, F., Zhu, J., Chen, C., Sun, G., Ma, S., & Yang, X. (2012). Hexagonal and cubic Ni nanocrystals grown on graphene: Phase-controlled synthesis, characterization and their enhanced microwave absorption properties. *Journal of Materials Chemistry*, *22*(30), 15190–15197. https://doi.org/10.1039/c2jm31171b

Chen, Y., Pang, L., Li, Y., Luo, H., Duan, G., Mei, C., Xu, W., Zhou, W., Liu, K., & Jiang, S. (2020). Ultra-thin and highly flexible cellulose nanofiber/silver nanowire conductive paper for effective electromagnetic interference shielding. *Composites Part A: Applied*

Science and Manufacturing, *135*, 105960. https://doi.org/https://doi.org/10.1016/j.compositesa.2020.105960

Chen, Z., Xu, C., Ma, C., Ren, W., & Cheng, H. M. (2013). Lightweight and flexible graphene foam composites for high-performance electromagnetic interference shielding. *Advanced Materials*, *25*(9), 1296–1300. https://doi.org/10.1002/adma.201204196

Cheng, J., Li, C., Xiong, Y., Zhang, H., Raza, H., Ullah, S., Wu, J., Zheng, G., Cao, Q., Zhang, D., Zheng, Q., & Che, R. (2022). Recent Advances in Design Strategies and Multifunctionality of Flexible Electromagnetic Interference Shielding Materials. In *Nano-Micro Letters* (Vol. 14, Issue 1). Springer Nature Singapore. https://doi.org/10.1007/s40820-022-00823-7

Cheng, W., Zhang, Y., Tian, W., Liu, J., Lu, J., Wang, B., Xing, W., & Hu, Y. (2020). Highly Efficient MXene-Coated Flame Retardant Cotton Fabric for Electromagnetic Interference Shielding. *Industrial and Engineering Chemistry Research*, *59*(31), 14025–14036. https://doi.org/10.1021/acs.iecr.0c02618

Cheng, Y.-L., Lee, C.-Y., Huang, Y.-L., Buckner, C. A., Lafrenie, R. M., Dénommée, J. A., Caswell, J. M., Want, D. A., Gan, G. G., Leong, Y. C., Bee, P. C., Chin, E., Teh, A. K. H., Picco, S., Villegas, L., Tonelli, F., Merlo, M., Rigau, J., Diaz, D., … Mathijssen, R. H. J. (2016). Lightweight Electromagnetic Interference Shielding Materials and Their Mechanisms. *Intechopen*, *11*(tourism), 13. https://doi.org/10.5772/intechopen.82270

Choi, H.-J., sung Kim, M., Ahn, D., Young Yeo, sang, & Lee, sohee. (n.d.). *electrical percolation threshold of carbon black in a polymer matrix and its application to antistatic fibre*. https://doi.org/10.1038/s41598-019-42495-1

Choi, H. J., Kim, M. S., Ahn, D., Yeo, S. Y., & Lee, S. (2019). Electrical percolation threshold of carbon black in a polymer matrix and its application to antistatic fibre. *Scientific Reports*, *9*(1), 1–12. https://doi.org/10.1038/s41598-019-42495-1

Choi, Jaewon, Lee, J., Choi, J., Jung, D., & Shim, S. E. (2010). Electrospun PEDOT: PSS/PVP nanofibers as the chemiresistor in chemical vapour sensing. *Synthetic Metals*, *160*(13–14), 1415–1421.

Choi, Jaeyoo, Lee, J. Y., Lee, H., Park, C. R., & Kim, H. (2014). Enhanced thermoelectric properties of the flexible tellurium nanowire film hybridized with single-walled carbon nanotube. *Synthetic Metals*, *198*, 340–344. https://doi.org/10.1016/j.synthmet.2014.10.037

Choi, Jaeyoo, Lee, K., Park, C. R., & Kim, H. (2015). Enhanced thermopower in flexible tellurium nanowire films doped using single-walled carbon nanotubes with a rationally designed work function. *Carbon*, *94*, 577–584. https://doi.org/10.1016/j.carbon.2015.07.043

Choi, Jeongan, Joon Yang, B., Bae, G.-N., & Hee Jung, J. (2015). Herbal Extract Incorporated

Nanofiber Fabricated by an Electrospinning Technique and its Application to Antimicrobial Air Filtration. *ACS Applied Materials & Interfaces*, *7*(45), 25313–25320. https://doi.org/10.1021/acsami.5b07441

Chung, D. D. L. (2001). Electromagnetic interference shielding effectiveness of carbon materials. *Carbon*, *39*(2), 279–285. https://doi.org/10.1016/S0008-6223(00)00184-6

Chung, D. D. L. (2020). Materials for electromagnetic interference shielding. *Materials Chemistry and Physics*, *255*(June), 350–354. https://doi.org/10.1016/j.matchemphys.2020.123587

Cui, C., Xiang, C., Geng, L., Lai, X., Guo, R., Zhang, Y., Xiao, H., Lan, J., Lin, S., & Jiang, S. (2019). Flexible and ultrathin electrospun regenerate cellulose nanofibers and d-Ti3C2Tx (MXene) composite film for electromagnetic interference shielding. *Journal of Alloys and Compounds*, *788*, 1246–1255. https://doi.org/https://doi.org/10.1016/j.jallcom.2019.02.294

Cui, G. Y., Wang, C. Y., Xiang, G. Q., & Zhou, B. (2018). An electrochemical sensor based on nitrogen doped carbon material prepared from nitrogen-containing precursors. *IOP Conference Series: Materials Science and Engineering*, *292*(1), 0–6. https://doi.org/10.1088/1757-899X/292/1/012034

Das, N. C., Chaki, T. K., Khastgir, D., & Chakraborty, A. (2001). Electromagnetic interference shielding effectiveness of conductive carbon black and carbon fiber-filled composites based on rubber and rubber blends. *Advances in Polymer Technology*, *20*(3), 226–236. https://doi.org/10.1002/adv.1018

Das, P., Ganguly, S., Perelshtein, I., Margel, S., & Gedanken, A. (2022). Acoustic Green Synthesis of Graphene-Gallium Nanoparticles and PEDOT:PSS Hybrid Coating for Textile To Mitigate Electromagnetic Radiation Pollution. *ACS Applied Nano Materials*, *5*(1), 1644–1655. https://doi.org/10.1021/acsanm.1c04425

Davoodi, P., Gill, E. L., Wang, W., & Shery Huang, Y. Y. (2021). Advances and innovations in electrospinning technology. *Biomedical Applications of Electrospinning and Electrospraying*, 45–81. https://doi.org/10.1016/B978-0-12-822476-2.00004-2

Deepa, K. S., Shaiju, P., Sebastian, M. T., Gowd, E. B., & James, J. (2014). Poly(vinylidene fluoride)-La0.5Sr0.5CoO3-δ composites: The influence of LSCO particle size on the structure and dielectric properties. *Physical Chemistry Chemical Physics*, *16*(32), 17008–17017. https://doi.org/10.1039/C4CP01924E

Deeraj, B. D. S., George, G., Dhineshbabu, N. R., Bose, S., & Joseph, K. (2021). Electrospun ZrO2@carbon nanofiber mats and their epoxy composites as effective EMI shields in Ku band. *Materials Research Bulletin*, *144*(June), 111477. https://doi.org/10.1016/j.materresbull.2021.111477

Dijith, K. S., Pillai, S., & Surendran, K. P. (2017). Thermophysical and Microwave Shielding

Properties of La0.5Sr0.5CoO3−δ and its Composite with Epoxy. *Journal of Electronic Materials*, *46*(8), 5158–5167. https://doi.org/10.1007/s11664-017-5520-y

Dong, Q., Wang, G., Hu, H., Yang, J., Qian, B., Ling, Z., & Qiu, J. (2013). Ultrasound-assisted preparation of electrospun carbon nanofiber/graphene composite electrode for supercapacitors. *Journal of Power Sources*, *243*, 350–353. https://doi.org/10.1016/j.jpowsour.2013.06.060

Dong, S., Li, J., Zhang, S., Li, N., Li, B., Zhang, Q., & Ge, L. (2022). Excellent microwave absorption of lightweight PAN-based carbon nanofibers prepared by electrospinning. *Colloids and Surfaces A: Physicochemical and Engineering Aspects*, *651*, 129670. https://doi.org/https://doi.org/10.1016/j.colsurfa.2022.129670

Elahi, M. F., & Lu, W. (2013a). Core-shell Fibers for Biomedical Applications-A Review. *Journal of Bioengineering & Biomedical Science*, *03*(01). https://doi.org/10.4172/2155-9538.1000121

Elahi, M. F., & Lu, W. (2013b). Core-shell Fibers for Biomedical Applications-A Review. *Journal of Bioengineering & Biomedical Science*, *03*(01), 1–14. https://doi.org/10.4172/2155-9538.1000121

Erbil, H. Y. (2020). Practical Applications of Superhydrophobic Materials and Coatings: Problems and Perspectives. *Langmuir*, *36*(10), 2493–2509. https://doi.org/10.1021/acs.langmuir.9b03908

Fadil, F., Affandi, N. D. N., Misnon, M. I., Bonnia, N. N., Harun, A. M., & Alam, M. K. (2021). Review on electrospun nanofiber-applied products. *Polymers*, *13*(13), 1–31. https://doi.org/10.3390/polym13132087

Faisal, M., & Khasim, S. (2013). Polyaniline-antimony oxide composites for effective broadband EMI shielding. *Iranian Polymer Journal (English Edition)*, *22*(7), 473–480. https://doi.org/10.1007/s13726-013-0149-z

Fang, Y.-S., Yuan, J., Liu, T.-T., Wang, Q.-Q., Cao, W.-Q., & Cao, M.-S. (2023). Clipping electron transport and polarization relaxation of Ti3C2Tx based nanocomposites towards multifunction. *Carbon*, *201*, 371–380. https://doi.org/https://doi.org/10.1016/j.carbon.2022.09.043

Feng, Y., Hu, K., Zhang, M., Ding, W., Kong, X., Sheng, Z., & Liu, Q. (2022). Engineering A-site cation deficiency into LaCoO3 thin sheets for improved microwave absorption performance. *Journal of Materials Science*, *57*(1), 204–216. https://doi.org/10.1007/s10853-021-06650-2

Funda, S., Ohki, T., Liu, Q., Hossain, J., Ishimaru, Y., Ueno, K., & Shirai, H. (2016). Correlation between the fine structure of spin-coated PEDOT: PSS and the photovoltaic performance of organic/crystalline-silicon heterojunction solar cells. *Journal of Applied Physics*, *120*(3), 33103.

Galceran, M., Pujol, · M C, Aguiló, · M, Díaz, · F, Aguiló, M., & Díaz, F. (2007). Sol-gel modified Pechini method for obtaining nanocrystalline KRE(WO 4) 2 (RE = Gd and Yb). *J Sol-Gel Sci Techn*, *42*, 79–88. https://doi.org/10.1007/s10971-006-1517-3

Ganguly, S., Bhawal, P., Ravindren, R., & Das, N. C. (2018). Polymer Nanocomposites for Electromagnetic Interference Shielding: A Review. *Journal of Nanoscience and Nanotechnology*, *18*(11), 7641–7669. https://doi.org/10.1166/jnn.2018.15828

Gao, L., Wang, X., Wang, H., & Lei, Q. (2018). Improvement of dielectric performance and interfacial polarization of polyvinylidene fluoride composites with CaCu3Ti4O12@Ni hybrid nanofibers. *Journal of Materials Science: Materials in Electronics*, *29*(12), 10600–10613. https://doi.org/10.1007/s10854-018-9124-y

Geetha, S., Satheesh Kumar, K. K., Rao, C. R. K., Vijayan, M., & Trivedi, D. C. (2009). EMI Shielding: Methods and Materials-A Review. *J Appl Polym Sci*, *112*. https://doi.org/10.1002/app.29812

Gehring, M., Tempel, H., Merlen, A., Schierholz, R., Eichel, R. A., & Kungl, H. (2019). Carbonisation temperature dependence of electrochemical activity of nitrogen-doped carbon fibres from electrospinning as air-cathodes for aqueous-alkaline metal-air batteries. *RSC Advances*, *9*(47), 27231–27241. https://doi.org/10.1039/c9ra03805a

Ghosh, S., Ganguly, S., Remanan, S., & Das, N. C. (2019a). Fabrication and investigation of 3D tuned PEG/PEDOT: PSS treated conductive and durable cotton fabric for superior electrical conductivity and flexible electromagnetic interference shielding. *Composites Science and Technology*, *181*(April), 107682. https://doi.org/10.1016/j.compscitech.2019.107682

Ghosh, S., Ganguly, S., Remanan, S., & Das, N. C. (2019b). Fabrication and investigation of 3D tuned PEG/PEDOT: PSS treated conductive and durable cotton fabric for superior electrical conductivity and flexible electromagnetic interference shielding. *Composites Science and Technology*, *181*(June), 107682. https://doi.org/10.1016/j.compscitech.2019.107682

Ghosh, S., Mondal, S., Ganguly, S., Remanan, S., Singha, N., & Ch Das, N. (2018). Carbon Nanostructures Based Mechanically Robust Conducting Cotton Fabric for Improved Electromagnetic Interference Shielding. *Fibers and Polymers*, *19*(5), 1064–1073. https://doi.org/10.1007/s12221-018-7995-4

Goel, S., Tyagi, A., Garg, A., Kumar, S., Baskey, H. B., Gupta, R. K., & Tyagi, S. (2021). Microwave absorption study of composites based on CQD@BaTiO3 core shell and BaFe12O19 nanoparticles. *Journal of Alloys and Compounds*, *855*, 157411. https://doi.org/10.1016/j.jallcom.2020.157411

Graham, K., Ouyang, M., Raether, T., Grafe, T., Mcdonald, B., & Knauf, P. (2002). Polymeric Nanofibers in Air Filtration Applications. *Fifteenth Annual Technical Conference & Expo of the American Filtration & Separation Society*, 9–12.

Guo, H., Chen, Y., Li, Y., Zhou, W., Xu, W., Pang, L., Fan, X., & Jiang, S. (2021). Electrospun fibrous materials and their applications for electromagnetic interference shielding: A review. *Composites Part A: Applied Science and Manufacturing*, *143*, 106309.

Guo, H., Wang, F., Luo, H., Li, Y., Lou, Z., Ji, Y., Liu, X., Shen, B., Peng, Y., Liu, K., & Jiang, S. (2021). Flexible TaC/C electrospun non–woven fabrics with multiple spatial-scale conductive frameworks for efficient electromagnetic interference shielding. *Composites Part A: Applied Science and Manufacturing*, *151*, 106662. https://doi.org/https://doi.org/10.1016/j.compositesa.2021.106662

Guo, Y., Pan, L., Yang, X., Ruan, K., Han, Y., Kong, J., & Gu, J. (2019). Simultaneous improvement of thermal conductivities and electromagnetic interference shielding performances in polystyrene composites via constructing interconnection oriented networks based on electrospinning technology. *Composites Part A: Applied Science and Manufacturing*, *124*, 105484. https://doi.org/https://doi.org/10.1016/j.compositesa.2019.105484

Gupta, S., & Tai, N. H. (2019). Carbon materials and their composites for electromagnetic interference shielding effectiveness in X-band. *Carbon*, *152*, 159–187. https://doi.org/10.1016/j.carbon.2019.06.002

Han, C., Zhang, M., Cao, W. Q., & Cao, M. S. (2021a). Electrospinning and in-situ hierarchical thermal treatment to tailor C–NiCo2O4 nanofibers for tunable microwave absorption. *Carbon*, *171*, 953–962. https://doi.org/10.1016/j.carbon.2020.09.067

Han, C., Zhang, M., Cao, W. Q., & Cao, M. S. (2021b). Electrospinning and in-situ hierarchical thermal treatment to tailor C–NiCo2O4 nanofibers for tunable microwave absorption. *Carbon*, *171*, 953–962. https://doi.org/10.1016/j.carbon.2020.09.067

Han, M., Zhou, Z., Li, Y., Chen, Q., & Chen, M. (2021). Highly Conductive Tellurium and Telluride in Energy Storage. *ChemElectroChem*, *8*(23), 4412–4426. https://doi.org/10.1002/celc.202100735

Hashemi, S. A., Ghaffarkhah, A., Hosseini, E., Bahrani, S., Najmi, P., Omidifar, N., Mousavi, S. M., Amini, M., Ghaedi, M., Ramakrishna, S., & Arjmand, M. (2022). Recent progress on hybrid fibrous electromagnetic shields: Key protectors of living species against electromagnetic radiation. *Matter*, *5*(11), 3807–3868. https://doi.org/https://doi.org/10.1016/j.matt.2022.09.012

He, J., Lv, W., Chen, Y., Wen, K., Xu, C., Zhang, W., Li, Y., Qin, W., & He, W. (2017). Tellurium-Impregnated Porous Cobalt-Doped Carbon Polyhedra as Superior Cathodes for Lithium-Tellurium Batteries. *ACS Nano*, *11*(8), 8144–8152. https://doi.org/10.1021/acsnano.7b03057

He, X.-X., Zheng, J., Yu, G.-F., You, M.-H., Yu, M., Ning, X., & Long, Y.-Z. (2017). Near-Field Electrospinning: Progress and Applications. *The Journal of Physical Chemistry C*, *121*(16), 8663–8678. https://doi.org/10.1021/acs.jpcc.6b12783

Hone, J., Llaguno, M. C., Nemes, N. M., Johnson, A. T., Fischer, J. E., Walters, D. A., Casavant, M. J., Schmidt, J., & Smalley, R. E. (2000). Electrical and thermal transport properties of magnetically aligned single wall carbon nanotube films. *Applied Physics Letters*, *77*(5), 666–668. https://doi.org/10.1063/1.127079

Hoque, M. E., Nuge, T., Yeow, T. K., & Nordin, N. (2019). Electrospun Matrices from Natural Polymers for Skin Regeneration. *Nanostructured Polymer Composites for Biomedical Applications*, 87–104. https://doi.org/10.1016/B978-0-12-816771-7.00005-3

Hou, Y., Cheng, L., Zhang, Y., Du, X., Zhao, Y., & Yang, Z. (2021). High temperature electromagnetic interference shielding of lightweight and flexible ZrC/SiC nanofiber mats. *Chemical Engineering Journal*, *404*(April 2020). https://doi.org/10.1016/j.cej.2020.126521

Hsiao, S.-T., M. Ma, C.-C., Liao, W.-H., Wang, Y.-S., Li, S.-M., Huang, Y.-C., Yang, R.-B., & Liang, W.-F. (2014). Lightweight and Flexible Reduced Graphene Oxide/Water-Borne Polyurethane Composites with High Electrical Conductivity and Excellent Electromagnetic Interference Shielding Performance. *ACS Applied Materials & Interfaces*, *6*(13), 10667–10678. https://doi.org/10.1021/am502412q

Hu, H., Zhang, F., Lim, S., Blanloeuil, P., Yao, Y., Guo, Y., & Wang, C. H. (2019). Surface functionalisation of carbon nanofiber and barium titanate by polydopamine to enhance the energy storage density of their nanocomposites. *Composites Part B: Engineering*, *178*(June), 107459. https://doi.org/10.1016/j.compositesb.2019.107459

Hu, Y., Feng, B., Zhang, W., Yan, C., Yao, Q., Shao, C., Yu, F., Li, F., & Fu, Y. (2019). Electrospun gelatin/PCL and collagen/PCL scaffolds for modulating responses of bone marrow endothelial progenitor cells. *Experimental and Therapeutic Medicine*, *1*, 3717–3726. https://doi.org/10.3892/etm.2019.7387

Huang, F., Wang, S., Ding, W., Zhang, M., Kong, X., Sheng, Z., & Liu, Q. (2021). Sulfur-doped biomass-derived hollow carbon microtubes toward excellent microwave absorption performance. *Journal of Materials Science: Materials in Electronics*, *32*(5), 6260–6268. https://doi.org/10.1007/s10854-021-05341-7

Huang, L., Li, J., Li, Y., He, X., & Yuan, Y. (2019). Lightweight and flexible hybrid film based on delicate design of electrospun nanofibers for high-performance electromagnetic interference shielding. *Nanoscale*, *11*(17), 8616–8625. https://doi.org/10.1039/c9nr02102g

Huang, Z.-M., Zhang, Y.-Z., Kotaki, M., & Ramakrishna, S. (2003). A review on polymer nanofibers by electrospinning and their applications in nanocomposites. *Composites Science and Technology*, *63*(15), 2223–2253.

Hung, L. X., Yen, N. H., Hue, T. T., Thuan, D. N., Thang, P. N., Hanh, V. T. H., Nhung, V. C., Laverdant, J., Huong, N. T. M., & Nga, P. T. (2022). Fabrication and optical properties of sulfur- and nitrogen-doped graphene quantum dots by the microwave–hydrothermal

approach. *Journal of Nanoparticle Research*, *24*(10). https://doi.org/10.1007/s11051-022-05579-0

Huo, K.-L., Yang, S.-H., Zong, J.-Y., Chu, J.-J., Wang, Y.-D., & Cao, M.-S. (2023). Carbon-based EM functional materials and multi-band microwave devices: Current progress and perspectives. *Carbon*, *213*, 118193. https://doi.org/https://doi.org/10.1016/j.carbon.2023.118193

Im, J. S., Kim, J. G., Bae, T. S., & Lee, Y. S. (2011). Effect of heat treatment on ZrO2-embedded electrospun carbon fibers used for efficient electromagnetic interference shielding. *Journal of Physics and Chemistry of Solids*, *72*(10), 1175–1179. https://doi.org/10.1016/J.JPCS.2011.07.012

Im, J. S., Kim, J. G., Lee, S.-H., & Lee, Y.-S. (2010a). Enhanced adhesion and dispersion of carbon nanotube in PANI/PEO electrospun fibers for shielding effectiveness of electromagnetic interference. *Colloids and Surfaces A: Physicochemical and Engineering Aspects*, *364*(1), 151–157. https://doi.org/https://doi.org/10.1016/j.colsurfa.2010.05.015

Im, J. S., Kim, J. G., Lee, S. H., & Lee, Y. S. (2010b). Effective electromagnetic interference shielding by electrospun carbon fibers involving Fe2O3/BaTiO3/MWCNT additives. *Materials Chemistry and Physics*, *124*(1), 434–438. https://doi.org/10.1016/j.matchemphys.2010.06.062

Im, J. S., Kim, J. G., & Lee, Y. S. (2009). Fluorination effects of carbon black additives for electrical properties and EMI shielding efficiency by improved dispersion and adhesion. *Carbon*, *47*(11), 2640–2647. https://doi.org/10.1016/j.carbon.2009.05.017

Iqbal, S., & Ahmad, S. (2020). Conducting polymer composites: An efficient EMI shielding material. In *Materials for Potential EMI Shielding Applications*. Elsevier Inc. https://doi.org/10.1016/b978-0-12-817590-3.00016-6

Isaac, B., Taylor, R. M., & Reifsnider, K. (2021). Mechanical and dielectric properties of aligned electrospun fibers. *Fibers*, *9*(1), 1–32. https://doi.org/10.3390/fib9010004

Islam, I., Sultana, S., Kumer Ray, S., Parvin Nur, H., Hossain, M., & Md. Ajmotgir, W. (2018). Electrical and Tensile Properties of Carbon Black Reinforced Polyvinyl Chloride Conductive Composites. *C*, *4*(1), 15. https://doi.org/10.3390/c4010015

Jalaja, K., Kumar, P. R. A., Dey, T., Kundu, S. C., & James, N. R. (2014). Modified dextran cross-linked electrospun gelatin nanofibres for biomedical applications. *Carbohydrate Polymers*, *114*, 467–475. https://doi.org/10.1016/J.CARBPOL.2014.08.023

Jalaja, K., Naskar, D., Kundu, S. C., & James, N. R. (2016). Potential of electrospun core–shell structured gelatin–chitosan nanofibers for biomedical applications. *Carbohydrate Polymers*, *136*, 1098–1107. https://doi.org/10.1016/J.CARBPOL.2015.10.014

Ji, H., Zhao, R., Zhang, N., Jin, C., Lu, X., & Wang, C. (2018). Lightweight and flexible electrospun polymer nanofiber/metal nanoparticle hybrid membrane for high-

performance electromagnetic interference shielding. *NPG Asia Materials*, *10*(8), 749–760. https://doi.org/10.1038/s41427-018-0070-1

Ji Park, E., Kyoung Cho, Y., Han Kim, D., Jeong, M.-G., Ho Kim, Y., & Dok Kim, Y. (2014). Hydrophobic Polydimethylsiloxane (PDMS) Coating of Mesoporous Silica and Its Use as a Preconcentrating Agent of Gas Analytes. *Langmuir*, *30*(34), 10256–10262. https://doi.org/10.1021/la502915r

Jiang, D., Murugadoss, V., Wang, Y., Lin, J., Ding, T., Wang, Z., Shao, Q., Wang, C., Liu, H., Lu, N., Wei, R., Subramania, A., & Guo, Z. (2019). Electromagnetic Interference Shielding Polymers and Nanocomposites - A Review. *Polymer Reviews*, *59*(2), 280–337. https://doi.org/10.1080/15583724.2018.1546737

Jiang, J. J., Li, D., Li, S. J., Wang, Z. H., Wang, Y., He, J., Liu, W., & Zhang, Z. D. (2015). Electromagnetic wave absorption and dielectric-modulation of metallic perovskite lanthanum nickel oxide. *RSC Advances*, *5*(19), 14584–14591. https://doi.org/10.1039/c5ra00139k

Jiang, S., Hou, H., Agarwal, S., & Greiner, A. (2016). Polyimide Nanofibers by “Green” Electrospinning via Aqueous Solution for Filtration Applications. *ACS Sustainable Chemistry & Engineering*, *4*(9), 4797–4804. https://doi.org/10.1021/acssuschemeng.6b01031

Jiang, Y., Fu, X., Tian, R., Zhang, W., Du, H., Fu, C., Zhang, Z., Xie, P., Xin, J., & Fan, R. (2020). Nitrogen-doped carbon nanofibers with sulfur heteroatoms for improving microwave absorption. *Journal of Materials Science*, *55*(14), 5832–5842. https://doi.org/10.1007/S10853-020-04430-Y

Jing, P., Liu, K., Soule, L., Wang, J., Li, T., Zhao, B., & Liu, M. (2021). Engineering the architecture and oxygen deficiency of T-Nb2O5-carbon-graphene composite for high-rate lithium-ion batteries. *Nano Energy*, *89*(PB), 106398. https://doi.org/10.1016/j.nanoen.2021.106398

Joseph, J., V. Nair, S., & Menon, D. (2015). Integrating Substrateless Electrospinning with Textile Technology for Creating Biodegradable Three-Dimensional Structures. *Nano Letters*, *15*(8), 5420–5426. https://doi.org/10.1021/acs.nanolett.5b01815

Kaliyaraj Selva Kumar, A., Zhang, Y., Li, D., & Compton, R. G. (2020). A mini-review: How reliable is the drop casting technique? *Electrochemistry Communications*, *121*(November), 106867. https://doi.org/10.1016/j.elecom.2020.106867

Kang, K., Kim, H., Choi, E., Shim, H. J., Cui, Y., Gao, Y., Huh, H., & Pyo, S. G. (n.d.). Electro-Magnetic Interference Shielding Effect of Electrospun Carbon Nanofiber Web Containing BaTiO3 and Fe3O4 Nanoparticles. In *Journal of Nanoscience and Nanotechnology* (Vol. 17, Issue 10, pp. 7689–7694). https://www.ingentaconnect.com/content/asp/jnn/2017/00000017/00000010/art00116

Kannan, S. K., Hareendrakrishnakumar, H., & Joseph, M. G. (2021). Efficient polysulfide shuttle mitigation by graphene-lithium cobalt vanadate hybrid for advanced lithium-sulfur batteries. *Journal of Electroanalytical Chemistry*, *899*(June), 115665. https://doi.org/10.1016/j.jelechem.2021.115665

Kausar, A. (2016). Electromagnetic Interference Shielding of Polyaniline/Poloxalene/Carbon Black Composite. *International Journal of Materials and Chemistry*, *6*(1), 6–11. https://doi.org/10.5923/j.ijmc.20160601.02

Kerkeni, L., Ruano, P., Delgado, L. L., Picco, S., Villegas, L., Tonelli, F., Merlo, M., Rigau, J., Diaz, D., & Masuelli, M. (2016). We are IntechOpen , the world ' s leading publisher of Open Access books Built by scientists , for scientists TOP 1 %. *Intech*, *tourism*, 13.

Khatkhatay, F., Chen, A., Lee, J. H., Zhang, W., Abdel-Raziq, H., & Wang, H. (2013). Ferroelectric properties of vertically aligned nanostructured BaTiO 3-CeO2 thin films and their integration on silicon. *ACS Applied Materials and Interfaces*, *5*(23), 12541–12547. https://doi.org/10.1021/am403834k

Khosla, A., Shah, S., Shiblee, M. N. I., Mir, S. H., Nagahara, L. A., Thundat, T., Shekar, P. K., Kawakami, M., & Furukawa, H. (2018). Carbon fiber doped thermosetting elastomer for flexible sensors: physical properties and microfabrication. *Scientific Reports*, *8*(1), 1–9. https://doi.org/10.1038/s41598-018-30846-3

Kim, C. K., Ji, J. M., Zhou, H., Lu, C., & Kim, H. K. (2020a). Tellurium-doped, mesoporous carbon nanomaterials as transparent metal-free counter electrodes for high-performance bifacial dye-sensitized solar cells. *Nanomaterials*, *10*(1). https://doi.org/10.3390/nano10010029

Kim, C. K., Ji, J. M., Zhou, H., Lu, C., & Kim, H. K. (2020b). Tellurium-doped, mesoporous carbon nanomaterials as transparent metal-free counter electrodes for high-performance bifacial dye-sensitized solar cells. *Nanomaterials*, *10*(1), 0–7. https://doi.org/10.3390/nano10010029

Kim, H.-R., Kim, B.-S., & Kim, I.-S. (2012). Fabrication and EMI shielding effectiveness of Ag-decorated highly porous poly (vinyl alcohol)/Fe2O3 nanofibrous composites. *Materials Chemistry and Physics*, *135*(2–3), 1024–1029.

Kim, H., Fujimori, K., Kim, B., & Kim, I. (2012). *Lightweight nanofibrous EMI shielding nanowebs prepared by electrospinning and metallization*. *72*, 1233–1239. https://doi.org/10.1016/j.compscitech.2012.04.009

Kim, H. R., Kim, B. S., & Kim, I. S. (2012). Fabrication and EMI shielding effectiveness of Ag-decorated highly porous poly(vinyl alcohol)/Fe 2O 3 nanofibrous composites. *Materials Chemistry and Physics*, *135*(2–3), 1024–1029. https://doi.org/10.1016/j.matchemphys.2012.06.008

Kim, Jaeyeon, Lee, S., Kim, C., Park, Y., Kim, M. H., & Seol, J. H. (2020). Electromagnetic

interference shield of highly thermal-conducting, light-weight, and flexible electrospun nylon 66 nanofiber-silver multi-layer film. *Polymers*, *12*(8), 1–19. https://doi.org/10.3390/polym12081805

Kim, Jinyoung, Kim, G., Kim, S. Y., Lee, S., Kim, Y., Lee, J., Kim, J., Jung, Y. C., Kwon, J., & Han, H. (2021). Fabrication of highly flexible electromagnetic interference shielding polyimide carbon black composite using hot-pressing method. *Composites Part B: Engineering*, *221*, 109010. https://doi.org/10.1016/j.compositesb.2021.109010

Kim, M., Kim, S., Seong, Y. C., Yang, K. H., & Choi, H. (2021). Multiwalled Carbon Nanotube Buckypaper/Polyacrylonitrile Nanofiber Composite Membranes for Electromagnetic Interference Shielding. *ACS Applied Nano Materials*, *4*(1), 729–738. https://doi.org/10.1021/acsanm.0c03040

Kim, S., Lee, K. Y., & Lim, J.-H. (2020). Fabrication of PEDOT: PSS-PVP nanofiber-embedded Sb2Te3 thermoelectric films by multi-step coating and their improved thermoelectric properties. *Materials*, *13*(12), 2835.

Koka, A., Zhou, Z., & Sodano, H. A. (2014). Vertically aligned BaTiO3 nanowire arrays for energy harvesting. *Energy and Environmental Science*, *7*(1), 288–296. https://doi.org/10.1039/c3ee42540a

Koka, A., Zhou, Z., Tang, H., & Sodano, H. A. (2014). Controlled synthesis of ultra-long vertically aligned BaTiO3 nanowire arrays for sensing and energy harvesting applications. *Nanotechnology*, *25*(37). https://doi.org/10.1088/0957-4484/25/37/375603

Kowsari, E., & Mallakmohamadi, M. (2012). Electrospun PAN nano fi ber process control by ionic liquids and electromagnetic wave absorbing properties. *Materials Letters*, *79*, 7–10. https://doi.org/10.1016/j.matlet.2012.03.075

Kruželák, J., Kvasničáková, A., Hložeková, K., & Hudec, I. (2021). Progress in polymers and polymer composites used as efficient materials for EMI shielding. *Nanoscale Advances*, *3*(1), 123–172. https://doi.org/10.1039/d0na00760a

Kuekha, R., Mubarak, T. H., & Azhdar, B. (2022). Electromagnetic Interference Shielding and Characterization of Ni2+Substituted Cobalt Nanoferrites Prepared by Sol-Gel Auto Combustion Method. *Advances in Materials Science and Engineering*, *2022*. https://doi.org/10.1155/2022/3992402

Kumar, P. (2019). Ultrathin 2D Nanomaterials for Electromagnetic Interference Shielding. *Advanced Materials Interfaces*, *6*(24), 1901454. https://doi.org/https://doi.org/10.1002/admi.201901454

Kumar, P., Kumar, A., Cho, K. Y., Das, T. K., & Sudarsan, V. (2017). An asymmetric electrically conducting self-aligned graphene/polymer composite thin film for efficient electromagnetic interference shielding. *AIP Advances*, *7*(1). https://doi.org/10.1063/1.4973535

Kumar, Rajeev, Choudhary, H. K., Anupama, A. V., Menon, A. V., Pawar, S. P., Bose, S., & Sahoo, B. (2019). Nitrogen doping as a fundamental way to enhance the EMI shielding behavior of cobalt particle-embedded carbonaceous nanostructures. *New Journal of Chemistry*, *43*(14), 5568–5580. https://doi.org/10.1039/c9nj00639g

Kumar, Rajesh, Sahoo, S., Joanni, E., Singh, R. K., Tan, W. K., Kar, K. K., & Matsuda, A. (2021). Recent progress on carbon-based composite materials for microwave electromagnetic interference shielding. *Carbon*, *177*, 304–331. https://doi.org/10.1016/j.carbon.2021.02.091

Kumari, N., Gaurav, K., Samdarshi, S. K., Bhattacharyya, A. S., Paul, S., Rajbongshi, B. M., & Mohanty, K. (2020). Dependence of photoactivity of niobium pentoxide (Nb2O5) on crystalline phase and electrokinetic potential of the hydrocolloid. *Solar Energy Materials and Solar Cells*, *208*(December 2019), 110408. https://doi.org/10.1016/j.solmat.2020.110408

Lai, H., Li, W., Xu, L., Wang, X., Jiao, H., Fan, Z., Lei, Z., & Yuan, Y. (2020a). Scalable fabrication of highly crosslinked conductive nanofibrous films and their applications in energy storage and electromagnetic interference shielding. *Chemical Engineering Journal*, *400*, 125322. https://doi.org/10.1016/j.cej.2020.125322

Lai, H., Li, W., Xu, L., Wang, X., Jiao, H., Fan, Z., Lei, Z., & Yuan, Y. (2020b). Scalable fabrication of highly crosslinked conductive nanofibrous films and their applications in energy storage and electromagnetic interference shielding. *Chemical Engineering Journal*, *400*. https://doi.org/10.1016/j.cej.2020.125322

Lan, C., Guo, M., Li, C., Qiu, Y., Ma, Y., & Sun, J. (2020). Axial Alignment of Carbon Nanotubes on Fibers to Enable Highly Conductive Fabrics for Electromagnetic Interference Shielding. *ACS Applied Materials and Interfaces*, *12*(6), 7477–7485. https://doi.org/10.1021/acsami.9b21698

Lee, B.-S. (n.d.). *polymers A Review of Recent Advancements in Electrospun Anode Materials to Improve Rechargeable Lithium Battery Performance*. https://doi.org/10.3390/polym12092035

Lee, B. S., Yoon, J., Jung, C., Kim, D. Y., Jeon, S. Y., Kim, K. H., Park, J. H., Park, H., Lee, K. H., Kang, Y. S., Park, J. H., Jung, H., Yu, W. R., & Doo, S. G. (2016). Silicon/Carbon Nanotube/BaTiO3 Nanocomposite Anode: Evidence for Enhanced Lithium-Ion Mobility Induced by the Local Piezoelectric Potential. *ACS Nano*, *10*(2), 2617–2627. https://doi.org/10.1021/acsnano.5b07674

Lee, J. H., Kim, Y. S., Ru, H. J., Lee, S. Y., & Park, S. J. (2022). Highly Flexible Fabrics/Epoxy Composites with Hybrid Carbon Nanofillers for Absorption-Dominated Electromagnetic Interference Shielding. *Nano-Micro Letters*, *14*(1), 1–17. https://doi.org/10.1007/s40820-022-00926-1

Lee, J., Liu, Y., Liu, Y., Park, S. J., Park, M., & Kim, H. Y. (2017). Ultrahigh electromagnetic

interference shielding performance of lightweight, flexible, and highly conductive copper-clad carbon fiber nonwoven fabrics. *Journal of Materials Chemistry C*, *5*(31), 7853–7861. https://doi.org/10.1039/c7tc02074k

Lee, S., Choi, H., & Eom, K. S. (2019). Enhancing the electrochemical performances of a tellurium-based cathode for a high-volumetric capacity Li battery via a high-energy ball mill with sulfur edge-functionalized carbon. *Journal of Power Sources*, *430*(March), 112–119. https://doi.org/10.1016/j.jpowsour.2019.05.002

Lee, S. H., Kang, D., & Oh, I. K. (2017). Multilayered graphene-carbon nanotube-iron oxide three-dimensional heterostructure for flexible electromagnetic interference shielding film. *Carbon*, *111*, 248–257. https://doi.org/10.1016/j.carbon.2016.10.003

Lee, T.-W., Lee, S.-E., & Gyu Jeong, Y. (2016). Highly Effective Electromagnetic Interference Shielding Materials based on Silver Nanowire/Cellulose Papers. *ACS Applied Materials & Interfaces*, *8*(20), 13123–13132. https://doi.org/10.1021/acsami.6b02218

Li, D., Wang, Y., & Xia, Y. (2003). Electrospinning of polymeric and ceramic nanofibers as uniaxially aligned arrays. *Nano Letters*, *3*(8), 1167–1171. https://doi.org/10.1021/nl0344256

Li, J., Su, S., Zhou, L., Kundrát, V., Abbot, A. M., Mushtaq, F., Ouyang, D., James, D., Roberts, D., & Ye, H. (2013). Carbon nanowalls grown by microwave plasma enhanced chemical vapor deposition during the carbonization of polyacrylonitrile fibers. *Journal of Applied Physics*, *113*(2). https://doi.org/10.1063/1.4774218

Li, S., Xu, Q., Uchaker, E., Cao, X., & Cao, G. (2016). Comparison of amorphous, pseudohexagonal and orthorhombic Nb2O5 for high-rate lithium ion insertion. *CrystEngComm*, *18*(14), 2532–2540. https://doi.org/10.1039/c5ce02069g

Li, T., Luo, G., Liu, K., Li, X., Sun, D., Xu, L., Li, Y., & Tang, Y. (2018). Encapsulation of Ni3Fe Nanoparticles in N-Doped Carbon Nanotube–Grafted Carbon Nanofibers as High-Efficiency Hydrogen Evolution Electrocatalysts. *Advanced Functional Materials*, *28*(51), 1–9. https://doi.org/10.1002/adfm.201805828

Li, W., Zhang, L.-S., Wang, Q., Yu, Y., Chen, Z., Cao, C.-Y., & Song, W.-G. (n.d.). *Low-cost synthesis of graphitic carbon nanofibers as excellent room temperature sensors for explosive gases †*. https://doi.org/10.1039/c2jm32031b

Li, W., Zhang, L. S., Wang, Q., Yu, Y., Chen, Z., Cao, C. Y., & Song, W. G. (2012). Low-cost synthesis of graphitic carbon nanofibers as excellent room temperature sensors for explosive gases. *Journal of Materials Chemistry*, *22*(30), 15342–15347. https://doi.org/10.1039/C2JM32031B

Li, Yan, Abedalwafa, M. A., Tang, L., Li, D., & Wang, L. (2018). Electrospun nanofibers for sensors. In *Electrospinning: Nanofabrication and Applications*. https://doi.org/10.1016/B978-0-323-51270-1.00018-2

Li, Yang, Wang, Y., Cui, G., Zhu, T., Zhang, J., Yu, C., Cui, J., Wu, J., Tan, H. H., Zhang, Y., & Wu, Y. (2020). Carbon-Coated Self-Assembled Ultrathin T-Nb2O5Nanosheets for High-Rate Lithium-Ion Storage with Superior Cycling Stability. *ACS Applied Energy Materials*, *3*(12), 12037–12045. https://doi.org/10.1021/acsaem.0c02180

Li, Yifu, Li, Q., & Tan, Z. (2019a). A review of electrospun nanofiber-based separators for rechargeable lithium-ion batteries. *Journal of Power Sources*, *443*(August), 227262. https://doi.org/10.1016/j.jpowsour.2019.227262

Li, Yifu, Li, Q., & Tan, Z. (2019b). A review of electrospun nanofiber-based separators for rechargeable lithium-ion batteries. *Journal of Power Sources*, *443*, 227262. https://doi.org/10.1016/J.JPOWSOUR.2019.227262

Li, Yiping, Dai, X., Bai, Y., Liu, Y., Wang, Y., Liu, O., Yan, F., Tang, Z., Zhang, X., & Deng, X. (2017). Electroactive BaTiO3 nanoparticle-functionalized fibrous scaffolds enhance osteogenic differentiation of mesenchymal stem cells. *International Journal of Nanomedicine*, *12*(null), 4007–4018. https://doi.org/10.2147/IJN.S135605

Liang, J., Zhao, H., Yue, L., Fan, G., Li, T., Lu, S., Chen, G., Gao, S., Asiri, A. M., & Sun, X. (2020). *Recent advances in electrospun nanofibers for supercapacitors*. https://doi.org/10.1039/d0ta05100d

Lim, E., Kim, H., Jo, C., Chun, J., Ku, K., Kim, S., Lee, H. I., Nam, I. S., Yoon, S., Kang, K., & Lee, J. (2014). Advanced hybrid supercapacitor based on a mesoporous niobium pentoxide/carbon as high-performance anode. *ACS Nano*, *8*(9), 8968–8978. https://doi.org/10.1021/nn501972w

Lin, Jiande, Yuan, Y., Su, Q., Pan, A., Dinesh, S., Peng, C., Cao, G., & Liang, S. (2018). Facile synthesis of Nb2O5/carbon nanocomposites as advanced anode materials for lithium-ion batteries. *Electrochimica Acta*, *292*, 63–71. https://doi.org/10.1016/j.electacta.2018.09.138

Lin, Jun, Yu, M., Lin, C., & Liu, X. (2007). Multiform Oxide Optical Materials via the Versatile Pechini-Type Sol−Gel Process: Synthesis and Characteristics. *The Journal of Physical Chemistry C*, *111*(16), 5835–5845. https://doi.org/10.1021/jp070062c

Liu, J., Zhao, Z., & Zhang, L. (2021). Toward the application of electromagnetic wave absorption by two-dimension materials. *Journal of Materials Science: Materials in Electronics*, *32*(21), 25562–25576. https://doi.org/10.1007/s10854-020-03800-1

Liu, Y., Wang, J., Xu, Y., Zhu, Y., Bigio, D., & Wang, C. (2014). Lithium-tellurium batteries based on tellurium/porous carbon composite. *Journal of Materials Chemistry A*, *2*(31), 12201–12207. https://doi.org/10.1039/c4ta02075h

Louwet, F., Groenendaal, L., Dhaen, J., Manca, J., Van Luppen, J., Verdonck, E., & Leenders, L. (2003). PEDOT/PSS: Synthesis, characterization, properties and applications. *Synthetic Metals*, *135–136*, 115–117. https://doi.org/10.1016/S0379-6779(02)00518-0

Lu, P., Hu, X., Li, Y., Zhang, M., Liu, X., He, Y., Dong, F., Fu, M., & Zhang, Z. (2018). One-step preparation of a novel SrCO3/g-C3N4 nano-composite and its application in selective adsorption of crystal violet. *RSC Advances*, *8*(12), 6315–6325. https://doi.org/10.1039/c7ra11565b

Lu, S., Cai, W., Cao, N., Qian, H., Lu, Z., & Cui, S. (2022). Understanding the Extraordinary Flexibility of Polydimethylsiloxane through Single-Molecule Mechanics. *ACS Materials Letters*, *4*(2), 329–335. https://doi.org/10.1021/acsmaterialslett.1c00655

Lu, X., Wang, C., & Wei, Y. (2009). One-dimensional composite nanomaterials: Synthesis by electrospinning and their applications. *Small*, *5*(21), 2349–2370.

Luo, C. J., Stoyanov, S. D., Stride, E., Pelan, E., & Edirisinghe, M. (2012). Electrospinning versus fibre production methods: from specifics to technological convergence. *This Journal Is Cite This: Chem. Soc. Rev*, *41*, 4708–4735. https://doi.org/10.1039/c2cs35083a

Luxa, J., Oliveira, F. M., Jellet, C. W., Gusmão, R., & Sofer, Z. (2023). Freestanding Foils of NbSe2 and Carbon Nanotubes for Efficient Electromagnetic Shielding. *ACS Applied Nano Materials*, *6*(5), 3333–3343. https://doi.org/10.1021/acsanm.2c05119

Lv, H., Guo, Y., Wu, G., Ji, G., Zhao, Y., & Xu, Z. J. (2017). Interface Polarization Strategy to Solve Electromagnetic Wave Interference Issue. *ACS Applied Materials and Interfaces*, *9*(6), 5660–5668. https://doi.org/10.1021/acsami.6b16223

Ma, L., Wu, Y., Wu, Z., Xia, P., He, Y., Zhang, L., Fan, H., Tong, C., Zhang, L., Gao, X., & Deng, L. (2023). Enhanced dielectric loss in N-doped three-dimensional porous carbon for microwave absorption. *Materials Today Advances*, *20*, 100434. https://doi.org/https://doi.org/10.1016/j.mtadv.2023.100434

Mamun, A., Blachowicz, T., & Sabantina, L. (2021). Electrospun nanofiber mats for filtering applications technology, structure and materials. *Polymers*, *13*(9), 1–14. https://doi.org/10.3390/polym13091368

Maruthi, N., Faisal, M., & Raghavendra, N. (2021). Conducting polymer based composites as efficient EMI shielding materials: A comprehensive review and future prospects. *Synthetic Metals*, *272*(December 2020), 116664. https://doi.org/10.1016/j.synthmet.2020.116664

Maruthi, N., Faisal, M., Raghavendra, N., Prasanna, B. P., Manohara, S. R., & Revanasiddappa, M. (2021). Promising EMI shielding effectiveness and anticorrosive properties of PANI-Nb2O5 nanocomposites: Multifunctional approach. *Synthetic Metals*, *275*, 116744. https://doi.org/10.1016/J.SYNTHMET.2021.116744

McCann, J. T., Chen, J. I. L., Li, D., Ye, Z. G., & Xia, Y. (2006). Electrospinning of polycrystalline barium titanate nanofibers with controllable morphology and alignment. *Chemical Physics Letters*, *424*(1–3), 162–166. https://doi.org/10.1016/j.cplett.2006.04.082

Mefford, J. T., Rong, X., Abakumov, A. M., Hardin, W. G., Dai, S., Kolpak, A. M., Johnston, K. P., & Stevenson, K. J. (2016). Water electrolysis on La1-xSrxCoO3-δ perovskite electrocatalysts. *Nature Communications*, *7*. https://doi.org/10.1038/ncomms11053

Mendoza-Diaz, M. I., Garcia-Gutierrez, D. F., Sepulveda-Guzman, S., Moreno-Cortez, I. E., & Garcia-Gutierrez, D. I. (2019). Tuning the optoelectronic properties of PEDOT: PSS-PVP core–shell electrospun nanofibers by solvent-quantum dot doping and phase inversion. *Nanotechnology*, *30*(39), 395601.

Meng, J., He, Q., Xu, L., Zhang, X., Liu, F., Wang, X., Li, Q., Xu, X., Zhang, G., Niu, C., Xiao, Z., Liu, Z., Zhu, Z., Zhao, Y., & Mai, L. (2019). Identification of Phase Control of Carbon-Confined Nb 2 O 5 Nanoparticles toward High-Performance Lithium Storage. *Advanced Energy Materials*, *9*(18), 1–11. https://doi.org/10.1002/aenm.201802695

Mohan, L., Kumar, T. N., Karakkad, S., & Krishnan, S. T. (2021). Development of Cost-Effective Carbon Nanofiber Epoxy Nanocomposites for Lightweight Wideband EMI Shielding Application. *IEEE Transactions on Nanotechnology*, *20*, 627–634. https://doi.org/10.1109/tnano.2021.3103955

Monfared, M., Taghizadeh, S., Zare-Hoseinabadi, A., Mousavi, S. M., Hashemi, S. A., Ranjbar, S., & Amani, A. M. (2019). Emerging frontiers in drug release control by core–shell nanofibers: a review. *Drug Metabolism Reviews*, *51*(4), 589–611. https://doi.org/10.1080/03602532.2019.1642912

Moon, Y.-E., Yun, J., & Kim, H.-I. (2013). Synergetic improvement in electromagnetic interference shielding characteristics of polyaniline-coated graphite oxide/γ-Fe2O3/BaTiO3 nanocomposites. *Journal of Industrial and Engineering Chemistry*, *19*(2), 493–497. https://doi.org/https://doi.org/10.1016/j.jiec.2012.09.002

Moradipour, P., Limoee, M., Janfaza, S., & Behbood, L. (2021). Core-Shell Nanofibers Based on Polycaprolactone/Polyvinyl Alcohol and Polycaprolactone/Collagen for Biomedical Applications. *Journal of Pharmaceutical Innovation*, *0123456789*. https://doi.org/10.1007/s12247-021-09568-z

Morais, L. A., Adán, C., Araujo, A. S., Guedes, A. P. M. A., & Marugán, J. (2017). Synthesis, Characterization, and Photonic Efficiency of Novel Photocatalytic Niobium Oxide Materials. *Global Challenges*, *1*(9), 1700066. https://doi.org/10.1002/gch2.201700066

Moreira, M. L., Mambrini, G. P., Volanti, D. P., Leite, E. R., Orlandi, M. O., Pizani, P. S., Mastelaro, V. R., Paiva-Santos, C. O., Longo, E., & Varela, J. A. (2008). Hydrothermal microwave: A new route to obtain photoluminescent crystalline BaTiO3 nanoparticles. *Chemistry of Materials*, *20*(16), 5381–5387. https://doi.org/10.1021/cm801638d

Morvan, J., Buyuktanir, E., West, J. L., & Jákli, A. (2012). Highly piezoelectric biocompatible and soft composite fibers. *Applied Physics Letters*, *100*(6), 1–5. https://doi.org/10.1063/1.3683482

Nagaraju, P., Vasudevan, R., Alsalme, A., Alghamdi, A., Arivanandhan, M., & Jayavel, R. (2020). Surfactant-free synthesis of Nb2O5 nanoparticles anchored graphene nanocomposites with enhanced electrochemical performance for supercapacitor electrodes. *Nanomaterials*, *10*(1). https://doi.org/10.3390/nano10010160

Nakhaei, O., Shahtahmassebi, N., & Roknabadi, M. R. (2016). Co-electrospinning fabrication and study of structural and electromagnetic interference-shielding effectiveness of TiO 2 / SiO 2 core – shell nanofibers. *Applied Physics A*, *122*(5), 1–10. https://doi.org/10.1007/s00339-016-0072-1

Nasouri, K., & Shoushtari, A. M. (2017a). Designing, modeling and manufacturing of lightweight carbon nanotubes/polymer composite nanofibers for electromagnetic interference shielding application. *Composites Science and Technology*, *145*, 46–54. https://doi.org/https://doi.org/10.1016/j.compscitech.2017.03.041

Nasouri, K., & Shoushtari, A. M. (2017b). Effects of diameter and surface area of electrospun nanocomposite fibers on electromagnetic interference shielding. *Polymer Science - Series A*, *59*(5), 718–725. https://doi.org/10.1134/S0965545X17050133

Nasouri, K., & Valipour, P. (2015). Fabrication of polyamide 6/carbon nanotubes composite electrospun nanofibers for microwave absorption application. *Polymer Science - Series A*, *57*(3), 359–364. https://doi.org/10.1134/S0965545X15030098

Nishio, K., Molla, S., Okugaki, T., Nakanishi, S., Nitta, I., & Kotani, Y. (2015). Oxygen reduction and evolution reactions of air electrodes using a perovskite oxide as an electrocatalyst. *Journal of Power Sources*, *278*, 645–651. https://doi.org/10.1016/j.jpowsour.2014.12.100

Ohkawa, H., Matsubara, M., Yasuda, N., & Ozawa, N. (1992). Tellurium-carbon (TeC:H) films for a write-once read many (WORM) optical disk memory. *Diamond and Related Materials*, *1*(5–6), 697–704. https://doi.org/10.1016/0925-9635(92)90194-S

Oliveira, F. M., Luxa, J., Bouša, D., Sofer, Z., & Gusmão, R. (2022). Electromagnetic Interference Shielding by Reduced Graphene Oxide Foils. *ACS Applied Nano Materials*, *5*(5), 6792–6800. https://doi.org/10.1021/acsanm.2c00785

Orasugh, J. T., & Ray, S. S. (2022). Graphene-Based Electrospun Fibrous Materials with Enhanced EMI Shielding: Recent Developments and Future Perspectives. *ACS Omega*, *7*(38), 33699–33718. https://doi.org/10.1021/acsomega.2c03579

Otieno, F., Shumbula, N. P., Airo, M., Mbuso, M., Moloto, N., Erasmus, R. M., Quandt, A., & Wamwangi, D. (2017a). Improved efficiency of organic solar cells using Au NPs incorporated into PEDOT: PSS buffer layer. *AIP Advances*, *7*(8), 85302.

Otieno, F., Shumbula, N. P., Airo, M., Mbuso, M., Moloto, N., Erasmus, R. M., Quandt, A., & Wamwangi, D. (2017b). Improved efficiency of organic solar cells using Au NPs incorporated into PEDOT:PSS buffer layer. *AIP Advances*, *7*(8).

https://doi.org/10.1063/1.4995803

Pan, T., Zhang, Y., Wang, C., Gao, H., Wen, B., & Yao, B. (2020). Mulberry-like polyaniline-based flexible composite fabrics with effective electromagnetic shielding capability. *Composites Science and Technology*, *188*(December 2019), 107991. https://doi.org/10.1016/j.compscitech.2020.107991

Park, D., Ju, H., & Kim, J. (2018). Preparation and thermoelectric properties of two types of nanostructured tellurium with multi-walled carbon nanotubes. *Journal of Alloys and Compounds*, *748*, 305–313. https://doi.org/10.1016/j.jallcom.2018.03.176

Partheniadis, I., Nikolakakis, I., Laidmäe, I., & Heinämäki, J. (2020). A mini-review: Needleless electrospinning of nanofibers for pharmaceutical and biomedical applications. *Processes*, *8*(6). https://doi.org/10.3390/PR8060673

Peidavosi, N., Azami, M., Beheshtizadeh, N., & Ramazani Saadatabadi, A. (2022). Piezoelectric conductive electrospun nanocomposite PCL/Polyaniline/Barium Titanate scaffold for tissue engineering applications. *Scientific Reports*, *12*(1), 1–13. https://doi.org/10.1038/s41598-022-25332-w

Placet, V., & Delobelle, P. (2015). Mechanical properties of bulk polydimethylsiloxane for microfluidics over a large range of frequencies and aging times. *Journal of Micromechanics and Microengineering*, *25*(3), 1–8. https://doi.org/10.1088/0960-1317/25/3/035009

Qamar, M., Abdalwadoud, M., Ahmed, M. I., Azad, A. M., Merzougui, B., Bukola, S., Yamani, Z. H., & Siddiqui, M. N. (2015). Single-Pot Synthesis of 〈001〉-Faceted N-Doped Nb2O5/Reduced Graphene Oxide Nanocomposite for Efficient Photoelectrochemical Water Splitting. *ACS Applied Materials and Interfaces*, *7*(32), 17954–17962. https://doi.org/10.1021/acsami.5b04667

Qanati, M. V., Rasooli, A., & Rezvani, M. (2022). Main structural and mechanical properties of electrospun PAN-based carbon nanofibers as a function of carbonization maximum temperature. *Polymer Bulletin*, *79*(1), 331–355. https://doi.org/10.1007/s00289-020-03520-w

Qavamnia, S. S., & Nasouri, K. (2016). Facile fabrication of carbon nanotubes/polystyrene composite nanofibers for high-performance electromagnetic interference shielding. *Fibers and Polymers*, *17*(12), 1977–1984. https://doi.org/10.1007/s12221-016-6676-4

Qian, K., Zhou, J., Miao, M., Wu, H., Thaiboonrod, S., Fang, J., & Feng, X. (2023). Highly Ordered Thermoplastic Polyurethane/Aramid Nanofiber Conductive Foams Modulated by Kevlar Polyanion for Piezoresistive Sensing and Electromagnetic Interference Shielding. *Nano-Micro Letters*, *15*(1), 1–18. https://doi.org/10.1007/s40820-023-01062-0

Qing, Y., Zhou, W., Luo, F., & Zhu, D. (2011). Optimization of electromagnetic matching of

carbonyl iron/BaTiO3 composites for microwave absorption. *Journal of Magnetism and Magnetic Materials*, *323*(5), 600–606. https://doi.org/10.1016/j.jmmm.2010.10.021

Raba, A. M., Bautista, J., & Murillo, E. (2016). Synthesis and characterization of the oxide nanoparticles obtained by the polymeric precursor method. *Journal of Physics: Conference Series*, *687*(1). https://doi.org/10.1088/1742-6596/687/1/012084

Ramlow, H., de Souza, G. B., Fonseca, M. P., Raizer, A., Rambo, C. R., & Machado, R. A. F. (2023). Lightweight and flexible nanostructured C/SiCN nanofiber nonwoven for electromagnetic reflection shielding of 5G C-Band frequencies. *Journal of Materials Science: Materials in Electronics*, *34*(22), 1–15. https://doi.org/10.1007/s10854-023-11037-x

Ran, J., Guo, M., Zhong, L., & Fu, H. (2019). In situ growth of BaTiO3 nanotube on the surface of reduced graphene oxide: A lightweight electromagnetic absorber. *Journal of Alloys and Compounds*, *773*, 423–431. https://doi.org/10.1016/j.jallcom.2018.09.142

Rani, P., Ahamed, M. B., & Deshmukh, K. (2020). Dielectric and electromagnetic interference shielding properties of carbon black nanoparticles reinforced PVA/PEG blend nanocomposite films. *Materials Research Express*, *7*(6). https://doi.org/10.1088/2053-1591/ab9853

Rani, P., Basha, S. K. J., Deshmukh, K., & Pasha, S. K. K. (2023). *Chapter 29 - Functionalized nanofibers for EMI shielding and microwave absorption applications* (K. Deshmukh, S. K. K. Pasha, A. Barhoum, & C. B. T.-F. N. Mustansar Hussain (eds.); pp. 831–866). Elsevier. https://doi.org/https://doi.org/10.1016/B978-0-323-99461-3.00023-6

Rathore, P., & D. Schiffman, J. (2020). Beyond the Single-Nozzle: Coaxial Electrospinning Enables Innovative Nanofiber Chemistries, Geometries, and Applications. *ACS Applied Materials & Interfaces*, *13*(1), 48–66. https://doi.org/10.1021/acsami.0c17706

Ravindra, R., & Badekai Ramachandra, B. (2011). High yield synthesis of carbon nanofibers in an environmental friendly route. *Applied Nanoscience (Switzerland)*, *1*(2), 103–108. https://doi.org/10.1007/s13204-011-0014-3

Ravindren, R., Mondal, S., Nath, K., & Das, N. C. (2019). Synergistic effect of double percolated co-supportive MWCNT-CB conductive network for high-performance EMI shielding application. *Polymers for Advanced Technologies*, *30*(6), 1506–1517. https://doi.org/10.1002/pat.4582

Revathi, V., Dinesh Kumar, S., Subramanian, V., & Chellamuthu, M. (2015). BMFO-PVDF electrospun fiber based tunable metamaterial structures for electromagnetic interference shielding in microwave frequency region. *EPJ Applied Physics*, *72*(2), 1–7. https://doi.org/10.1051/epjap/2015150368

Robinson, A. J., Pérez-Nava, A., Ali, S. C., González-Campos, J. B., Holloway, J. L., & Cosgriff-Hernandez, E. M. (2021). Comparative analysis of fiber alignment methods in

electrospinning. *Matter*, *4*(3), 821–844. https://doi.org/10.1016/j.matt.2020.12.022

Rubeziene, V., Baltusnikaite-Guzaitiene, J., Abraitiene, A., Sankauskaite, A., Ragulis, P., Santos, G., & Pimenta, J. (2021). Development and investigation of PEDOT:PSS composition coated fabrics intended for microwave shielding and absorption. *Polymers*, *13*(8), 1–21. https://doi.org/10.3390/polym13081191

Sagitha, P., Reshmi, C. R., Manaf, O., Sundaran, S. P., Juraij, K., & Sujith, A. (2020). Development of nanocomposite membranes by electrospun nanofibrous materials. *Nanocomposite Membranes for Water and Gas Separation*, 199–218. https://doi.org/10.1016/B978-0-12-816710-6.00008-0

Saha, B., & Schatz, G. C. (2012). Carbonization in Polyacrylonitrile (PAN) Based Carbon Fibers Studied by ReaxFF Molecular Dynamics Simulations. *The Journal of Physical Chemistry B*, *116*(15), 4684–4692. https://doi.org/10.1021/jp300581b

Saini, P., & Aror, M. (2012). Microwave Absorption and EMI Shielding Behavior of Nanocomposites Based on Intrinsically Conducting Polymers, Graphene and Carbon Nanotubes. *New Polymers for Special Applications*, *September*. https://doi.org/10.5772/48779

Saini, P., Arora, M., Gupta, G., Gupta, B. K., Singh, V. N., & Choudhary, V. (2013). High permittivity polyaniline-barium titanate nanocomposites with excellent electromagnetic interference shielding response. *Nanoscale*, *5*(10), 4330–4336. https://doi.org/10.1039/c3nr00634d

Sajid, H. M., Afzal, H., Irfan, M., Saleem, M., Jan, R., Javed, S., & Akram, M. A. (2022). Design of Multilayered 2D Nanomaterial Composite Structures for EMI Shielding Analysis. *ACS Omega*, *7*(40), 35586–35594. https://doi.org/10.1021/acsomega.2c03186

Salimbeygi, G., Nasouri, K., Shoushtari, A. M., Malek, R., & Mazaheri, F. (2013). Fabrication of polyvinyl alcohol/multi-walled carbon nanotubes composite electrospun nanofibres and their application as microwave absorbing material. *Micro & Nano Letters*, *8*(8), 455–459. https://doi.org/https://doi.org/10.1049/mnl.2013.0381

Sankar, S. S., Rathishkumar, A., Geetha, K., & Kundu, S. (2021). Electrospinning as a tool in fabricating hydrated porous cobalt phosphate fibrous network as high rate OER electrocatalysts in alkaline and neutral media. *International Journal of Hydrogen Energy*, *46*(17), 10366–10376. https://doi.org/10.1016/j.ijhydene.2020.12.131

Sankaran, S., Deshmukh, K., Ahamed, M. B., & Khadheer Pasha, S. K. (2018). Recent advances in electromagnetic interference shielding properties of metal and carbon filler reinforced flexible polymer composites: A review. *Composites Part A: Applied Science and Manufacturing*, *114*, 49–71. https://doi.org/10.1016/j.compositesa.2018.08.006

Sarika, P. R., Cinthya, K., Jayakrishnan, A., Anilkumar, P. R., & James, N. R. (2014). Modified gum arabic cross-linked gelatin scaffold for biomedical applications. *Materials Science*

and Engineering: C, *43*, 272–279. https://doi.org/10.1016/J.MSEC.2014.06.042

Sarkar, B., Li, X., Quenneville, E., Carignan, L. P., Wu, K., & Cicoira, F. (2021). Lightweight and flexible conducting polymer sponges and hydrogels for electromagnetic interference shielding. *Journal of Materials Chemistry C*, *9*(46), 16558–16565. https://doi.org/10.1039/d1tc04008a

Schierholz, R., Kröger, D., Weinrich, H., Gehring, M., Tempel, H., Kungl, H., Mayer, J., & Eichel, R. A. (2019). The carbonization of polyacrylonitrile-derived electrospun carbon nanofibers studied by: In situ transmission electron microscopy. *RSC Advances*, *9*(11), 6267–6277. https://doi.org/10.1039/c8ra10491c

Schiffman, J. D., & Schauer, C. L. (2008). A review: electrospinning of biopolymer nanofibers and their applications. *Polymer Reviews*, *48*(2), 317–352.

Seo, M. H., Park, H. W., Lee, D. U., Park, M. G., & Chen, Z. (2015). Design of Highly Active Perovskite Oxides for Oxygen Evolution Reaction by Combining Experimental and ab Initio Studies. *ACS Catalysis*, *5*(7), 4337–4344. https://doi.org/10.1021/acscatal.5b00114

Shahzad, F., Alhabeb, M., Hatter, C. B., Anasori, B., Hong, S. M., Koo, C. M., & Gogotsi, Y. (2016). Electromagnetic interference shielding with 2D transition metal carbides (MXenes). *Science*, *353*(6304), 1137–1140. https://doi.org/10.1126/science.aag2421

Shahzad, F., Kumar, P., Yu, S., Lee, S., Kim, Y. H., Hong, S. M., & Koo, C. M. (2015). Sulfur-doped graphene laminates for EMI shielding applications. *Journal of Materials Chemistry C*, *3*(38), 9802–9810. https://doi.org/10.1039/c5tc02166a

Shahzad, F., Yu, S., Kumar, P., Lee, J. W., Kim, Y. H., Hong, S. M., & Koo, C. M. (2015). Sulfur doped graphene/polystyrene nanocomposites for electromagnetic interference shielding. *Composite Structures*, *133*, 1267–1275. https://doi.org/10.1016/j.compstruct.2015.07.036

Shanmugapriya, S., Zhu, P., Yan, C., Asiri, A. M., Zhang, X., & Selvan, R. K. (2019). Multifunctional high-performance electrocatalytic properties of Nb2O5 incorporated carbon nanofibers as Pt support catalyst. *Advanced Materials Interfaces*, *6*(17), 1900565.

Shao, S., Ma, T., & Fernando, G. F. (2021). Electro-spinning of highly-aligned polyacrylonitrile nano-fibres with continuous spooling. *Scientific Reports*, *11*(1), 1–14. https://doi.org/10.1038/s41598-021-99890-w

Sharbati, M. T. (2016). *Graphene Quantum Dot-Based Organic Light Emitting Diodes*. *September*.

Shayesteh Zeraati, A., Alireza Mirkhani, S., Sharif, F., Akbari, A., P. L. Roberts, E., & Sundararaj, U. (2021). Electrochemically Exfoliated Graphite Nanosheet Films for Electromagnetic Interference Shields. *ACS Applied Nano Materials*, *4*(7), 7221–7233. https://doi.org/10.1021/acsanm.1c01172

Shen, B., Zhai, W., & Zheng, W. (2014). Ultrathin flexible graphene film: An excellent thermal conducting material with efficient EMI shielding. *Advanced Functional Materials*, *24*(28), 4542–4548. https://doi.org/10.1002/adfm.201400079

Shi, H., Liu, C., Jiang, Q., & Xu, J. (2015). Effective Approaches to Improve the Electrical Conductivity of PEDOT:PSS: A Review. *Advanced Electronic Materials*, *1*(4), 1–16. https://doi.org/10.1002/aelm.201500017

Shi, K., & P. Giapis, K. (2018). Scalable Fabrication of Supercapacitors by Nozzle-Free Electrospinning. *ACS Applied Energy Materials*, *1*(2), 296–300. https://doi.org/10.1021/acsaem.7b00227

Shi, X., Zhou, W., Ma, D., Ma, Q., Bridges, D., Ma, Y., & Hu, A. (2015). *Electrospinning of Nanofibers and Their Applications for Energy Devices*. https://doi.org/10.1155/2015/140716

Shi, Y., Hu, M., Xing, Y., & Li, Y. (2020). Temperature-dependent thermal and mechanical properties of flexible functional PDMS/paraffin composites. *Materials and Design*, *185*(October), 108219. https://doi.org/10.1016/j.matdes.2019.108219

Shin, H. K., Park, M., Kang, P. H., Choi, H. S., & Park, S. J. (2014). Preparation and characterization of polyacrylonitrile-based carbon fibers produced by electron beam irradiation pretreatment. *Journal of Industrial and Engineering Chemistry*, *20*(5), 3789–3792. https://doi.org/10.1016/j.jiec.2013.12.080

Shingange, K., Swart, H. C., & Mhlongo, G. H. (2020). Design of porous p-type LaCoO3 nanofibers with remarkable response and selectivity to ethanol at low operating temperature. *Sensors and Actuators, B: Chemical*, *308*. https://doi.org/10.1016/j.snb.2020.127670

Shokrani Havigh, R., & Mahmoudi Chenari, H. (2022a). A comprehensive study on the effect of carbonization temperature on the physical and chemical properties of carbon fibers. *Scientific Reports*, *12*(1), 1–15. https://doi.org/10.1038/s41598-022-15085-x

Shokrani Havigh, R., & Mahmoudi Chenari, H. (2022b). A comprehensive study on the effect of carbonization temperature on the physical and chemical properties of carbon fibers. *Scientific Reports*, *12*(1), 1–14. https://doi.org/10.1038/s41598-022-15085-x

Shukla, V. (2019). Nanoscale advances review of electromagnetic interference shielding. *Nanosc. Adv.*, *1*(5), 1640–1671.

Singh, A. K., Shishkin, A., Koppel, T., & Gupta, N. (2018). A review of porous lightweight composite materials for electromagnetic interference shielding. *Composites Part B: Engineering*, *149*, 188–197. https://doi.org/10.1016/j.compositesb.2018.05.027

Singh, M., Yadav, B. C., Ranjan, A., Kaur, M., & Gupta, S. K. (2017). Synthesis and characterization of perovskite barium titanate thin film and its application as LPG sensor. *Sensors and Actuators, B: Chemical*, *241*(October), 1170–1178.

https://doi.org/10.1016/j.snb.2016.10.018

Singhal, A., Bisht, A., & Irusta, S. (2018). Enhanced oxygen evolution activity of Co3−xNixO4 compared to Co3O4 by low Ni doping. *Journal of Electroanalytical Chemistry*, *823*, 482–491. https://doi.org/10.1016/j.jelechem.2018.06.051

Soares, B. G., Barra, G. M. O., & Indrusiak, T. (2021). Conducting polymeric composites based on intrinsically conducting polymers as electromagnetic interference shielding/microwave absorbing materials—a review. *Journal of Composites Science*, *5*(7). https://doi.org/10.3390/jcs5070173

Somalu, M. (2016). Preparation of lanthanum strontium cobalt oxide powder by a modified sol-gel method. *Malaysian Journal of Analytical Science*, *20*(6), 1458–1466.

Song, W. L., Cao, M. S., Lu, M. M., Yang, J., Ju, H. F., Hou, Z. L., Liu, J., Yuan, J., & Fan, L. Z. (2013). Alignment of graphene sheets in wax composites for electromagnetic interference shielding improvement. *Nanotechnology*, *24*(11). https://doi.org/10.1088/0957-4484/24/11/115708

Song, W. L., Wang, J., Fan, L. Z., Li, Y., Wang, C. Y., & Cao, M. S. (2014). Interfacial engineering of carbon nanofiber-graphene-carbon nanofiber heterojunctions in flexible lightweight electromagnetic shielding networks. *ACS Applied Materials and Interfaces*, *6*(13), 10516–10523. https://doi.org/10.1021/am502103u

Stoerzinger, K. A., Renshaw Wang, X., Hwang, J., Rao, R. R., Hong, W. T., Rouleau, C. M., Lee, D., Yu, Y., Crumlin, E. J., & Shao-Horn, Y. (2018). Speciation and Electronic Structure of La1−xSrxCoO3−δ During Oxygen Electrolysis. *Topics in Catalysis*, *61*(20), 2161–2174. https://doi.org/10.1007/s11244-018-1070-7

Storck, J. L., Brockhagen, B., Grothe, T., Sabantina, L., Kaltschmidt, B., Tuvshinbayar, K., Braun, L., Tanzli, E., Hütten, A., & Ehrmann, A. (2021). Stabilization and Carbonization of PAN Nanofiber Mats Electrospun on Metal Substrates. *C*, *7*(1), 12. https://doi.org/10.3390/c7010012

Su, Z., Yi, S., Zhang, W., Xu, X., Zhang, Y., & Zhou, S. (2023). Ultrafine Vacancy - Rich - Nb 2 O 5 Semiconductors Confined in Carbon Nanosheets Boost Dielectric Polarization for High - Attenuation Microwave Absorption. *Nano-Micro Letters*, *0123456789*, 1–16. https://doi.org/10.1007/s40820-023-01151-0

Suen, N. T., Hung, S. F., Quan, Q., Zhang, N., Xu, Y. J., & Chen, H. M. (2017). Electrocatalysis for the oxygen evolution reaction: Recent development and future perspectives. In *Chemical Society Reviews* (Vol. 46, Issue 2, pp. 337–365). https://doi.org/10.1039/c6cs00328a

Sun, H., Mei, L., Liang, J., Zhao, Z., Lee, C., Fei, H., Ding, M., Lau, J., Li, M., Wang, C., Xu, X., Hao, G., Papandrea, B., Shakir, I., Dunn, B., Huang, Y., & Duan, X. (2017). Three-dimensional holey-graphene/niobia composite architectures for ultrahigh-rate energy

storage. *Science*, *356*(6338), 599–604. https://doi.org/10.1126/science.aam5852

Sun, K., Zhang, S., Li, P., Xia, Y., Zhang, X., Du, D., Isikgor, F. H., & Ouyang, J. (2015). Review on application of PEDOTs and PEDOT:PSS in energy conversion and storage devices. *Journal of Materials Science: Materials in Electronics*, *26*(7), 4438–4462. https://doi.org/10.1007/s10854-015-2895-5

Sun, R., Zhang, H. Bin, Liu, J., Xie, X., Yang, R., Li, Y., Hong, S., & Yu, Z. Z. (2017). Highly Conductive Transition Metal Carbide/Carbonitride(MXene)@polystyrene Nanocomposites Fabricated by Electrostatic Assembly for Highly Efficient Electromagnetic Interference Shielding. *Advanced Functional Materials*, *27*(45), 1–11. https://doi.org/10.1002/adfm.201702807

Sun, Y. C., Leaker, B. D., Lee, J. E., Nam, R., & Naguib, H. E. (2019). Shape programming of polymeric based electrothermal actuator (ETA) via artificially induced stress relaxation. *Scientific Reports*, *9*(1), 1–13. https://doi.org/10.1038/s41598-019-47949-0

Sundarrajan, S., Tan, K. L., Lim, S. H., & Ramakrishna, S. (2014). Electrospun nanofibers for air filtration applications. *Procedia Engineering*, *75*, 159–163. https://doi.org/10.1016/j.proeng.2013.11.034

Sushma Devi, P., Nonganbi Chanu, S., Dasgupta, P., Sankar Swain, B., & Prasad Swain, B. (2022). Structural, optical, thermal and electrochemical properties of rGO/ PEDOT:PSS/PVP composite for supercapacitor electrode application. *Applied Physics A*, *128*, 403. https://doi.org/10.1007/s00339-022-05556-3

Sushmita, K., Madras, G., & Bose, S. (2020). Polymer nanocomposites containing sEMIconductors as advanced materials for EMI shielding. *ACS Applied Materials and Interfaces*. https://doi.org/10.1021/acsomega.9b03641

Tang, Ben Zhong, Alaa S. Abd-El-Aziz, S. C. (2014). *Electrospinning Series Editors : Titles in the Series :* , www.rsc.org

Tang, H., Chen, W., Wang, J., Dugger, T., Cruz, L., & Kisailus, D. (2018). Electrocatalytic N-Doped Graphitic Nanofiber – Metal/Metal Oxide Nanoparticle Composites. *Small*, *14*(11). https://doi.org/10.1002/smll.201703459

Teixeira, I., Castro, I., Carvalho, V., Rodrigues, C., Souza, A., Lima, R., Teixeira, S., & Ribeiro, J. (2021). Polydimethylsiloxane mechanical properties: A systematic review. *AIMS Materials Science*, *8*(6), 952–973. https://doi.org/10.3934/matersci.2021058

Triani, R. M., Mariani, F. E., De Assis Gomes, L. F., De Oliveira, P. G. B., Totten, G. E., & Casteletti, L. C. (2019). Improvement of the tribological characteristics of AISI 8620, 8640 and 52100 steels through thermo-reactive treatments. *Lubricants*, *7*(8), 1–13. https://doi.org/10.3390/lubricants7080063

Umeshbabu, E., & Ranga Rao, G. (2017). High Electrocatalytic Activity of Pt/C Catalyst Promoted by TT-Nb2O5 Nanoparticles under Acidic Conditions. *ChemistrySelect*, *2*(15),

4204–4212. https://doi.org/https://doi.org/10.1002/slct.201700256

Umeshbabu, E., & Ranga Rao, G. (2017). High Electrocatalytic Activity of Pt/C Catalyst Promoted by TT-Nb2O5 Nanoparticles under Acidic Conditions. *ChemistrySelect*, *2*(15), 4204–4212.

Van Bellingen, C., Probst, N., & Grivei, E. (2002). Specific conductive carbon blacks in plastics applications. *Polymers and Polymer Composites*, *10*(1), 63–71. https://doi.org/10.1177/096739110201000105

Wanasinghe, D., Aslani, F., Ma, G., & Habibi, D. (2020). *Review of Polymer Composites with Diverse Nanofillers for Electromagnetic Interference Shielding*. https://doi.org/10.3390/nano10030541

Wang, C., Liu, Y., Jia, Z., Zhao, W., & Wu, G. (2023a). Multicomponent Nanoparticles Synergistic One-Dimensional Nanofibers as Heterostructure Absorbers for Tunable and Efficient Microwave Absorption. *Nano-Micro Letters*, *15*(1). https://doi.org/10.1007/s40820-022-00986-3

Wang, C., Liu, Y., Jia, Z., Zhao, W., & Wu, G. (2023b). Multicomponent Nanoparticles Synergistic One-Dimensional Nanofibers as Heterostructure Absorbers for Tunable and Efficient Microwave Absorption. *Nano-Micro Letters*, *15*(1), 13.

Wang, J., Manivannan, A., & Wu, N. (2008). Sol-gel derived La0.6Sr0.4CoO3 nanoparticles, nanotubes, nanowires and thin films. *Thin Solid Films*, *517*(2), 582–587. https://doi.org/10.1016/j.tsf.2008.06.095

Wang, L., Ma, Z., Zhang, Y., Chen, L., Cao, D., Gu, J., Chen, C. L., Key, S., & Wang, # Lei. (2021). *Polymer-based EMI shielding composites with 3D conductive networks: A mini-review*. https://doi.org/10.1002/sus2.21

Wang, L., Qiu, H., Liang, C., Song, P., Han, Y., Han, Y., Gu, J., Kong, J., Pan, D., & Guo, Z. (2019). Electromagnetic interference shielding MWCNT-Fe3O4@Ag/epoxy nanocomposites with satisfactory thermal conductivity and high thermal stability. *Carbon*, *141*, 506–514. https://doi.org/10.1016/j.carbon.2018.10.003

Wang, T., Chen, Z., Gong, W., Xu, F., Song, X., He, X., & Fan, M. (2023). Electrospun Carbon Nanofibers and Their Applications in Several Areas. *ACS Omega*, *8*(25), 22316–22330. https://doi.org/10.1021/acsomega.3c01114

Wang, X., Huang, K., Yuan, L., Xi, S., Yan, W., Geng, Z., Cong, Y., Sun, Y., Tan, H., Wu, X., Li, L., & Feng, S. (2018). Activation of Surface Oxygen Sites in a Cobalt-Based Perovskite Model Catalyst for CO Oxidation [Rapid-communication]. *Journal of Physical Chemistry Letters*, *9*(15), 4146–4154. https://doi.org/10.1021/acs.jpclett.8b01623

Wang, X. Y., Liao, S. Y., Wan, Y. J., Zhu, P. L., Hu, Y. G., Zhao, T., Sun, R., & Wong, C. P. (2022). Electromagnetic interference shielding materials: recent progress, structure design, and future perspective. *Journal of Materials Chemistry C*, *10*(1), 44–72.

https://doi.org/10.1039/d1tc04702g

Wang, Y., Wang, W., Xu, R., Zhu, M., & Yu, D. (2019). Flexible, durable and thermal conducting thiol-modified rGO-WPU/cotton fabric for robust electromagnetic interference shielding. *Chemical Engineering Journal*, *360*, 817–828. https://doi.org/10.1016/j.cej.2018.12.045

Xi, G., Wang, C., Wang, X., Qian, Y., & Xiao, H. (2008). Te/carbon and Se/carbon nanocables: Size-controlled in situ hydrothermal synthesis and applications in preparing metal M/carbon nanocables (M = tellurides and selenides). *Journal of Physical Chemistry C*, *112*(4), 965–971. https://doi.org/10.1021/jp0764539

Xiang, J., Li, J., Zhang, X., Ye, Q., Xu, J., & Shen, X. (2014). Magnetic carbon nanofibers containing uniformly dispersed Fe/Co/Ni nanoparticles as stable and high-performance electromagnetic wave absorbers. *Journal of Materials Chemistry A*, *2*(40), 16905–16914. https://doi.org/10.1039/c4ta03732d

Xie, G., Jiao, H., & Li, X. (2008). Magnetic properties of Ni-Co-B coated carbon nanofibers. *Journal of Dispersion Science and Technology*, *29*(4), 475–477. https://doi.org/10.1080/01932690701727108

Xu, J., Xin, S., Liu, J. W., Wang, J. L., Lei, Y., & Yu, S. H. (2016). Elastic Carbon Nanotube Aerogel Meets Tellurium Nanowires: A Binder- and Collector-Free Electrode for Li-Te Batteries. *Advanced Functional Materials*, *26*(21), 3580–3588. https://doi.org/10.1002/adfm.201600640

Xu, L., Liang, H. W., Li, H. H., Wang, K., Yang, Y., Song, L. T., Wang, X., & Yu, S. H. (2015). Understanding the stability and reactivity of ultrathin tellurium nanowires in solution: An emerging platform for chemical transformation and material design. *Nano Research*, *8*(4), 1081–1097. https://doi.org/10.1007/s12274-014-0586-9

Xue, J., Wu, T., Dai, Y., & Xia, Y. (2019a). Electrospinning and electrospun nanofibers: Methods, materials, and applications. *Chemical Reviews*, *119*(8), 5298–5415. https://doi.org/10.1021/acs.chemrev.8b00593

Xue, J., Wu, T., Dai, Y., & Xia, Y. (2019b). Electrospinning and electrospun nanofibers: Methods, materials, and applications [Review-article]. *Chemical Reviews*, *119*(8), 5298–5415. https://doi.org/10.1021/acs.chemrev.8b00593

Xue, W. D., & Zhao, R. (2014). A simple approach towards nitrogen-doped graphene and metal/graphene by solid-state pyrolysis of metal phthalocyanine. *New Journal of Chemistry*, *38*(7), 2993–2998. https://doi.org/10.1039/c4nj00331d

Yadav, A. K., Mohammad, N., & Khanna, P. K. (2023). Novel synthesis of polyaniline/tellurium (PANI/Te) nanocomposite and its EMI shielding behavior. *Materials Advances*, 4409–4416. https://doi.org/10.1039/d3ma00394a

Yan, Jing, & Jeong, Y. G. (2017). Roles of carbon nanotube and BaTiO3 nanofiber in the

electrical, dielectric and piezoelectric properties of flexible nanocomposite generators. *Composites Science and Technology*, *144*, 1–10. https://doi.org/10.1016/j.compscitech.2017.03.015

Yan, Jun, Zheng, Q., Wang, S.-P., Tian, Y.-Z., Gong, W.-Q., Gao, F., Qiu, J.-J., Li, L., Yang, S.-H., & Cao, M.-S. (2023). Multifunctional Organic–Inorganic Hybrid Perovskite Microcrystalline Engineering and Electromagnetic Response Switching Multi-Band Devices. *Advanced Materials*, *35*(25), 2300015. https://doi.org/https://doi.org/10.1002/adma.202300015

Yang, B., Fang, J., Xu, C., Cao, H., Zhang, R., Zhao, B., Huang, M., Wang, X., Lv, H., & Che, R. (2022). One-Dimensional Magnetic FeCoNi Alloy Toward Low-Frequency Electromagnetic Wave Absorption. *Nano-Micro Letters*, *14*(1). https://doi.org/10.1007/S40820-022-00920-7

Yang, C., Jia, Z., Xu, Z., Wang, K., Guan, Z., & Wang, L. (2009). Comparisons of fibers properties between vertical and horizontal type electrospinning systems. *Annual Report - Conference on Electrical Insulation and Dielectric Phenomena, CEIDP*, 204–207. https://doi.org/10.1109/CEIDP.2009.5377758

Yang, D., Kong, X., Ni, Y., Xu, Y., Huang, S., Shang, G., Xue, H., Guo, W., & Zhang, L. (2018). Enhancement of Dielectric Performance of Polymer Composites via Constructing BaTiO3-Poly(dopamine)-Ag Nanoparticles through Mussel-Inspired Surface Functionalization. *ACS Omega*, *3*(10), 14087–14096. https://doi.org/10.1021/acsomega.8b02367

Yang, Yan, Deng, H., & Fu, Q. (2020). Recent progress on PEDOT:PSS based polymer blends and composites for flexible electronics and thermoelectric devices. *Materials Chemistry Frontiers*, *4*(11), 3130–3152. https://doi.org/10.1039/d0qm00308e

Yang, Yonglai, Gupta, M. C., Dudley, K. L., & Lawrence, R. W. (2005). A comparative study of EMI shielding properties of carbon nanofiber and multi-walled carbon nanotube filled polymer composites. *Journal of Nanoscience and Nanotechnology*, *5*(6), 927–931. https://doi.org/10.1166/jnn.2005.115

Ye, D., Peng, Z., Liu, J., & Huang, Y. (2022). Self-Limited ultraviolet laser sintering of liquid metal particles for μm-Thick flexible electronics devices. *Materials & Design*, *223*, 111189. https://doi.org/https://doi.org/10.1016/j.matdes.2022.111189

Yongjian Xu, Yan Liu, Shenglin Chen, Y. N. (2020). Current Overview of Carbon Fiber : Toward Green. *BioResources*, *15*(3), 7234–7259.

Yousefi, N., Sun, X., Lin, X., Shen, X., Jia, J., Zhang, B., Tang, B., Chan, M., & Kim, J. K. (2014). Highly aligned graphene/polymer nanocomposites with excellent dielectric properties for high-performance electromagnetic interference shielding. *Advanced Materials*, *26*(31), 5480–5487. https://doi.org/10.1002/adma.201305293

Yuan, Y., Yin, W., Yang, M., Xu, F., Zhao, X., Li, J., Peng, Q., He, X., Du, S., & Li, Y. (2018). Lightweight, flexible and strong core-shell non-woven fabrics covered by reduced graphene oxide for high-performance electromagnetic interference shielding. *Carbon*, *130*, 59–68. https://doi.org/10.1016/j.carbon.2017.12.122

Zahid, M., Anum, R., Siddique, S., Shakir, H. M. F., & Rehan, Z. A. (2021a). Polyaniline-based nanocomposites for electromagnetic interference shielding applications: A review. In *Journal of Thermoplastic Composite Materials* (Issue June). https://doi.org/10.1177/08927057211022408

Zahid, M., Anum, R., Siddique, S., Shakir, H. M. F., & Rehan, Z. A. (2021b). Polyaniline-based nanocomposites for electromagnetic interference shielding applications: A review. In *Journal of Thermoplastic Composite Materials*. https://doi.org/10.1177/08927057211022408

Zalewski, K., Chyłek, Z., & Trzciński, W. A. (2021). A Review of Polysiloxanes in Terms of Their Application in Explosives. *Polymers*, *13*(7). https://doi.org/10.3390/polym13071080

Zambonino, M. C., Quizhpe, E. M., Jaramillo, F. E., Rahman, A., Vispo, N. S., Jeffryes, C., & Dahoumane, S. A. (2021). Green synthesis of selenium and tellurium nanoparticles: Current trends, biological properties and biomedical applications. *International Journal of Molecular Sciences*, *22*(3), 1–34. https://doi.org/10.3390/ijms22030989

Zargham, S., Bazgir, S., Tavakoli, A., Rashidi, A. S., & Damerchely, R. (2012). The effect of flow rate on morphology and deposition area of electrospun nylon 6 nanofiber. *Journal of Engineered Fibers and Fabrics*, *7*(4), 42–49. https://doi.org/10.1177/155892501200700414

Zhang, F., Zhang, Z., Liu, Y., & Leng, J. (2014). Electrospun nanofiber membranes for electrically activated shape memory nanocomposites. *Smart Materials and Structures*, *23*(6). https://doi.org/10.1088/0964-1726/23/6/065020

Zhang, H.-D., Yan, X., Zhang, Z.-H., Yu, G.-F., Han, W.-P., Zhang, J.-C., & Long, Y.-Z. (2016). Electrospun PEDOT: PSS/PVP nanofibers for CO gas sensing with quartz crystal microbalance technique. *International Journal of Polymer Science*, *2016*.

Zhang, Li, Wang, L., Holt, C. M. B., Navessin, T., Malek, K., Eikerling, M. H., & Mitlin, D. (2010). Oxygen reduction reaction activity and electrochemical stability of thin-film bilayer systems of platinum on niobium oxide. *The Journal of Physical Chemistry C*, *114*(39), 16463–16474.

Zhang, Liying, Wang, L. B., See, K. Y., & Ma, J. (2013). Effect of carbon nanofiber reinforcement on electromagnetic interference shielding effectiveness of syntactic foam. *Journal of Materials Science*, *48*(21), 7757–7763. https://doi.org/10.1007/s10853-013-7597-x

Zhang, M., Han, C., Cao, W. Q., Cao, M. S., Yang, H. J., & Yuan, J. (2021). A Nano-Micro Engineering Nanofiber for Electromagnetic Absorber, Green Shielding and Sensor. *Nano-Micro Letters*, *13*(1). https://doi.org/10.1007/s40820-020-00552-9

Zhang, Shijie, Li, J., Jin, X., & Wu, G. (2023). Current advances of transition metal dichalcogenides in electromagnetic wave absorption: A brief review. *International Journal of Minerals, Metallurgy and Materials*, *30*(3), 428–445.

Zhang, Shuo, & Jia, Z. (1998). *Multicomponent Heterostructures As Flexible Electromagnetic Wave Absorbers*. 1–13.

Zhang, T., Huang, D., Yang, Y., Kang, F., & Gu, J. (2013). Fe3O4/carbon composite nanofiber absorber with enhanced microwave absorption performance. *Materials Science and Engineering: B*, *178*(1), 1–9. https://doi.org/10.1016/J.MSEB.2012.06.005

Zhang, Ximing, Fan, Y., Wang, J., Xian, G., Liu, Z., Xie, A., Wang, Y., Li, J., Liu, Y., Gao, J., & Kong, L. B. (2022a). Synergistic effect of niobium oxide and cobalt on electromagnetic properties of dodecahedron-carbon composites. *Journal of Solid State Chemistry*, *311*(November 2021), 123122. https://doi.org/10.1016/j.jssc.2022.123122

Zhang, Ximing, Fan, Y., Wang, J., Xian, G., Liu, Z., Xie, A., Wang, Y., Li, J., Liu, Y., Gao, J., & Kong, L. B. (2022b). Synergistic effect of niobium oxide and cobalt on electromagnetic properties of dodecahedron-carbon composites. *Journal of Solid State Chemistry*, *311*, 123122. https://doi.org/10.1016/J.JSSC.2022.123122

Zhang, Xinci, Xu, J., Yuan, H., Zhang, S., Ouyang, Q., Zhu, C., Zhang, X., & Chen, Y. (2019). Large-Scale Synthesis of Three-Dimensional Reduced Graphene Oxide/Nitrogen-Doped Carbon Nanotube Heteronanostructures as Highly Efficient Electromagnetic Wave Absorbing Materials. *ACS Applied Materials & Interfaces*, *11*(42), 39100–39108. https://doi.org/10.1021/acsami.9b13751

Zhang, Xuefeng, Wang, M., Tu, J., & Jiao, S. (2021). Hierarchical N-doped porous carbon hosts for stabilizing tellurium in promoting Al-Te batteries. *Journal of Energy Chemistry*, *57*, 378–385. https://doi.org/10.1016/j.jechem.2020.09.015

Zhang, Yali, & Gu, J. (2022). A Perspective for Developing Polymer-Based Electromagnetic Interference Shielding Composites. *Nano-Micro Letters*, *14*(1), 1–9. https://doi.org/10.1007/s40820-022-00843-3

Zhang, Yang, Pan, T., & Yang, Z. (2020). Flexible polyethylene terephthalate/polyaniline composite paper with bending durability and effective electromagnetic shielding performance. *Chemical Engineering Journal*, *389*(December 2019), 124433. https://doi.org/10.1016/j.cej.2020.124433

Zhang, Yang, Yang, Z., Pan, T., Gao, H., Guan, H., Xu, J., & Zhang, Z. (2020). Construction of natural fiber/polyaniline core-shell heterostructures with tunable and excellent electromagnetic shielding capability via a facile secondary doping strategy. *Composites*

Part A: Applied Science and Manufacturing, *137*(February), 105994. https://doi.org/10.1016/j.compositesa.2020.105994

Zhang, Yue, Lu, W., Zhao, P., Tao, L., Liu, Y., Manaig, D., Freschi, D. J., & Liu, J. (2021). The role of carbon pore structure in tellurium/carbon cathodes for lithium-tellurium batteries. *Electrochimica Acta*, *388*, 138621. https://doi.org/10.1016/j.electacta.2021.138621

Zhang, Zhenfang, Ji, D., He, H., & Ramakrishna, S. (2021). Electrospun ultrafine fibers for advanced face masks. *Materials Science and Engineering R: Reports*, *143*(July 2020), 100594. https://doi.org/10.1016/j.mser.2020.100594

Zhang, Zhichun, Zhang, F., Jiang, X., Liu, Y., Guo, Z., & Leng, J. (2014). Electrospinning and microwave absorption of polyaniline/polyacrylonitrile/multiwalled carbon nanotubes nanocomposite fibers. *Fibers and Polymers*, *15*(11), 2290–2296. https://doi.org/10.1007/s12221-014-2290-5

Zhang, Zhu, Wang, G. H., Gu, W., Zhao, Y., Tang, S., & Ji, G. (2022). A breathable and flexible fiber cloth based on cellulose/polyaniline cellular membrane for microwave shielding and absorbing applications. *Journal of Colloid and Interface Science*, *605*, 193–203. https://doi.org/10.1016/j.jcis.2021.07.085

Zhang, Ziyu, Zhao, Y., Li, Z., Zhang, L., Liu, Z., Long, Z., Li, Y., Liu, Y., Fan, R., Sun, K., & Zhang, Z. (2022). Synthesis of carbon/SiO2 core-sheath nanofibers with Co-Fe nanoparticles embedded in via electrospinning for high-performance microwave absorption. *Advanced Composites and Hybrid Materials*, *5*(1), 513–524. https://doi.org/10.1007/s42114-021-00350-w

Zhao, K., Wang, W., Yang, Y., Wang, K., & Yu, D. G. (2019). From Taylor cone to solid nanofiber in tri-axial electrospinning: Size relationships. *Results in Physics*, *15*, 102770. https://doi.org/10.1016/j.rinp.2019.102770

Zhen, D., Zhao, B., Shin, H. C., Bu, Y., Ding, Y., He, G., & Liu, M. (2017). Electrospun Porous Perovskite La0.6Sr0.4Co1–xFexO3–δ Nanofibers for Efficient Oxygen Evolution Reaction. *Advanced Materials Interfaces*, *4*(13), 1–8. https://doi.org/10.1002/admi.201700146

Zheng, Q., Cao, W. Q., Zhai, H., & Cao, M. S. (2023). Tailoring carbon-based nanofiber microstructures for electromagnetic absorption, shielding, and devices. *Materials Chemistry Frontiers*, 1737–1759. https://doi.org/10.1039/d2qm01271e

Zheng, Q., Wang, J., Yu, M., Cao, W.-Q., Zhai, H., & Cao, M.-S. (2023). Heterodimensional structure porous nanofibers embedded confining magnetic nanocrystals for electromagnetic functional material and device. *Carbon*, *210*, 118049. https://doi.org/https://doi.org/10.1016/j.carbon.2023.118049

Zhong, W. (2016). Nanofibres for Medical Textiles. *Advances in Smart Medical Textiles:*

Treatments and Health Monitoring, 57–70. https://doi.org/10.1016/B978-1-78242-379-9.00003-7

Zhou, M., Tan, S., Wang, J., Wu, Y., Liang, L., & Ji, G. (2023). "Three-in-One" Multi-Scale Structural Design of Carbon Fiber-Based Composites for Personal Electromagnetic Protection and Thermal Management. *Nano-Micro Letters*, *15*(1), 1–17. https://doi.org/10.1007/s40820-023-01144-z

Zhou, Z., Tang, H., & Sodano, H. A. (2013). Vertically Aligned Arrays of BaTiO3 Nanowires. *ACS Applied Materials & Interfaces*, *5*(22), 11894–11899. https://doi.org/10.1021/am403587q

Zhu, H., Fan, L., Wang, K., Liu, H., Zhang, J., & Yan, S. (2023). Progress in the Synthesis and Application of Tellurium Nanomaterials. *Nanomaterials*, *13*(14). https://doi.org/10.3390/nano13142057

Zhu, M., Han, J., Wang, F., Shao, W., Xiong, R., Zhang, Q., Pan, H., Yang, Y., Samal, S. K., Zhang, F., & Huang, C. (2017). Electrospun Nanofibers Membranes for Effective Air Filtration. *Macromolecular Materials and Engineering*, *302*(1), 1–27. https://doi.org/10.1002/mame.201600353

Zhu, S., Xu, P., Liu, J., & Sun, J. (2020). Atomic layer deposition and structure optimization of ultrathin Nb2O5 films on carbon nanotubes for high-rate and long-life lithium ion storage. *Electrochimica Acta*, *331*(xxxx), 135268. https://doi.org/10.1016/j.electacta.2019.135268

Zhu, Y. X., Wang, S. F., Zhang, Y. S., Wu, Z. G., Zhong, B., Li, D. R., Wang, F. Y., Feng, J. J., Tang, J., Zhuo, R. F., & Yan, P. X. (2021). Large-scale preparation of Co nanoparticles as an additive in carbon fiber for microwave absorption enhancement in C band. *Scientific Reports*, *11*(1), 1–14. https://doi.org/10.1038/s41598-021-81848-7

Zou, D., Li, J., Deng, J., Jin, Y., & Chen, M. (2021). Continuous Preparation of Size-Controllable BaTiO3Nanoparticles in a Rotor-Stator Spinning Disk Reactor. *Industrial and Engineering Chemistry Research*, *60*(40), 14511–14518. https://doi.org/10.1021/acs.iecr.1c02152

List of Publications Based on Thesis

International Journals

1. **Govind Kumar Sharma,** Nirmala R. James; Progress in Electrospun Polymer Composite Fibers for Microwave Absorption and Electromagnetic Interference Shielding. *ACS Appl. Electron. Mater.* **2021**, *3* (11), 4657–4680. https://doi.org/10.1021/acsaelm.1c00827

2. **Govind Kumar Sharma**, Nirmala R. James; Carbon Black Incorporated Carbon Nanofiber Based Polydimethylsiloxane Composite for Electromagnetic Interference Shielding. *Carbon Trends* **2022**, *8*, 100177. https://doi.org/10.1016/J.CARTRE.2022.100177.

3. **Govind Kumar Sharma**, Nirmala R. James; Highly Flexible , PEDOT : PSS-Polyvinylpyrrolidone Coated Carbon Nanofiber-Polydimethylsiloxane Composite for Electromagnetic Interference Shielding. *Synth. Met.* **2023**, *296* (May), 117376. https://doi.org/10.1016/j.synthmet.2023.117376.

4. **Govind Kumar Sharma**, Nirmala R. James; Flexible N-Doped Carbon Nanofiber-Polydimethylsiloxane composite containing La0.85Sr.15CoO3-δ Nanoparticles for Green EMI Shielding. *ACS Applied Nano Materials*. **2023**, 6, 7, 6024–6035. https://doi.org/10.1021/acsanm.3c00382

5. **Govind Kumar Sharma**; Harel, P. G.; Nirmala R. James. Flexible N-Doped Carbon Nanofiber Containing Nb_2O_5 Nanoparticle and its polydimethylsiloxane composite for Electromagnetic Interference Shielding. Carbon N. Y. **2023**, 214 (August), 118367. https://doi.org/10.1016/j.carbon.2023.118367.

6. **Govind Kumar Sharma,** Sneha L Joseph, and Nirmala Rachel James; Recent Progress in Poly (3,4-Ethylene Dioxythiophene): Polystyrene Sulfonate Based Composite Materials for Electromagnetic Interference Shielding. Advance materials Technologies, **2023**, 2301203. https://doi.org/10.1002/admt.202301203

7. **Govind Kumar Sharma** and Nirmala R. James; Aligned, carbon nanofibers containing barium titanate and their polydimethylsiloxane composites for electromagnetic interference shielding, Carbon, **2024**, 220, 118846. https://doi.org/10.1016/j.carbon.2024.118846.

8. **Govind Kumar Sharma,** Sneha L Joseph, Athira M. S, and Nirmala R. James; Tellurium Nanoparticles Incorporated into Electrospun Polyacrylonitrile Nanofibers, followed by Carbonization and their Polydimethylsiloxane Composites for Electromagnetic Interference Shielding. ACS applied Nano Materials**, 2024,** 7, 6, 5819-5830. https://doi.org/10.1021/acsanm.3c04810

Book Chapter

1. **Govind Kumar Sharma,** Nirmala R. James. Electrospinning: The Techniques and Applications. *Intechopen* **2022**, 13. http://dx.doi.org/10.5772/intechopen.105804

Other Publications

1. **Govind Kumar Sharma,** Jalaja K, Ramya P R, N.R. James, "Electrospun Gelatin Nanofibers Fabrication, Cross-linking and Bio-Medical Applications: A Review". "*Biomedical materials and devices*". **2022**, No. 0123456789. https://doi.org/10.1007/s44174-022-00042-z.

2. Raji S, **Govind Kumar Sharma**, K. Prabhakaran; Carbon Foams by Solid State Foaming of Short Vermicelli Bonded by Phenol-Formaldehyde for thermal insulation and Electromagnetic Interference Shielding. *ACS Applied Engineering Materials*. **2023**, 1,3,913-923. https://doi.org/10.1021/acsaenm.2c00067

3. Raji, S.; **Govind Kumar Sharma**; Aranya, B. R.; Prabhakaran, K. Carbon Composite Foams from the Wasted Banana Leaf for EMI Shielding and Thermal Insulation. *Carbon N. Y.* **2023**, 118259. https://doi.org/10.1016/j.carbon.2023.118259.

List of Conferences/Seminars attended

Oral Presentation

1. **Govind Kumar Sharma** and Nirmala Rachel James; Nitrogen doped Carbon Nanofiber coated with PEDOT:PSS-polyvinylpyrrolidone and their PDMS composites as flexible high performance Electromagnetic Interference Shielding Material. 17th International conference on Polymer Science and Technology, **SPSI-MACRO-2023**, organized by IIT Guwahati, December 10-13th, 2023.

2. **Govind Kumar Sharma**, Prashant Govind Harel, and Nirmala Rachel James; Flexible Nb_2O_5 Nanoparticle incorporated N-doped Carbon Nanofiber and its PDMS Composite for EMI Shielding. "Polymer Processing Society Asia-Australasia Regional Conference" **PPS-2023**, organized by PPA Mumbai, VSSC, IIST Thiruvananthapuram, 29th Nov-2nd Dec 2023.

3. **Govind Kumar Sharma** and Nirmala Rachel James, Flexible N-Doped CNF-PDMS Composite Containing $La_{0.85}Sr_{0.15}CoO_3$ nanoparticles for Green EMI Shielding, National Conference on "New Developments in Polymeric Materials" **DPM-2023**, organized by SPSI Thiruvananthapuram Chapter, March 02-03rd, 2023.
4. **Govind Kumar Sharma** and Nirmala Rachel James, Flexible, Carbon Black incorporated CNF-based PDMS composites for EMI shielding. International conference on "Emerging Trends in Advanced Functional Materials" **ETAFM-2022**, organized by Catholicate College Pathanamthitta, August 11-12th, 2022.
5. **Govind Kumar Sharma** and Nirmala Rachel James, Annual technical seminar, "Materials research society of India", **Trivandrum chapter – 2022** Organized jointly by MRSI, Trivandrum Chapter and (SCTIMST), April 2022

Poster Presentation

1. **Govind Kumar Sharma** and Nirmala Rachel James, Highly Flexible PEDOT:PSS-PVP Coated CNF-PDMS composites for EMI shielding, National conference on "Advanced Materials and Manufacturing Technologies" **AMMT-2023**, organized by CSIR-NIIST, February 23-24th, 2023.

2. **Govind Kumar Sharma** and Nirmala Rachel James, Highly Flexible PEDOT:PSS-PVP Coated Carbon Nanofiber-Polydimethylsiloxane composites for EMI shielding, National conference on "Recent trends in materials science and technology" **NCMST-2022**, organized by IIST Thiruvananthapuram, December 28-30th, 2022.
3. **Govind Kumar Sharma** and Nirmala Rachel James, Flexible, Carbon Black incorporated CNF-based PDMS composites for EMI shielding, International Conference on "Science and technology of polymers and Advanced Materials through Innovation, Entrepreneurship and Industry" **SPSI-MACRO-2022**, organized by CSIR-NCL and IISER Pune, December 02-04th, 2022.

Conference attended

1. Participated in National conferences on "Frontiers of Aerospace Systems and Technology" (FAST-2022), Organized by Vikram Sarabhai Space Centre, July,7-8th, 2022.
2. Participated in National conference on "Recent trends in materials science and technology" organized by IIST, Trivandrum. Date: 28-29th December 2021.
3. Participated in National conference on "Recent trends in materials science and technology" organized by IIST, Trivandrum. Date: 7-9th December 2020.

Awards

- **Best Oral Presentation**: SPSI-MACRO-2023, organized by IIT Guwahati, December 10-13th, 2023.
- **Best Poster Presentation**: NCMST-2022, organized by IIST Thiruvananthapuram, December 28-30th, 2022.
- **Best Sport Caption**: Intra-college tournament held at IIST Thiruvananthapuram, Academic session April-2021 to April 2022.